INTERFERENCE SUPPRESSION
FOR 121.5/243 MHz SARSAT SIGNALS

By

XIANGQUN SUN, B. Sc. (E. C. N. University), M. Eng. (McMaster University)

A Thesis
Submitted to the School of Graduate Studies
in Partial Fulfilment of the Requirements
for the Degree
Doctor of Philosophy

McMaster University
May 2000

INTERFERENCE SUPPRESSION
FOR 121.5/243 MHz SARSAT SIGNALS

DOCTOR OF PHILOSOPHY (2000) MCMASTER UNIVERSITY
(Electrical and Computer Engineering) Hamilton, Ontario

TITLE:	**Interference Suppression** **For 121.5/243 MHz SARSAT Signals**
AUTHOR:	Xiangqun Sun B. Sc. (East China Normal University) M. Eng. (McMaster University)
SUPERVISOR:	Dr. C. R. Carter Professor Department of Electrical and Computer Engineering
NUMBER OF PAGES:	xxvi, 210

ABSTRACT

When an aircraft or marine vessel is in distress, the emergency unit is activated either automatically or by manually setting a switch. The signal is then received by an orbiting satellite as it sweeps out a path over the search and rescue satellite aided tracking (SARSAT) region of interest. Due to the relative motion between the satellite and the Emergency Locator Transmitter (ELT) or the Emergency Position Indicating Radio Beacon (EPIRB) unit, the signal received at the spacecraft is Doppler shifted. A repeater on board the satellite relays the signal to an earth station where the signal is analyzed to extract the position of the accident.

The zero Doppler shift frequency, occurring at the inflection point of the Doppler curve, is the point of closest approach of the satellite to the accident site. Consequently, this frequency must be determined with as much accuracy as possible since the slope of the Doppler curve at this point is used to calculate the range from satellite to the transmitting source. With the range and the known position of the satellite, the location of the emergency signal source can be estimated. This estimate is passed to a Rescue Coordination Center (RCC) which speedily dispatches search aircraft to the emergency site.

The 121.5 MHz ELT and EPIRB cost less than U.S.$200 and their use will continue well into the 21st century. There are about 500,000 units in operation but unfortunately many problems plague the 121.5 MHz ELT/EPIRB beacons since they were never intended for the COSPAS/SARSAT mode of operation. In addition, interference emanating from myriad sources on earth adds to the uplinked ELT signals. It is the reduction in this interference which is examined in this thesis.

New processing techniques for detecting ELT signals in an interfering background are investigated, based on not only computer simulations but also experimental data. The new methods involve the use of the Geometrically Averaged Spectrum (GAS) and the Harmonically Averaged Spectrum (HAS) in addition to the Arithmetically Averaged Spectrum (AAS) adopted by the existing system.

Specifically, this thesis investigates the theoretical performance of AAS, GAS and HAS averaging in practical circumstances involving signals, noise and interference. It is shown that the carrier peaks of good ELT signals can be substantially enhanced in an interfering background. The treatise identifies certain types of interference such as Carrier interference with strong or weak AM, On-Off Modulation interference, Swept Carrier interference, and Ringing Response interference. Using computer simulation, it is demonstrated that under certain conditions the effects of background interference can be greatly reduced and the detection of ELT carrier peaks can be improved by employing a combination of AAS, GAS and HAS averaging. Real SARSAT pass data signals are fed into the computer and processed using AAS, GAS and HAS averaging. The background interference postulated in this thesis is found to exist and real ELT signals are identified. ELT signals representing the NIC model and a new model, called the Frequency Modulated ELT (FME) model, are identified along with a new

ELT signal for which a model cannot presently be envisaged.

The results of letting AAS, GAS, and HAS work together are compared to that of using only AAS. It is seen that the new strategy shows superior performance over the original method in a congested signal environment even though interference power exceeds ELT signal power.

Acknowledgements

I would like to express sincere gratitude to my supervisor Dr. C.R. Carter for his constant support, supervision, and encouragement throughout the course of this work. Without his guidance, this work would not be possible.

I also gratefully acknowledge the contributions of Dr. T.Z. Luo and Dr. P.C. Yip for serving on my supervisory committee.

It is my pleasure to acknowledge the interesting discussions with Dr. S.H. Chisholm, Dr. J.P. Reilly, Dr. A.F. Vaz, Dr. E. Sekerinski, and many other people with whom I have worked in the Communications Research Laboratory of McMaster University.

Finally, I would like to give cordial thanks to my whole family. I am especially indebted to my wife, Minya Zhang, and my daughter, Nike Sun. Without their constant understanding, support, and love, I would not have been able to successfully complete this work.

Contents

3 Nonlinear Spectral Averaging 52

List of Figures

List of Acronyms

AAS	Arithmetically Averaged Spectrum	18
AAV	Arithmetically Averaged Value	17
AM	Amplitude Modulation	80
CCO	Crystal Controlled Oscillator	29
CNDR	Carrier-to-Noise Density Ratio	22
COSPAS	COsmicheskaya Systyema Poiska Avariynich Sudov[1]	1
ELT	Emergency Locator Transmitter	3
EPIRB	Emergency Position Indicating Radio Beacon	3
FFT	Fast Fourier Transform	3
FM	Frequency-Modulated	44
FME	Frequency-Modulated ELT	44
GAS	Geometrically Averaged Spectrum	18
GAV	Geometrically Averaged Value	17
HAS	Harmonically Averaged Spectrum	18
HAV	Harmonically Averaged Value	17
ICE	Ideal Coherent ELT	19
LUT	Local User Terminal	1
MCC	Mission Control Center	1
NCE	Non-Coherent ELT	36

---

1 In Russian language: translates to "Space System for the Detection of Vessels in Distress."

NIC	Non-Ideal Coherent ELT	27
RCC	Rescue Coordination Center	5
SAR	Search And Rescue	3
SARSAT	Search And Rescue Satellite Aided Tracking	1
SPOC	Search and Rescue Point of Contact	1

List of Symbols

A	12
$A(f)$	53
$A(f_d)$	61
$A(f_u)$	61
$A^*(f)$	62
$A^*(f_d)$	65
$A^*(f_u)$	65
$A^{fme}(f)$	46
$A^{ice}(f)$	23
$A^{nce}(f)$	38
$A^{nic}(f)$	30
$\mathrm{AAS}(f)$	18
C	88
d	12
$F(f)$	16

$\mathcal{F}[\cdot]$	14
$F_i(f)$	15
$F_i'(f)$	15
$F_k(f)$	18
$F^{fme}(f)$	45
$F_k^{fme}(f)$	46
$F^{ice}(f)$	20
$F_k^{ice}(f)$	22
$F^{nce}(f)$	36
$F_k^{nce}(f)$	38
$F^{nic}(f)$	29
$F_k^{nic}(f)$	30
f	94
f_c	12
$f_c(t)$	44
f_{cco}	29
f_d	56
f_p	27
f_s	29
f_u	56
$G(f)$	53

$G(f_d)$	61
$G(f_u)$	61
$G^*(f)$	62
$G^*(f_d)$	65
$G^*(f_u)$	65
$G^{fme}(f)$	46
$G^{ice}(f)$	23
$G^{nce}(f)$	38
$G^{nic}(f)$	33
$\mathrm{GAS}(f)$	18
$g(t)$	14
$H(f)$	53
$H(f_d)$	61
$H(f_u)$	61
$H^*(f)$	62
$H^{fme}(f)$	46
$H^{ice}(f)$	23
$H^{nce}(f)$	41
$H^{nic}(f)$	33
$\mathrm{HAS}(f)$	18
h	72

I_{G-A}	65
I_{H-A}	65
K	18
K_1	88
K_2	88
k	18
ℓ	94
M	10
N	10
N_f	22
N_k	89
$S_1(f_d)$	56
$S_2(f_d)$	56
$S_3(f_d)$	56
$S_1(f_u)$	61
$S_2(f_u)$	61
$S_3(f_u)$	61
$S_{\max}(f)$	71
$S_{\mathrm{mid}}(f)$	71
$S_{\mathrm{mid}}(f_d)$	61
$S_{\mathrm{mid}}(f_u)$	61

$S_{\min}(f)$	71
$S_{k+1}(f)$	71
$S_1(f)$	72
$S_{\frac{K+1}{2}}(f)$	72
$S_K(f)$	72
$S_k(f)$	18
$S^{ice}(f)$	21
$S_k^{ice}(f)$	22
$S^{nic}(f)$	30
$S_k^{nic}(f)$	30
$S^{nce}(f)$	38
$S_k^{nce}(f)$	38
$S_k^{fme}(f)$	46
$s(t)$	12
$s_i(t)$	12
$s_i'(t)$	14
T	14
$\mathcal{T}$	16
T_1	10
T_D	10
T_M	10

T_S	10
T_i	12
$\mathcal{T}_k$	45
T_s	22
t_i	12
W_{bin}	194
$\beta^{nic}(f)$	95
$\gamma^{ice}(f)$	93
$\gamma^{nic}(f)$	95
Θ_i	36
Θ_{i_k}	96
θ_i	14
θ_0	20
Δf_c	44
$\Delta_S(f)$	71
$\Delta_S(f_u)$	61
$\Delta_S(f_d)$	61
$\Delta_{A-G}(f)$	62
$\Delta_{A-H}(f)$	62
$\Delta^*_{A-G}(f)$	62
$\Delta^*_{A-H}(f)$	62

$\Delta_{A-G}(f_u)$	65
$\Delta_{A-G}(f_d)$	65
$\Delta^*_{A-G}(f_u)$	65
$\Delta^*_{A-G}(f_d)$	65
$\Delta_{A-H}(f_u)$	65
$\Delta_{A-H}(f_d)$	65
$\Delta^*_{A-H}(f_u)$	65
$\Delta^*_{A-H}(f_d)$	65
$\eta(f)$	81
$\eta(f_d)$	86
$\eta(f_u)$	86
ϵ	88
$\frac{\Delta_S(f)}{S_{\text{mid}}(f)}$	77
$\frac{\Delta_S(f_d)}{S_{\text{mid}}(f_d)}$	63
$\frac{\Delta_S(f_u)}{S_{\text{mid}}(f_u)}$	63

Chapter 1

Introduction

1.1 COSPAS/SARSAT

The COSPAS/SARSAT system, illustrated in Fig. 1.1, is well described in the literature [1-6]. From the Russian language, COSPAS (COsmicheskaya Systyema Poiska Avariynich Sudov) translates to Space System for the Detection of Vessels in Distress while SARSAT is the acronym for Search And Rescue Satellite Aided Tracking [7]. The system currently employs a network of six satellites in near polar orbits around the earth ranging from 850 to 1000 km (SARSAT 2, 3, 4, and 6 are American satellites while COSPAS 4 and 6 are Russian satellites [8]). The four original member nations consisting of the United States, Canada, France and the Soviet Union have now been joined by 25 other nations [9] that operate 35 Local User Terminals (LUTs) [10] and 15 Mission Control Centers (MCCs) [9] worldwide or serve as Search and Rescue Points of Contact (SPOCs) [9]. COSPAS/SARSAT became operational in 1985 and is already responsible for saving more than 6200 lives

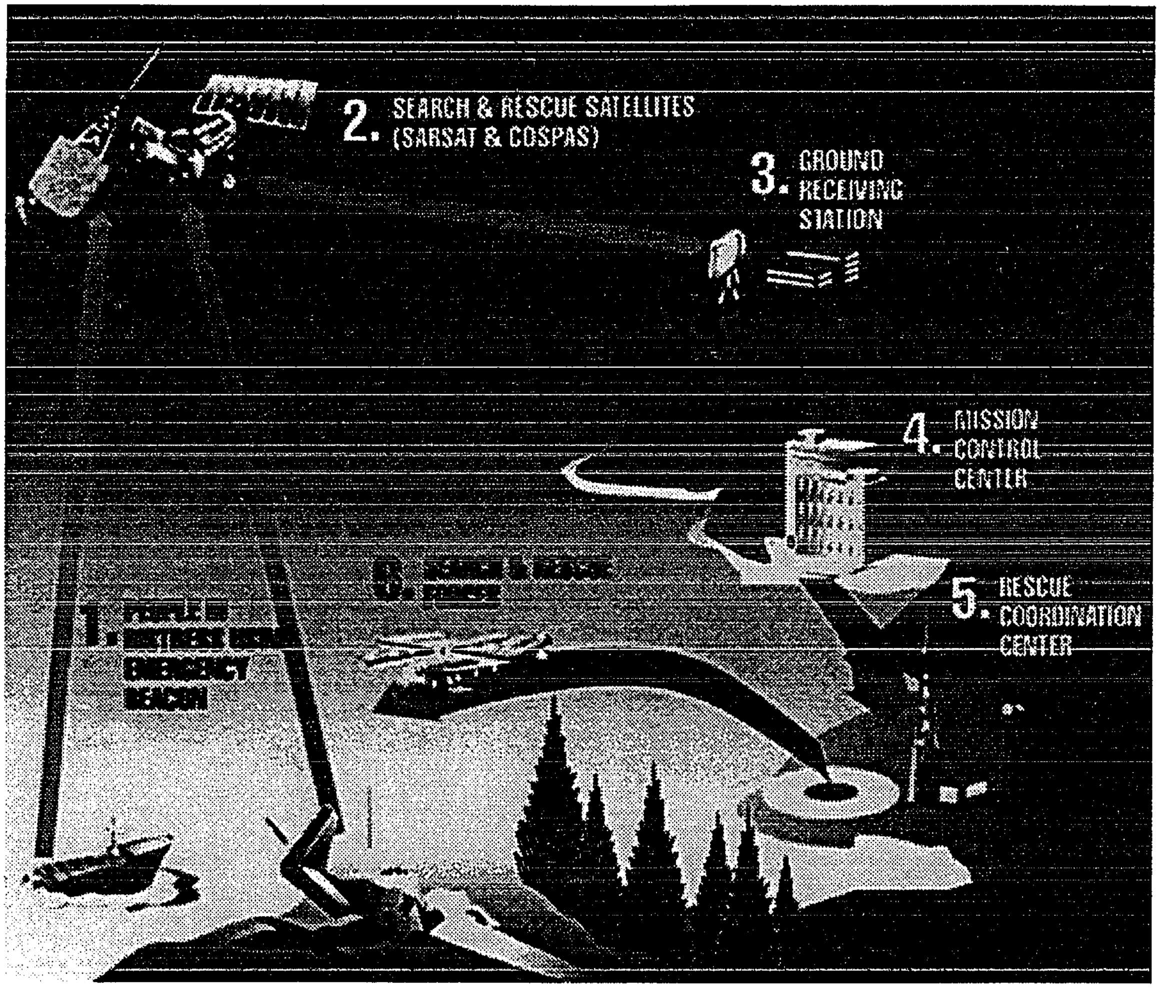

Figure 1.1: The COSPAS/SARSAT system [11].

and many millions of dollars by eliminating costly grid searches by Search And Rescue (SAR) aircraft.

The 121.5 MHz Emergency Locator Transmitter (ELT) and the Emergency Position Indicating Radio Beacon (EPIRB) cost less than U.S.$200 and their use will continue well into the 21st century. There are about 500,000 units in operation. Ideally, the ELT signal should be easily detectable, provide accurate location, and identify the aircraft or marine vessel. Unfortunately, many problems plague the 121.5 MHz ELT/EPIRB beacons since they were never intended for the COSPAS/SARSAT mode of operation. The problems include: 1) Interaction between the modulator and the carrier oscillator producing frequency pulling [12] which greatly reduces the effectiveness of any simple Fast Fourier Transform (FFT) signal processor. 2) No effective means of identifying the signal as a 121.5 MHz beacon from its modulation. 3) Frequency congestion in the 121.5 MHz band causing a high satellite false alert rate (99.8% [13]) requiring confirmation before search and rescue forces can be deployed. 4) Ambiguity in location leading to the need for two or more satellite passes to determine if the signal is from a 121.5 MHz beacon, delaying rescue by an average of 4 to 6 hours. In some cases, a rescue can be delayed as long as 12 hours. 5) Poor accuracy since the location estimate is presently not much better than 20 km which leaves considerable territory to be covered. 6) Low signal-to-noise ratio since the transmitter power is only about 100 mW which requires the most sophisticated signal processing for detection. 7) No way of verifying who originated the signal. 8) Interference emanating from myriad sources on earth which adds to the uplinked ELT signals [14]. Interference can: a) mask an ELT signal; b) affect the location estimate;

c) give false alerts; and d) increase the computational burden. It is this last item which is examined in this thesis.

The human tragedy for families in not locating distressed aircraft is immense and there are many cases of this. In geophysical surveying alone, there have been three crashes in recent years [15]. In May of 1996, a small geophysical survey plane carrying four Canadians working in Peru disappeared without a trace. An ELT signal was apparently received by the SARSAT system but no location was obtained due possibly to low signal-to-noise ratio or background interference.

Larger aircraft also go missing. For instance, in September 1990, a Peruvian Boeing 727 jet passenger aircraft crashed off the coast of Newfoundland [16]. A number of aircraft and several ships joined in the search but after approximately a week, with no signs of wreckage having been found, it was concluded that there was no longer any hope of finding survivors [16, 17]. In fact, nearly two months later, the air search after 610 fruitless hours was called off with rescue officials having only a vague idea where the plane ditched [18]. Signals from the emergency locator transmitter (ELT) were apparently received by a COSPAS-SARSAT satellite and relayed to a local user terminal (LUT) on the ground for processing [17]; however, the signal processing strategy employed in the LUT (based on the averaged 1K FFT) was unable to provide a location due to a possible combination of a poor quality ELT signal, background interference, and the fact that the signal data were not retained thus eliminating any possibility of signal enhancement involving more sophisticated techniques. Poor geometry too, could have played a role.

1.2 Method of Operation

When an aircraft or marine vessel is in distress [21], the emergency unit is activated either automatically or by manually setting a switch. The signal is then received by an orbiting satellite as it sweeps out a path over the search and rescue (SAR) region of interest as shown in Fig. 1.2. Due to the relative motion between the satellite and ELT or EPIRB unit, the signal received at the spacecraft is Doppler shifted, as illustrated in Fig. 1.3. A repeater on board the satellite relays the signal to an earth station where the signal is analyzed to extract the position of the accident. (Note that it is necessary for both the accident site and earth station to be within sight of the satellite simultaneously.)

The zero Doppler shift frequency, occurring at the inflection point of the Doppler curve (see Fig. 1.3), is the point of closest approach of the satellite to the accident site [21]. Consequently, this frequency must be determined with as much accuracy as possible since the slope of the Doppler curve at this point is used to calculate the range from satellite to the transmitting source. With the range and the known position of the satellite, the location of the emergency signal source can be estimated. This estimate is passed to a Rescue Coordination Center (RCC) which speedily dispatches search aircraft to the emergency site.

1.3 Scope of Thesis

In this thesis, new processing techniques for detecting ELT signals in an interfering background are investigated, based on not only theoretical analyses but also com-

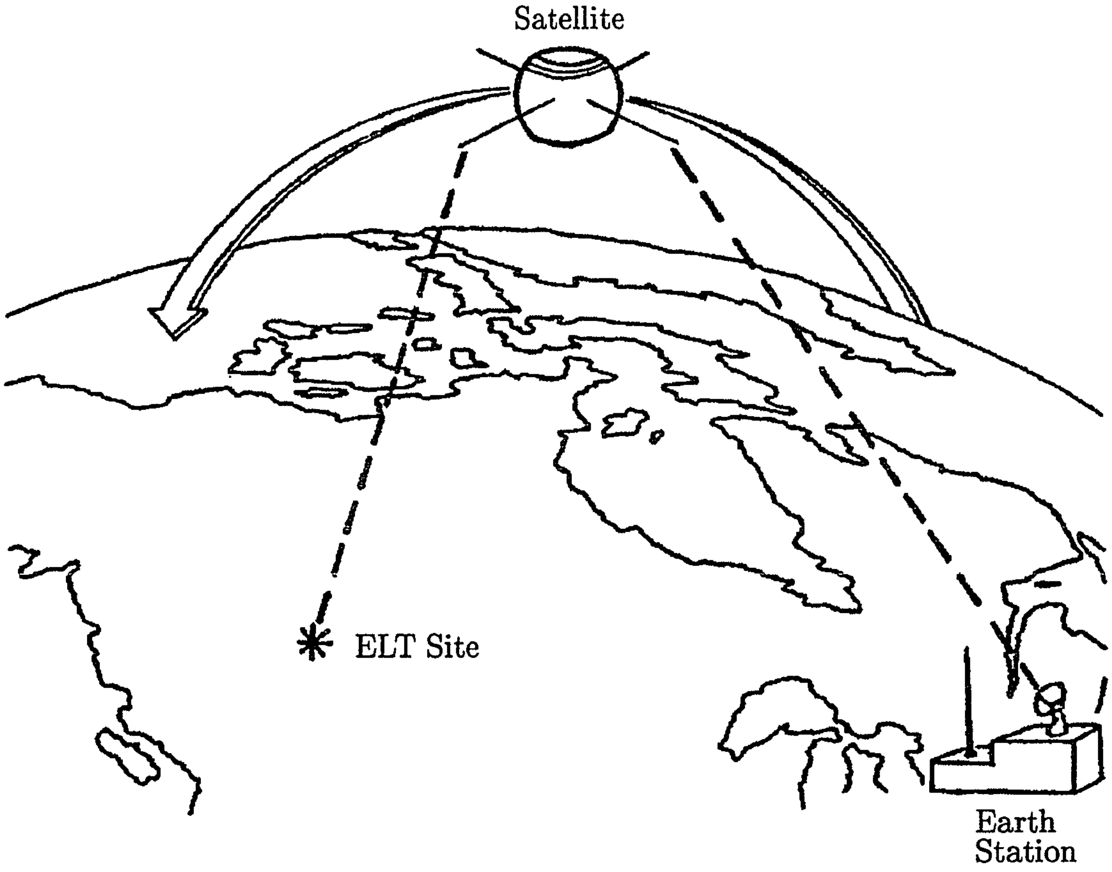

Figure 1.2: ELT Site, Satellite, and Earth Station.

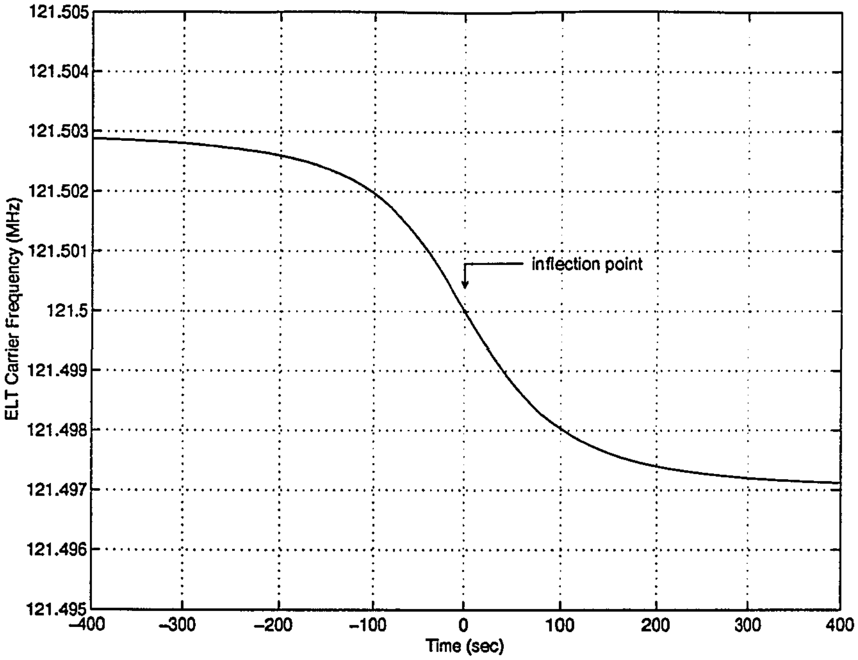

Figure 1.3: ELT carrier frequency versus time showing the Doppler shift

puter simulations and experimental processings. The new methods involve the use of the Geometrically Averaged Spectrum (GAS) and the Harmonically Averaged Spectrum (HAS) in addition to the Arithmetically Averaged Spectrum (AAS) adopted by the existing system. The results of letting AAS, GAS, and HAS work together are compared to that of using only AAS. It is seen that the new strategy shows superior performance over the original method in a congested signal environment even though interference power greatly exceeds ELT signal power.

Chapter 2 provides an overview of the theoretical spectra of certain types of ELT signals, presents through computer simulation the spectra of contiguous blocks of these ELT signals, and shows how these spectra can be combined by the AAS, the GAS and the HAS. The chapter ends with the presentation of a new ELT signal model postulating that the ELT crystal oscillator may be continuously frequency pulled over the entire modulation sweep producing an FM characteristic.

Chapter 3 investigates the theoretical performance of AAS, GAS and HAS averaging in practical circumstances involving signals, noise and interference. It is shown that the carrier peaks of good ELT signals can be substantially enhanced in an interfering background.

Chapter 4 identifies certain types of interference such as Carrier interference with strong or weak AM, On-Off Modulation interference, Swept Carrier interference, and Ringing Response interference. Using computer simulation, it is demonstrated that under certain conditions the effects of background interference can be greatly reduced and the detection of ELT carrier peaks can be improved by employing a combination of AAS, GAS and HAS averaging.

Chapter 5 describes how real SARSAT pass data signals are fed into the computer and processed using AAS, GAS and HAS averaging. The background interference postulated in Chapter 4 is found to exist and real ELT signals are identified. Certain advantages are realized by employing the GAS and the HAS as compared to the AAS averaging. ELT signals representing the NIC model and the FME model are identified along with a new ELT signal for which a model cannot presently be envisaged.

Finally, Chapter 6 presents conclusions.

Chapter 2

ELT Signal Structures and Spectra

2.1 Introduction

This chapter examines parameter models of ELT signals which include two types of frequency-pulling due to the modulation [12]. The objective of the analysis for these parameter models of ELT signals is to provide an analytic base on which we can carry out the discussion for the problem of interference reduction in ELT signal processing. It is expected that interference suppression as introduced in this thesis will reduce location ambiguities, minimize rescue dispatch delay time, and improve ELT location estimates by enhancing the ELT signal.

Specifically, in Section 2.2, we discuss the dynamic signal modeling first. Then we examine three different averaged spectra one of which is the traditional averaged spectrum while the other two are first introduced to ELT signal processing by this thesis. In Section 2.3, we describe the mathematical model for each of the four kinds of ELT signals respectively. The first three ELT signal models can be found in the literature [12] while the fourth is new. We calculate the theoretical spectrum of each ELT signal model directly after that model has been discussed.

2.2 ELT Signal Modeling

The typical ELT signal may be represented by a modulated carrier waveform [12], as illustrated in Fig. 2.1(a) where the carrier frequency of 121.5 MHz is employed for civilian purposes. A summary of the pertinent specifications [12] is given in Table 2.1. For the simulations in this thesis, the modulation is presented in an exponential manner as shown in Fig. 2.1(b) with the initial pulse-null duration T_1 being approximately 0.7 ms and the final pulse-null duration T_M being about 1.6 ms. The total sweep period of the signal, T_S, can be varied from 0.25 s to 0.5 s depending on the particular ELT unit modeled.

The time interval T_S corresponds to a complete sweep and is assumed to contain M pulse-null pairs. The time interval T_D corresponds to a data record or window length having an arbitrary duration containing N pulse-null pairs of an ELT signal.

2.2.1 Dynamic Signal Modeling

As described above, the ELT signal corresponding to a time interval T_D, as illustrated in Fig. 2.1, can be represented by a set of N pulse-null pairs in the time domain. Before proceeding, let two assumptions be made here. The first assumption is that T_D is much less than T_S. This assumption is realistic since T_D is typically 20 to 50 ms and T_S is typically 0.25 to 0.5 s. The second assumption is that the leading edge

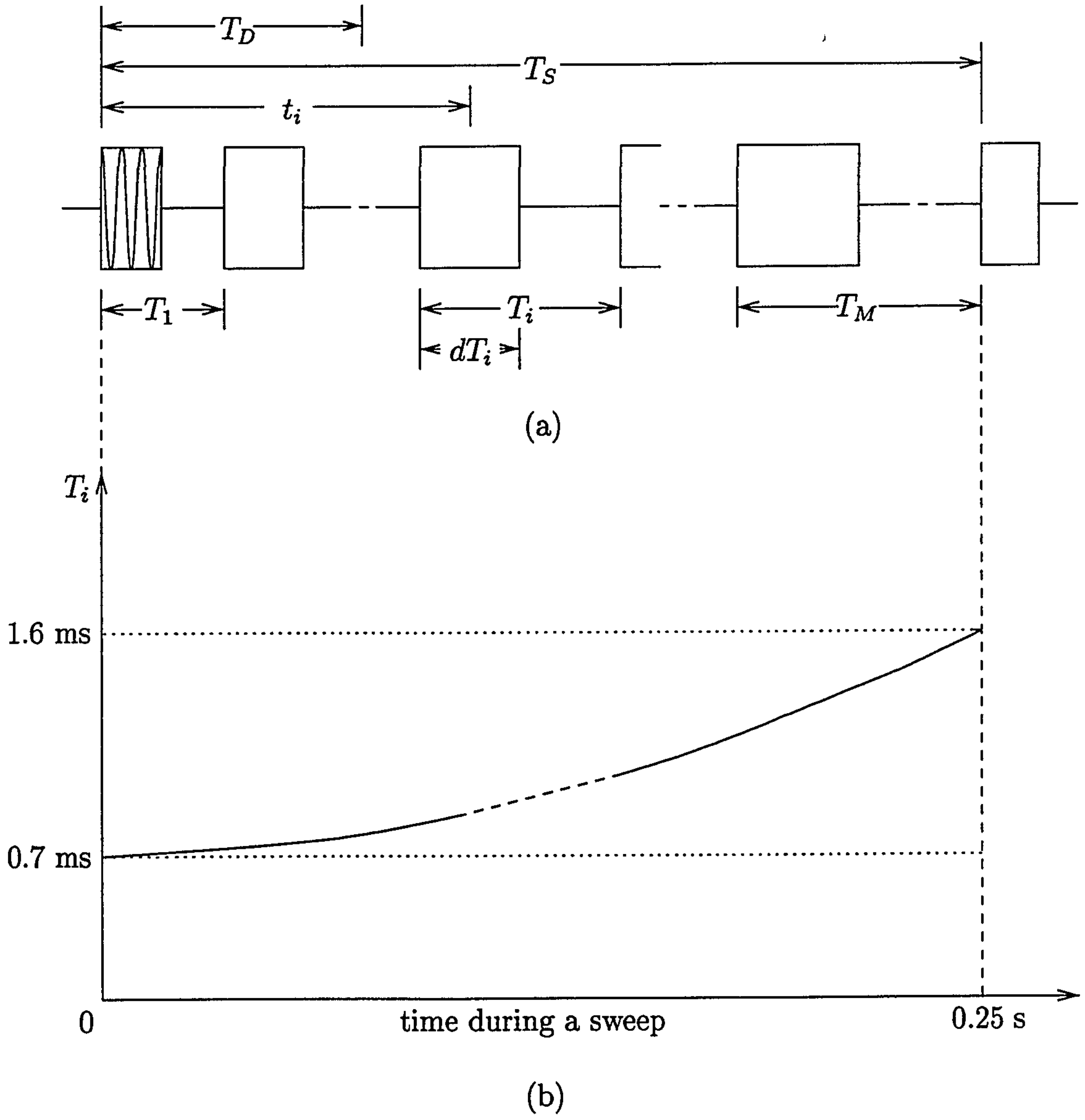

Figure 2.1: A typical ELT signal: (a) ELT signal comprising M pulse-null pairs of carrier; (b) Variation in duration of the pulse-null pairs versus sweep time.

of the time interval T_D used in the following development begins at the rising edge of a pulse-null pair. This assumption is also justifiable since $T_i \ll T_D$, where T_i is the duration of the ith pulse-null pair.

Carrier frequency	121.5 MHz†
Frequency tolerance	± 50 ppm
Power output	approximately 100 mW
Modulation type	pulse
Pulse duration	33% - 55%
Percentage modulation	> 85%
Modulation frequency	downward swept
Sweep rate	2 - 4 sweeps/second
Modulation frequency change	700 Hz minimum
Modulation frequency limits	300 - 1600 Hz

† optional 243 MHz

Table 2.1: The pertinent specifications for ELT signal

Then mathematically, with these two assumptions, we have, referring to Fig. 2.2 [12]

$$s(t) = \sum_{i=1}^{N} s_i(t) \tag{2.2.1}$$

where $s_i(t)$ is the ith pulse of the ELT signal within the time interval T_D. Specifically,

$$s_i(t) = \begin{cases} A\cos(2\pi f_c t + \theta_i) & t_i - \frac{T_i d}{2} \leq t < t_i + \frac{T_i d}{2} \\ 0 & \text{otherwise} \end{cases} \tag{2.2.2}$$

where A is the amplitude, f_c is the carrier frequency, t_i is the time shift measured at the center of the ith pulse, T_i is the duration of the ith pulse-null pair, d is the

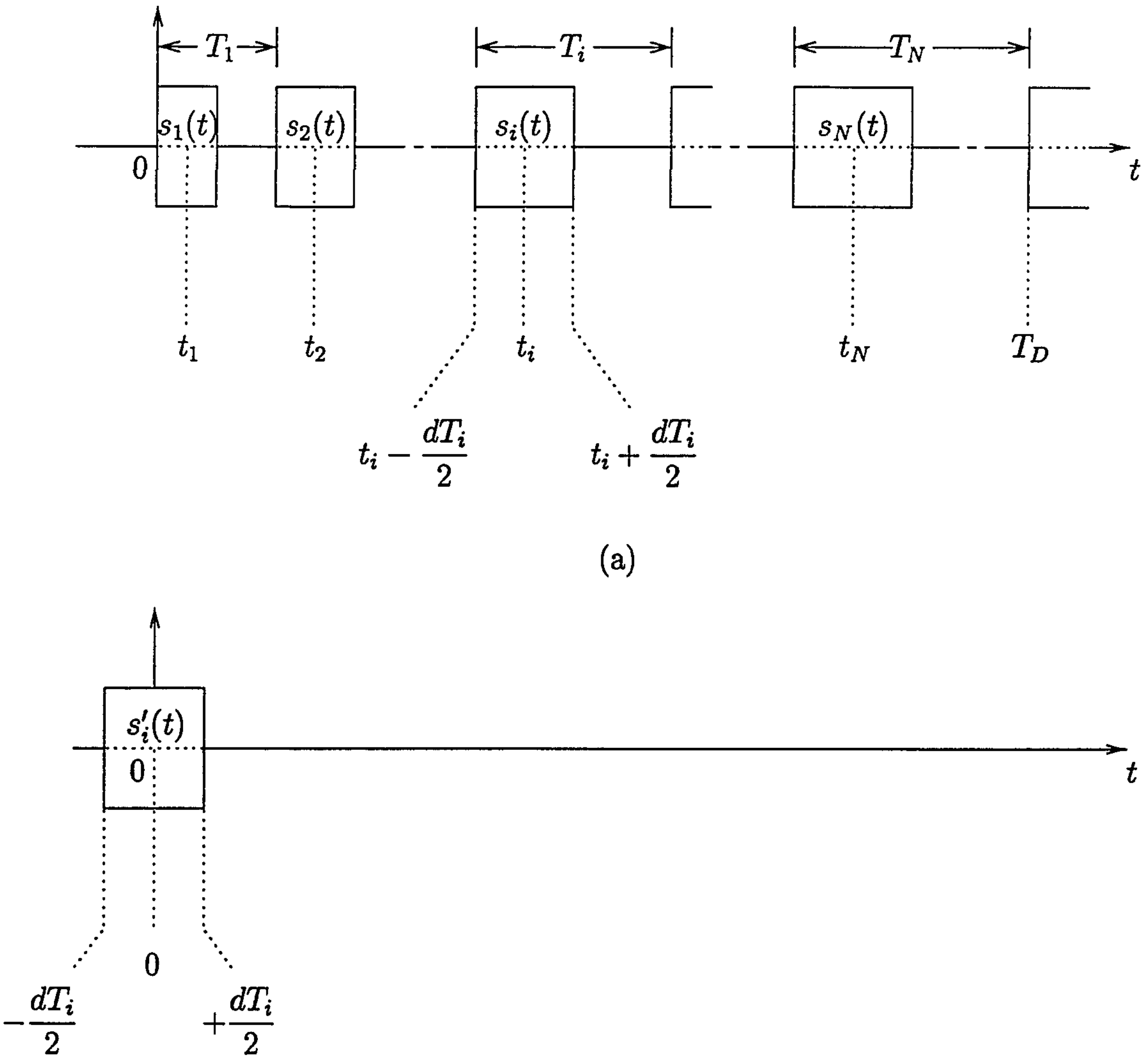

(a)

(b)

Figure 2.2: The instantaneous phase at the central point: (a) The ith pulse of the ELT signal within the time interval T_D; (b) $s'_i(t)$ which is $s_i(t+t_i)$ (see equation (2.2.4)).

duty cycle, and θ_i is the phase shift of the ith pulse of the ELT signal within the time interval T_D.

2.2.2 Calculating $F(f)$

Let $s_i'(t)$ be

$$s_i'(t) = \begin{cases} A\cos(2\pi f_c t + 2\pi f_c t_i + \theta_i) & 0 - \frac{T_i d}{2} \le t < 0 + \frac{T_i d}{2} \\ 0 & \text{otherwise} \end{cases} \tag{2.2.3}$$

Then, we have

$$\begin{aligned} s_i(t) &\overset{(a)}{=} \begin{cases} A\cos(2\pi f_c t + \theta_i) & t_i - \frac{T_i d}{2} \le t < t_i + \frac{T_i d}{2} \\ 0 & \text{otherwise} \end{cases} \\ &\overset{(b)}{=} \begin{cases} A\cos[2\pi f_c (t - t_i) + 2\pi f_c t_i + \theta_i] & 0 - \frac{T_i d}{2} \le t - t_i < 0 + \frac{T_i d}{2} \\ 0 & \text{otherwise} \end{cases} \\ &\overset{(c)}{=} s_i'(t - t_i) \end{aligned} \tag{2.2.4}$$

where $\overset{(a)}{=}$ is due to (2.2.2), $\overset{(b)}{=}$ is due to a simple arithmetic rearrangement, and $\overset{(c)}{=}$ is due to (2.2.3). That is, $s_i(t)$ is a time-delayed version of $s_i'(t)$.

Define *the Fourier Transform* of a function $g(t)$ to be [23]

$$\mathcal{F}\left[g(t)\right] \triangleq \int_{-\infty}^{\infty} g(t)e^{-j2\pi f t}dt \tag{2.2.5}$$

where $\mathcal{F}[\cdot]$ denotes *the Fourier transform* of its argument. Then, for a time domain function which has the form

$$g(t) = \begin{cases} A\cos(2\pi f_c t + \theta) & -\frac{T}{2} \le t < \frac{T}{2} \\ 0 & \text{otherwise} \end{cases}$$

$$= \begin{cases} A\dfrac{e^{j(2\pi f_c t+\theta)} + e^{-j(2\pi f_c t+\theta)}}{2} & -\frac{T}{2} \leq t < \frac{T}{2} \\ 0 & \text{otherwise} \end{cases}$$

$$= \begin{cases} \dfrac{A}{2}e^{-j2\pi f_c t}e^{-j\theta} + \dfrac{A}{2}e^{j2\pi f_c t}e^{j\theta} & -\frac{T}{2} \leq t < \frac{T}{2} \\ 0 & \text{otherwise} \end{cases} \tag{2.2.6}$$

it is well known that in the special case of $f_c T \gg 1$ and for positive frequencies [23]

$$\mathcal{F}[g(t)] = \frac{AT}{2} \cdot \mathrm{sinc}[(f - f_c)T] \cdot e^{j\theta} \tag{2.2.7}$$

where [23]

$$\mathrm{sinc}(x) \triangleq \frac{\sin(\pi x)}{\pi x} \tag{2.2.8}$$

With $s_i'(t)$ defined as in (2.2.3),

$$\begin{aligned} F_i'(f) &\triangleq \mathcal{F}[s_i'(t)] \\ &= \frac{AT_i d}{2} \cdot \mathrm{sinc}[(f - f_c)T_i d] \cdot e^{j(2\pi f_c t_i + \theta_i)} \end{aligned} \tag{2.2.9}$$

Equivalently,

$$\begin{aligned} F_i(f) &\triangleq \mathcal{F}[s_i(t)] \\ &\overset{(a)}{=} \mathcal{F}[s_i'(t - t_i)] \\ &\overset{(b)}{=} \mathcal{F}[s_i'(t)]\, e^{-j2\pi f t_i} \\ &= F_i'(f) e^{-j2\pi f t_i} \\ &\overset{(c)}{=} \frac{AT_i d}{2} \cdot \mathrm{sinc}[(f - f_c)T_i d] \cdot e^{j(2\pi f_c t_i + \theta_i)} \cdot e^{-j2\pi f t_i} \\ &= \frac{AT_i d}{2} \cdot \mathrm{sinc}[(f - f_c)T_i d] \cdot e^{-j[2\pi(f - f_c)t_i - \theta_i]} \end{aligned} \tag{2.2.10}$$

where $\overset{(a)}{=}$ is due to (2.2.4), $\overset{(b)}{=}$ is due to *the time shifting property of the Fourier transform* [23], and $\overset{(c)}{=}$ is due to (2.2.9). Consequently,

$$\begin{aligned} F(f) &\triangleq \mathcal{F}[s(t)] \\ &\overset{(a)}{=} \mathcal{F}\left[\sum_{i=1}^{N} s_i(t)\right] \\ &\overset{(b)}{=} \sum_{i=1}^{N} \mathcal{F}[s_i(t)] \\ &= \sum_{i=1}^{N} F_i(f) \\ &\overset{(c)}{=} \sum_{i=1}^{N} \frac{AT_i d}{2} \cdot \text{sinc}[(f-f_c)T_i d] \cdot e^{-j[2\pi(f-f_c)t_i-\theta_i]} \end{aligned} \tag{2.2.11}$$

where $\overset{(a)}{=}$ is due to (2.2.1), $\overset{(b)}{=}$ is due to *the linearity (superposition) property of the Fourier transform* [23], and $\overset{(c)}{=}$ is due to (2.2.10).

2.2.3 Modify the Expression of $F(f)$

If the window length of a data record which is to be processed is short compared to the length of a complete sweep of the ELT signal, *i.e.*, if

$$T_D \ll T_S \tag{2.2.12}$$

then, for the N pulse-null pairs within the window length of a data record, T_i is nearly constant [12]. Thus, a quantity which can be referred to as the average duration of pulse-null pairs may be naturally expressed as

$$\mathcal{T} \triangleq T_D/N \tag{2.2.13}$$

Consequently, the above observation that T_i is nearly constant can be written as [12]

$$T_i \approx \mathcal{T} \qquad i = 1, 2, \cdots, N \tag{2.2.14}$$

Furthermore, for the N pulses within the window length of a data record, t_i (see Fig. 2.1) is very nearly given by

$$t_i \approx \left(i - 1 + \frac{d}{2}\right)\mathcal{T} \qquad i = 1, 2, \cdots, N \tag{2.2.15}$$

Thus, (2.2.11) can be re-written as

$$\begin{aligned} F(f) &\approx \sum_{i=1}^{N} \frac{A\mathcal{T}d}{2} \cdot \mathrm{sinc}[(f - f_c)\mathcal{T}d] \cdot e^{-j[2\pi(f-f_c)(i-1+\frac{d}{2})\mathcal{T}-\theta_i]} \\ &= e^{-j2\pi(f-f_c)\frac{\mathcal{T}d}{2}} \cdot \frac{A\mathcal{T}d}{2} \cdot \mathrm{sinc}[(f - f_c)\mathcal{T}d] \cdot \sum_{i=1}^{N} e^{-j[2\pi(f-f_c)(i-1)\mathcal{T}-\theta_i]} \end{aligned} \tag{2.2.16}$$

2.2.4 Three Different Averaged Spectra

Suppose we are given K numbers and we want to calculate the averaged value of these K numbers. Let the value of the kth number be denoted as V_k, $k = 1, 2, ..., K$. Then, the Arithmetically Averaged Value (AAV) can be expressed as

$$\mathrm{AAV} \triangleq \frac{1}{K} \sum_{k=1}^{K} V_k \tag{2.2.17}$$

and, the Geometrically Averaged Value (GAV) can be expressed as

$$\mathrm{GAV} \triangleq \left[\prod_{k=1}^{K} V_k\right]^{\frac{1}{K}} \tag{2.2.18}$$

and, the Harmonically Averaged Value (HAV) can be expressed as

$$\mathrm{HAV} \triangleq \frac{1}{\frac{1}{K} \sum_{k=1}^{K} \frac{1}{V_k}} \tag{2.2.19}$$

respectively. Mathematically, it can be proved that [30-35]

$$\text{AAV} \geq \text{GAV} \geq \text{HAV} \tag{2.2.20}$$

More specifically, if and only if

$$V_1 = V_2 = \ldots = V_{K-1} = V_K \tag{2.2.21}$$

then

$$\text{AAV} = \text{GAV} = \text{HAV} \tag{2.2.22}$$

otherwise,

$$\text{AAV} > \text{GAV} > \text{HAV} \tag{2.2.23}$$

First, let us represent the above theorem in terms of calculating the averaged spectrum as follows. Let the *Fourier Transform* calculated from the kth data window record be denoted as $F_k(f)$ and let the periodogram obtained from the kth FFT operation be

$$S_k(f) \triangleq |F_k(f)|^2 \qquad k = 1, 2, \ldots, K \tag{2.2.24}$$

Then, the Arithmetically Averaged Spectrum (AAS) can be expressed as

$$\text{AAS}(f) \triangleq \frac{1}{K}\sum_{k=1}^{K} S_k(f) \tag{2.2.25}$$

and, the Geometrically Averaged Spectrum (GAS) can be expressed as

$$\text{GAS}(f) \triangleq \left[\prod_{k=1}^{K} S_k(f)\right]^{\frac{1}{K}} \tag{2.2.26}$$

and, the Harmonically Averaged Spectrum (HAS) can be expressed as

$$\text{HAS}(f) \triangleq \frac{1}{\frac{1}{K}\sum_{k=1}^{K}\frac{1}{S_k(f)}} \tag{2.2.27}$$

respectively. Mathematically, it can be proved from (2.2.20) that

$$\mathrm{AAS}(f) \geq \mathrm{GAS}(f) \geq \mathrm{HAS}(f) \tag{2.2.28}$$

More specifically, if and only if

$$S_1(f) = S_2(f) = \ldots = S_{K-1}(f) = S_K(f) \tag{2.2.29}$$

then

$$\mathrm{AAS}(f) = \mathrm{GAS}(f) = \mathrm{HAS}(f) \tag{2.2.30}$$

otherwise,

$$\mathrm{AAS}(f) > \mathrm{GAS}(f) > \mathrm{HAS}(f) \tag{2.2.31}$$

Consequently, $\mathrm{AAS}(f)$, $\mathrm{GAS}(f)$, and $\mathrm{HAS}(f)$ could have different shapes. But the question is: How are the spectra of ELT signals affected by these different averaging strategies? This matter is now examined.

2.3 Theoretical Spectra of ELT Signals

This section is devoted to the study of the spectra of ELT signals with no noise or interference. To support the results obtained by analyses, appropriate computer simulations are required. First of all, the mimicry to the variation in duration of the pulse-null pairs of an ELT signal is required.

2.3.1 Ideal Coherent ELT Signal

The first ELT signal model, called the Ideal Coherent ELT (ICE) signal model [12], includes those units which can be assumed to contain an ideal crystal controlled

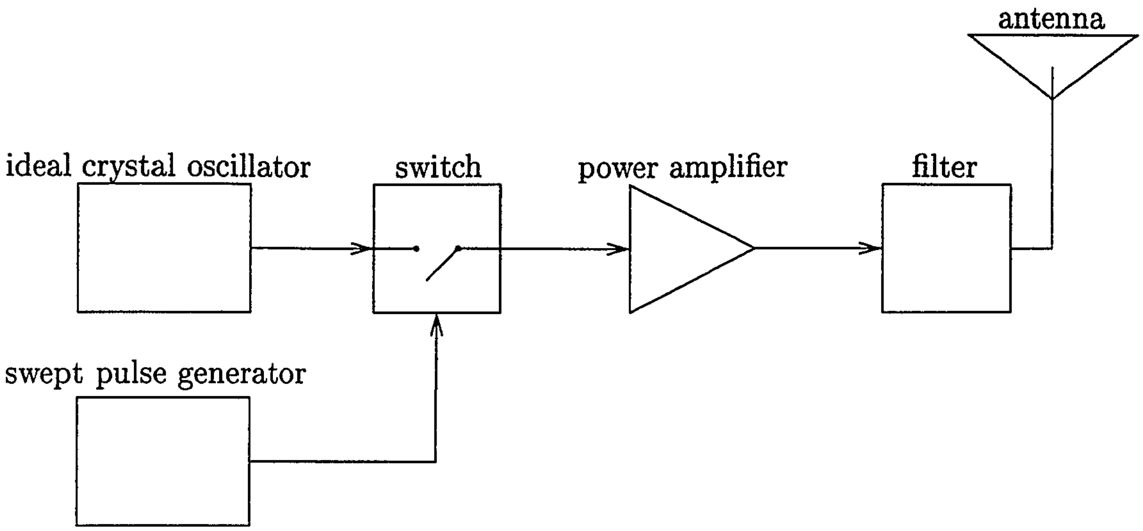

Figure 2.3: Block diagram for the Ideal Coherent ELT (ICE).

oscillator as illustrated in Fig. 2.3, and certain ELT signals, such as Pointer, are in this category. This ideal crystal controlled oscillator has constant frequency f_c over the entire signal and is switched to the power amplifier by the pulse modulator signal. It can be seen that, in Fig. 2.4, the phase from pulse to pulse is continuous. Hence,

$$\theta_i = \theta_0; \qquad i = 1, 2, 3, 4, \cdots, N \qquad \text{for ICE model} \tag{2.3.1}$$

where θ_0 is the phase of the unmodulated carrier at the time instant of $t = 0$ within the window length T_D of a data record. Substituting this relation in (2.2.16) yields

$$\begin{aligned} F^{ice}(f) &\overset{(a)}{=} e^{-j2\pi(f-f_c)\frac{\mathcal{T}d}{2}} \cdot \frac{A\mathcal{T}d}{2} \cdot \operatorname{sinc}[(f-f_c)\mathcal{T}d] \cdot \sum_{i=1}^{N} e^{-j[2\pi(f-f_c)(i-1)\mathcal{T}-\theta_0]} \\ &\overset{(b)}{=} e^{-j\left[2\pi(f-f_c)\frac{\mathcal{T}d}{2}-\theta_0\right]} \cdot \frac{A\mathcal{T}d}{2} \cdot \operatorname{sinc}[(f-f_c)\mathcal{T}d] \cdot \frac{1-e^{-j2\pi(f-f_c)N\mathcal{T}}}{1-e^{-j2\pi(f-f_c)\mathcal{T}}} \\ &\overset{(c)}{=} e^{-j\left[2\pi(f-f_c)\frac{\mathcal{T}d}{2}-\theta_0\right]} \cdot \frac{A\mathcal{T}d}{2} \cdot \operatorname{sinc}[(f-f_c)\mathcal{T}d] \cdot \frac{1-e^{-j2\pi(f-f_c)T_D}}{1-e^{-j2\pi(f-f_c)\mathcal{T}}} \end{aligned} \tag{2.3.2}$$

where $\overset{(a)}{=}$ is due to (2.3.1) and (2.2.16), $\overset{(b)}{=}$ is due to the rule for calculating the

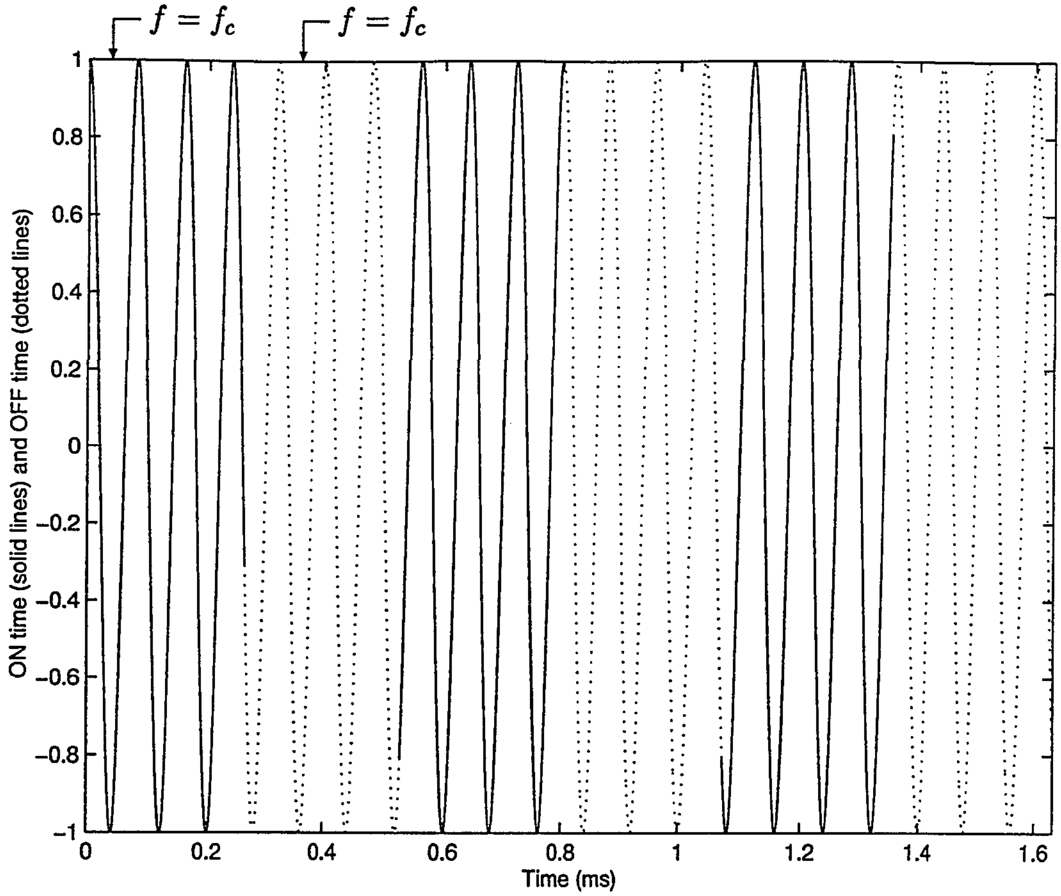

Figure 2.4: The phase continuity in the Ideal Coherent ELT (ICE) signal.

summation of the geometrical progression, and $\overset{(c)}{=}$ is due to (2.2.13).

The spectrum of the Ideal Coherent ELT (ICE) signal model is given by

$$\begin{aligned} S^{ice}(f) &\triangleq \left|F^{ice}(f)\right|^2 \\ &= \left[\frac{A\mathcal{T}d}{2}\right]^2 \cdot \mathrm{sinc}^2[(f-f_c)\mathcal{T}d] \cdot \left[\frac{\sin[\pi(f-f_c)T_D]}{\sin[\pi(f-f_c)\mathcal{T}]}\right]^2 \qquad (2.3.3) \end{aligned}$$

This spectrum is highly idealized and does not often exist in practice. Using the Ideal Coherent ELT (ICE) signal model, an ELT signal can be generated by computer and the spectrum can be calculated by employing a sequence of 24 consecutive Blackman windowed 2048-point periodograms [12] as illustrated in Fig. 2.5. The dynamic range

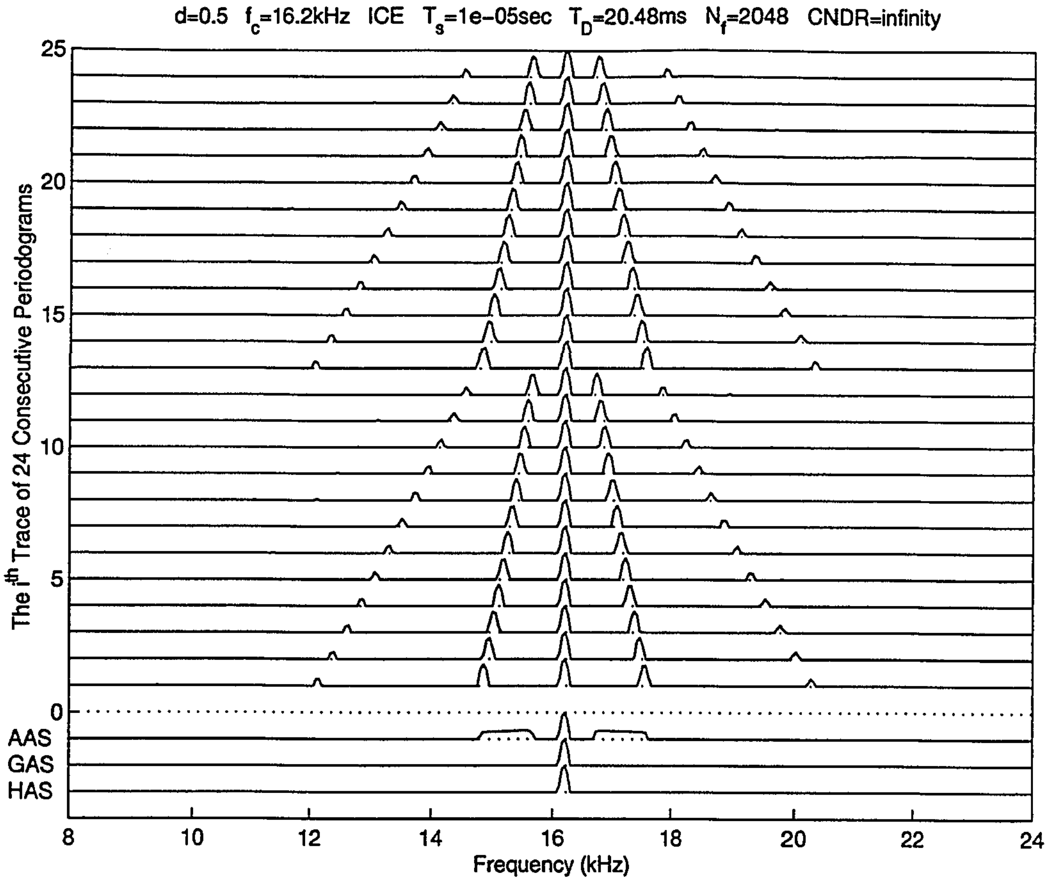

Figure 2.5: Periodograms of the ELT signal in the ICE model

of each of the 24 periodograms is 20 dB and approximately two sweeps of the ELT signal are provided. Also note that in Fig. 2.5 and sequential figures, T_s is the sampling time interval, N_f is the number of samples used to calculate an FFT, and CNDR denotes Carrier-to-Noise Density Ratio [21]. In the window length, T_D, one might see any where from 213 to 230 pulses, and with 200 to 70 samples/pulse; the closest eigen frequency is 16.211 kHz. Therefore, there is an inherent error due to the FFT resolution.

Let the *Fourier Transform* calculated from the kth data window record of the ICE signal be denoted as $F_k^{ice}(f)$ and let $S_k^{ice}(f)$ be the kth periodogram of the ICE signal, then we have

$$S_k^{ice}(f) \triangleq \left|F_k^{ice}(f)\right|^2 \qquad k = 1, 2, ..., K \tag{2.3.4}$$

In our computer simulation, we usually let K be equal to 24 to ensure at least one sweep of the signal. Then, the curve in Fig. 2.6 is the Arithmetically Averaged Spectrum (AAS)

$$A^{ice}(f) \triangleq \frac{1}{24}\sum_{k=1}^{24} S_k^{ice}(f) \tag{2.3.5}$$

of the ICE signal, while the curve in Fig. 2.7 is the Geometrically Averaged Spectrum (GAS)

$$G^{ice}(f) \triangleq \left[\prod_{k=1}^{24} S_k^{ice}(f)\right]^{\frac{1}{24}} \tag{2.3.6}$$

of the ICE signal, and the curve in Fig. 2.8 is the Harmonically Averaged Spectrum (HAS)

$$H^{ice}(f) \triangleq \frac{1}{\frac{1}{24}\sum_{k=1}^{24}\frac{1}{S_k^{ice}(f)}} \tag{2.3.7}$$

of the ICE signal.

It can be seen from Fig. 2.5 that from the 1st periodogram to the 24th periodogram, all of the carrier peaks have not only the same frequency (which is 16.2 kHz in this example) but also equal height. This causes the carrier peaks in Fig. 2.6, Fig. 2.7, and Fig. 2.8 to occur at the same frequency and to have equal height. On the other hand (see Fig. 2.5), from the 1st periodogram to the 24th periodogram, the first lower sideband sweeps from 14.7 kHz to 15.8 kHz while the first upper sideband sweeps from 17.7 kHz to 16.6 kHz in this example. For the AAS, the sideband energy is spread from 14.7 kHz to 15.8 kHz and from 16.6 kHz to 17.7 kHz, respectively,

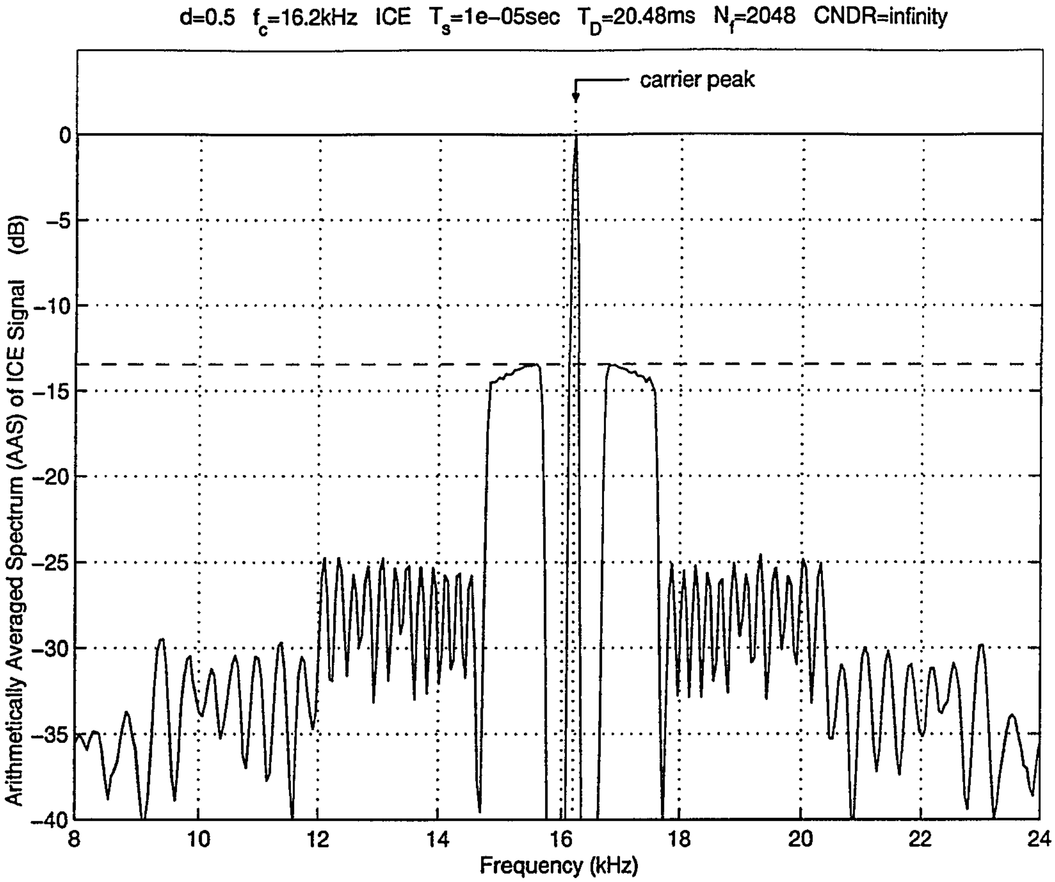

Figure 2.6: Arithmetically Averaged Spectrum (AAS) of the ICE Signal

thus reducing the magnitude in Fig. 2.6. However, for the GAS in Fig. 2.7 and the HAS in Fig. 2.8 respectively, the averaging produces an additional reduction in sideband levels due to (2.2.31). A similar discussion applies to the second lower sideband and the second upper sideband. Also note the perfect symmetry with respect to the carrier frequency (which is 16.2 kHz in this example) in Figs. 2.5, 2.6, 2.7, and 2.8.

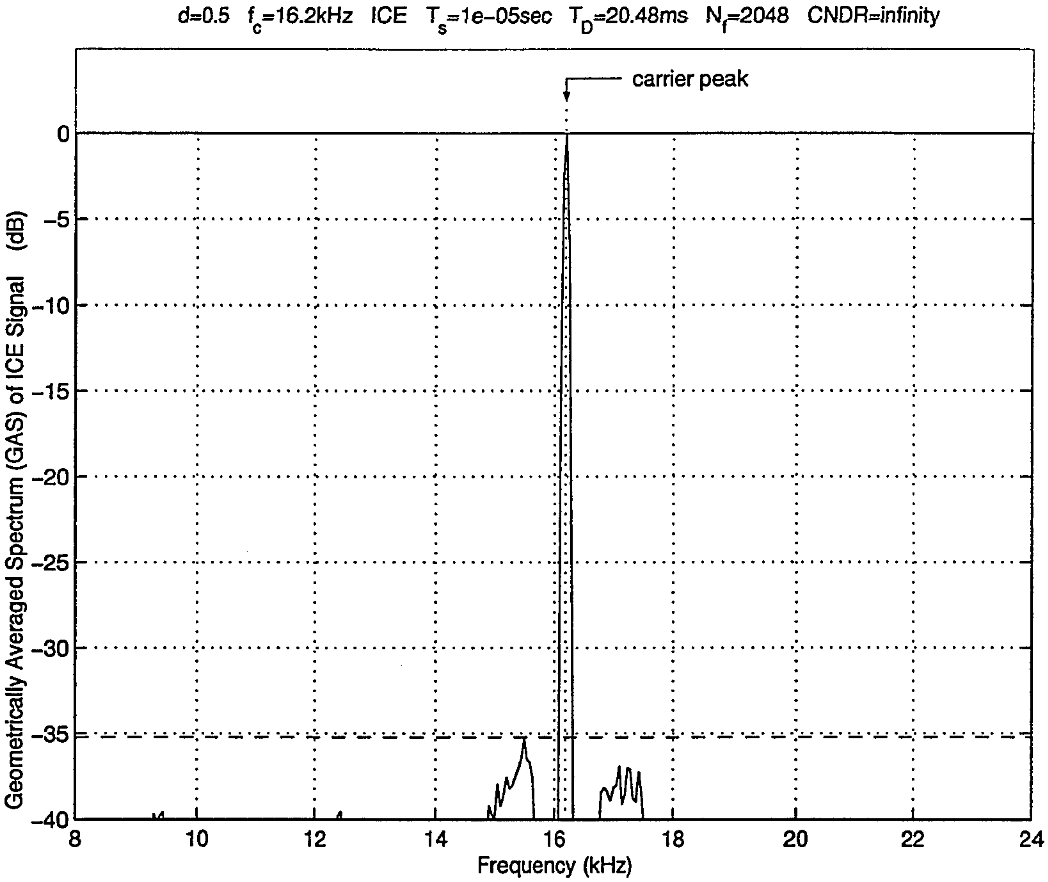

Figure 2.7: Geometrically Averaged Spectrum (GAS) of the ICE Signal

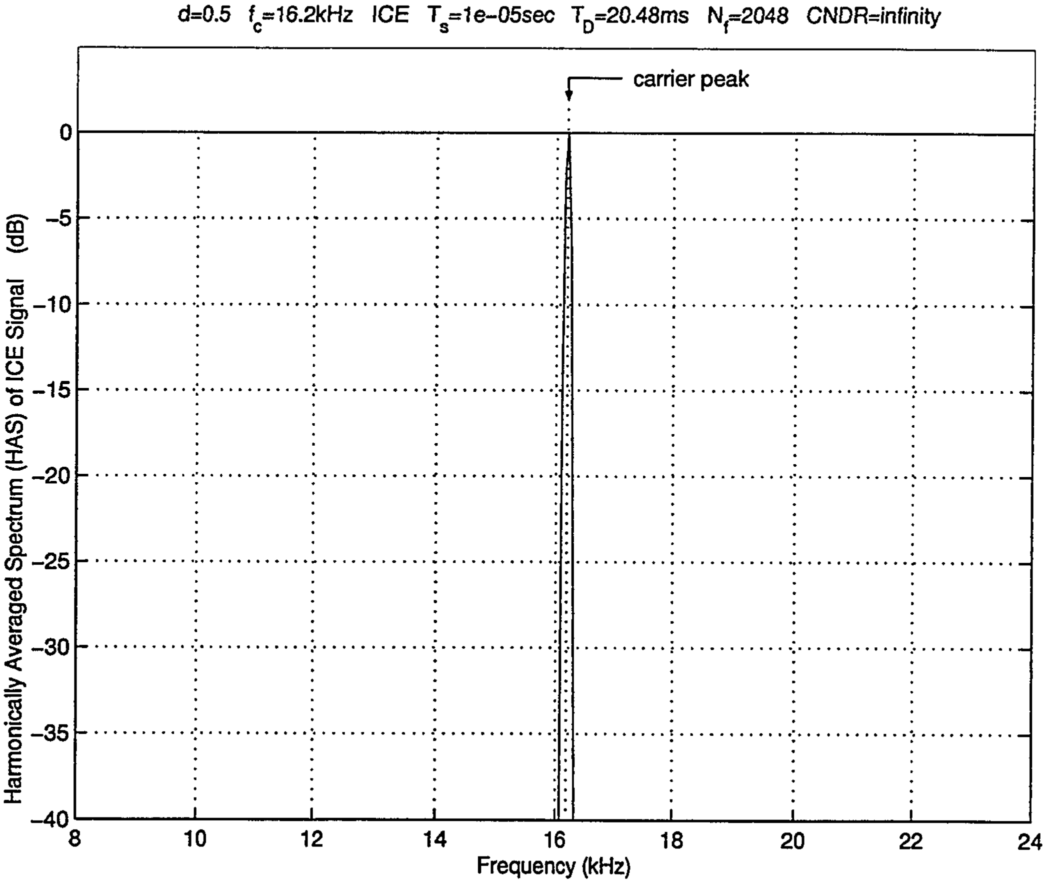

Figure 2.8: Harmonically Averaged Spectrum (HAS) of the ICE Signal

2.3.2 Non-Ideal Coherent ELT Signal

Many ELT units such as Narco [12] can be characterized by the Non-Ideal Coherent (NIC) ELT signal model, where it is assumed that the frequency of the crystal controlled oscillator during the ON time is slightly different from the value during the OFF time. This effect (referred to as *frequency pulling*) is caused by a variation in power supply voltage feeding the oscillator due to loading of the power amplifier, or a variation in the input impedance to the switch as seen by the crystal controlled oscillator as the switch opens and closes, as demonstrated in Fig. 2.9. For this case, it is assumed that the crystal controlled oscillator operates at frequency f_c when the switch is closed and $f_c + f_p$ (where f_p can be referred to as *the frequency shift*) when the switch is open, as illustrated in Fig. 2.10, and the oscillator changes frequency instantaneously with the change in voltage.

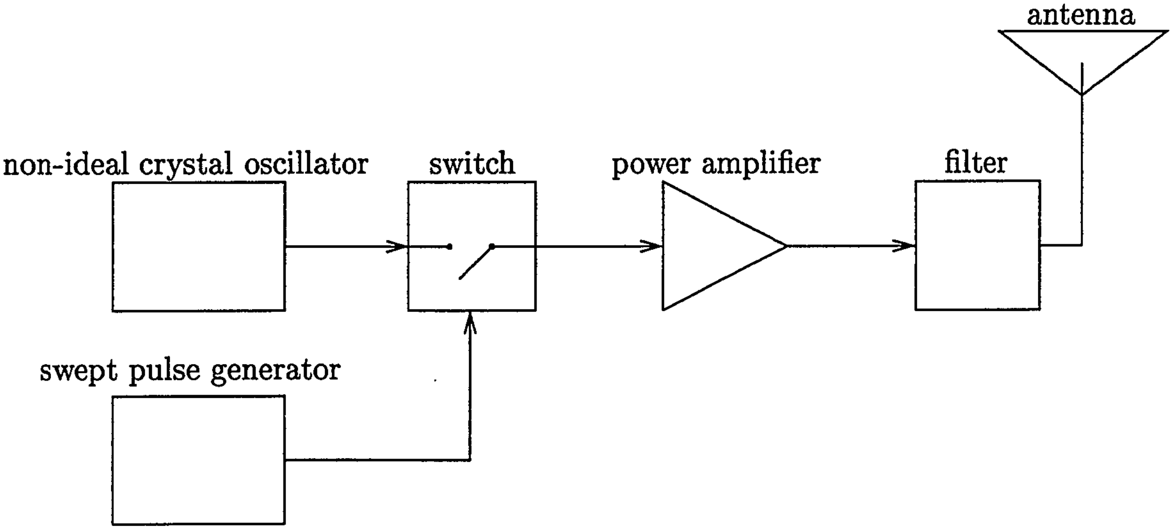

Figure 2.9: Block diagram for the Non-Ideal Coherent (NIC) ELT.

Operating Frequency of Crystal Controlled Oscillator:

More clearly, let the operating frequency of the Crystal Controlled Oscillator

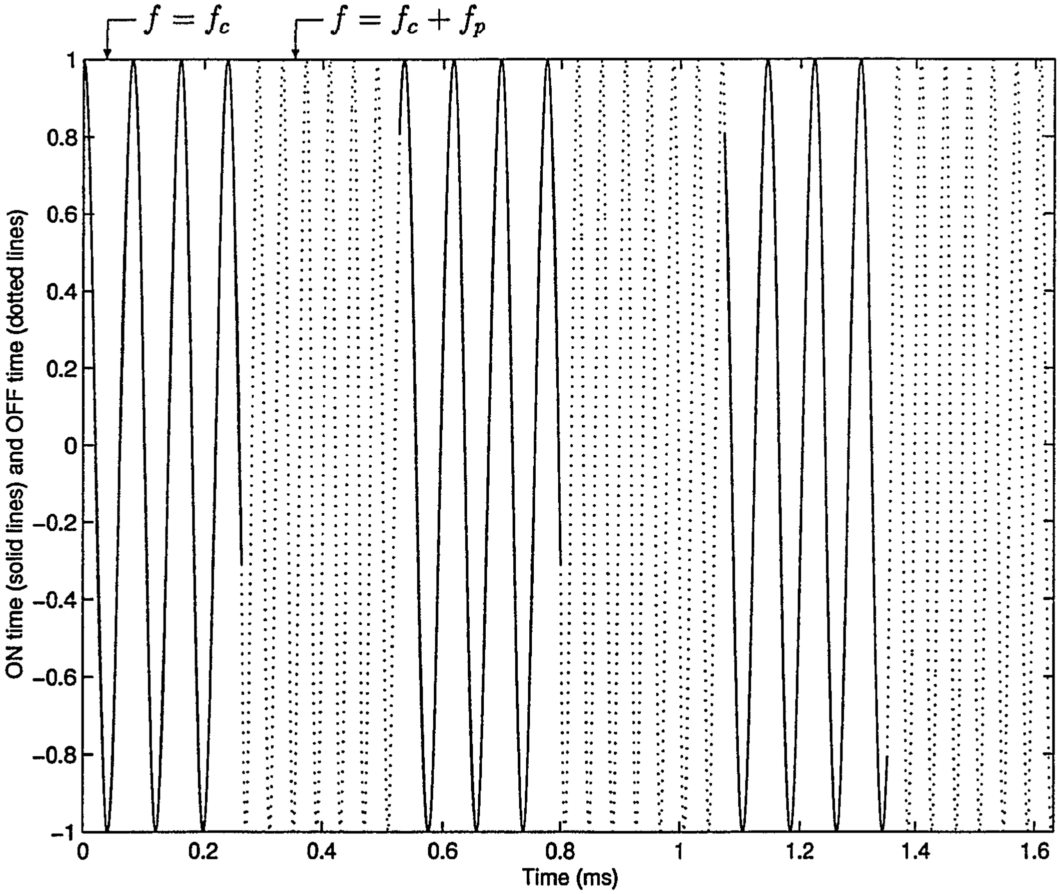

Figure 2.10: The phase shift in the Non-Ideal Coherent (NIC) ELT signal.

(CCO) be denoted as f_{cco}, then we have

$$f_{cco} = \begin{cases} f_c & \text{when the switch is closed} \\ f_c + f_p & \text{when the switch is open} \end{cases} \tag{2.3.8}$$

where f_p is *the frequency shift*. Hence, there is a phase shift from pulse to pulse given by

$$\theta_i = \begin{cases} \theta_0; & i = 1 \\ \theta_0 + \sum\limits_{j=1}^{i-1} 2\pi f_p (1-d)\mathcal{T}_j; & i = 2, 3, 4, \cdots, N \end{cases} \qquad \text{for NIC model} \tag{2.3.9}$$

where θ_0 is the phase of the unmodulated carrier at the time instant of $t = 0$ within the window length T_D of a data record. Introduce *the scaled frequency shift* [12]

$$f_s \triangleq (1-d) f_p \tag{2.3.10}$$

and using (2.2.14), we can re-write (2.3.9) as

$$\begin{aligned} \theta_i &= \begin{cases} \theta_0; & i = 1 \\ \theta_0 + \sum\limits_{j=1}^{i-1} 2\pi f_s \mathcal{T}; & i = 2, 3, 4, \cdots, N \end{cases} \\ &= \theta_0 + (i-1) 2\pi f_s \mathcal{T}; \qquad i = 1, 2, 3, 4, \cdots, N \qquad \text{for NIC model} \end{aligned} \tag{2.3.11}$$

Substituting this relation in (2.2.16) produces

$$\begin{aligned} F^{nic}(f) &\overset{(a)}{=} e^{-j2\pi(f-f_c)\frac{\mathcal{T}d}{2}} \cdot \frac{A\mathcal{T}d}{2} \cdot \mathrm{sinc}[(f-f_c)\mathcal{T}d] \cdot \sum_{i=1}^{N} e^{-j[2\pi(f-f_c)(i-1)\mathcal{T} - \theta_0 - (i-1)2\pi f_s \mathcal{T}]} \\ &= e^{-j\left[2\pi(f-f_c)\frac{\mathcal{T}d}{2} - \theta_0\right]} \cdot \frac{A\mathcal{T}d}{2} \cdot \mathrm{sinc}[(f-f_c)\mathcal{T}d] \cdot \sum_{i=1}^{N} e^{-j2\pi(f-f_c-f_s)(i-1)\mathcal{T}} \\ &\overset{(b)}{=} e^{-j\left[2\pi(f-f_c)\frac{\mathcal{T}d}{2} - \theta_0\right]} \cdot \frac{A\mathcal{T}d}{2} \cdot \mathrm{sinc}[(f-f_c)\mathcal{T}d] \cdot \frac{1 - e^{-j2\pi(f-f_c-f_s)N\mathcal{T}}}{1 - e^{-j2\pi(f-f_c-f_s)\mathcal{T}}} \\ &\overset{(c)}{=} e^{-j\left[2\pi(f-f_c)\frac{\mathcal{T}d}{2} - \theta_0\right]} \cdot \frac{A\mathcal{T}d}{2} \cdot \mathrm{sinc}[(f-f_c)\mathcal{T}d] \cdot \frac{1 - e^{-j2\pi(f-f_c-f_s)T_D}}{1 - e^{-j2\pi(f-f_c-f_s)\mathcal{T}}} \end{aligned} \tag{2.3.12}$$

where $\overset{(a)}{=}$ is due to (2.3.11) and (2.2.16), $\overset{(b)}{=}$ is due to the rule for calculating the summation of the geometrical progression, and $\overset{(c)}{=}$ is due to (2.2.13). □

Based on this model, it can be shown that the spectrum of the Non-Ideal Coherent (NIC) ELT signal model is given by

$$\begin{aligned} S^{nic}(f) &\triangleq \left|F^{nic}(f)\right|^2 \\ &= \left[\frac{A\mathcal{T}d}{2}\right]^2 \cdot \operatorname{sinc}^2[(f-f_c)\mathcal{T}d] \cdot \left[\frac{\sin[\pi(f-f_c-f_s)T_D]}{\sin[\pi(f-f_c-f_s)\mathcal{T}]}\right]^2 \end{aligned} \quad (2.3.13)$$

The spectrum of the NIC signal is capable of being closely related to a wide range of actual ELT signals. Using the Non-Ideal Coherent (NIC) ELT signal model, an ELT signal can be generated by computer and the spectrum can be calculated by employing a sequence of 24 consecutive Blackman windowed 2048-point periodograms [12] as illustrated in Fig. 2.11. The dynamic range of each of the 24 periodograms is 20 dB and approximately two sweeps of the ELT signal are provided.

Let the *Fourier Transform* calculated from the kth data window record of the NIC signal be denoted as $F_k^{nic}(f)$ and let $S_k^{nic}(f)$ be the kth periodogram of the NIC signal, then we have

$$S_k^{nic}(f) \triangleq \left|F_k^{nic}(f)\right|^2 \qquad k = 1, 2, ..., K \quad (2.3.14)$$

In our computer simulation, we usually let K be equal to 24. Then, the curve in Fig. 2.12 is the Arithmetically Averaged Spectrum (AAS)

$$A^{nic}(f) \triangleq \frac{1}{24}\sum_{k=1}^{24} S_k^{nic}(f) \quad (2.3.15)$$

of the NIC signal, while the curve in Fig. 2.13 is the Geometrically Averaged Spectrum

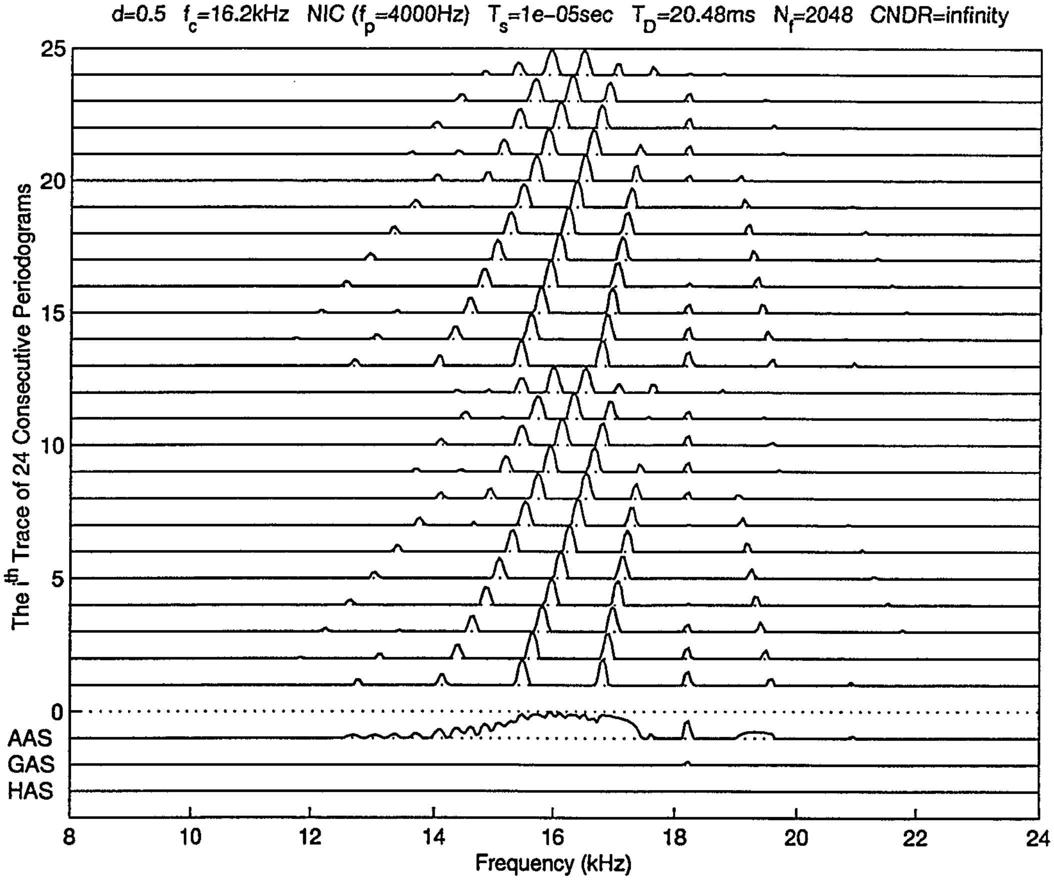

Figure 2.11: Periodograms of the ELT signal in the NIC model

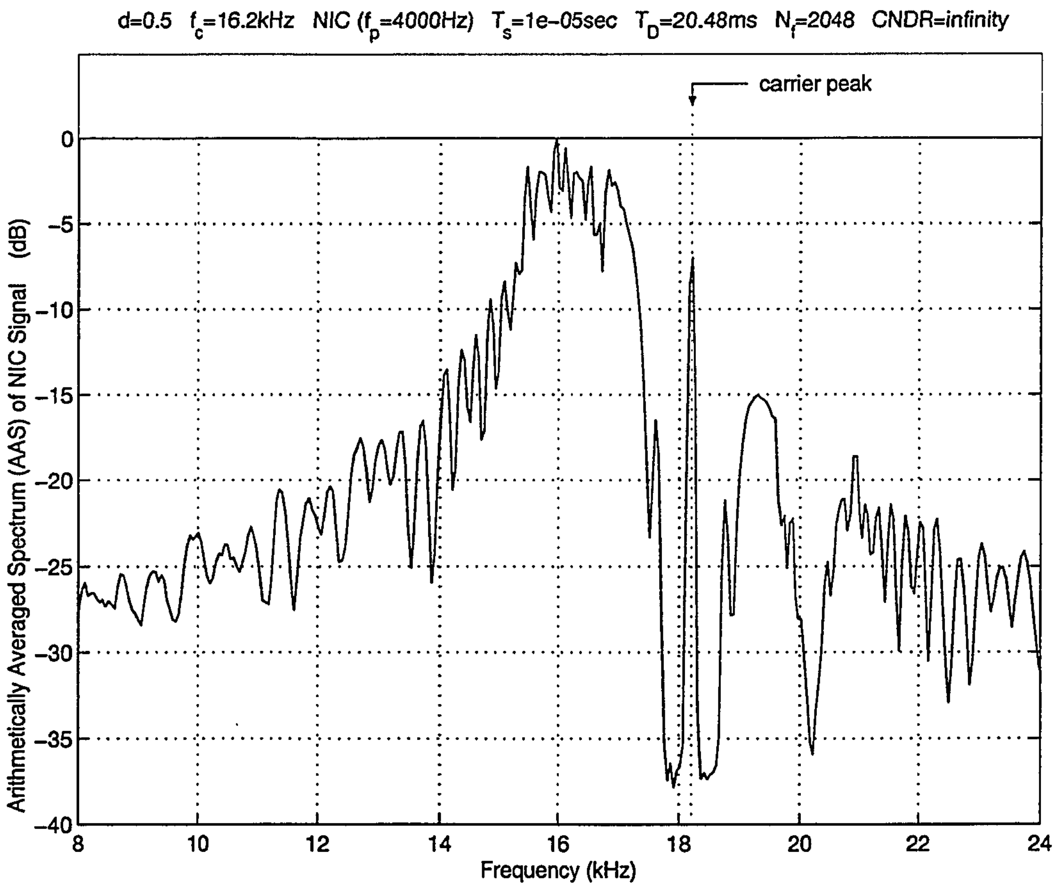

Figure 2.12: Arithmetically Averaged Spectrum (AAS) of the NIC Signal

(GAS)

$$G^{nic}(f) \triangleq \left[\prod_{k=1}^{24} S_k^{nic}(f) \right]^{\frac{1}{24}} \tag{2.3.16}$$

of the NIC signal, and the curve in Fig. 2.14 is the Harmonically Averaged Spectrum (HAS)

$$H^{nic}(f) \triangleq \frac{1}{\frac{1}{24} \sum_{k=1}^{24} \frac{1}{S_k^{nic}(f)}} \tag{2.3.17}$$

of the NIC signal.

It can be seen from Fig. 2.11 that the spectral carrier peak has shifted to 18.2 kHz which is larger (by 2 kHz due to frequency pulling) than the oscillator carrier frequency which is 16.2 kHz in this example. Also see that the carrier peak disappears for a considerable portion of the sweep time due to the 20 dB dynamic range limitation. Furthermore, the lower set of sidelobes is enhanced while the upper set of sidelobes is diminished.

More specifically, it can be seen from Fig. 2.11 that from the 1st periodogram to the 24th periodogram, all of the carrier peaks have the same frequency (which is 18.2 kHz in this example) but different magnitudes. This causes the carrier peaks in Fig. 2.12, Fig. 2.13, and Fig. 2.14 to occur at the same frequency but to have different heights. On the other hand (also see Fig. 2.11), from the 1st periodogram to the 24th periodogram, the first lower sideband sweeps from 16.7 kHz to 17.8 kHz while the first upper sideband sweeps from 19.7 kHz to 18.6 kHz in this example. The lower sideband for the AAS in Fig. 2.12 is significantly higher than either the carrier peak or the upper sideband. By employing GAS and HAS, as depicted in Figs. 2.13 and 2.14, the carrier peak exceeds both sidebands. A similar discussion applies to

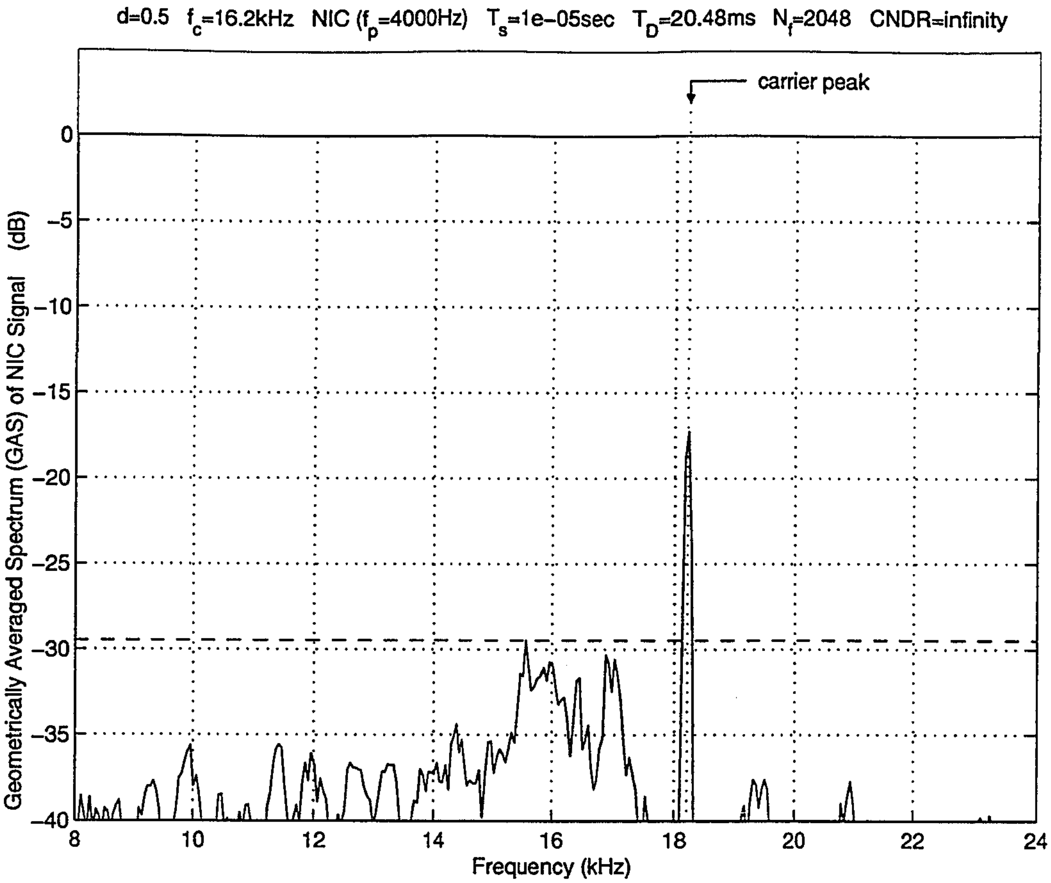

Figure 2.13: Geometrically Averaged Spectrum (GAS) of the NIC Signal

the second lower sideband and the second upper sideband. Also note the asymmetry with respect to the shifted carrier frequency (which is 18.2 kHz in this example) in Figs. 2.11, 2.12, 2.13, and 2.14.

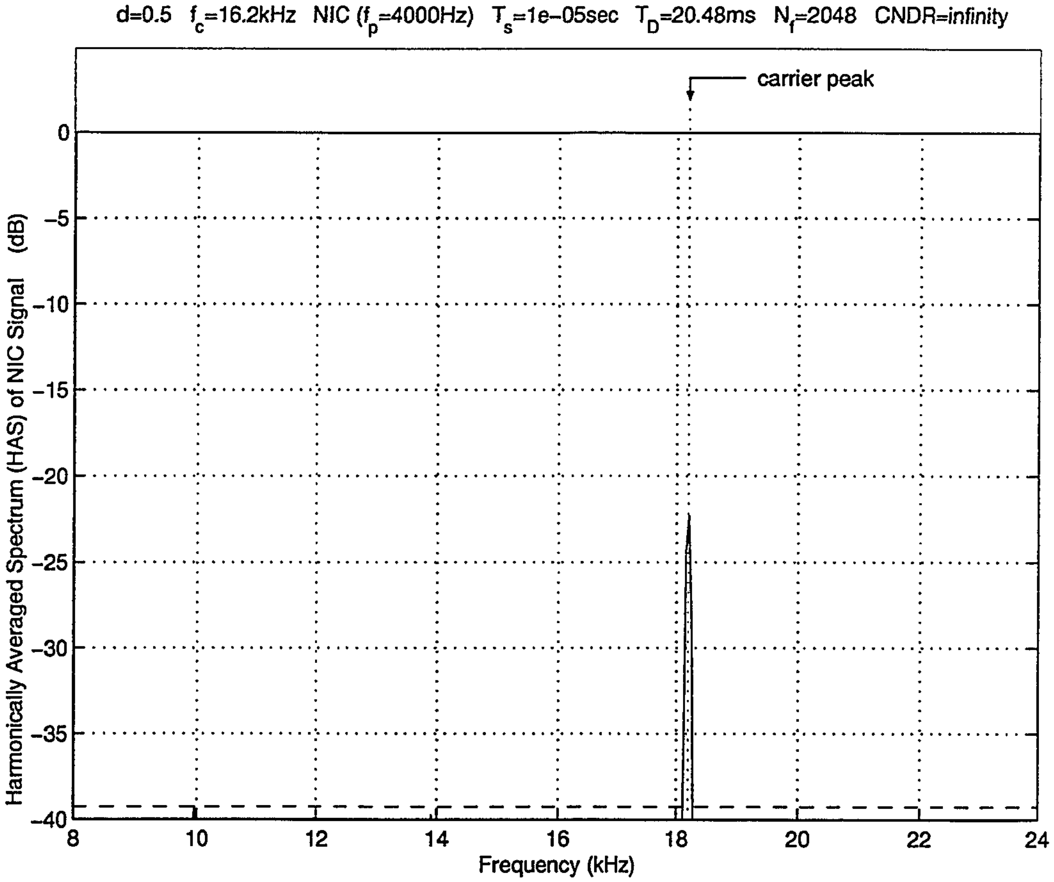

Figure 2.14: Harmonically Averaged Spectrum (HAS) of the NIC Signal

2.3.3 Non-Coherent ELT Signal

The third model for ELT units, called the Non-Coherent ELT (NCE) signal model [12], includes those ELT units which can be represented by a crystal controlled oscillator switched ON and OFF by the pulse modulator signal, as shown in Fig. 2.15. In this case, the phase from pulse to pulse is no longer related, as shown in Fig. 2.16.

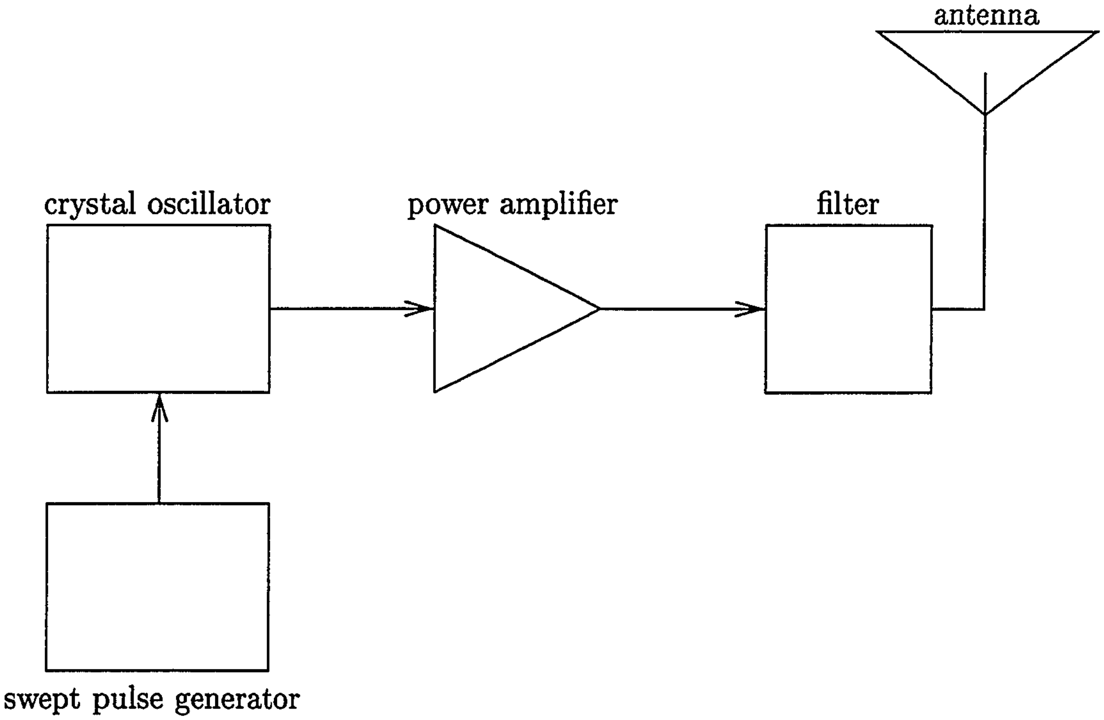

Figure 2.15: Block diagram for the Non-Coherent ELT (NCE).

With Θ_i being assumed to be a random variable distributed uniformly between 0 and 2π, we have

$$\theta_i = \Theta_i; \quad i = 1, 2, 3, 4, \cdots, N \quad \text{for NCE model} \tag{2.3.18}$$

Substituting this relation in (2.2.16) produces

$$F^{nce}(f) \;=\; e^{-j2\pi(f-f_c)\frac{\mathcal{T}d}{2}} \cdot \frac{A\mathcal{T}d}{2} \cdot \mathrm{sinc}[(f-f_c)\mathcal{T}d] \cdot \sum_{i=1}^{N} e^{-j[2\pi(f-f_c)(i-1)\mathcal{T}-\Theta_i]}$$

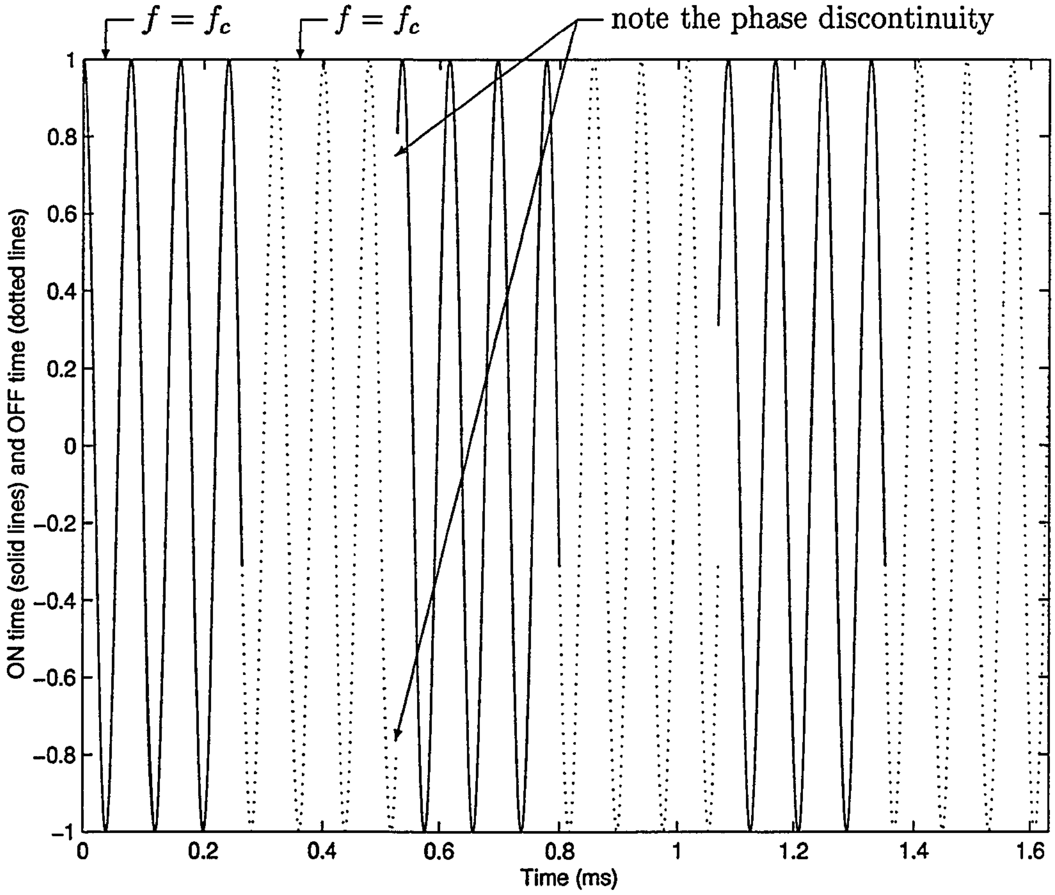

Figure 2.16: The phase discontinuity in the Non-Coherent ELT (NCE) signal.

(2.3.19)

The spectrum of the Non-Coherent ELT (NCE) signal model is given by

$$\begin{aligned} S^{nce}(f) &\triangleq |F^{nce}(f)|^2 \\ &= \left[\frac{A\mathcal{T}d}{2}\right]^2 \cdot \mathrm{sinc}^2[(f-f_c)\mathcal{T}d] \cdot \left|\sum_{i=1}^{N} e^{-j[2\pi(f-f_c)(i-1)\mathcal{T}-\Theta_i]}\right|^2 \end{aligned} \qquad (2.3.20)$$

This spectrum is capable of representing a class of ELT signals having very poor spectral properties. The very broad averaged spectrum of the NCE signal is difficult to process for carrier frequency measurement. Using the Non-Coherent ELT (NCE) signal model, an ELT signal can be generated by computer and the spectrum can be calculated by employing a sequence of 24 consecutive Blackman windowed 2048-point periodograms [12] as illustrated in Fig. 2.17. The dynamic range of each of the 24 periodograms is 20 dB and approximately two sweeps of the ELT signal are provided.

Let the *Fourier Transform* calculated from the kth data window record of the NCE signal be denoted as $F_k^{nce}(f)$ and let $S_k^{nce}(f)$ be the kth periodogram of the NCE signal, then we have

$$S_k^{nce}(f) \triangleq |F_k^{nce}(f)|^2 \qquad k = 1, 2, ..., K \qquad (2.3.21)$$

In our computer simulation we usually let K be equal to 24. Then, the curve in Fig. 2.18 is the Arithmetically Averaged Spectrum (AAS)

$$A^{nce}(f) \triangleq \frac{1}{24}\sum_{k=1}^{24} S_k^{nce}(f) \qquad (2.3.22)$$

of the NCE signal, while the curve in Fig. 2.19 is the Geometrically Averaged Spectrum (GAS)

$$G^{nce}(f) \triangleq \left[\prod_{k=1}^{24} S_k^{nce}(f)\right]^{\frac{1}{24}} \qquad (2.3.23)$$

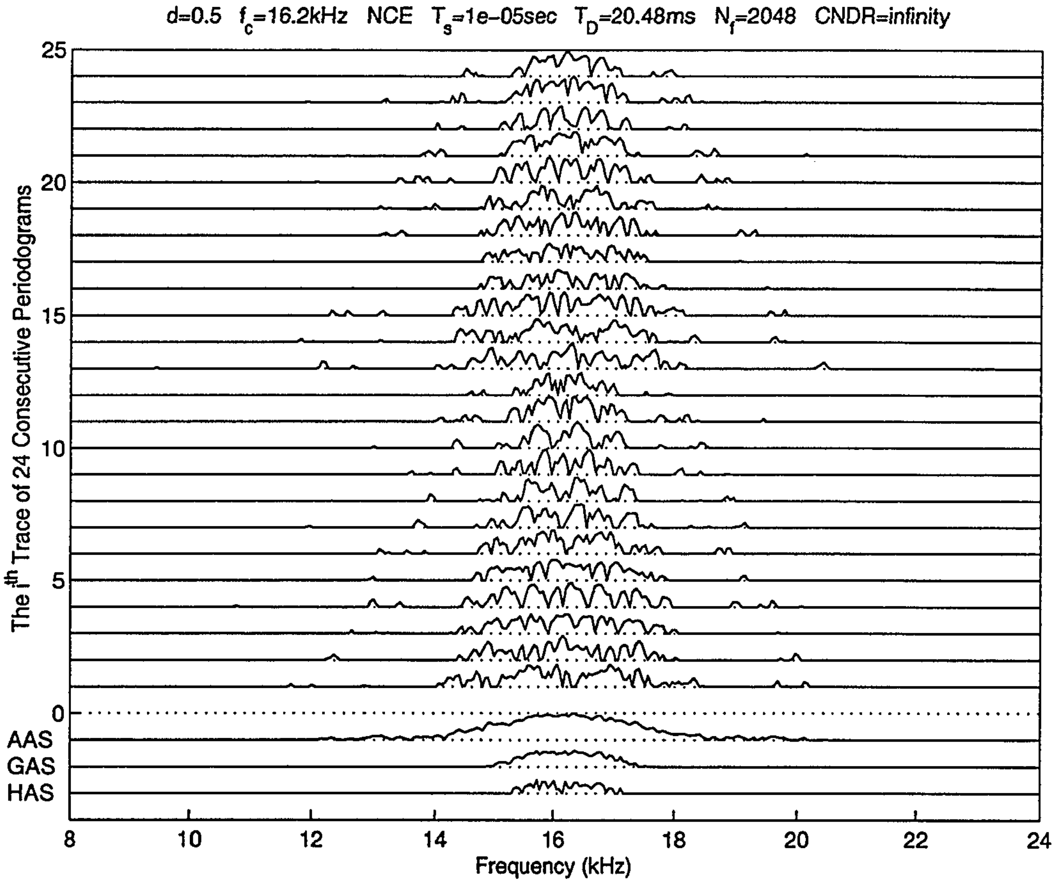

Figure 2.17: Periodograms of the ELT signal in the NCE model

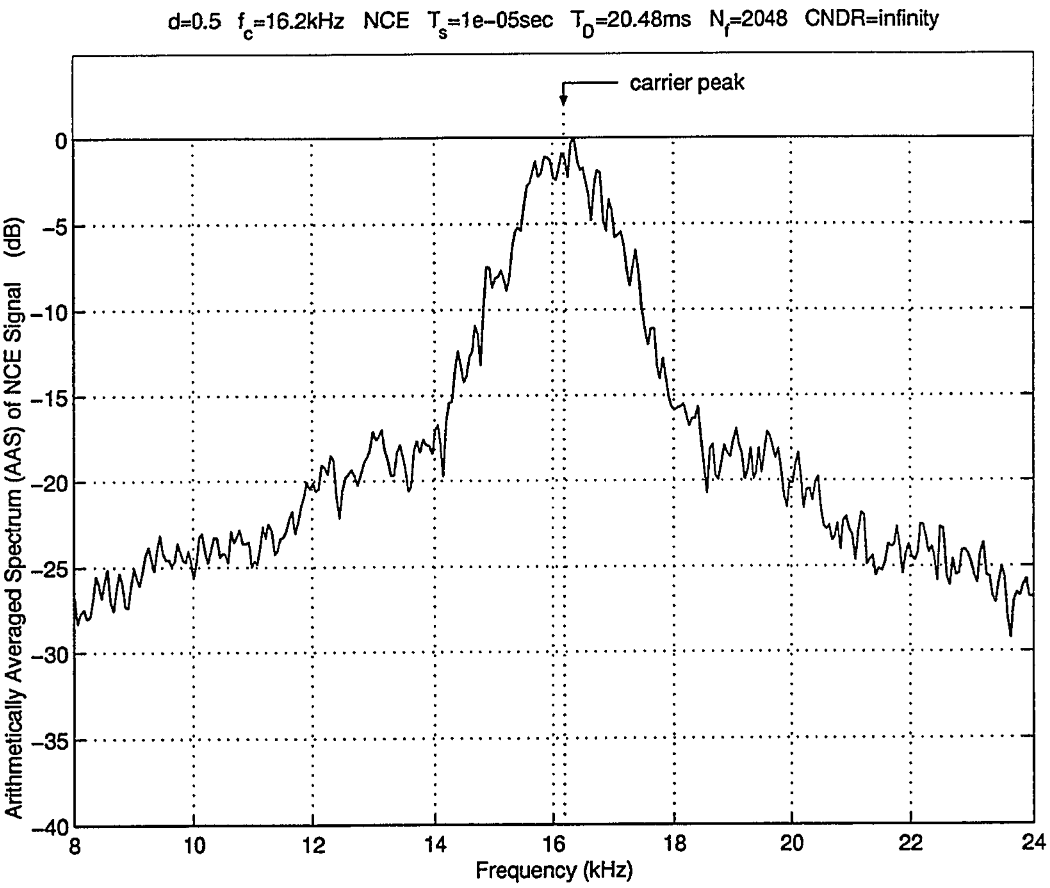

Figure 2.18: Arithmetically Averaged Spectrum (AAS) of the NCE Signal

of the NCE signal, and the curve in Fig. 2.20 is the Harmonically Averaged Spectrum (HAS)

$$H^{nce}(f) \triangleq \frac{1}{\frac{1}{24}\sum_{k=1}^{24}\frac{1}{S_k^{nce}(f)}} \tag{2.3.24}$$

of the NCE signal.

It can be seen from Fig. 2.17 that from the 1st periodogram to the 24th periodogram, there is no detected carrier peak resulting in no carrier peak in Figs. 2.18, 2.19, and 2.20. The frequency interval between the left end which sweeps from 14.7 kHz to 15.8 kHz and the right end which sweeps from 17.7 kHz to 16.6 kHz is continuously occupied. This fact and the other fact that the spectral height at every frequency between these two ends changes from the 1st periodogram to the 24th periodogram cause the averaged spectra in Figs. 2.18, 2.19, and 2.20 to have different heights. Also note the symmetry (in a very rough sense) with respect to the carrier frequency (which is 16.2 kHz in this example) in Figs. 2.17, 2.18, 2.19, and 2.20. However, the carrier peak still cannot be detected.

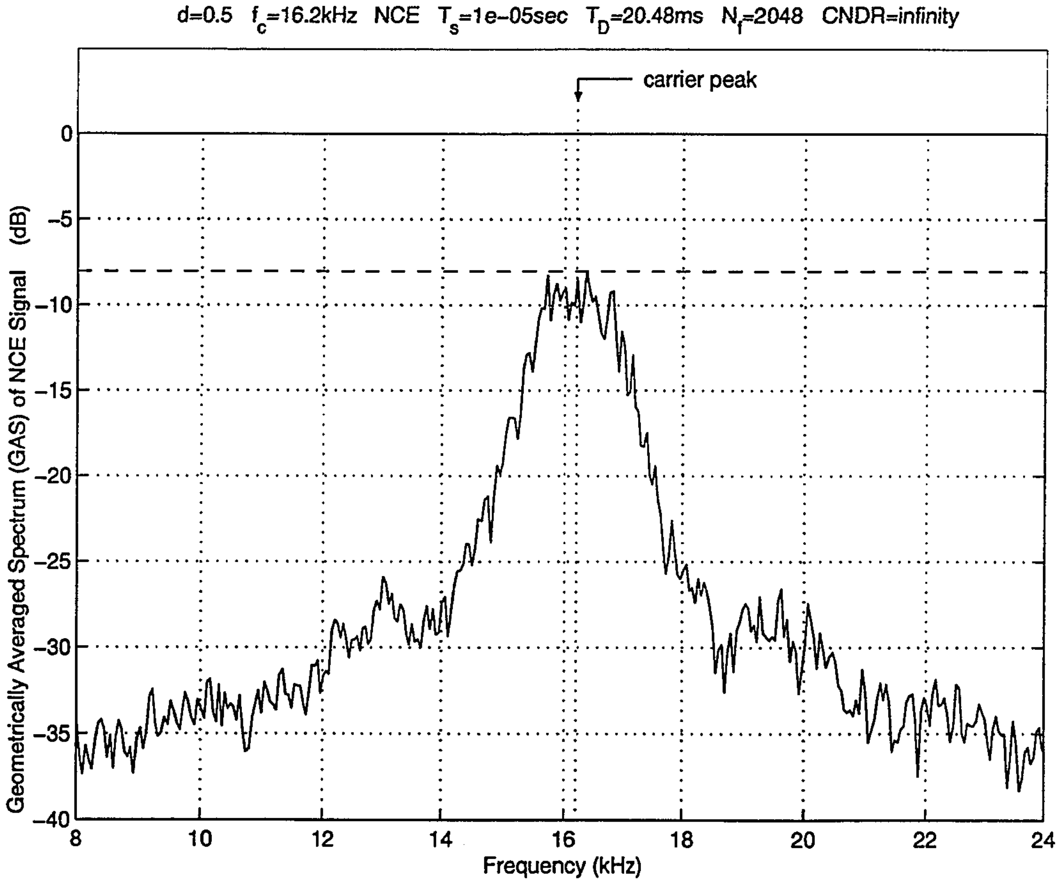

Figure 2.19: Geometrically Averaged Spectrum (GAS) of the NCE Signal

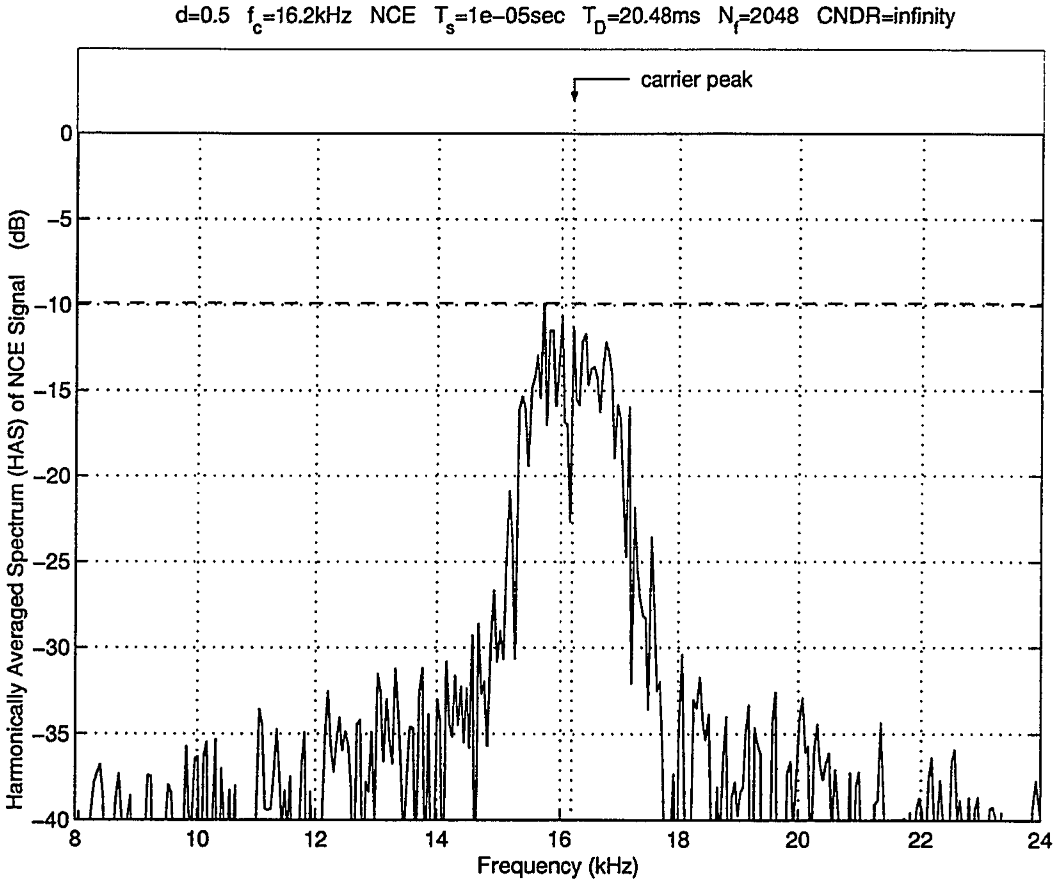

Figure 2.20: Harmonically Averaged Spectrum (HAS) of the NCE Signal

2.3.4 Frequency-Modulated ELT (FME) Signal

There is another possibility in which the voltage supplying the crystal oscillator varies slowly over the modulation sweep. Instead of being a constant, the carrier frequency f_c of an ICE signal could now become $f_c(t)$ which is a function of time t. For example, we could have

$$f_c(t) = f_c + \Delta f_c \cdot \frac{t}{T_S} \qquad 0 \le t \le T_S \tag{2.3.25}$$

where the time interval T_S corresponds to a complete sweep, f_c is the nominal carrier frequency, and Δf_c is the maximum frequency deviation.

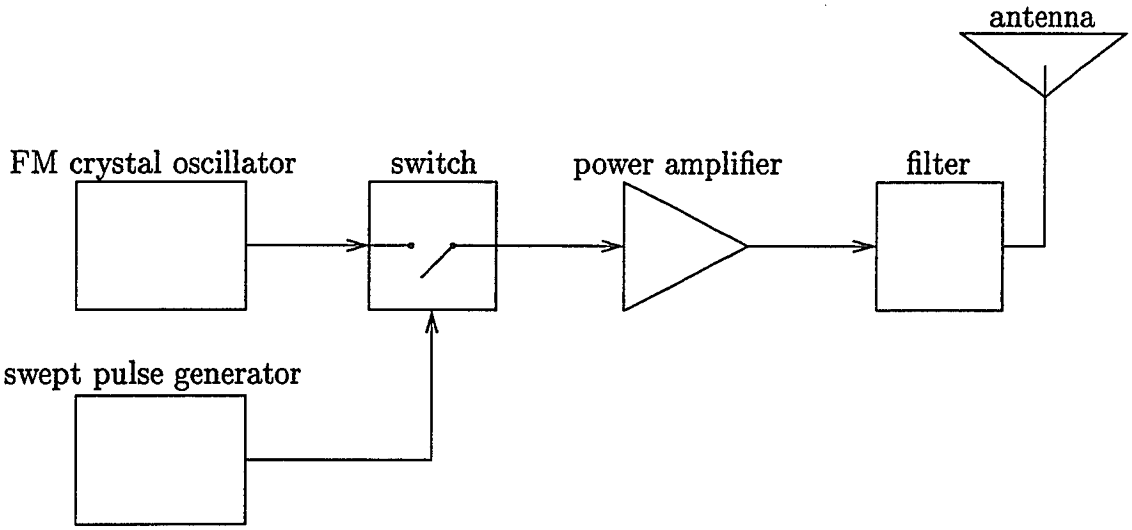

Figure 2.21: Block diagram for the Frequency-Modulated ELT (FME).

We call this new model the Frequency-Modulated ELT (FME) signal model, illustrated in Fig. 2.21. The FM in this figure means Frequency-Modulated. The waveform is depicted in Fig. 2.22 where it is seen that the frequency gradually decreases from f_c. Note that, Δf_c has a negative value in this example. If, within the kth interval of duration T_D which is the time interval corresponding to the data used

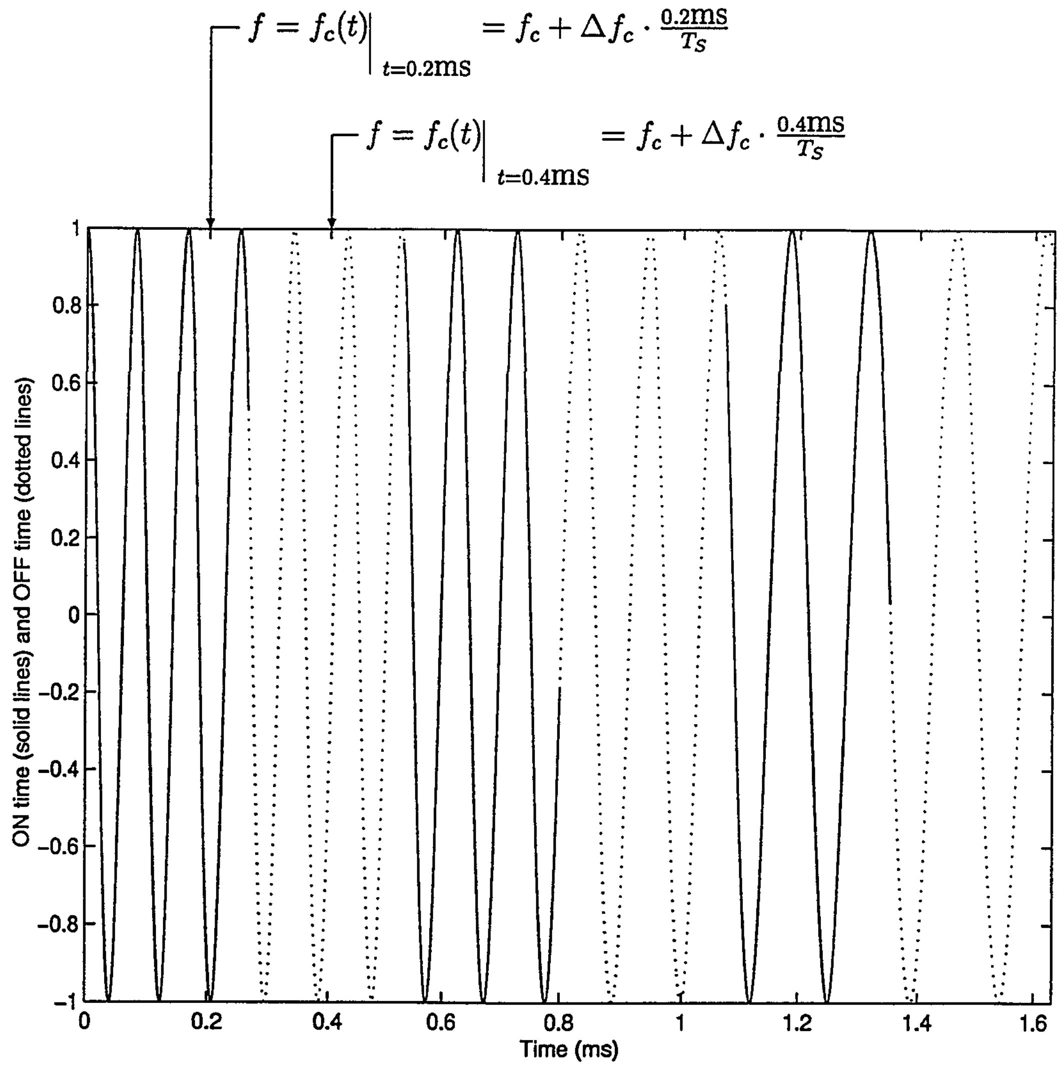

Figure 2.22: The frequency deviation in the Frequency-Modulated ELT (FME) signal.

to calculate the kth periodogram, the deviation of $f_c(t)$ in (2.3.25) is not too large, then we can use a constant to approximate $f_c(t)$ such that

$$f_c(t) \approx f_c\left(\left(k - \frac{1}{2}\right) T_D\right) \qquad (k-1)T_D \leq t < kT_D \qquad (2.3.26)$$

Because of the dependency of $F^{fme}(f)$ on $f_c(t)$, we can not simply use (2.3.2) here. By substituting $f_c((k-\frac{1}{2})T_D)$ and $\mathcal{T}_k$ (which is the value of $\mathcal{T}$ when $(k-1)T_D \leq t < kT_D$) for f_c and $\mathcal{T}$ in the right hand side of (2.3.2), the kth *Fourier Transform* of the FME signal model is given by

$$\begin{aligned} F_k^{fme}(f) &= e^{-j\left[2\pi\left(f-f_c\left(\left(k-\frac{1}{2}\right)T_D\right)\right)\frac{\mathcal{T}_k d}{2}-\theta_0\right]} \cdot \frac{A\mathcal{T}_k d}{2} \cdot \mathrm{sinc}\left[\left(f - f_c\left(\left(k-\frac{1}{2}\right)T_D\right)\right)\mathcal{T}_k d\right] \\ &\quad \cdot \frac{1-e^{-j2\pi\left(f-f_c\left(\left(k-\frac{1}{2}\right)T_D\right)\right)T_D}}{1-e^{-j2\pi\left(f-f_c\left(\left(k-\frac{1}{2}\right)T_D\right)\right)\mathcal{T}_k}} \end{aligned} \tag{2.3.27}$$

Then, the kth periodogram of the Frequency-Modulated ELT (FME) signal model is given by

$$\begin{aligned} S_k^{fme}(f) &\triangleq \left|F_k^{fme}(f)\right|^2 \\ &= \left[\frac{A\mathcal{T}_k d}{2}\right]^2 \cdot \mathrm{sinc}^2\left[\left(f - f_c\left(\left(k-\frac{1}{2}\right)T_D\right)\right)\mathcal{T}_k d\right] \\ &\quad \cdot \left[\frac{\sin[\pi(f-f_c((k-\frac{1}{2})T_D))T_D]}{\sin[\pi(f-f_c((k-\frac{1}{2})T_D))\mathcal{T}_k]}\right]^2 \end{aligned} \tag{2.3.28}$$

Using the FME signal model, an ELT signal can be generated by computer and the spectrum can be calculated as discussed in the previous models and illustrated in Fig. 2.23.

The curve in Fig. 2.24 is the Arithmetically Averaged Spectrum (AAS)

$$A^{fme}(f) \triangleq \frac{1}{24}\sum_{k=1}^{24} S_k^{fme}(f) \tag{2.3.29}$$

of the FME signal, while the curve in Fig. 2.25 is the Geometrically Averaged Spectrum (GAS)

$$G^{fme}(f) \triangleq \left[\prod_{k=1}^{24} S_k^{fme}(f)\right]^{\frac{1}{24}} \tag{2.3.30}$$

of the FME signal, and the curve in Fig. 2.26 is the Harmonically Averaged Spectrum (HAS)

$$H^{fme}(f) \triangleq \frac{1}{\frac{1}{24}\sum_{k=1}^{24}\frac{1}{S_k^{fme}(f)}} \tag{2.3.31}$$

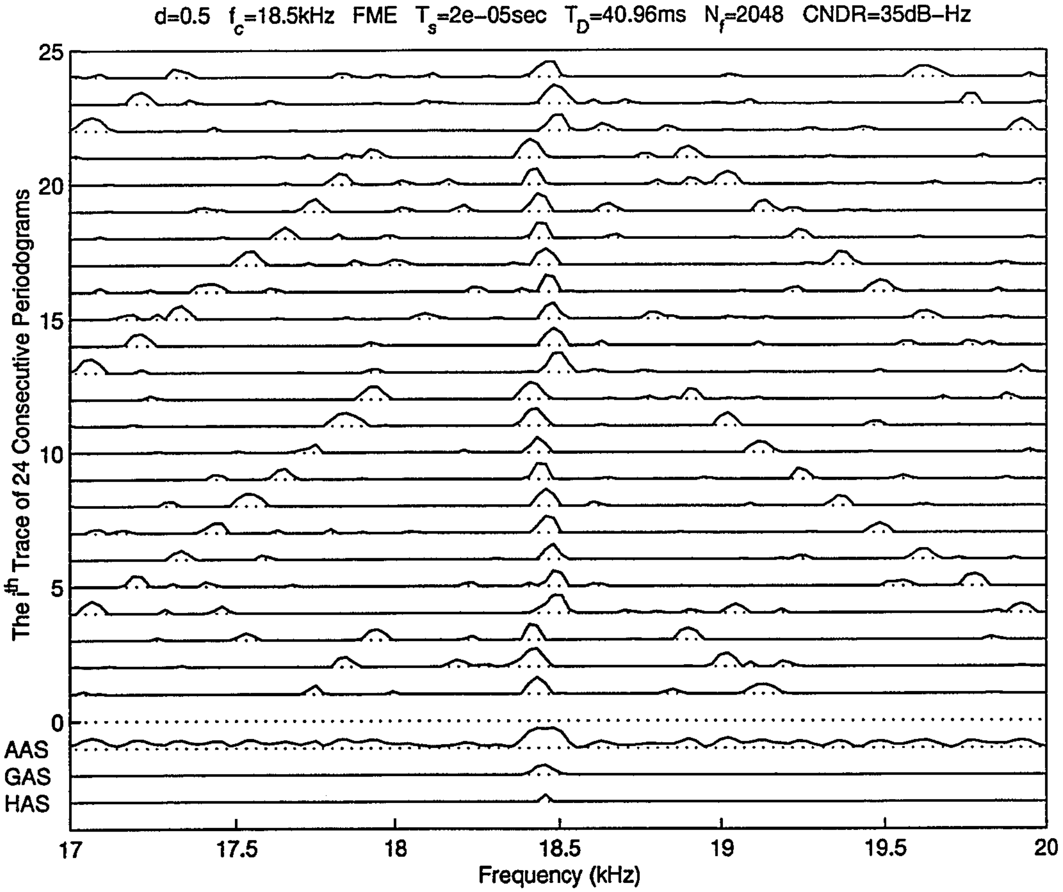

Figure 2.23: Periodograms of the ELT signal in the FME model

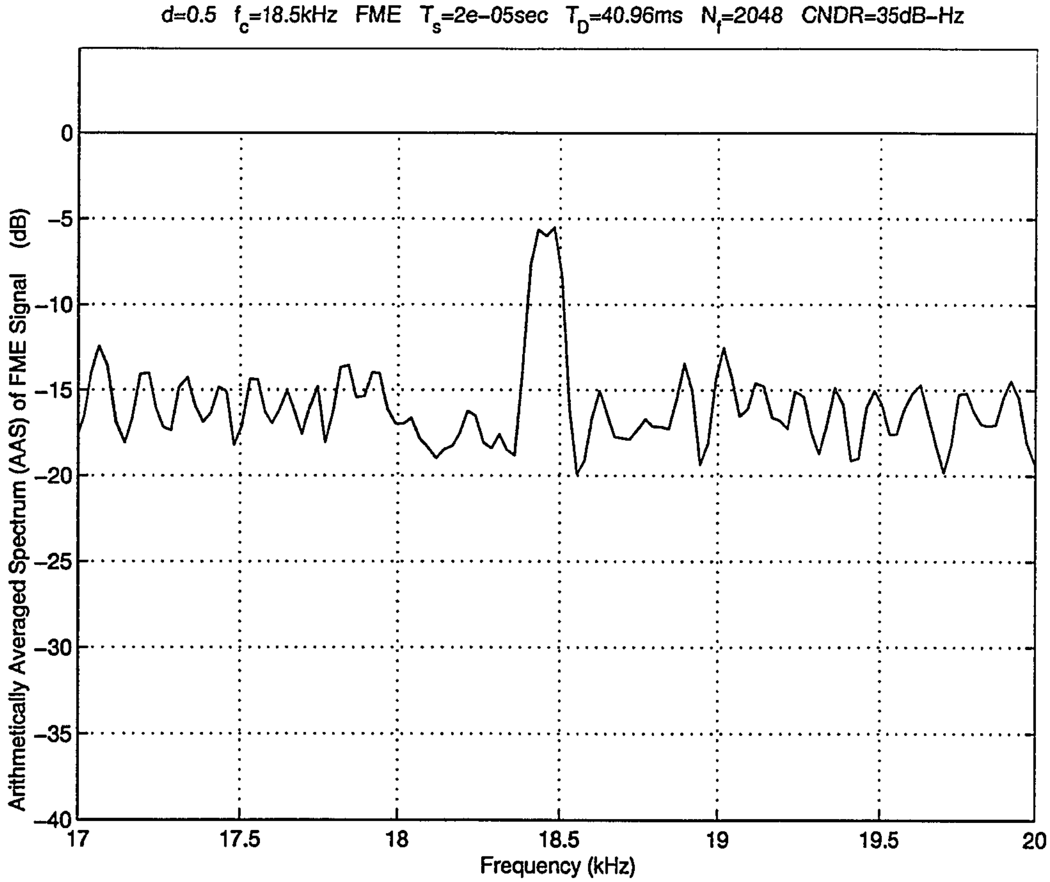

Figure 2.24: Arithmetically Averaged Spectrum (AAS) of the FME Signal

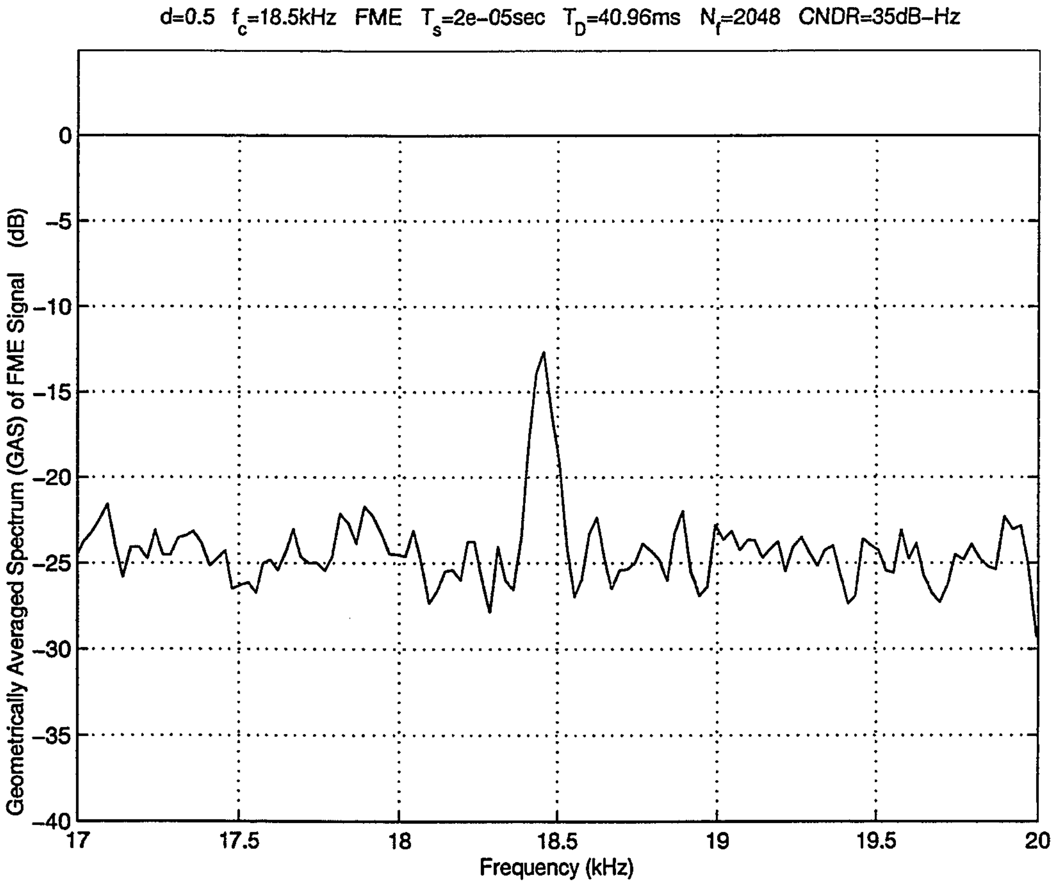

Figure 2.25: Geometrically Averaged Spectrum (GAS) of the FME Signal

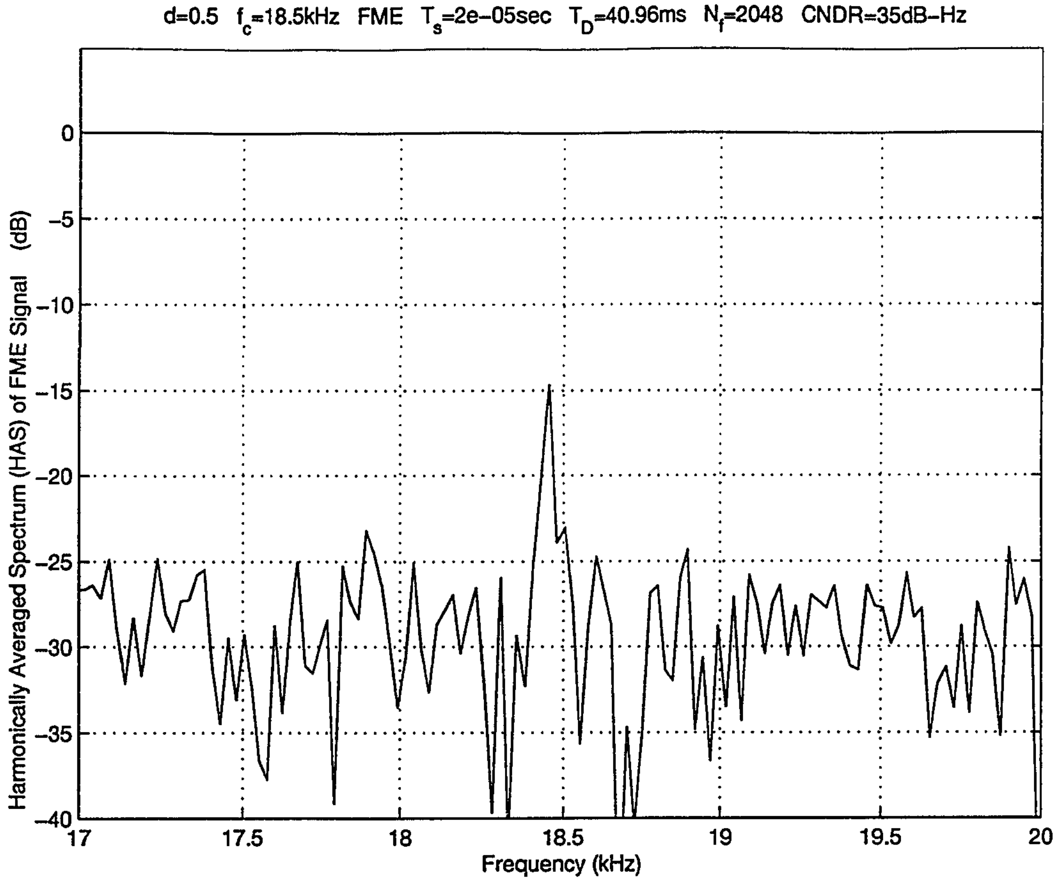

Figure 2.26: Harmonically Averaged Spectrum (HAS) of the FME Signal

of the FME signal.

It can be seen from Fig. 2.23 that from the first periodogram of every sweep (*i.e.*, periodograms 4, 13, and 22 in this example) to the last periodogram of every sweep (*i.e.*, periodograms 3, 12, and 21 in this example), the carrier peaks move away from the carrier frequency (which is 18.5 kHz in this example) gradually to the left. In Fig. 2.24, the carrier peak has the characteristic shape of a demodulated FM signal with a width equal to the frequency deviation Δf_c. However, GAS and HAS averaging reduces the width to a single peak as shown in Figs. 2.25 and 2.26, respectively.

2.4 Summary

In Section 2.3, we described the mathematical model for each one of the four kinds of ELT signals respectively. The first three ELT signal models (which are the Ideal Coherent ELT (ICE) signal model, the Non-Ideal Coherent (NIC) ELT signal model, and the Non-Coherent ELT (NCE) signal model) can be found in the literature while the fourth (which is the Frequency-Modulated ELT (FME) signal model) is new. We calculate the theoretical spectrum of each ELT signal model directly after that model has been discussed.

For the ICE signal, it is shown that all methods are effective in detecting the carrier peak; however, the GAS and HAS greatly reduce the sidelobe levels. For the NIC signal, the AAS detects the carrier peak but also creates a large sideband component; while the GAS and HAS reduce the carrier peaks to some extent, they still enhance the carrier peaks relative to the sidebands. No method discussed here is successful in detecting carrier peaks for NCE signals. Finally, the FME signal can be detected using all three methods.

It appears that the combination of AAS, GAS, and HAS could provide better Doppler curve than AAS alone. Therefore, the accuracy of location estimate could improve.

Chapter 3

Nonlinear Spectral Averaging

3.1 Introduction

In this chapter, the properties of GAS and HAS are investigated *vis-à-vis* AAS. Specifically, the contents of this chapter include: 1) A taste involving spectral heights of 3 consecutive periodograms and a single frequency which shows that GAS and HAS tend to be different from AAS in an understandable way. 2) A detailed scenario involving 4 elaborately designed examples which provide specific results indicating when GAS and HAS are superior to AAS. 3) A generalized set of relationships which show the decisive role played by a special ratio. It will be shown that the values of GAS and HAS depend on this ratio while the difference between AAS and GAS and the difference between AAS and HAS are monotonic functions of this ratio. 4) Theoretical analyses for the spectra and the shapes of AAS, GAS, and HAS of ICE, NIC, and NCE ELT signals. 5) Computer simulation for two different values of CNDR involving ICE and NIC ELT signals with the application of AAS, GAS and HAS.

3.2 AAS, GAS and HAS for Three Signals

3.2.1 A Taste

Suppose we compute K consecutive periodograms (where the kth periodogram is denoted as $S_k(f)$ while $k = 1, 2, \cdots, K-1, K$) of an averaged spectrum. Examples for $K = 24$ consecutive periodograms can be found in Figs. 2.5, 2.11, or 2.17. We represent here the AAS as

$$A(f) \triangleq \frac{1}{K}\sum_{k=1}^{K} S_k(f) \tag{3.2.1}$$

the GAS as

$$G(f) \triangleq \left[\prod_{k=1}^{K} S_k(f)\right]^{\frac{1}{K}} \tag{3.2.2}$$

and the HAS as

$$H(f) \triangleq \frac{1}{\frac{1}{K}\sum_{k=1}^{K}\frac{1}{S_k(f)}} \tag{3.2.3}$$

With no exceptions [30-35], we always have

$$A(f) \geq G(f) \geq H(f) \tag{3.2.4}$$

where the two equal signs hold if and only if

$$S_1(f) = S_2(f) = \cdots = S_{K-1}(f) = S_K(f) \tag{3.2.5}$$

in (3.2.1), (3.2.2), and (3.2.3).

First, let us get some taste with the special case of $K = 3$ to prepare us for the general discussion. Assume three spectral peaks of amplitude $S_{\text{mid}}(f) - \Delta_S(f)$,

$S_{\mathrm{mid}}(f)$, and $S_{\mathrm{mid}}(f)+\Delta_S(f)$. Then, for AAS we have

$$\begin{aligned} A(f) &= \frac{1}{3}\sum_{k=1}^{3} S_k(f) \\ &= \frac{1}{3}\left\{[S_{\mathrm{mid}}(f)-\Delta_S(f)]+S_{\mathrm{mid}}(f)+[S_{\mathrm{mid}}(f)+\Delta_S(f)]\right\} \\ &= S_{\mathrm{mid}}(f) \end{aligned} \tag{3.2.6}$$

For GAS we have

$$\begin{aligned} G(f) &= \left[\prod_{k=1}^{3} S_k(f)\right]^{\frac{1}{3}} \\ &= \left\{[S_{\mathrm{mid}}(f)-\Delta_S(f)]\cdot S_{\mathrm{mid}}(f)\cdot[S_{\mathrm{mid}}(f)+\Delta_S(f)]\right\}^{\frac{1}{3}} \\ &= \left\{[S_{\mathrm{mid}}^2(f)-\Delta_S^2(f)]S_{\mathrm{mid}}(f)\right\}^{\frac{1}{3}} \\ &= \left[1-\left(\frac{\Delta_S(f)}{S_{\mathrm{mid}}(f)}\right)^2\right]^{\frac{1}{3}}\cdot S_{\mathrm{mid}}(f) \end{aligned} \tag{3.2.7}$$

If $\frac{\Delta_S(f)}{S_{\mathrm{mid}}(f)}=0$, we have

$$G(f)=S_{\mathrm{mid}}(f)=A(f) \tag{3.2.8}$$

For HAS we have

$$\begin{aligned} H(f) &= \frac{1}{\frac{1}{3}\sum_{k=1}^{3}\frac{1}{S_k(f)}} \\ &= \frac{1}{\frac{1}{3}\left(\frac{1}{S_{\mathrm{mid}}(f)-\Delta_S(f)}+\frac{1}{S_{\mathrm{mid}}(f)}+\frac{1}{S_{\mathrm{mid}}(f)+\Delta_S(f)}\right)} \\ &= \frac{3}{\frac{1}{S_{\mathrm{mid}}(f)}+\frac{[S_{\mathrm{mid}}(f)+\Delta_S(f)]+[S_{\mathrm{mid}}(f)-\Delta_S(f)]}{[S_{\mathrm{mid}}(f)-\Delta_S(f)][S_{\mathrm{mid}}(f)+\Delta_S(f)]}} \\ &= \frac{3}{\frac{1}{S_{\mathrm{mid}}(f)}+\frac{2S_{\mathrm{mid}}(f)}{S_{\mathrm{mid}}^2(f)-\Delta_S^2(f)}} \end{aligned}$$

$$= \frac{3}{\frac{1}{S_{\text{mid}}(f)} + \frac{2S_{\text{mid}}(f)}{S^2_{\text{mid}}(f)\left[1 - \left(\frac{\Delta_S(f)}{S_{\text{mid}}(f)}\right)^2\right]}}$$

$$= \frac{3}{1 + \frac{2}{1 - \left(\frac{\Delta_S(f)}{S_{\text{mid}}(f)}\right)^2}} \cdot S_{\text{mid}}(f) \qquad (3.2.9)$$

If $\frac{\Delta_S(f)}{S_{\text{mid}}(f)} = 0$, we have

$$H(f) = S_{\text{mid}}(f) = A(f) \qquad (3.2.10)$$

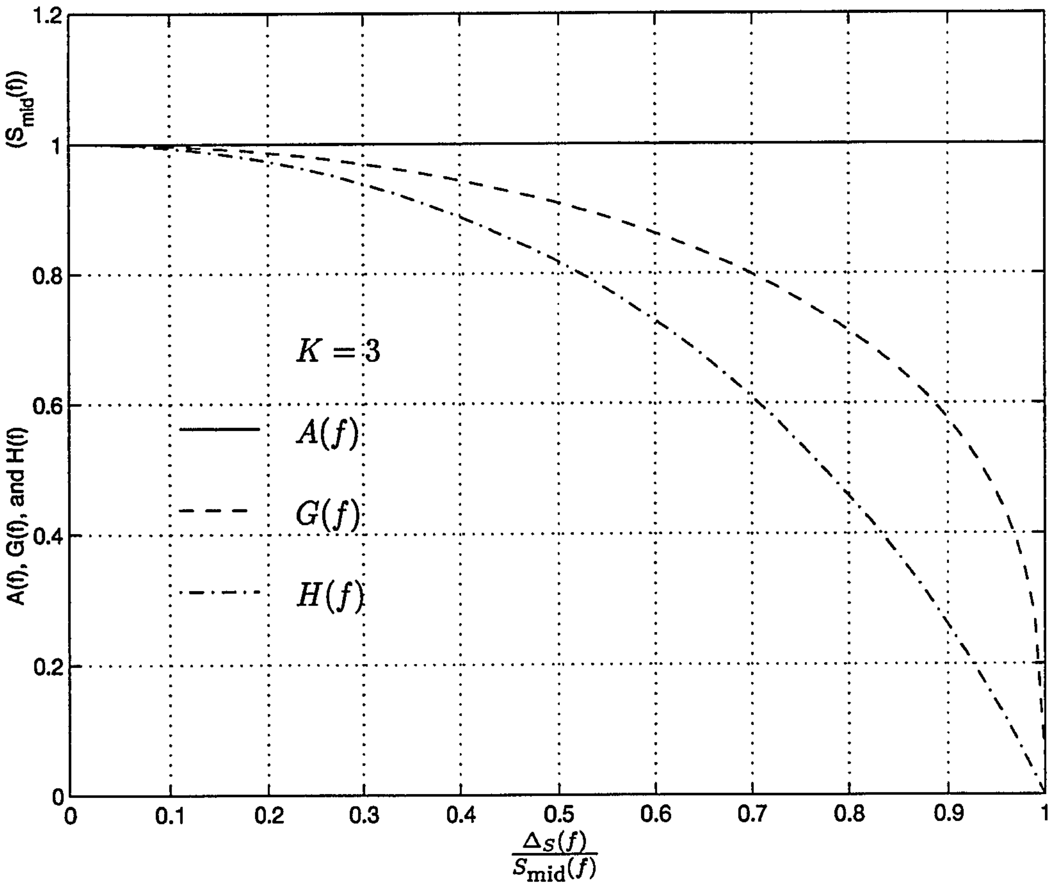

Figure 3.1: The dependences of $G(f)$ and $H(f)$ on $\frac{\Delta_S(f)}{S_{\text{mid}}(f)}$ with $K = 3$

A plot of $A(f)$, $G(f)$, and $H(f)$ is provided with $K = 3$ in Fig. 3.1 where it is seen that if all spectral peaks have the same amplitude, *i.e.*, $\frac{\Delta_S(f)}{S_{\text{mid}}(f)} = 0$, then $A(f) =$

$G(f) = H(f)$. If the variation in spectral peaks is moderate, *e.g.*, $\frac{\Delta_S(f)}{S_{\text{mid}}(f)} = 0.5$, which is typical of ELT signal peaks, then a 10% to 20% reduction in overall average is provided by $G(f)$ and $H(f)$. Conversely, if there is a large variation in spectral peaks, *e.g.*, $\frac{\Delta_S(f)}{S_{\text{mid}}(f)} = 0.95$, which is typical of interference, then a large reduction in overall average is provided by $G(f)$ and $H(f)$, ranging from 50% to 90%.

The significant conclusion, which will become apparent at the end of Subsection 3.3.1, is that the ratio $\frac{\Delta_S(f)}{S_{\text{mid}}(f)}$ plays the decisive role in our problem, not $\Delta_S(f)$ alone nor $S_{\text{mid}}(f)$ alone.

3.2.2 Comparing AAS, GAS and HAS for 2 Different Frequencies f_u and f_d

In this subsection, we concentrate our attention on two arbitrary but different frequencies f_d and f_u (see Figs. 3.2(a), 3.3(a), 3.4(a), and 3.5(a)) within the frequency band of interest. Generally, frequency f_d could be related to a desired signal such as the carrier peak of an ELT signal while frequency f_u could be related to an undesired signal such as interference.

Note that, when certain frequency components within the two sidebands of an ELT signal become too strong, they could interfere with detecting and estimating the ELT signal carrier peak which is now treated as the desired signal. In this sense, any one of these frequency components can also be treated as the undesired signal.

See Figs. 3.2(a), 3.3(a), 3.4(a), and 3.5(a). Assume that $S_1(f_d)$, $S_2(f_d)$, and $S_3(f_d)$ are the spectral heights at frequency f_d for the 1st periodogram, the 2nd periodogram,

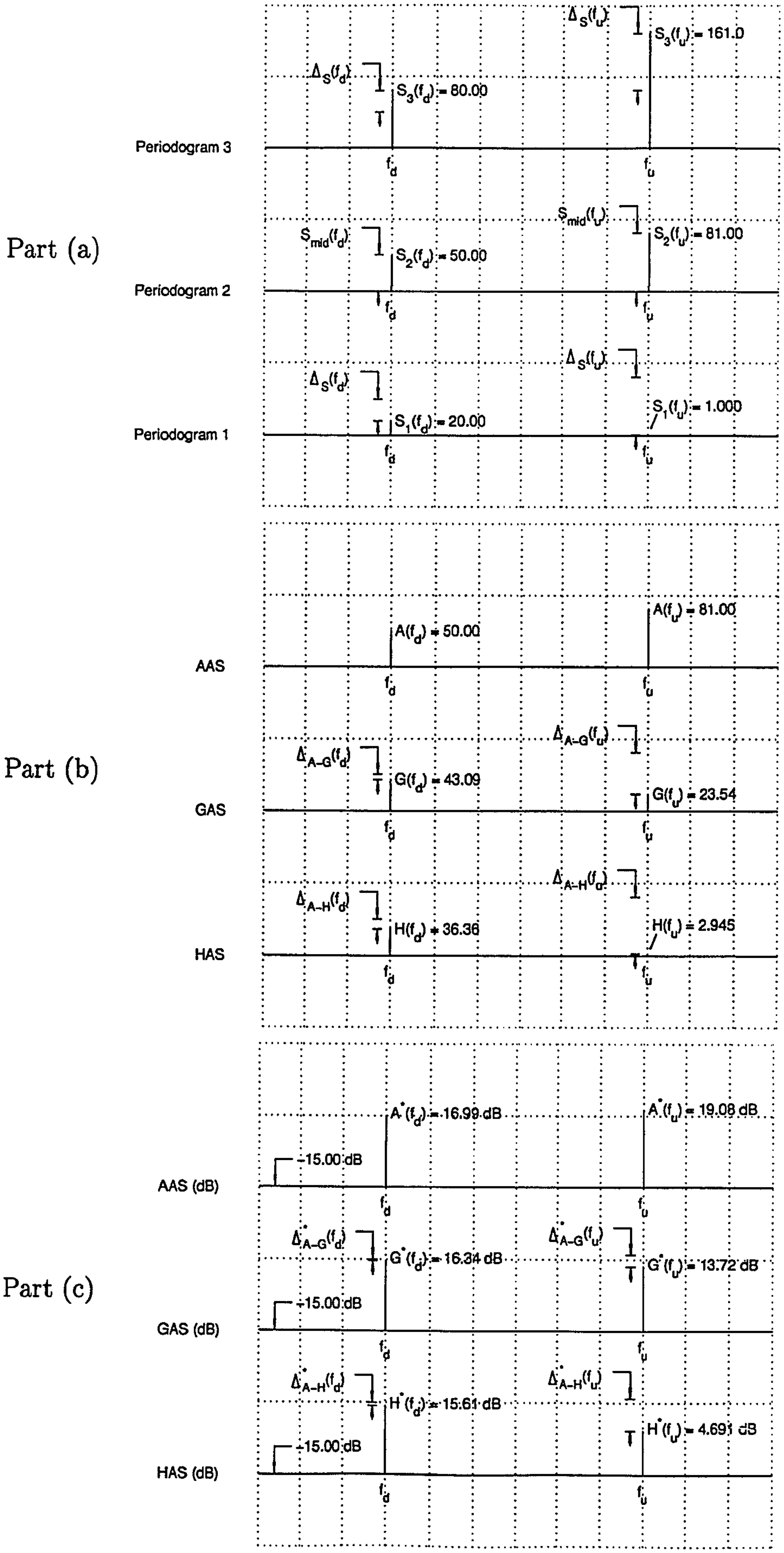

Figure 3.2: Example 3.1 for Demonstrating the Transitional Point

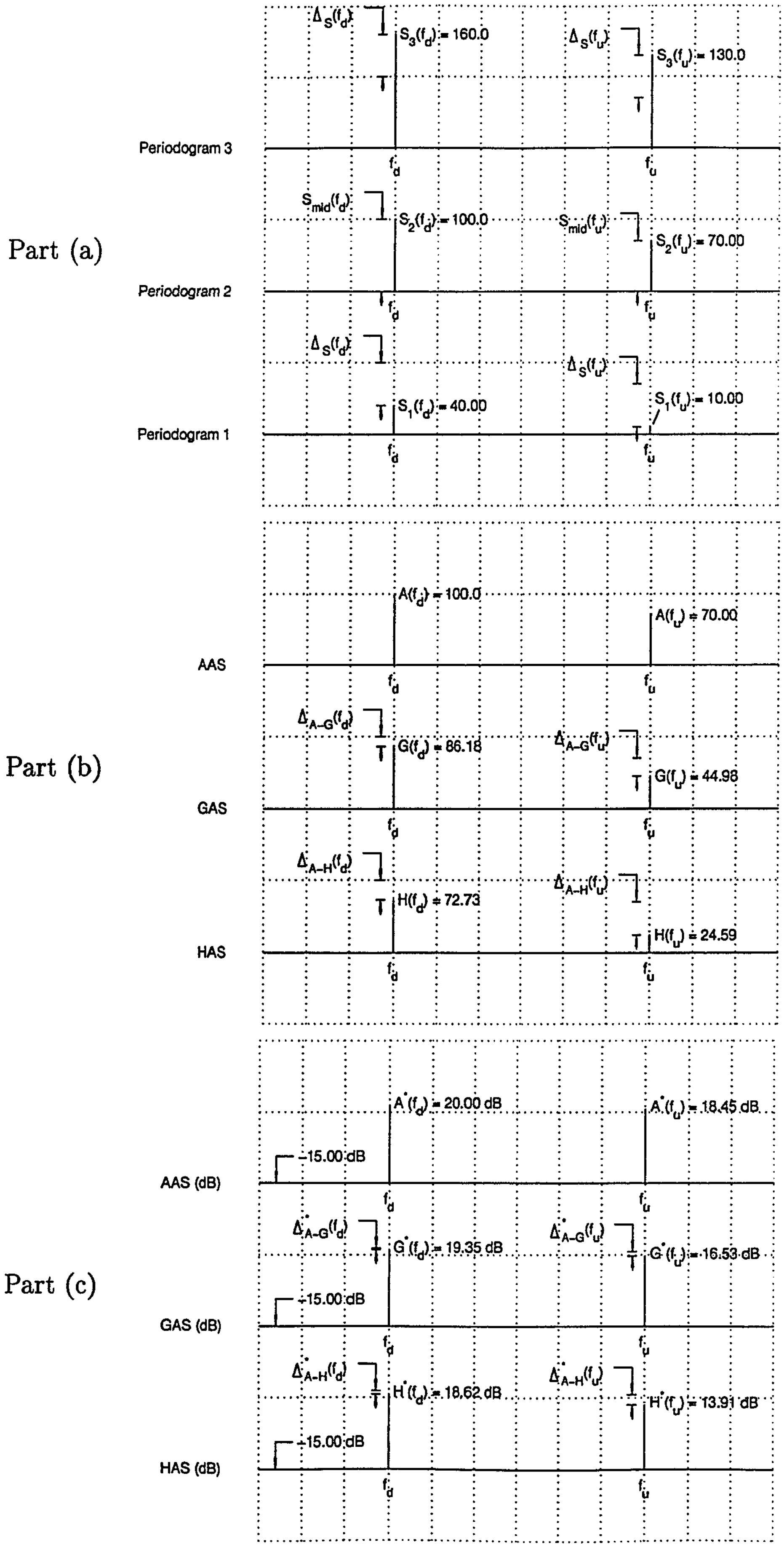

Figure 3.3: Example 3.2 for Demonstrating the Transitional Point

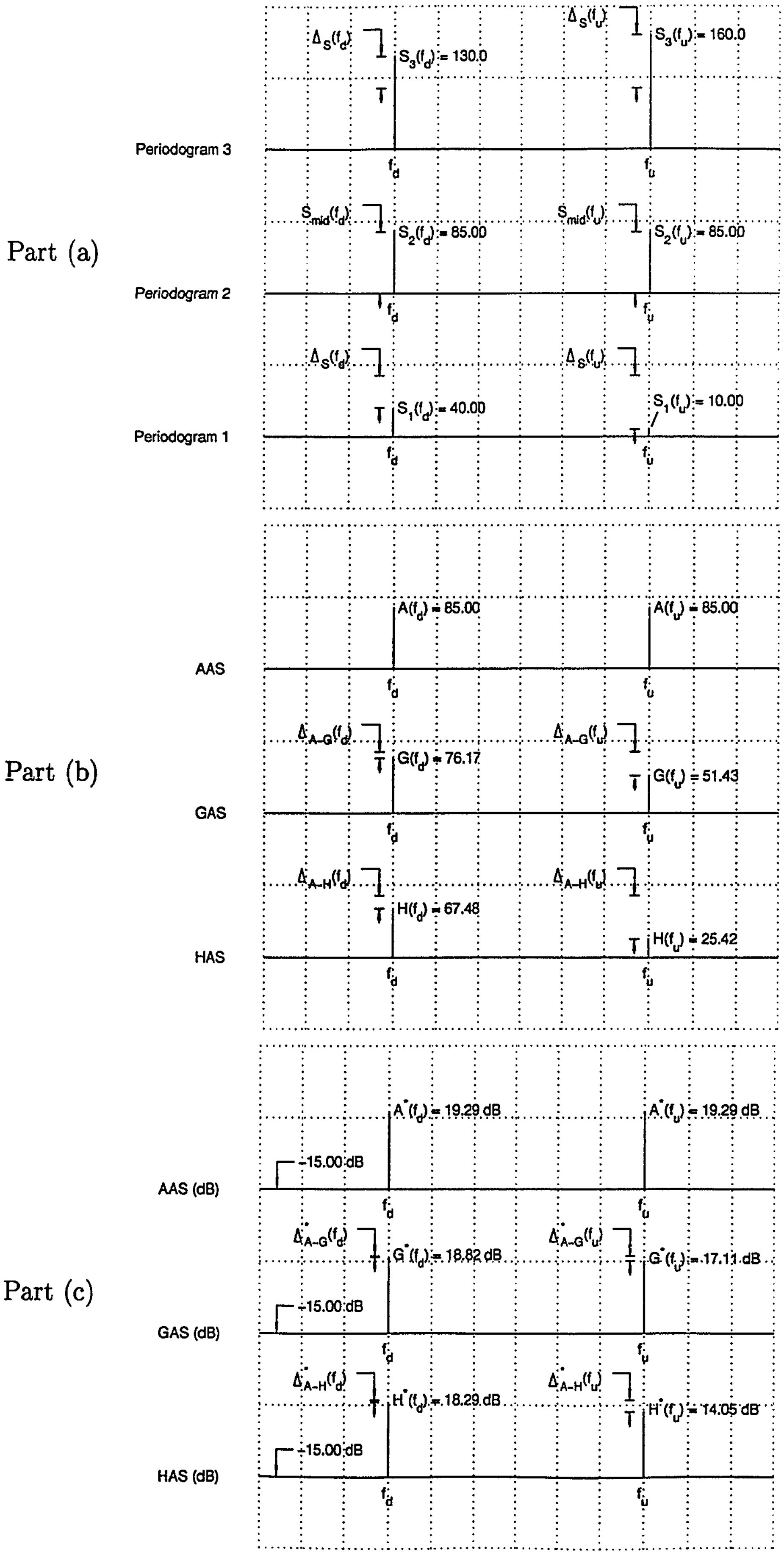

Figure 3.4: Example 3.3 for Demonstrating the Transitional Point

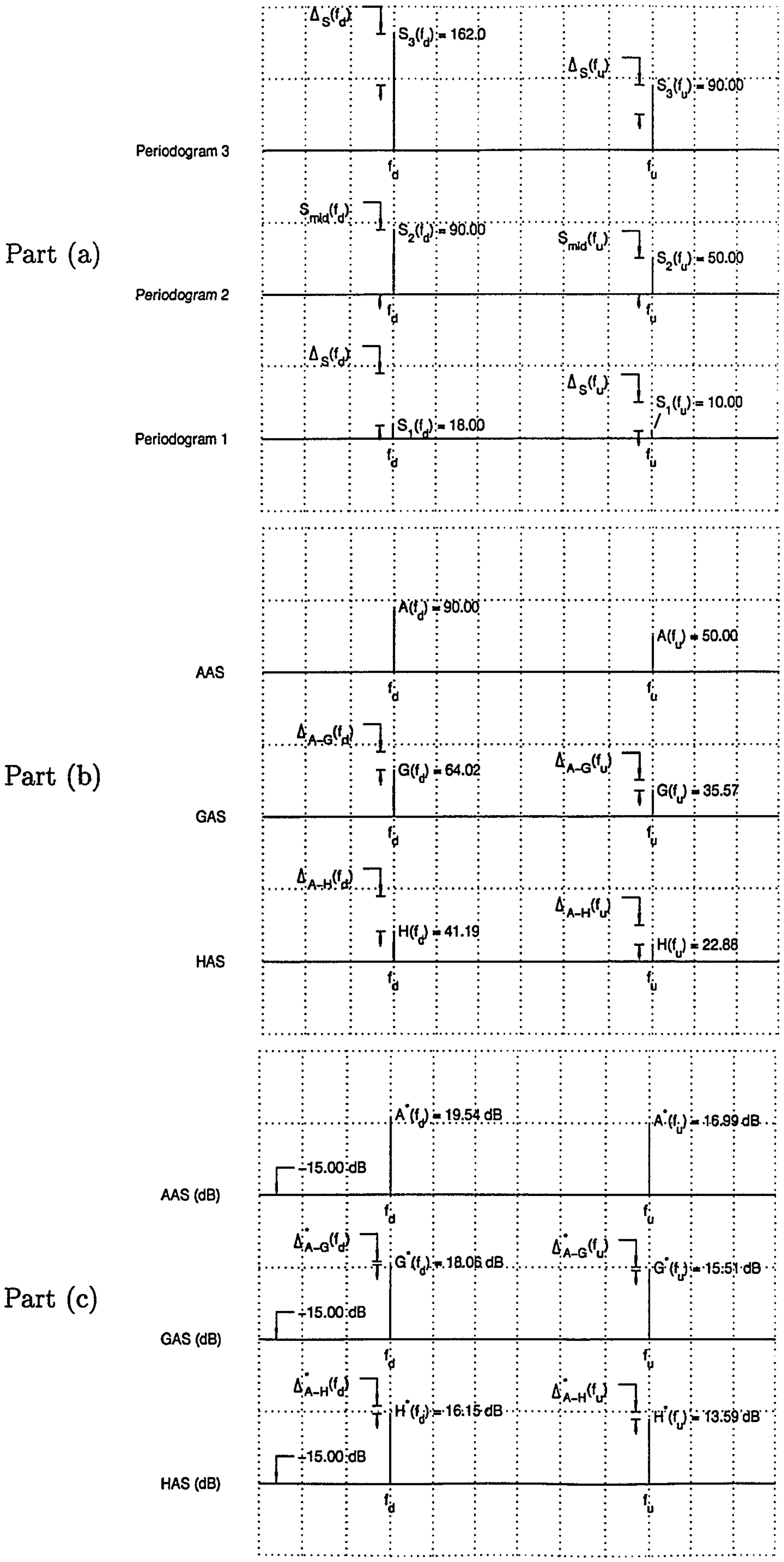

Figure 3.5: Example 3.4 for Demonstrating the Transitional Point

and the 3rd periodogram respectively. These spectral heights can be expressed as

$$\begin{aligned} S_1(f_d) &= S_{\text{mid}}(f_d) - \Delta_S(f_d) \\ S_2(f_d) &= S_{\text{mid}}(f_d) \\ S_3(f_d) &= S_{\text{mid}}(f_d) + \Delta_S(f_d) \end{aligned} \tag{3.2.11}$$

In a similar way, assume that $S_1(f_u)$, $S_2(f_u)$, and $S_3(f_u)$ are the spectral heights at frequency f_u for the 1st periodogram, the 2nd periodogram, and the 3rd periodogram respectively. These spectral heights can be expressed as

$$\begin{aligned} S_1(f_u) &= S_{\text{mid}}(f_u) - \Delta_S(f_u) \\ S_2(f_u) &= S_{\text{mid}}(f_u) \\ S_3(f_u) &= S_{\text{mid}}(f_u) + \Delta_S(f_u) \end{aligned} \tag{3.2.12}$$

Suppose (see Figs. 3.2(b), 3.3(b), 3.4(b), and 3.5(b)) that we are interested in the value of $A(f_d) - A(f_u)$ which is the difference between the AASs in (3.2.1) calculated at two different frequencies f_d and f_u, the value of $G(f_d) - G(f_u)$ which is the difference between the GASs in (3.2.2) calculated at two different frequencies f_d and f_u, and the value of $H(f_d) - H(f_u)$ which is the difference between the HASs in (3.2.3) calculated at two different frequencies f_d and f_u. While emphasizing that the above $A(f_d) - A(f_u)$, $G(f_d) - G(f_u)$, and $H(f_d) - H(f_u)$ are differences rather than ratios, it is possible to define the ratios as

$$10\log_{10} A(f_d) - 10\log_{10} A(f_u) = 10\log_{10}\frac{A(f_d)}{A(f_u)}, \tag{3.2.13}$$

$$10\log_{10} G(f_d) - 10\log_{10} G(f_u) = 10\log_{10}\frac{G(f_d)}{G(f_u)}, \tag{3.2.14}$$

and

$$10\log_{10} H(f_d) - 10\log_{10} H(f_u) = 10\log_{10}\frac{H(f_d)}{H(f_u)}. \tag{3.2.15}$$

We use differences for the moment for convenience although we will later convert our discussion to ratios.

Before entering the next subsection, we make some preparations here. We define (see Figs. 3.2(b), 3.3(b), 3.4(b), and 3.5(b))

$$\Delta_{A-G}(f) \triangleq A(f) - G(f) \tag{3.2.16}$$

and

$$\Delta_{A-H}(f) \triangleq A(f) - H(f) \tag{3.2.17}$$

We also define (see Figs. 3.2(c), 3.3(c), 3.4(c), and 3.5(c))

$$A^*(f) \triangleq 10\log_{10} A(f) \qquad \text{(dB)} \tag{3.2.18}$$

$$G^*(f) \triangleq 10\log_{10} G(f) \qquad \text{(dB)} \tag{3.2.19}$$

and

$$H^*(f) \triangleq 10\log_{10} H(f) \qquad \text{(dB)} \tag{3.2.20}$$

Then, the ratios of $\frac{A(f)}{G(f)}$ and $\frac{A(f)}{H(f)}$ in decibels can be obtained from

$$\begin{aligned}\Delta^*_{A-G}(f) &\triangleq A^*(f) - G^*(f)\\ &= 10\log_{10} A(f) - 10\log_{10} G(f)\\ &= 10\log_{10}\frac{A(f)}{G(f)} \qquad \text{(dB)}\end{aligned} \tag{3.2.21}$$

and

$$\Delta^*_{A-H}(f) \triangleq A^*(f) - H^*(f)$$

$$\begin{aligned} &= 10\log_{10} A(f) - 10\log_{10} H(f) \\ &= 10\log_{10}\frac{A(f)}{H(f)} \qquad \text{(dB)} \end{aligned} \tag{3.2.22}$$

3.2.3 Simple Examples

Consider the following 4 examples illustrating AAS, GAS and HAS averaging, the results of which are summarized in Table 3.1.

Example 3.1:

In this example (see Fig. 3.2),

$$\Delta_S(f_d) = 30.00 \tag{3.2.23}$$

and

$$S_{\text{mid}}(f_d) = 50.00 \tag{3.2.24}$$

so that

$$\frac{\Delta_S(f_d)}{S_{\text{mid}}(f_d)} = \frac{30.00}{50.00} = 0.60 \tag{3.2.25}$$

while

$$\Delta_S(f_u) = 80.00 \tag{3.2.26}$$

and

$$S_{\text{mid}}(f_u) = 81.00 \tag{3.2.27}$$

so that

$$\frac{\Delta_S(f_u)}{S_{\text{mid}}(f_u)} = \frac{80.00}{81.00} = 0.99 \tag{3.2.28}$$

This example therefore serves to demonstrate the case for $\Delta_S(f_d) < \Delta_S(f_u)$, $S_{\text{mid}}(f_d) < S_{\text{mid}}(f_u)$, and $\frac{\Delta_S(f_d)}{S_{\text{mid}}(f_d)} < \frac{\Delta_S(f_u)}{S_{\text{mid}}(f_u)}$ as shown in Fig. 3.2(a).

	Example 3.1	Example 3.2	Example 3.3	Example 3.4
$\Delta_S(f_d)$	30.00	60.00	45.00	72.00
$S_{\text{mid}}(f_d)$	50.00	100.0	85.00	90.00
$\frac{\Delta_S(f_d)}{S_{\text{mid}}(f_d)}$	0.60	0.60	0.53	0.80
$\Delta_S(f_u)$	80.00	60.00	75.00	40.00
$S_{\text{mid}}(f_u)$	81.00	70.00	85.00	50.00
$\frac{\Delta_S(f_u)}{S_{\text{mid}}(f_u)}$	0.99	0.86	0.88	0.80
$A^*(f_d)$	16.99 dB	20.00 dB	19.29 dB	19.54 dB
$G^*(f_d)$	16.34 dB	19.35 dB	18.82 dB	18.06 dB
$H^*(f_d)$	15.61 dB	18.62 dB	18.29 dB	16.15 dB
$A^*(f_u)$	19.08 dB	18.45 dB	19.29 dB	16.99 dB
$G^*(f_u)$	13.72 dB	16.53 dB	17.11 dB	15.51 dB
$H^*(f_u)$	4.691 dB	13.91 dB	14.05 dB	13.59 dB
$A^*(f_d) - A^*(f_u)$	-2.09 dB	1.55 dB	0 dB	2.55 dB
$G^*(f_d) - G^*(f_u)$	2.62 dB	2.82 dB	1.71 dB	2.55 dB
$H^*(f_d) - H^*(f_u)$	10.92 dB	4.71 dB	4.24 dB	2.55 dB
I_{G-A}	4.71 dB	1.27 dB	1.71 dB	0 dB
I_{H-A}	13.01 dB	3.16 dB	4.24 dB	0 dB

Table 3.1 Important Facts in Examples 3.1, 3.2, 3.3, and 3.4

From Fig. 3.2(b), it can be seen that although $A(f_d) < A(f_u)$, $A(f_d) > G(f_d)$, and $A(f_u) > G(f_u)$, we have $G(f_d) > G(f_u)$. In terms of dB, from Fig. 3.2(c), it can be seen that although $A^*(f_d) < A^*(f_u)$, $A^*(f_d) > G^*(f_d)$, and $A^*(f_u) > G^*(f_u)$, we have $G^*(f_d) > G^*(f_u)$. That is, in this example, GAS offers better performance than AAS. This dramatic result is obviously due to the fact that we have $\Delta_{A-G}(f_d) < \Delta_{A-G}(f_u)$ in Fig. 3.2(b). Or in terms of dB, we have $\Delta^*_{A-G}(f_d) < \Delta^*_{A-G}(f_u)$ in Fig. 3.2(c).

According to the specific values in this example, we have

$$A^*(f_d) - A^*(f_u) = 16.99 - 19.08 = -2.09 \text{ dB} \tag{3.2.29}$$

$$G^*(f_d) - G^*(f_u) = 16.34 - 13.72 = 2.62 \text{ dB} \tag{3.2.30}$$

$$H^*(f_d) - H^*(f_u) = 15.61 - 4.691 = 10.92 \text{ dB} \tag{3.2.31}$$

Define the improvement factor of GAS over AAS to be

$$I_{G-A} = (G^*(f_d) - G^*(f_u)) - (A^*(f_d) - A^*(f_u)) \tag{3.2.32}$$

According to the specific values, we get an improvement of

$$I_{G-A} = 2.62 - (-2.09) = 4.71 \text{ dB} \tag{3.2.33}$$

Note that, for AAS we have $A(f_d) < A(f_u)$, *i.e.*, the desired peak is lower than the undesired peak while for GAS we have $G(f_d) > G(f_u)$, *i.e.*, the desired peak is higher than the undesired peak. Similarly, in this example, HAS offers better performance than AAS, since we have $\Delta_{A-H}(f_d) < \Delta_{A-H}(f_u)$ in Fig. 3.2(b). Or in terms of dB, we have $\Delta^*_{A-H}(f_d) < \Delta^*_{A-H}(f_u)$ in Fig. 3.2(c).

Define the improvement factor of HAS over AAS to be

$$I_{H-A} = (H^*(f_d) - H^*(f_u)) - (A^*(f_d) - A^*(f_u)) \tag{3.2.34}$$

According to the specific values, we get an improvement of

$$I_{H-A} = 10.92 - (-2.09) = 13.01 \text{ dB} \tag{3.2.35}$$

The comments offered for the GAS part applies to this HAS part in a similar way.

We emphasize the fact that $\frac{\Delta_S(f_d)}{S_{\text{mid}}(f_d)} < \frac{\Delta_S(f_u)}{S_{\text{mid}}(f_u)}$ in this example where GAS and HAS offer better performance than AAS.

Example 3.2:

In this example (see Fig. 3.3),

$$\Delta_S(f_d) = 60.00 \tag{3.2.36}$$

and

$$S_{\text{mid}}(f_d) = 100.0 \tag{3.2.37}$$

so that

$$\frac{\Delta_S(f_d)}{S_{\text{mid}}(f_d)} = \frac{60.00}{100.0} = 0.60 \tag{3.2.38}$$

while

$$\Delta_S(f_u) = 60.00 \tag{3.2.39}$$

and

$$S_{\text{mid}}(f_u) = 70.00 \tag{3.2.40}$$

so that

$$\frac{\Delta_S(f_u)}{S_{\text{mid}}(f_u)} = \frac{60.00}{70.00} = 0.86 \tag{3.2.41}$$

This example therefore serves to demonstrate the case for $\Delta_S(f_d) = \Delta_S(f_u)$, $S_{\text{mid}}(f_d) > S_{\text{mid}}(f_u)$, and $\frac{\Delta_S(f_d)}{S_{\text{mid}}(f_d)} < \frac{\Delta_S(f_u)}{S_{\text{mid}}(f_u)}$ as shown in Fig. 3.3(a).

From Fig. 3.3(b), it can be seen that in this case we have $\Delta_{A-G}(f_d) < \Delta_{A-G}(f_u)$ and $\Delta_{A-H}(f_d) < \Delta_{A-H}(f_u)$. In terms of dB, from Fig. 3.3(c), it can be seen that in this case we have $\Delta^*_{A-G}(f_d) < \Delta^*_{A-G}(f_u)$ and $\Delta^*_{A-H}(f_d) < \Delta^*_{A-H}(f_u)$. That is, in this example, GAS and HAS offer better performance than AAS.

According to the specific values in this example, we have

$$A^*(f_d) - A^*(f_u) = 20.00 - 18.45 = 1.55 \text{ dB} \tag{3.2.42}$$

$$G^*(f_d) - G^*(f_u) = 19.35 - 16.53 = 2.82 \text{ dB} \tag{3.2.43}$$

$$H^*(f_d) - H^*(f_u) = 18.62 - 13.91 = 4.71 \text{ dB} \tag{3.2.44}$$

Therefore, we get an improvement of

$$I_{G-A} = 2.82 - 1.55 = 1.27 \text{ dB} \tag{3.2.45}$$

or

$$I_{H-A} = 4.71 - 1.55 = 3.16 \text{ dB} \tag{3.2.46}$$

Note that, although we have $\Delta_S(f_d) = \Delta_S(f_u)$ in this example, we do not have $(A^*(f_d) - A^*(f_u)) = (G^*(f_d) - G^*(f_u)) = (H^*(f_d) - H^*(f_u))$ in this example.

We emphasize the fact that $\frac{\Delta_S(f_d)}{S_{\text{mid}}(f_d)} < \frac{\Delta_S(f_u)}{S_{\text{mid}}(f_u)}$ in this example where GAS and HAS offer better performance than AAS.

Example 3.3:

In this example (see Fig. 3.4),

$$\Delta_S(f_d) = 45.00 \tag{3.2.47}$$

and

$$S_{\text{mid}}(f_d) = 85.00 \tag{3.2.48}$$

so that

$$\frac{\Delta_S(f_d)}{S_{\text{mid}}(f_d)} = \frac{45.00}{85.00} = 0.53 \qquad (3.2.49)$$

while

$$\Delta_S(f_u) = 75.00 \qquad (3.2.50)$$

and

$$S_{\text{mid}}(f_u) = 85.00 \qquad (3.2.51)$$

so that

$$\frac{\Delta_S(f_u)}{S_{\text{mid}}(f_u)} = \frac{75.00}{85.00} = 0.88 \qquad (3.2.52)$$

This example therefore serves to demonstrate the case for $\Delta_S(f_d) < \Delta_S(f_u)$, $S_{\text{mid}}(f_d) = S_{\text{mid}}(f_u)$, and $\frac{\Delta_S(f_d)}{S_{\text{mid}}(f_d)} < \frac{\Delta_S(f_u)}{S_{\text{mid}}(f_u)}$ as shown in Fig. 3.4(a).

From Fig. 3.4(b), it can be seen that in this case we have $\Delta_{A-G}(f_d) < \Delta_{A-G}(f_u)$ and $\Delta_{A-H}(f_d) < \Delta_{A-H}(f_u)$. In terms of dB, from Fig. 3.4(c), it can be seen that in this case we have $\Delta^*_{A-G}(f_d) < \Delta^*_{A-G}(f_u)$ and $\Delta^*_{A-H}(f_d) < \Delta^*_{A-H}(f_u)$. That is, in this example, GAS or HAS offers better performance than AAS.

According to the specific values in this example, we have

$$\begin{aligned} A^*(f_d) - A^*(f_u) &= 19.29 - 19.29 = 0 \text{ dB} && (3.2.53) \\ G^*(f_d) - G^*(f_u) &= 18.82 - 17.11 = 1.71 \text{ dB} && (3.2.54) \\ H^*(f_d) - H^*(f_u) &= 18.29 - 14.05 = 4.24 \text{ dB} && (3.2.55) \end{aligned}$$

Therefore, we get an improvement of

$$I_{G-A} = 1.71 - 0 = 1.71 \text{ dB} \qquad (3.2.56)$$

or

$$I_{H-A} = 4.24 - 0 = 4.24 \text{ dB} \tag{3.2.57}$$

Note that, although we have $S_{\text{mid}}(f_d) = S_{\text{mid}}(f_u)$ in this example, we do not have $(A^*(f_d) - A^*(f_u)) = (G^*(f_d) - G^*(f_u)) = (H^*(f_d) - H^*(f_u))$ in this example.

We emphasize the fact that $\frac{\Delta_S(f_d)}{S_{\text{mid}}(f_d)} < \frac{\Delta_S(f_u)}{S_{\text{mid}}(f_u)}$ in this example where GAS and HAS offer better performance than AAS.

Example 3.4:

In this example (see Fig. 3.5),

$$\Delta_S(f_d) = 72.00 \tag{3.2.58}$$

and

$$S_{\text{mid}}(f_d) = 90.00 \tag{3.2.59}$$

so that

$$\frac{\Delta_S(f_d)}{S_{\text{mid}}(f_d)} = \frac{72.00}{90.00} = 0.80 \tag{3.2.60}$$

while

$$\Delta_S(f_u) = 40.00 \tag{3.2.61}$$

and

$$S_{\text{mid}}(f_u) = 50.00 \tag{3.2.62}$$

so that

$$\frac{\Delta_S(f_u)}{S_{\text{mid}}(f_u)} = \frac{40.00}{50.00} = 0.80 \tag{3.2.63}$$

This example therefore serves to demonstrate the case for $\Delta_S(f_d) > \Delta_S(f_u)$, $S_{\text{mid}}(f_d) > S_{\text{mid}}(f_u)$, and $\frac{\Delta_S(f_d)}{S_{\text{mid}}(f_d)} = \frac{\Delta_S(f_u)}{S_{\text{mid}}(f_u)}$ as shown in Fig. 3.5(a).

From Fig. 3.5(b), it can be seen that in this case we have $\Delta_{A-G}(f_d) > \Delta_{A-G}(f_u)$ and $\Delta_{A-H}(f_d) > \Delta_{A-H}(f_u)$. In terms of dB, from Fig. 3.5(c), it can be seen that in this case we have $\Delta^*_{A-G}(f_d) = \Delta^*_{A-G}(f_u)$ and $\Delta^*_{A-H}(f_d) = \Delta^*_{A-H}(f_u)$. That is, in this example, GAS and HAS offer the same performance as AAS.

According to the specific values in this example, we have

$$A^*(f_d) - A^*(f_u) = 19.54 - 16.99 = 2.55 \text{ dB} \tag{3.2.64}$$

$$G^*(f_d) - G^*(f_u) = 18.06 - 15.51 = 2.55 \text{ dB} \tag{3.2.65}$$

$$H^*(f_d) - H^*(f_u) = 16.15 - 13.59 = 2.55 \text{ dB} \tag{3.2.66}$$

Therefore, we get an improvement of

$$I_{G-A} = 2.55 - 2.55 = 0 \text{ dB} \tag{3.2.67}$$

or

$$I_{H-A} = 2.55 - 2.55 = 0 \text{ dB} \tag{3.2.68}$$

Note that, although we have neither $\Delta_S(f_d) = \Delta_S(f_u)$ nor $S_{\text{mid}}(f_d) = S_{\text{mid}}(f_u)$ in this example, we do have $(A^*(f_d) - A^*(f_u)) = (G^*(f_d) - G^*(f_u)) = (H^*(f_d) - H^*(f_u))$ in this example.

We emphasize the fact that $\frac{\Delta_S(f_d)}{S_{\text{mid}}(f_d)} = \frac{\Delta_S(f_u)}{S_{\text{mid}}(f_u)}$ in this example where AAS, GAS, and HAS offer the same performance.

After we have familiarized ourselves with the situation described in Example 3.1 (see Fig. 3.2), Example 3.2 (see Fig. 3.3), Example 3.3 (see Fig. 3.4), and Example 3.4 (see Fig. 3.5), a question naturally arises now. That is: Mathematically, under what condition will we have $\Delta^*_{A-G}(f_d) < \Delta^*_{A-G}(f_u)$ and $\Delta^*_{A-H}(f_d) < \Delta^*_{A-H}(f_u)$?

3.3 Generalized Relationships

3.3.1 Mathematical Treatment

Suppose we have

$$K \geq 3 \qquad \text{being a positive odd integer} \tag{3.3.1}$$

and recall (3.2.1), (3.2.2), and (3.2.3). Then rank the spectra at each frequency f such that

$$S_1(f) \leq S_2(f) \leq \cdots \leq S_{K-1}(f) \leq S_K(f) \tag{3.3.2}$$

The justification for this re-ordering is that we are calculating the averaged value of $S_k(f)$, $k = 1, 2, \cdots, K-1, K$, and the result of this calculation will not be affected by any kind of re-ordering imposed on $S_k(f)$.

At each frequency f, define the maximum spectral peak, the minimum spectral peak, the middle spectral peak, the approximate difference between any 2 consecutive spectral peaks to be $S_{\max}(f)$, $S_{\min}(f)$, $S_{\text{mid}}(f)$, and $\Delta_S(f)$ respectively. Then,

$$\begin{aligned}
S_{\max}(f) &= \max\{S_1(f), S_2(f), \cdots, S_{K-1}(f), S_K(f)\} && (3.3.3)\\
S_{\min}(f) &= \min\{S_1(f), S_2(f), \cdots, S_{K-1}(f), S_K(f)\} && (3.3.4)\\
S_{\text{mid}}(f) &= \frac{S_{\max}(f) + S_{\min}(f)}{2} && (3.3.5)\\
\Delta_S(f) &= \frac{S_{\max}(f) - S_{\min}(f)}{K-1} && (3.3.6)
\end{aligned}$$

If the differences between $S_k(f)$ and $S_{k+1}(f)$ where $k = 1, 2, \cdots, K-2, K-1$ are equal, then

$$S_k(f) = S_{\text{mid}}(f) + \left(k - 1 - \frac{K-1}{2}\right)\Delta_S(f) \qquad k = 1, 2, \cdots, K-1, K \tag{3.3.7}$$

The reason for this simplifying assumption is that exact relationships can be derived for AAS, GAS, and HAS. Check (3.3.7) for the three special cases of k, namely: $k = 1$ which is the first; $k = \frac{K+1}{2}$ which is the middle; and, $k = K$ which is the last. When $k = 1$, we have

$$\begin{aligned} S_1(f) &\overset{(a)}{=} S_{\text{mid}}(f) + \left(1 - 1 - \frac{K-1}{2}\right)\Delta_S(f) \\ &\overset{(b)}{=} \frac{S_{\max}(f) + S_{\min}(f)}{2} - \frac{K-1}{2}\cdot\frac{S_{\max}(f) - S_{\min}(f)}{K-1} \\ &= S_{\min}(f) \end{aligned} \tag{3.3.8}$$

where $\overset{(a)}{=}$ is due to (3.3.7) and $k = 1$ while $\overset{(b)}{=}$ is due to (3.3.5) and (3.3.6). When $k = \frac{K+1}{2}$, we have

$$\begin{aligned} S_{\frac{K+1}{2}}(f) &\overset{(a)}{=} S_{\text{mid}}(f) + \left(\frac{K+1}{2} - 1 - \frac{K-1}{2}\right)\Delta_S(f) \\ &\overset{(b)}{=} \frac{S_{\max}(f) + S_{\min}(f)}{2} - 0\cdot\Delta_S(f) \\ &= \frac{S_{\max}(f) + S_{\min}(f)}{2} \end{aligned} \tag{3.3.9}$$

where $\overset{(a)}{=}$ is due to (3.3.7) and $k = \frac{K+1}{2}$ while $\overset{(b)}{=}$ is due to (3.3.5). When $k = K$, we have

$$\begin{aligned} S_K(f) &\overset{(a)}{=} S_{\text{mid}}(f) + \left(K - 1 - \frac{K-1}{2}\right)\Delta_S(f) \\ &\overset{(b)}{=} \frac{S_{\max}(f) + S_{\min}(f)}{2} + \frac{K-1}{2}\cdot\frac{S_{\max}(f) - S_{\min}(f)}{K-1} \\ &= S_{\max}(f) \end{aligned} \tag{3.3.10}$$

where $\overset{(a)}{=}$ is due to (3.3.7) and $k = K$ while $\overset{(b)}{=}$ is due to (3.3.5) and (3.3.6).

There is a symmetry in (3.3.7) which will greatly facilitate the following development. To see this symmetry easily, we need to use a new parameter h to exchange the original parameter k in (3.3.7). Specifically, let

$$h = k - 1 - \frac{K-1}{2} \qquad k = 1, 2, \cdots, K-1, K \tag{3.3.11}$$

where the range of h is

$$h = -\frac{K-1}{2}, \cdots, -1, 0, 1, \cdots, \frac{K-1}{2} \tag{3.3.12}$$

Using (3.3.11) in (3.3.7), we have

$$\begin{aligned} S_k(f) &\overset{(a)}{=} S_{\text{mid}}(f) + \left(k - 1 - \frac{K-1}{2}\right)\Delta_S(f) \\ &\overset{(b)}{=} S_{\text{mid}}(f) + h \cdot \Delta_S(f) \qquad h = -\frac{K-1}{2}, \cdots, -1, 0, 1, \cdots, \frac{K-1}{2} \end{aligned} \tag{3.3.13}$$

where $\overset{(a)}{=}$ is due to (3.3.7) while $\overset{(b)}{=}$ is due to (3.3.11). At first, by the above discussion, we have

$$\begin{aligned} A(f) &\overset{(a)}{=} \frac{1}{K}\sum_{k=1}^{K} S_k(f) \\ &\overset{(b)}{=} \frac{1}{K}\sum_{h=-\frac{K-1}{2}}^{\frac{K-1}{2}} [S_{\text{mid}}(f) + h \cdot \Delta_S(f)] \\ &\overset{(c)}{=} \frac{1}{K}\left[[S_{\text{mid}}(f) + 0 \cdot \Delta_S(f)] + \sum_{h=1}^{\frac{K-1}{2}} [S_{\text{mid}}(f) - h\Delta_S(f)] + [S_{\text{mid}}(f) + h\Delta_S(f)]\right] \\ &= \frac{1}{K}\left[S_{\text{mid}}(f) + \sum_{h=1}^{\frac{K-1}{2}} 2S_{\text{mid}}(f)\right] \\ &= S_{\text{mid}}(f) \end{aligned} \tag{3.3.14}$$

where $\overset{(a)}{=}$ is due to (3.2.1), $\overset{(b)}{=}$ is due to (3.3.11) and (3.3.13), while $\overset{(c)}{=}$ is due to the symmetry among the elements of summation so that we can move the element corresponding to $h = 0$ out of the summation symbol and change the lower limit of the summation from $h = -\frac{K-1}{2}$ to $h = 1$. That is, from double sided to single sided.

Secondly, by the above discussion, we have

$$\begin{aligned}
G(f) &\overset{(a)}{=} \left[\prod_{k=1}^{K} S_k(f)\right]^{\frac{1}{K}} \\
&\overset{(b)}{=} \left[\prod_{h=-\frac{K-1}{2}}^{\frac{K-1}{2}} [S_{\text{mid}}(f) + h \cdot \Delta_S(f)]\right]^{\frac{1}{K}} \\
&\overset{(c)}{=} \left[[S_{\text{mid}}(f) + 0 \cdot \Delta_S(f)] \cdot \prod_{h=1}^{\frac{K-1}{2}} \{[S_{\text{mid}}(f) - h\Delta_S(f)] \cdot [S_{\text{mid}}(f) + h\Delta_S(f)]\}\right]^{\frac{1}{K}} \\
&= \left[S_{\text{mid}}(f) \cdot \prod_{h=1}^{\frac{K-1}{2}} [S_{\text{mid}}^2(f) - h^2\Delta_S^2(f)]\right]^{\frac{1}{K}} \\
&= \left\{S_{\text{mid}}(f) \cdot \prod_{h=1}^{\frac{K-1}{2}} \left[S_{\text{mid}}^2(f) \cdot \left(1 - h^2\frac{\Delta_S^2(f)}{S_{\text{mid}}^2(f)}\right)\right]\right\}^{\frac{1}{K}} \\
&= \left[S_{\text{mid}}(f) \cdot S_{\text{mid}}^{K-1}(f) \cdot \prod_{h=1}^{\frac{K-1}{2}} \left(1 - h^2\frac{\Delta_S^2(f)}{S_{\text{mid}}^2(f)}\right)\right]^{\frac{1}{K}} \\
&= S_{\text{mid}}(f) \cdot \left[\prod_{h=1}^{\frac{K-1}{2}} \left(1 - h^2\frac{\Delta_S^2(f)}{S_{\text{mid}}^2(f)}\right)\right]^{\frac{1}{K}} \qquad (3.3.15)
\end{aligned}$$

where $\overset{(a)}{=}$ is due to (3.2.2), $\overset{(b)}{=}$ is due to (3.3.11) and (3.3.13), while $\overset{(c)}{=}$ is due to the symmetry among the elements of the product so that we can move the element corresponding to $h = 0$ out of the product symbol and change the lower limit of the production from $h = -\frac{K-1}{2}$ to $h = 1$. That is, from double sided to single sided.

Finally, by the above discussion, we have

$$H(f) \overset{(a)}{=} \frac{1}{\frac{1}{K}\sum_{k=1}^{K}\frac{1}{S_k(f)}}$$

$$
\begin{aligned}
&\overset{(b)}{=} \frac{K}{\displaystyle\sum_{h=-\frac{K-1}{2}}^{\frac{K-1}{2}} \frac{1}{S_{\mathrm{mid}}(f)+h\cdot\Delta_S(f)}} \\
&\overset{(c)}{=} \frac{K}{\displaystyle\frac{1}{S_{\mathrm{mid}}(f)+0\cdot\Delta_S(f)}+\sum_{h=1}^{\frac{K-1}{2}}\left(\frac{1}{S_{\mathrm{mid}}(f)-h\Delta_S(f)}+\frac{1}{S_{\mathrm{mid}}(f)+h\Delta_S(f)}\right)} \\
&= \frac{K}{\displaystyle\frac{1}{S_{\mathrm{mid}}(f)}+\sum_{h=1}^{\frac{K-1}{2}}\frac{2S_{\mathrm{mid}}(f)}{S^2_{\mathrm{mid}}(f)-h^2\Delta^2_S(f)}} \\
&= \frac{K}{\displaystyle\frac{1}{S_{\mathrm{mid}}(f)}+\frac{2}{S_{\mathrm{mid}}(f)}\sum_{h=1}^{\frac{K-1}{2}}\frac{1}{1-h^2\left(\frac{\Delta_S(f)}{S_{\mathrm{mid}}(f)}\right)^2}} \\
&= \frac{KS_{\mathrm{mid}}(f)}{\displaystyle 1+2\sum_{h=1}^{\frac{K-1}{2}}\frac{1}{1-h^2\left(\frac{\Delta_S(f)}{S_{\mathrm{mid}}(f)}\right)^2}} \qquad (3.3.16)
\end{aligned}
$$

where $\overset{(a)}{=}$ is due to (3.2.3), $\overset{(b)}{=}$ is due to (3.3.11) and (3.3.13), while $\overset{(c)}{=}$ is due to the symmetry among the elements of summation so that we can move the element corresponding to $h = 0$ out of the summation symbol and change the lower limit of the summation from $h = -\frac{K-1}{2}$ to $h = 1$.

In terms of dB, we can calculate the ratio between the AAS and the GAS as below

$$
\begin{aligned}
&\Delta^*_{A-G}(f) \\
&\quad = 10\log_{10}\frac{A(f)}{G(f)} \\
&\quad = 10\log_{10}A(f) - 10\log_{10}G(f) \\
&\quad = 10\log_{10}S_{\mathrm{mid}}(f) - 10\log_{10}\left\{S_{\mathrm{mid}}(f)\cdot\left[\prod_{h=1}^{\frac{K-1}{2}}\left(1-h^2\frac{\Delta^2_S(f)}{S^2_{\mathrm{mid}}(f)}\right)\right]^{\frac{1}{K}}\right\}
\end{aligned}
$$

$$\begin{aligned}
&= 10\log_{10} S_{\text{mid}}(f) - 10\log_{10} S_{\text{mid}}(f) - 10\log_{10}\left[\prod_{h=1}^{\frac{K-1}{2}}\left(1 - h^2\frac{\Delta_S^2(f)}{S_{\text{mid}}^2(f)}\right)\right]^{\frac{1}{K}} \\
&= -10\log_{10}\left[\prod_{h=1}^{\frac{K-1}{2}}\left(1 - h^2\frac{\Delta_S^2(f)}{S_{\text{mid}}^2(f)}\right)\right]^{\frac{1}{K}} \\
&= -\frac{10}{K}\sum_{h=1}^{\frac{K-1}{2}}\log_{10}\left(1 - h^2\frac{\Delta_S^2(f)}{S_{\text{mid}}^2(f)}\right) \\
&= \frac{10}{K}\sum_{h=1}^{\frac{K-1}{2}}\log_{10}\left(\frac{1}{1 - h^2\left(\frac{\Delta_S(f)}{S_{\text{mid}}(f)}\right)^2}\right) \qquad \text{(dB)} \qquad (3.3.17)
\end{aligned}$$

In terms of dB, we can calculate the ratio between the AAS and the HAS as below

$$\begin{aligned}
&\Delta^*_{A-H}(f) \\
&= 10\log_{10}\frac{A(f)}{H(f)} \\
&= 10\log_{10} A(f) - 10\log_{10} H(f) \\
&= 10\log_{10} S_{\text{mid}}(f) - 10\log_{10}\left[\frac{KS_{\text{mid}}(f)}{1 + 2\sum_{h=1}^{\frac{K-1}{2}}\frac{1}{1 - h^2\left(\frac{\Delta_S(f)}{S_{\text{mid}}(f)}\right)^2}}\right] \\
&= 10\log_{10} S_{\text{mid}}(f) \\
&\qquad -10\log_{10} K - 10\log_{10} S_{\text{mid}}(f) + 10\log_{10}\left[1 + 2\sum_{h=1}^{\frac{K-1}{2}}\frac{1}{1 - h^2\left(\frac{\Delta_S(f)}{S_{\text{mid}}(f)}\right)^2}\right]
\end{aligned}$$

$$= 10\log_{10}\left(\frac{1+2\sum_{h=1}^{\frac{K-1}{2}}\frac{1}{1-h^2\left(\frac{\Delta_S(f)}{S_{\mathrm{mid}}(f)}\right)^2}}{K}\right) \quad \text{(dB)} \qquad (3.3.18)$$

From (3.3.17) and (3.3.18) it can be seen that the ratio $\frac{\Delta_S(f)}{S_{\mathrm{mid}}(f)}$ plays an important role in the ratios of $\frac{A(f)}{G(f)}$ and $\frac{A(f)}{H(f)}$.

In other words, as long as

$$\frac{\Delta_S(f_u)}{S_{\mathrm{mid}}(f_u)} > \frac{\Delta_S(f_d)}{S_{\mathrm{mid}}(f_d)} \qquad (3.3.19)$$

one will have (see (3.3.17) and (3.3.18))

$$\begin{aligned} &\Delta^*_{A-G}(f_u) - \Delta^*_{A-G}(f_d) \\ &= [10\log_{10} A(f_u) - 10\log_{10} G(f_u)] - [10\log_{10} A(f_d) - 10\log_{10} G(f_d)] \\ &> 0 \qquad \text{(dB)} \qquad (3.3.20) \end{aligned}$$

and

$$\begin{aligned} &\Delta^*_{A-H}(f_u) - \Delta^*_{A-H}(f_d) \\ &= [10\log_{10} A(f_u) - 10\log_{10} H(f_u)] - [10\log_{10} A(f_d) - 10\log_{10} H(f_d)] \\ &> 0 \qquad \text{(dB)} \qquad (3.3.21) \end{aligned}$$

That is, under the condition described in (3.3.19), one can benefit by using the GAS or the HAS instead of the AAS.

At this point, we review the situation described in Example 3.1 (see Fig. 3.2), Example 3.2 (see Fig. 3.3), Example 3.3 (see Fig. 3.4), and Example 3.4 (see Fig.

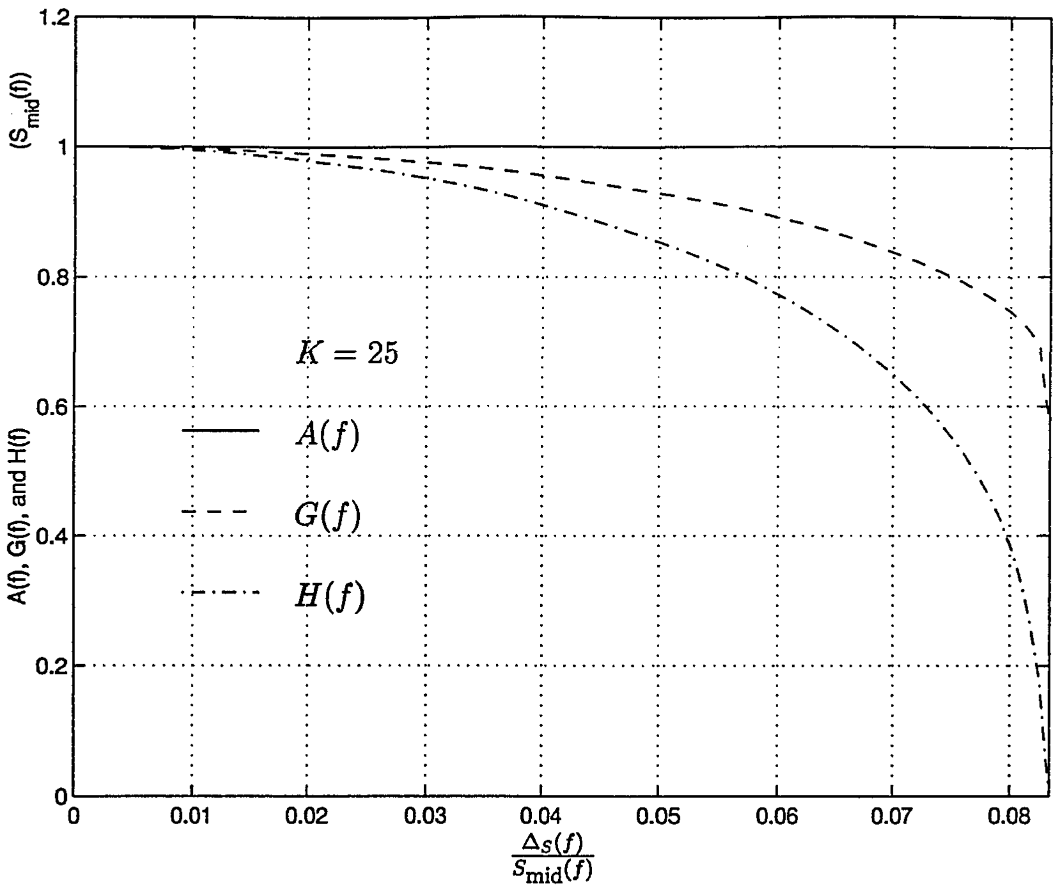

Figure 3.6: The dependences of $G(f)$ and $H(f)$ on $\frac{\Delta_S(f)}{S_{\text{mid}}(f)}$ with $K = 25$

3.5). Since the condition described in (3.3.19) is satisfied in Example 3.1, Example 3.2, and Example 3.3, GAS and HAS offer a better performance than AAS. Obviously, Example 3.4 corresponds to the transitional point where

$$\frac{\Delta_S(f_u)}{S_{\text{mid}}(f_u)} = \frac{\Delta_S(f_d)}{S_{\text{mid}}(f_d)} \tag{3.3.22}$$

so that GAS and HAS offer the same performance as AAS.

We employ Fig. 3.6 to summarize the following observations.

(1) The values of $G(f)$ and $H(f)$ depend on the value of $\frac{\Delta_S(f)}{S_{\text{mid}}(f)}$.

(2) The values of $A(f) - G(f)$ and $A(f) - H(f)$ are monotonic functions of the value of $\frac{\Delta s(f)}{S_{\text{mid}}(f)}$.

(3) Since different frequencies are occupied by different kinds of signals, the value of $\frac{\Delta s(f)}{S_{\text{mid}}(f)}$ changes from frequency to frequency within the whole frequency band of interest. Therefore the values of $A(f) - G(f)$ are different from frequency to frequency within the whole frequency band of interest. The curve of $G(f)$ is therefore not a simple translation downward from the curve of $A(f)$. That is, $G(f)$ has a different shape from the shape of $A(f)$. Different shapes of $A(f)$ and $G(f)$ tell that different kinds of signals are there.

(4) One will benefit by using $G(f)$ instead of $A(f)$ whenever the value of $A(f)-G(f)$ of the desired signal is less than the value of $A(f)-G(f)$ of the undesired signal or equally whenever the value of $\frac{\Delta s(f)}{S_{\text{mid}}(f)}$ of the desired signal is less than the value of $\frac{\Delta s(f)}{S_{\text{mid}}(f)}$ of the undesired signal. In other words, as long as

$$\frac{\Delta s(f_d)}{S_{\text{mid}}(f_d)} < \frac{\Delta s(f_u)}{S_{\text{mid}}(f_u)} \tag{3.3.23}$$

one will have

$$A(f_d) - G(f_d) < A(f_u) - G(f_u) \tag{3.3.24}$$

or

$$G(f_d) - G(f_u) > A(f_d) - A(f_u) \tag{3.3.25}$$

That is, $G(f)$ is better than $A(f)$.

(5) The value of $A(f)-G(f)$ of the ICE signal is less than the value of $A(f)-G(f)$ of the NIC signal, since the value of $\frac{\Delta s(f)}{S_{\text{mid}}(f)}$ of the ICE signal is less than the

value of $\frac{\Delta s(f)}{s_{\text{mid}}(f)}$ of the NIC signal.

(6) The value of $A(f) - G(f)$ of carrier interference with weak AM is less than the value of $A(f) - G(f)$ of carrier interference with strong AM, since the value of $\frac{\Delta s(f)}{s_{\text{mid}}(f)}$ of carrier interference with weak AM is less than the value of $\frac{\Delta s(f)}{s_{\text{mid}}(f)}$ of carrier interference with strong AM.

(7) The value of $A(f) - G(f)$ of the ICE signal is less than the value of $A(f) - G(f)$ of carrier interference with strong AM, since the value of $\frac{\Delta s(f)}{s_{\text{mid}}(f)}$ of the ICE signal is less than the value of $\frac{\Delta s(f)}{s_{\text{mid}}(f)}$ of carrier interference with strong AM.

(8) The value of $A(f) - G(f)$ of the ICE signal is less than the value of $A(f) - G(f)$ of noise level, since the value of $\frac{\Delta s(f)}{s_{\text{mid}}(f)}$ of the ICE signal is less than the value of $\frac{\Delta s(f)}{s_{\text{mid}}(f)}$ of noise level.

(9) The value of $A(f) - G(f)$ of the NIC signal is greater than the value of $A(f) - G(f)$ of carrier interference with weak AM, since the value of $\frac{\Delta s(f)}{s_{\text{mid}}(f)}$ of the NIC signal is greater than the value of $\frac{\Delta s(f)}{s_{\text{mid}}(f)}$ of carrier interference with weak AM.

(10) The above comments from (3) to (9) which apply to $A(f) - G(f)$ can also apply to $A(f) - H(f)$.

(11) The processing strategy based on using the combination of $A(f)$, $G(f)$, and $H(f)$ could be superior to the processing strategy based on using only one of $A(f)$, $G(f)$, and $H(f)$.

3.3.2 Another Approach for Approximating $S_k(f)$

Instead of using the approximation of (3.3.7), given by

$$S_k(f) = S_{\text{mid}}(f) + \left(k - 1 - \frac{K-1}{2}\right) \Delta_S(f) \qquad k = 1, 2, \cdots, K-1, K \tag{3.3.26}$$

we can use another arrangement such that

$$S_k(f) = S_{\text{mid}}(f) \cdot [\eta(f)]^{k-\frac{K+1}{2}} \qquad k = 1, 2, \cdots, K-1, K \tag{3.3.27}$$

where

$$\begin{aligned} K &\geq 3 \qquad \text{being a positive odd integer} && (3.3.28) \\ S_{\max}(f) &= \max\{S_1(f), S_2(f), \cdots, S_{K-1}(f), S_K(f)\} && (3.3.29) \\ S_{\min}(f) &= \min\{S_1(f), S_2(f), \cdots, S_{K-1}(f), S_K(f)\} && (3.3.30) \\ S_{\text{mid}}(f) &= [S_{\min}(f) \cdot S_{\max}(f)]^{\frac{1}{2}} && (3.3.31) \end{aligned}$$

while

$$\eta(f) = \left[\frac{S_{\max}(f)}{S_{\min}(f)}\right]^{\frac{1}{K-1}} \tag{3.3.32}$$

The reader can check (3.3.27) with the three special cases of $k = 1$ which is the first one, $k = \frac{K+1}{2}$ which is the middle one, and $k = K$ which is the last one. When $k = 1$, we have

$$\begin{aligned} S_1(f) &\overset{(a)}{=} S_{\text{mid}}(f) \cdot [\eta(f)]^{1-\frac{K+1}{2}} \\ &\overset{(b)}{=} [S_{\min}(f) \cdot S_{\max}(f)]^{\frac{1}{2}} \cdot \left\{\left[\frac{S_{\max}(f)}{S_{\min}(f)}\right]^{\frac{1}{K-1}}\right\}^{-\frac{K-1}{2}} \\ &= S_{\min}(f) \end{aligned} \tag{3.3.33}$$

where $\overset{(a)}{=}$ is due to (3.3.27) and $k=1$ while $\overset{(b)}{=}$ is due to (3.3.31) and (3.3.32). When $k=\frac{K+1}{2}$, we have

$$\begin{aligned} S_{\frac{K+1}{2}}(f) &\overset{(a)}{=} S_{\text{mid}}(f)\cdot[\eta(f)]^{\frac{K+1}{2}-\frac{K+1}{2}} \\ &\overset{(b)}{=} S_{\text{mid}}(f)\cdot[\eta(f)]^{0} \\ &= S_{\text{mid}}(f) \end{aligned} \tag{3.3.34}$$

where $\overset{(a)}{=}$ is due to (3.3.27) and $k=\frac{K+1}{2}$ while $\overset{(b)}{=}$ is due to (3.3.31). When $k=K$, we have

$$\begin{aligned} S_K(f) &\overset{(a)}{=} S_{\text{mid}}(f)\cdot[\eta(f)]^{K-\frac{K+1}{2}} \\ &\overset{(b)}{=} [S_{\text{min}}(f)\cdot S_{\text{max}}(f)]^{\frac{1}{2}}\cdot\left\{\left[\frac{S_{\text{max}}(f)}{S_{\text{min}}(f)}\right]^{\frac{1}{K-1}}\right\}^{\frac{K-1}{2}} \\ &= S_{\text{max}}(f) \end{aligned} \tag{3.3.35}$$

where $\overset{(a)}{=}$ is due to (3.3.27) and $k=K$ while $\overset{(b)}{=}$ is due to (3.3.31) and (3.3.32). If $K=3$ we have 3 elements such that

$$\begin{aligned} S_1(f) &= S_{\text{mid}}(f)\frac{1}{\eta(f)} \\ S_2(f) &= S_{\text{mid}}(f) \\ S_3(f) &= S_{\text{mid}}(f)\eta(f) \end{aligned} \tag{3.3.36}$$

For GAS, we have

$$\begin{aligned} G(f) &= \left[\prod_{k=1}^{3} S_k(f)\right]^{\frac{1}{3}} \\ &= \left[S_{\text{mid}}(f)\frac{1}{\eta(f)}\cdot S_{\text{mid}}(f)\cdot S_{\text{mid}}(f)\eta(f)\right]^{\frac{1}{3}} \\ &= S_{\text{mid}}(f) \end{aligned} \tag{3.3.37}$$

For AAS, we have

$$\begin{aligned} A(f) &= \frac{1}{3}\sum_{k=1}^{3} S_k(f) \\ &= \frac{1}{3}\left[S_{\text{mid}}(f)\frac{1}{\eta(f)} + S_{\text{mid}}(f) + S_{\text{mid}}(f)\eta(f)\right] \\ &= \frac{\dfrac{1}{\eta(f)} + 1 + \eta(f)}{3} \cdot S_{\text{mid}}(f) \end{aligned} \tag{3.3.38}$$

If $\eta(f) = 1.0$, we have

$$A(f) = \frac{\dfrac{1}{1.0} + 1 + 1.0}{3} \cdot S_{\text{mid}}(f) = S_{\text{mid}}(f) = G(f) \tag{3.3.39}$$

For HAS, we have

$$\begin{aligned} H(f) &= \frac{1}{\dfrac{1}{3}\displaystyle\sum_{k=1}^{3}\frac{1}{S_k(f)}} \\ &= \frac{3}{\dfrac{1}{S_{\text{mid}}(f)\dfrac{1}{\eta(f)}} + \dfrac{1}{S_{\text{mid}}(f)} + \dfrac{1}{S_{\text{mid}}(f)\eta(f)}} \\ &= \frac{3}{\eta(f) + 1 + \dfrac{1}{\eta(f)}} \cdot S_{\text{mid}}(f) \end{aligned} \tag{3.3.40}$$

If $\eta(f) = 1.0$, we have

$$H(f) = \frac{3}{1.0 + 1 + \dfrac{1}{1.0}} \cdot S_{\text{mid}}(f) = S_{\text{mid}}(f) = G(f) \tag{3.3.41}$$

We employ Fig. 3.7 to summarize the above results. In Fig. 3.8, for $K = 25$, it is seen that the following observations apply.

(1) The values of $A(f)$ and $H(f)$ depend on the value of $\eta(f)$.

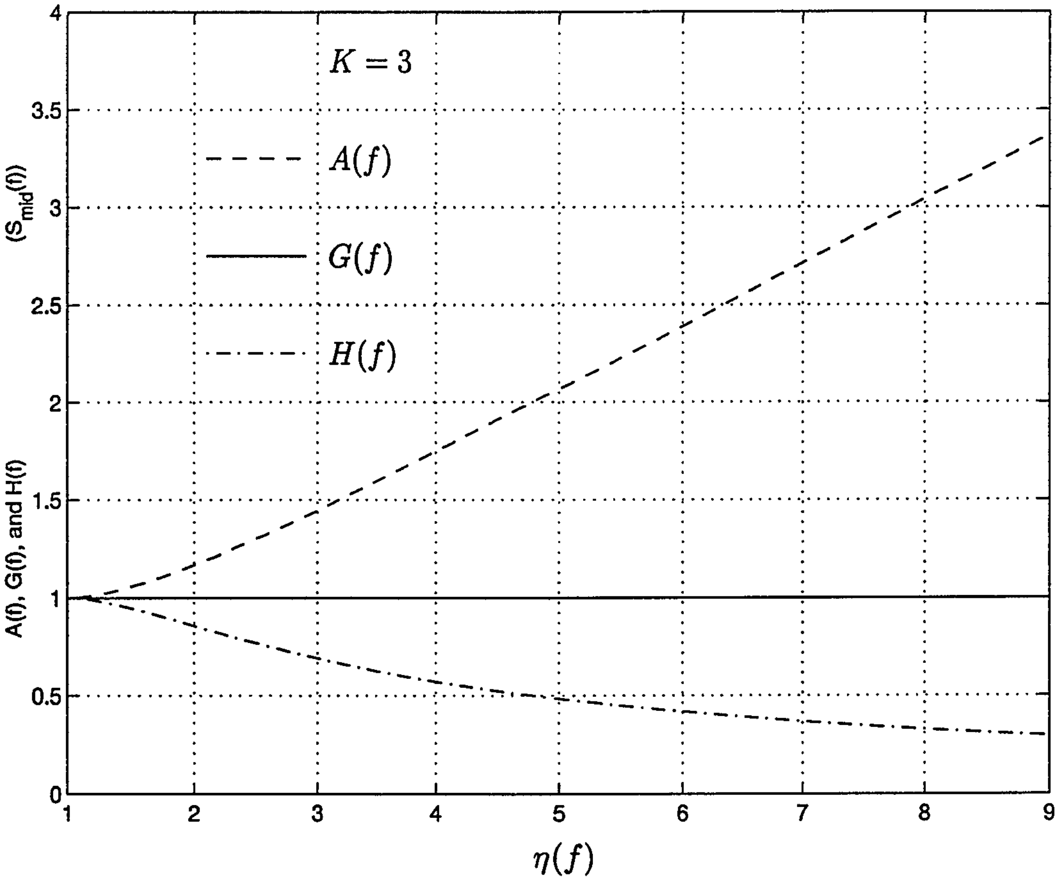

Figure 3.7: The dependences of $A(f)$ and $H(f)$ on $\eta(f)$ with $K = 3$

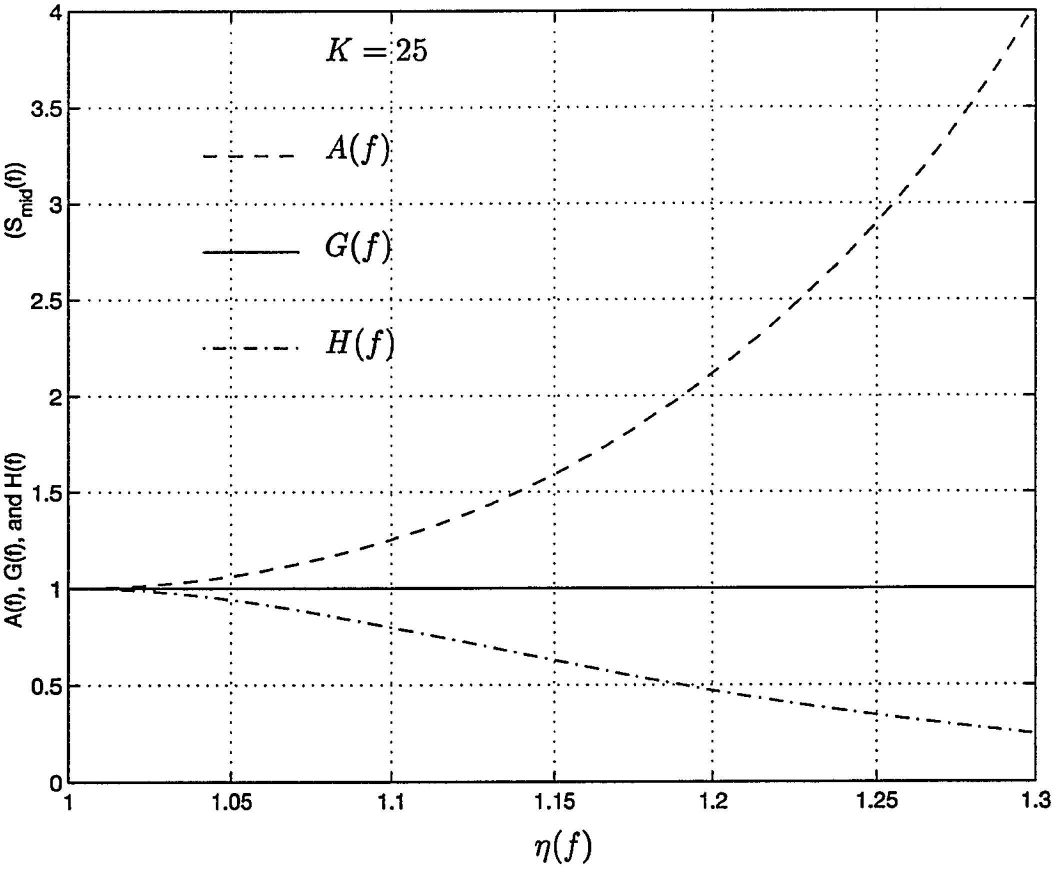

Figure 3.8: The dependences of $A(f)$ and $H(f)$ on $\eta(f)$ with $K = 25$

(2) The values of $A(f) - G(f)$ and $A(f) - H(f)$ are monotonic functions of the value of $\eta(f)$.

(3) Since different frequencies are occupied by different kinds of signals, the value of $\eta(f)$ changes from frequency to frequency within the whole frequency band of interest. Therefore the values of $A(f) - G(f)$ are different from frequency to frequency within the whole frequency band of interest. The curve of $G(f)$ is therefore not a simple translation downward from the curve of $A(f)$. That is, $G(f)$ has a different shape from the shape of $A(f)$. Different shapes of $A(f)$ and $G(f)$ tell that different kinds of signals are there.

(4) One will benefit by using $G(f)$ instead of $A(f)$ whenever the value of $A(f)-G(f)$ of the desired signal is less than the value of $A(f)-G(f)$ of the undesired signal or equally whenever the value of $\eta(f)$ of the desired signal is less than the value of $\eta(f)$ of the undesired signal. In other words, as long as

$$\eta(f_d) < \eta(f_u) \tag{3.3.42}$$

one will have

$$A(f_d) - G(f_d) < A(f_u) - G(f_u) \tag{3.3.43}$$

or

$$G(f_d) - G(f_u) > A(f_d) - A(f_u) \tag{3.3.44}$$

That is, $G(f)$ is better than $A(f)$.

(5) The value of $A(f)-G(f)$ of the ICE signal is less than the value of $A(f)-G(f)$ of the NIC signal, since the value of $\eta(f)$ of the ICE signal is less than the value

of $\eta(f)$ of the NIC signal.

(6) The value of $A(f) - G(f)$ of carrier interference with weak AM is less than the value of $A(f) - G(f)$ of carrier interference with strong AM, since the value of $\eta(f)$ of carrier interference with weak AM is less than the value of $\eta(f)$ of carrier interference with strong AM.

(7) The value of $A(f) - G(f)$ of the ICE signal is less than the value of $A(f) - G(f)$ of carrier interference with strong AM, since the value of $\eta(f)$ of the ICE signal is less than the value of $\eta(f)$ of carrier interference with strong AM.

(8) The value of $A(f) - G(f)$ of the ICE signal is less than the value of $A(f) - G(f)$ of noise level, since the value of $\eta(f)$ of the ICE signal is less than the value of $\eta(f)$ of noise level.

(9) The value of $A(f) - G(f)$ of the NIC signal is greater than the value of $A(f) - G(f)$ of carrier interference with weak AM, since the value of $\eta(f)$ of the NIC signal is greater than the value of $\eta(f)$ of carrier interference with weak AM.

(10) The above comments from (3) to (9) which apply to $A(f) - G(f)$ can also apply to $A(f) - H(f)$.

(11) The processing strategy based on using the combination of $A(f)$, $G(f)$, and $H(f)$ could be superior to the processing strategy based on using only one of $A(f)$, $G(f)$, and $H(f)$.

3.3.3 The Extreme Case

Let C be a constant while

$$\epsilon \to 0 \tag{3.3.45}$$

If

$$S_k(f) \approx C \qquad k = 1, \cdots, K_1 \tag{3.3.46}$$

and

$$S_k(f) \approx \epsilon \qquad k = (K - K_2 + 1), \cdots, K \tag{3.3.47}$$

where

$$K_1 + K_2 = K \tag{3.3.48}$$

then

$$\begin{aligned} A(f) &\approx \frac{1}{K}(K_1 \cdot C + K_2 \cdot \epsilon) \approx \frac{K_1}{K}C \\ G(f) &\approx \left(C^{K_1} \cdot \epsilon^{K_2}\right)^{\frac{1}{K}} \to 0 \\ H(f) &\approx \frac{1}{\frac{1}{K}\left(\frac{K_1}{C} + \frac{K_2}{\epsilon}\right)} \to 0 \end{aligned}$$

A good example for this extreme case is the On-Off Modulation interference.

3.4 Theoretical Analysis for ELT Signal Spectra

We can re-write the spectrum of the ICE signal in (2.3.3), the spectrum of the NIC signal in (2.3.13), and the spectrum of the NCE signal in (2.3.20) as the kth periodograms

$$S_k^{ice}(f) = \left[\frac{AT_kd}{2}\right]^2 \cdot \text{sinc}^2[(f - f_c)T_kd] \cdot \left[\frac{\sin[\pi(f - f_c)T_D]}{\sin[\pi(f - f_c)T_k]}\right]^2, \tag{3.4.1}$$

$$S_k^{nic}(f) = \left[\frac{A\mathcal{T}_k d}{2}\right]^2 \cdot \mathrm{sinc}^2[(f - f_c)\mathcal{T}_k d] \cdot \left[\frac{\sin[\pi(f - f_c - f_s)T_D]}{\sin[\pi(f - f_c - f_s)\mathcal{T}_k]}\right]^2, \tag{3.4.2}$$

and

$$S_k^{nce}(f) = \left[\frac{A\mathcal{T}_k d}{2}\right]^2 \cdot \mathrm{sinc}^2[(f - f_c)\mathcal{T}_k d] \cdot \left|\sum_{i_k=1}^{N_k} e^{-j\left[2\pi(f-f_c)(i_k-1)\mathcal{T}_k - \Theta_{i_k}\right]}\right|^2 \tag{3.4.3}$$

respectively. The important point which the above re-writing is intended to emphasize is that in (3.4.1), (3.4.2), and (3.4.3), $\mathcal{T}_k$ varies with k. Such an example has been provided in Table 3.2. According to (2.2.13), there is a relation such that

$$N_k = \frac{T_D}{\mathcal{T}_k} \tag{3.4.4}$$

Note that, for fixed T_D, $\mathcal{T}_k$ and N_k vary with k.

3.4.1 Arithmetically Averaged Spectra of ELT Signals

For the Ideal Coherent ELT (ICE) Signal Model, according to (3.2.1) we have

$$\begin{aligned} A^{ice}(f) &\triangleq \frac{1}{K}\sum_{k=1}^{K} S_k^{ice}(f) \\ &= \frac{1}{K}\sum_{k=1}^{K}\left(\left[\frac{A\mathcal{T}_k d}{2}\right]^2 \cdot \mathrm{sinc}^2[(f - f_c)\mathcal{T}_k d] \cdot \left[\frac{\sin[\pi(f - f_c)T_D]}{\sin[\pi(f - f_c)\mathcal{T}_k]}\right]^2\right) \end{aligned} \tag{3.4.5}$$

where the second equality is due to (3.4.1). An example of the AAS of ICE signal can be found in Fig. 2.6.

k	N_k	$\mathcal{T}_k$ (ms)	$\frac{1}{\mathcal{T}_k}$ (kHz)
01	27.943	0.7329	1.3644
02	27.172	0.7537	1.3268
03	23.922	0.8561	1.1680
04	22.934	0.8930	1.1198
05	20.121	1.0178	0.9825
06	19.555	1.0473	0.9548
07	17.434	1.1747	0.8513
08	16.036	1.2771	0.7830
09	13.675	1.4976	0.6677
10	12.671	1.6163	0.6187
11	11.329	1.8077	0.5532
12	9.9250	2.0635	0.4846

Table 3.2: $\mathcal{T}_k$ or $\frac{1}{\mathcal{T}_k}$ varies with k

For the Non-Ideal Coherent (NIC) ELT Signal Model, according to (3.2.1) we have

$$\begin{aligned} A^{nic}(f) &\triangleq \frac{1}{K}\sum_{k=1}^{K} S_k^{nic}(f) \\ &= \frac{1}{K}\sum_{k=1}^{K}\left(\left[\frac{A\mathcal{T}_k d}{2}\right]^2 \cdot \mathrm{sinc}^2[(f-f_c)\mathcal{T}_k d]\cdot\left[\frac{\sin[\pi(f-f_c-f_s)T_D]}{\sin[\pi(f-f_c-f_s)\mathcal{T}_k]}\right]^2\right) \end{aligned} \tag{3.4.6}$$

where the second equality is due to (3.4.2). An example of the AAS of NIC signal can be found in Fig. 2.12.

For the Non-Coherent ELT (NCE) Signal Model, according to (3.2.1) we have

$$\begin{aligned} A^{nce}(f) &\triangleq \frac{1}{K}\sum_{k=1}^{K} S_k^{nce}(f) \\ &= \frac{1}{K}\sum_{k=1}^{K}\left(\left[\frac{A\mathcal{T}_k d}{2}\right]^2 \cdot \mathrm{sinc}^2[(f-f_c)\mathcal{T}_k d] \cdot \left|\sum_{i_k=1}^{N_k} e^{-j\left[2\pi(f-f_c)(i_k-1)\mathcal{T}_k-\Theta_{i_k}\right]}\right|^2\right) \end{aligned} \tag{3.4.7}$$

where the second equality is due to (3.4.3). An example of the AAS of NCE signal can be found in Fig. 2.18.

3.4.2 Geometrically Averaged Spectra of ELT Signals

For the Ideal Coherent ELT (ICE) Signal Model, according to (3.2.2) we have

$$\begin{aligned} G^{ice}(f) &\triangleq \left[\prod_{k=1}^{K} S_k^{ice}(f)\right]^{\frac{1}{K}} \\ &= \left\{\prod_{k=1}^{K}\left(\left[\frac{A\mathcal{T}_k d}{2}\right]^2 \cdot \mathrm{sinc}^2[(f-f_c)\mathcal{T}_k d] \cdot \left[\frac{\sin[\pi(f-f_c)T_D]}{\sin[\pi(f-f_c)\mathcal{T}_k]}\right]^2\right)\right\}^{\frac{1}{K}} \end{aligned} \tag{3.4.8}$$

where the second equality is due to (3.4.1). An example of the GAS of ICE signal can be found in Fig. 2.7.

For the Non-Ideal Coherent (NIC) ELT Signal Model, according to (3.2.2) we have

$$\begin{aligned} G^{nic}(f) &\triangleq \left[\prod_{k=1}^{K} S_k^{nic}(f)\right]^{\frac{1}{K}} \\ &= \left\{\prod_{k=1}^{K}\left(\left[\frac{A\mathcal{T}_k d}{2}\right]^2 \cdot \mathrm{sinc}^2[(f-f_c)\mathcal{T}_k d] \cdot \left[\frac{\sin[\pi(f-f_c-f_s)T_D]}{\sin[\pi(f-f_c-f_s)\mathcal{T}_k]}\right]^2\right)\right\}^{\frac{1}{K}} \end{aligned} \tag{3.4.9}$$

where the second equality is due to (3.4.2). An example of the GAS of NIC signal can be found in Fig. 2.13.

For the Non-Coherent ELT (NCE) Signal Model, according to (3.2.2) we have

$$
\begin{aligned}
G^{nce}(f) &\triangleq \left[\prod_{k=1}^{K} S_k^{nce}(f)\right]^{\frac{1}{K}} \\
&= \left\{\prod_{k=1}^{K}\left(\left[\frac{A\mathcal{T}_k d}{2}\right]^2 \cdot \mathrm{sinc}^2[(f-f_c)\mathcal{T}_k d] \cdot \left|\sum_{i_k=1}^{N_k} e^{-j\left[2\pi(f-f_c)(i_k-1)\mathcal{T}_k-\Theta_{i_k}\right]}\right|^2\right)\right\}^{\frac{1}{K}}
\end{aligned}
\tag{3.4.10}
$$

where the second equality is due to (3.4.3). An example of the GAS of NCE signal can be found in Fig. 2.19.

3.4.3 Harmonically Averaged Spectra of ELT Signals

For the Ideal Coherent ELT (ICE) Signal Model, according to (3.2.3) we have

$$
\begin{aligned}
H^{ice}(f) &\triangleq \frac{1}{\frac{1}{K}\sum_{k=1}^{K}\frac{1}{S_k^{ice}(f)}} \\
&= \frac{K}{\sum_{k=1}^{K}\left(\left[\frac{2}{A\mathcal{T}_k d}\right]^2 \cdot \frac{1}{\mathrm{sinc}^2[(f-f_c)\mathcal{T}_k d]} \cdot \left[\frac{\sin[\pi(f-f_c)\mathcal{T}_k]}{\sin[\pi(f-f_c)T_D]}\right]^2\right)}
\end{aligned}
\tag{3.4.11}
$$

where the second equality is due to (3.4.1). An example of the HAS of ICE signal can be found in Fig. 2.8.

For the Non-Ideal Coherent (NIC) ELT Signal Model, according to (3.2.3) we have

$$
H^{nic}(f) \triangleq \frac{1}{\frac{1}{K}\sum_{k=1}^{K}\frac{1}{S_k^{nic}(f)}}
$$

$$= \frac{K}{\sum_{k=1}^{K}\left(\left[\frac{2}{AT_k d}\right]^2 \cdot \frac{1}{\mathrm{sinc}^2[(f-f_c)T_k d]} \cdot \left[\frac{\sin[\pi(f-f_c-f_s)T_k]}{\sin[\pi(f-f_c-f_s)T_D]}\right]^2\right)} \tag{3.4.12}$$

where the second equality is due to (3.4.2). An example of the HAS of NIC signal can be found in Fig. 2.14.

For the Non-Coherent ELT (NCE) Signal Model, according to (3.2.3) we have

$$\begin{aligned} H^{nce}(f) &\triangleq \frac{1}{\frac{1}{K}\sum_{k=1}^{K}\frac{1}{S_k^{nce}(f)}} \\ &= \frac{K}{\sum_{k=1}^{K}\left(\left[\frac{2}{AT_k d}\right]^2 \cdot \frac{1}{\mathrm{sinc}^2[(f-f_c)T_k d]} \cdot \frac{1}{\left|\sum_{i_k=1}^{N_k} e^{-j\left[2\pi(f-f_c)(i_k-1)T_k-\Theta_{i_k}\right]}\right|^2}\right)} \end{aligned} \tag{3.4.13}$$

where the second equality is due to (3.4.3). An example of the HAS of NCE signal can be found in Fig. 2.20.

3.4.4 Shape of $A^{ice}(f)$, $G^{ice}(f)$, or $H^{ice}(f)$

It can be easily recognized that in every one of the K components of $A^{ice}(f)$ in (3.4.5), $G^{ice}(f)$ in (3.4.8), or $H^{ice}(f)$ in (3.4.11), the factor

$$\gamma^{ice}(f) \triangleq \left[\frac{\sin[\pi(f-f_c)T_D]}{\sin[\pi(f-f_c)T_k]}\right]^2 \tag{3.4.14}$$

principally controls the shape of $A^{ice}(f)$, $G^{ice}(f)$, or $H^{ice}(f)$. This factor produces peaks in $A^{ice}(f)$, $G^{ice}(f)$, and $H^{ice}(f)$ at

$$f = f_c \pm \frac{\ell}{T_k} \qquad \begin{cases} \ell = 0 & \text{carrier peaks} \\ \ell = \pm 1, \pm 2, \cdots & \text{sideband peaks} \\ k = 1, \cdots, K & \end{cases} \tag{3.4.15}$$

and valleys between any two adjacent peaks.

The carrier peaks provided by all K components (of $A^{ice}(f)$, $G^{ice}(f)$, or $H^{ice}(f)$) are exactly at the same place

$$f = f_c \tag{3.4.16}$$

and cannot encounter any valley from the other $K-1$ components (of $A^{ice}(f)$, $G^{ice}(f)$, or $H^{ice}(f)$) by virtue of the arithmetically, geometrically, or harmonically averaging operation described respectively in (3.4.5), (3.4.8), or (3.4.11).

Note that, in (3.4.5), (3.4.8), or (3.4.11), T_k varies with k and such an example has been provided in Table 3.2. Therefore, the sideband peaks are apt to be diminished due to encountering valleys from the other $K-1$ components (of $A^{ice}(f)$, $G^{ice}(f)$, or $H^{ice}(f)$) by virtue of the arithmetically, geometrically, or harmonically averaging operation described respectively in (3.4.5), (3.4.8), or (3.4.11).

Consequently, we can quite certainly say that $A^{ice}(f)$, $G^{ice}(f)$, or $H^{ice}(f)$ should have only one peak at $f = f_c$ while $A^{ice}(f)$, $G^{ice}(f)$, or $H^{ice}(f)$ could have sidebands in both the left-hand side of $f = f_c$ and the right-hand side of $f = f_c$.

3.4.5 Shape of $A^{nic}(f)$, $G^{nic}(f)$, or $H^{nic}(f)$

It can be easily recognized that in every one of the K components of $A^{nic}(f)$ in (3.4.6), $G^{nic}(f)$ in (3.4.9), or $H^{nic}(f)$ in (3.4.12), the factor

$$\gamma^{nic}(f) \triangleq \left[\frac{\sin[\pi(f - f_c - f_s)T_D]}{\sin[\pi(f - f_c - f_s)\mathcal{T}_k]}\right]^2 \tag{3.4.17}$$

principally controls the shape of $A^{nic}(f)$, $G^{nic}(f)$, or $H^{nic}(f)$.

Discussing the shape of $A^{nic}(f)$ in (3.4.6), $G^{nic}(f)$ in (3.4.9), or $H^{nic}(f)$ in (3.4.12) by the same token used before, we can quite certainly say that, as long as the scaled frequency shift f_s in (2.3.10) is not too large, $A^{nic}(f)$ in (3.4.6), $G^{nic}(f)$ in (3.4.9), or $H^{nic}(f)$ in (3.4.12) should have only one peak at $f = f_c + f_s$ while $A^{nic}(f)$ in (3.4.6), $G^{nic}(f)$ in (3.4.9), or $H^{nic}(f)$ in (3.4.12) could have sidebands in both the left-hand side of $f = f_c + f_s$ and the right-hand side of $f = f_c + f_s$. If the scaled frequency shift f_s in (2.3.10) is too large, then the shape of $A^{nic}(f)$, $G^{nic}(f)$, or $H^{nic}(f)$ is also significantly affected by the factor

$$\beta^{nic}(f) \triangleq \operatorname{sinc}^2[(f - f_c)\mathcal{T}_k d] \tag{3.4.18}$$

in (3.4.6), (3.4.9), or (3.4.12) especially when $f_c + f_s$ falls in any one of the neighborhoods of frequency points

$$f = f_c \pm \frac{\ell}{\mathcal{T}_k d} \qquad \begin{cases} \ell = \pm 1, \pm 2, \cdots \\ k = 1, \cdots, K \end{cases} \tag{3.4.19}$$

that is, the zero points of the above factor. For example, it can be seen from Fig. 2.11 that the moved carrier peak disappears for a considerable portion of the sweep time. Note that, in Fig. 2.11 we used a range of 20 dB for showing periodograms. If we increase this range, these disappeared carrier peaks could re-appear. Nevertheless, it is not hard to imagine that now we could have $G^{nic}(f_c+f_s) \approx 0$ and $H^{nic}(f_c+f_s) \approx 0$ where $f_c + f_s$ is the position of the moved carrier peak.

Furthermore, one set of sidelobes is enhanced while the other set of sidelobes is diminished. After taking the arithmetically averaging operation on the K components of $A^{nic}(f)$ in (3.4.6), it is possible that one of the two sidebands mentioned above is even much higher than the moved carrier peak of $A^{nic}(f)$. This serious weakness of $A^{nic}(f)$ can be significantly overcome by using $G^{nic}(f)$ in (3.4.9) or $H^{nic}(f)$ in (3.4.12). The reasons that $G^{nic}(f)$ or $H^{nic}(f)$ may offer better performance have been provided in Section 3.3.

3.4.6 Shape of $A^{nce}(f)$, $G^{nce}(f)$, or $H^{nce}(f)$

Unfortunately, the same token used before does not apply to the discussion for the shape of $A^{nce}(f)$ in (3.4.7), $G^{nce}(f)$ in (3.4.10), or $H^{nce}(f)$ in (3.4.13), since (3.4.7), (3.4.10), (3.4.13) can not be simplified further due to the fact that Θ_{i_k} in (3.4.7), (3.4.10), or (3.4.13) is a random variable distributed uniformly between 0 and 2π.

We invite the reader to observe Fig. 2.17 for the NCE signal's periodograms again and compare this figure with Fig. 2.5 for the ICE signal's periodograms. The difference is that we have the 1st lower frequency peak, the carrier frequency peak, and the 1st upper frequency peak at all K periodograms in Fig. 2.5 while we do not have them in Fig. 2.17. Instead, we have some randomly distributed frequency buds within a frequency interval centralized at the carrier frequency at every periodogram in Fig. 2.17. Based on this observation, it is not hard to understand that why we have wide range frequency bands instead of thin carrier peaks in $A^{nce}(f)$, $G^{nce}(f)$, and $H^{nce}(f)$ shown in Figs. 2.18, 2.19, and 2.20 respectively.

3.5 Performance Study by Simulation

Normally, the spectra of continuous windows of data are averaged to increase the detectability and reliability in SARSAT signal processing [21, 24]. With the AAS or $A(f)$ represented in (3.2.1) plus the two new averaged spectra, namely, the GAS or $G(f)$ introduced in (3.2.2) and the HAS or $H(f)$ introduced in (3.2.3), we now have 3 different averaged spectra.

The performances of the AAS, the GAS, and the HAS have been tested by computer simulations. A part of the simulation results has been included here to support the analyses provided by this thesis. In the following examples, the number of Blackman windowed periodograms used in an averaging operation, K, equals 24.

Example 3.A

In this example, a single ICE signal is tested and the periodograms have been shown in Fig. 3.9(a). Here, the duty cycle d equals 0.5, the carrier frequency (after the mixer) f_c equals 16.2 kHz, the sampling period T_s equals 10^{-5} s, the window length T_D equals 20.48 ms, the number of samples used by the FFT, N_f, equals 2048, and the carrier-to-noise density ratio CNDR equals 25 dB-Hz. Note that, in the following discussion, all measurements are made to correspond to the level of the desired AAS carrier peak which has been normalized to 0 dB.

From the AAS in Fig. 3.9(b) it can be seen that, the level of the desired carrier peak equals 0 dB, the highest level of the sideband equals -8.36 dB, while the averaged background level equals about -11 dB. From the GAS in Fig. 3.9(c) it can be seen that, the level of the desired carrier peak equals -2.08 dB, the highest level of the sideband equals -12.78 dB, while the averaged background level equals about -15 dB.

From the HAS in Fig. 3.9(d) it can be seen that, the level of the desired carrier peak equals -2.30 dB, the highest level of the sideband equals -13.97 dB, while the averaged background level equals about -18 dB.

Thus, in this example and in terms of detectability and reliability, the performance of the GAS is better than that of the AAS by (12.78-2.08)-(8.36-0)=2.34 dB for the highest level of the sideband and by (15-2.08)-(11-0)=1.92 dB for the averaged background level while the performance of the HAS is better than that of the AAS by (13.97-2.30)-(8.36-0)=3.31 dB for the highest level of the sideband and by (18-2.30)-(11-0)=4.70 dB for the averaged background level.

Example 3.B

In this example, a single NIC signal with carrier frequency shift f_p equal to 1000 Hz is tested and the periodograms have been shown in Fig. 3.10(a). Here, the duty cycle d equals 0.5, the carrier frequency (after mixer) f_c equals 16.2 kHz and should appear at 16.7 kHz, the sampling period T_s equals 10^{-5} s, the window length T_D equals 20.48 ms, the number of samples used by the FFT, N_f, equals 2048, and the carrier-to-noise density ratio CNDR equals 25 dB-Hz. Note that, in the following discussion, all measurements are made to correspond to the level of the desired AAS carrier peak which has been normalized to 0 dB.

From the AAS in Fig. 3.10(b) it can be seen that, the level of the desired carrier peak equals 0 dB, the highest level of the sideband equals -6.04 dB, while the averaged background level equals about -10 dB. From the GAS in Fig. 3.10(c) it can be seen that, the level of the desired carrier peak equals -3.55 dB, the highest level of the sideband equals -12.91 dB, while the averaged background level equals about -15 dB.

From the HAS in Fig. 3.10(d) it can be seen that, the level of the desired carrier peak equals -4.02 dB, the highest level of the sideband equals -14.31 dB, while the averaged background level equals about -18 dB.

Thus, in this example and in terms of detectability and reliability, the performance of the GAS is better than that of the AAS by (12.91-3.55)-(6.04-0)=3.32 dB for the highest level of the sideband and by (15-3.55)-(10-0)=1.45 dB for the averaged background level while the performance of the HAS is better than that of the AAS by (14.31-4.02)-(6.04-0)=4.25 dB for the highest level of the sideband and by (18-4.02)-(10-0)=3.98 dB for the averaged background level.

Example 3.C

The example shown in Fig. 3.11 is similar to the example shown in Fig. 3.9 except that in Fig. 3.11 we have a different CNDR. Therefore, the explanation for Fig. 3.9 which has a CNDR = 25 dB-Hz applies, in a similar way, to Fig. 3.11 which has a CNDR = 18 dB-Hz.

From the AAS in Fig. 3.11(b) it can be seen that, the level of the desired carrier peak equals 0 dB, the highest level of the sideband equals -3.16 dB, while the averaged background level equals about -5 dB. From the GAS in Fig. 3.11(c) it can be seen that, the level of the desired carrier peak equals -5.84 dB, the highest level of the sideband equals -9.91 dB, while the averaged background level equals about -12 dB. From the HAS in Fig. 3.11(d) it can be seen that, the level of the desired carrier peak equals -7.18 dB, the highest level of the sideband equals -10.77 dB, while the averaged background level equals about -15 dB.

Thus, in this example and in terms of detectability and reliability, the performance of the GAS is better than that of the AAS by (9.91-5.84)-(3.16-0)=0.91 dB for the highest level of the sideband and by (12-5.84)-(5-0)=1.16 dB for the averaged background level while the performance of the HAS is better than that of the AAS by (10.77-7.18)-(3.16-0)=0.43 dB for the highest level of the sideband and by (15-7.18)-(5-0)=2.82 dB for the averaged background level.

Example 3.D

The example shown in Fig. 3.12 is similar to the example shown in Fig. 3.10 except that in Fig. 3.12 we have a different CNDR. Therefore, the explanation for Fig. 3.10 which has a CNDR = 25 dB-Hz applies, in a similar way, to Fig. 3.12 which has a CNDR = 18 dB-Hz.

From the AAS in Fig. 3.12(b) it can be seen that, the level of the desired carrier peak equals 0 dB, the highest level of the sideband equals -2.18 dB, while the averaged background level equals about -4 dB. From the GAS in Fig. 3.12(c) it can be seen that, the level of the desired carrier peak equals -6.63 dB, the highest level of the sideband equals -9.33 dB, while the averaged background level equals about -12 dB. From the HAS in Fig. 3.12(d) it can be seen that, the level of the desired carrier peak equals -8.28 dB, the highest level of the sideband equals -10.60 dB, while the averaged background level equals about -15 dB.

Thus, in this example and in terms of detectability and reliability, the performance of the GAS is better than that of the AAS by (9.33-6.63)-(2.18-0)=0.52 dB for the highest level of the sideband and by (12-6.63)-(4-0)=1.37 dB for the averaged background level while the performance of the HAS is better than that of the AAS by (10.60-8.28)-(2.18-0)=0.14 dB for the highest level of the sideband and by

(15-8.28)-(4-0)=2.72 dB for the averaged background level.

3.6 Summary

In this chapter, by making use of 2 highly idealized assumptions described in (3.3.7) and (3.3.27), we were able to obtain some understanding about the behaviors of the AAS, the GAS, and the HAS.

The significant conclusion derived in detail by this chapter is that neither $\Delta_S(f)$ alone nor $S_{\mathrm{mid}}(f)$ alone is sufficient to explain the behaviors of AAS, GAS, and HAS. Rather the ratio $\frac{\Delta_S(f)}{S_{\mathrm{mid}}(f)}$ plays the decisive role in our problem.

The emphases of this conclusion are not only that the values of $G(f)$ and $H(f)$ depend on the value of $\frac{\Delta_S(f)}{S_{\mathrm{mid}}(f)}$ but also that the values of $A(f)-G(f)$ and $A(f)-H(f)$ are monotonic functions of the value of $\frac{\Delta_S(f)}{S_{\mathrm{mid}}(f)}$.

We also discussed briefly another approach for approximating the kth spectral height, $S_k(f)$, to get a parallel conclusion such that the parameter $\eta(f)$ could govern the behaviors of AAS, GAS, and HAS.

The emphases of this conclusion are not only that the values of $A(f)$ and $H(f)$ depend on the value of $\eta(f)$ but also that the values of $A(f)-G(f)$ and $A(f)-H(f)$ are monotonic functions of the value of $\eta(f)$.

The properties of ELT signals and three different averaged spectra AAS, GAS, and HAS for SARSAT signal processing have been examined in detail.

Results of computer simulations have strongly confirmed the theoretical predictions for the performance comparison among the three different averaged spectra.

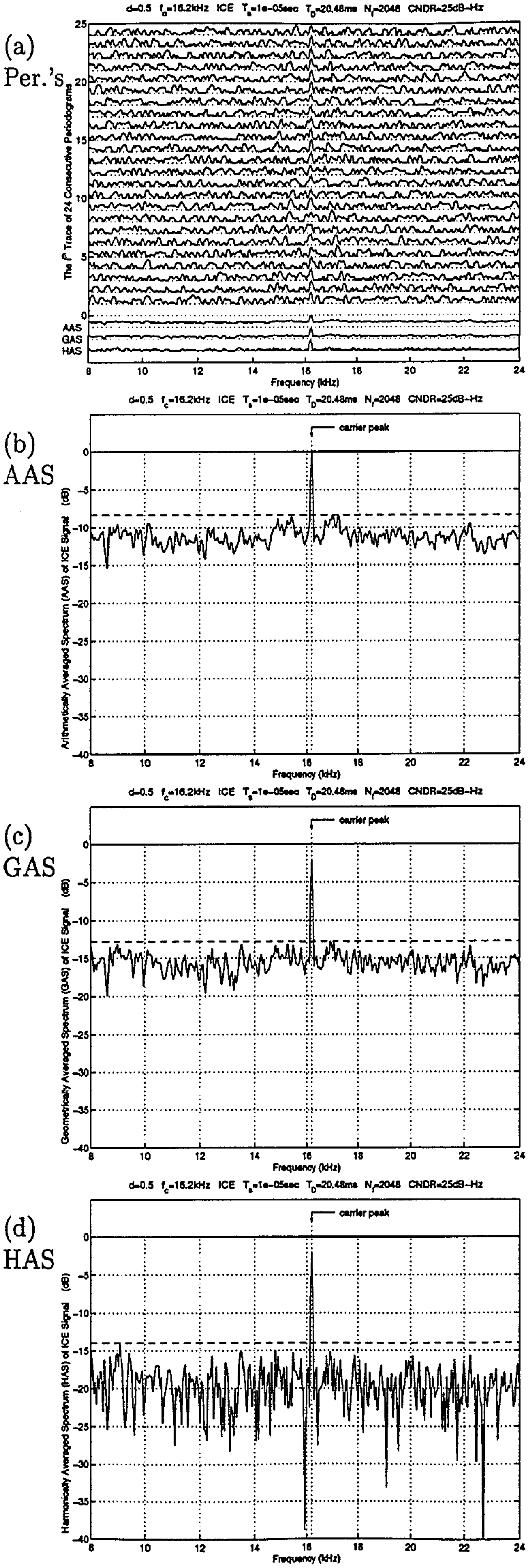

Figure 3.9: ICE (CNDR=25dB-Hz)

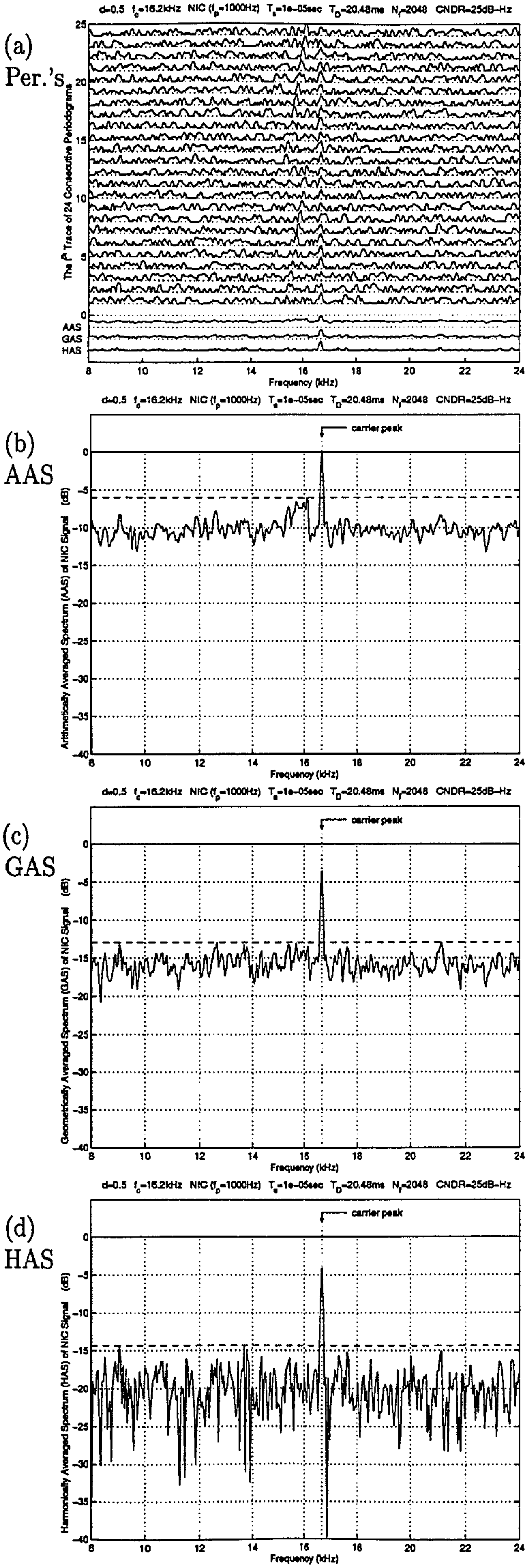

Figure 3.10: NIC (CNDR=25dB-Hz)

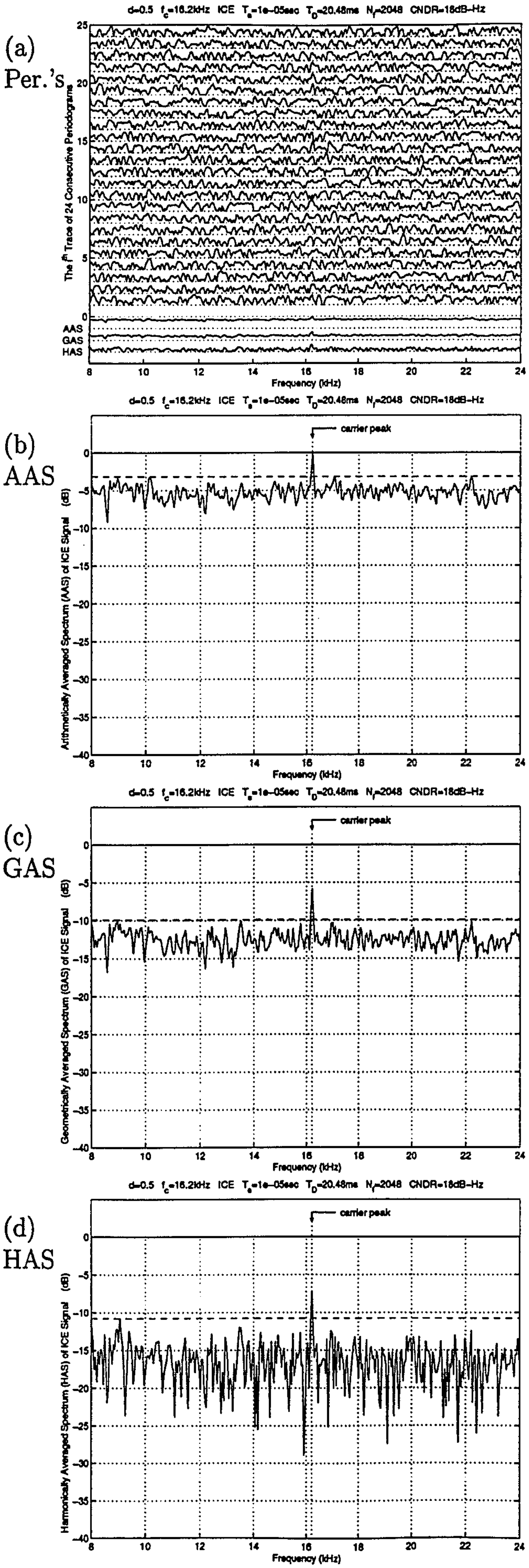

Figure 3.11: ICE (CNDR=18dB-Hz)

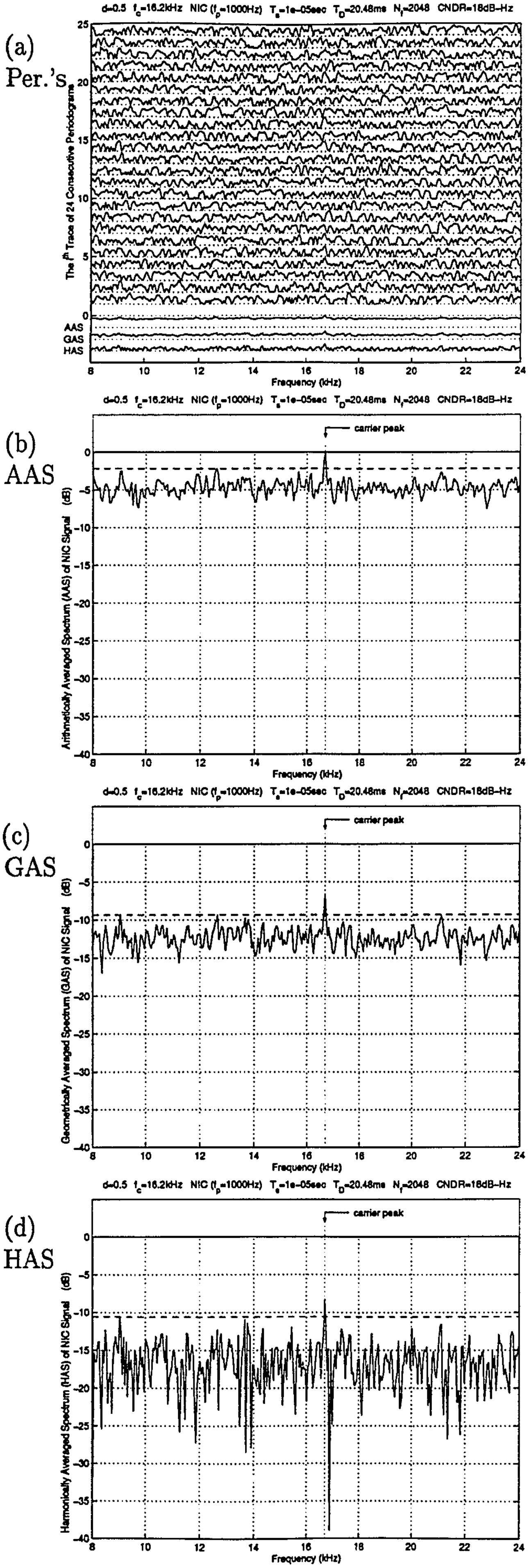

Figure 3.12: NIC (CNDR=18dB-Hz)

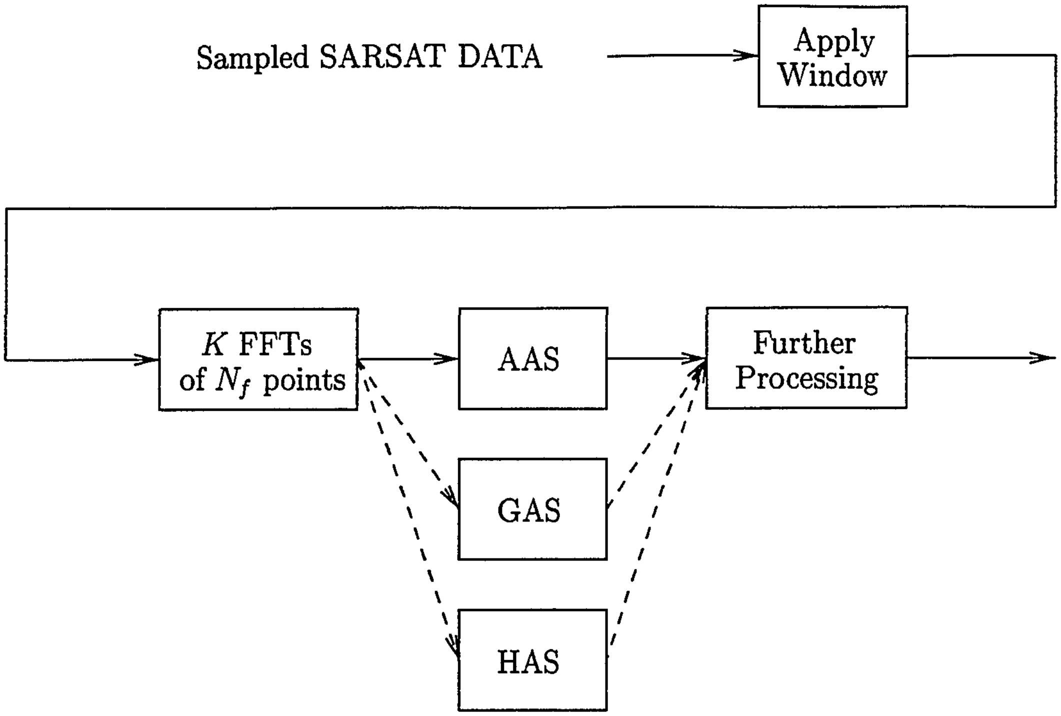

Figure 3.13: Let AAS, GAS, and HAS work together

Generally speaking, the processing strategy based on using the combination of $A(f)$, $G(f)$, and $H(f)$ could be superior to the processing strategy based on using only one of $A(f)$, $G(f)$, and $H(f)$. More specifically, by the "Let AAS, GAS, and HAS work together" strategy shown in Fig. 3.13, we will be able to:

(1) Fully exploit the periodograms already calculated from FFTs for the AAS by introducing the GAS and the HAS additional to AAS.

(2) Reduce interference by making use of the combination of AAS, GAS, and HAS.

(3) Achieve the advantages of GAS and HAS with very little overhead.

Chapter 4

Interference Suppression

4.1 Introduction

In this chapter, processing techniques for detecting ELT signals in an interfering background are investigated based on computer simulation. The new methods involve the use of the Geometrically Averaged Spectrum (GAS) and the Harmonically Averaged Spectrum (HAS). The results of these new methods are compared to the Arithmetically Averaged Spectrum (AAS) where it is shown that the GAS and HAS have superior performance over AAS in a congested signal environment. By a congested signal environment, we mean interference emanating from myriad sources on earth which adds to the uplinked ELT signals.

We review windowing techniques as applied to CW interference in Section 4.2 before discussing other kinds of interference. Interference involved in ELT signal processing can be divided into In-band interference and Ringing Response interference. In-band interference consists of modulated and unmodulated carriers which do not change frequency rapidly. Here the signals compete in amplitude and bandwidth with the desired signals. Examples of this include CW carrier, harmonics of transmitters, and voice transmissions. In this case, the threshold can be defined on a power density basis with the signal competing directly with the interference [14]. We discuss 3 types of in-band interference; namely, AM Carrier interference in Section 4.3, On-Off Modulation interference in Section 4.4, and Swept Carrier interference in Section 4.5.

Ringing Response interference is normally thought of as being due to a small number of high power, short duration pulses of carrier which enter the receiver forming a broadband spectrum of interference [14]. We discuss Ringing Response interference in Section 4.6.

Finally, we offer a summary in Section 4.7 to complete this chapter.

4.2 CW Interference and Windowing

4.2.1 Averaged Periodograms

Many ELT units can be characterized by the Non-Ideal Coherent (NIC) ELT signal model where the frequency of the crystal controlled oscillator (see Fig. 2.9) during the ON time is slightly different from the value during the OFF time. For this case, it is assumed that the crystal controlled oscillator operates at frequency f_c when the switch is closed and $f_c + f_p$ (where f_p can be referred to as *the frequency shift*) when the switch is open, as illustrated in Fig. 2.10, and the oscillator changes frequency instantaneously with the change in voltage.

One of the popular spectral estimation methods based on Fourier analysis is the periodogram (sometimes called the *sample spectrum*) [26]. The principal conclusions which result from the study of the periodogram are that the bias of the periodogram can be reduced if we are willing to accept an increase in variance, and vice versa, but both types of errors cannot be reduced simultaneously.

With N_s being the number of sample points used in a particular estimation, the main properties of the periodogram spectral estimator can be expressed as: (1) The mean of the periodogram estimates converges to the true value of the Power Spectral Density (PSD) as $N_s \to \infty$. (2) The variance of the periodogram estimates does not tend to zero as $N_s \to \infty$. (3) The periodogram is an inconsistent estimator in that even though the average value converges to the true value as the data record length N_s becomes large, the variance is a constant.

To circumvent this problem, the averaged periodogram can be used. For this estimator the data record is segmented into nonoverlapping blocks, which is then followed by an averaging of the periodograms for each block. The variance is then reduced by a factor equal approximately to the number of blocks averaged, but the bias is increased.

4.2.2 Sidelobe Problem

In many cases of practical interest, the data consist of sinusoidal or narrowband signals in white noise. For example, in the context related to ELT signal processing, although the typical ELT signal has a spectrum (see (2.3.13)) which is not really narrowband, what we are ultimately interested in is a very narrow portion at the location of the carrier peak. Any high level contents in the remaining part of the spectrum is considered to be destructive in estimating this quantity.

An example is shown in Fig. 4.1. A rectangle window of 64 time domain sample points is illustrated in part (a) of this figure. That is, no windowing technique is employed here. In part (b) of this figure, the corresponding Fourier transform is shown. Note that, the actual number of time domain samples used for calculating a periodogram in ELT signal processing is usually 1024, 2048, or 4096. Using 64 instead of 1024, 2048, or 4096 as the number of time domain samples, we show the details in the mainlobe and sidelobes due to the rectangle window in part (b). We use 2048 as the number of time domain samples in calculating the periodograms in parts (c), (d), and (e) of this figure. In these 3 parts, it can be seen that in the AAS, the GAS, and the HAS, the presence of the ELT carrier peak which is located at $f = 17.7$ kHz is nearly masked by the high level sidelobes of CW interference at $f = 17.2$ kHz. Details of the above AAS, GAS, and HAS are provided in parts (f), (g), and (h) of this figure.

4.2.3 Windowing Techniques

Without data windowing, a low level ELT signal may be masked by the sidelobes of high level interference if they are close in frequency. In such a situation it may be advantageous to apply a *data window* to the observed signal before computing the periodogram. Data windowing will reduce the magnitude of the periodogram at frequencies not near the signal frequency (sometimes referred to as *the leakage* or the sidelobe level) at the expense of increasing the bandwidth of the mainlobe [26].

Towards this issue, an investigation has been made and computer simulation re-

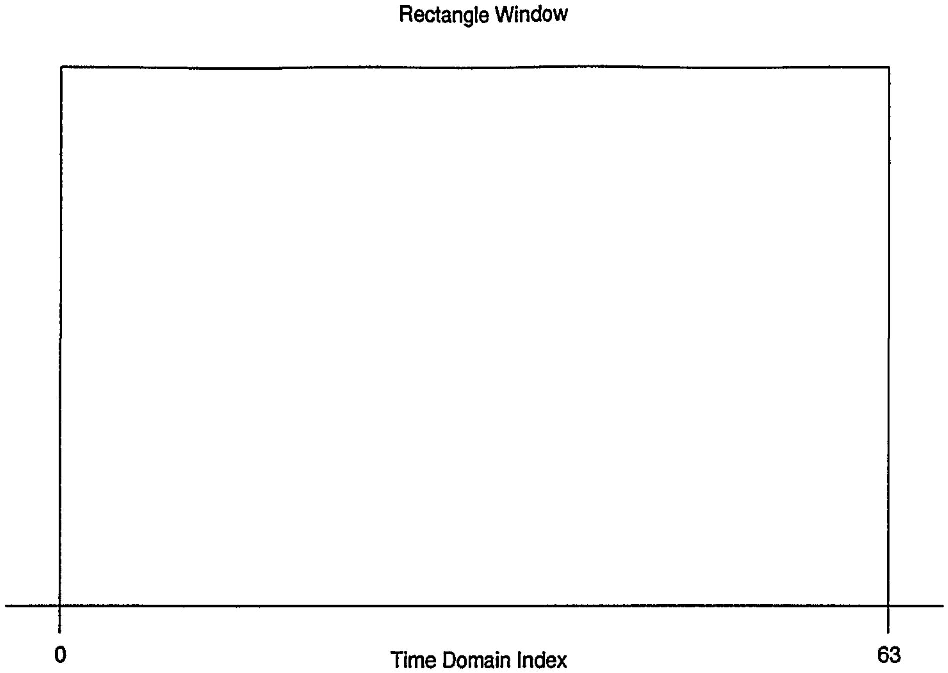

(a) Window of 64 Time Domain Samples

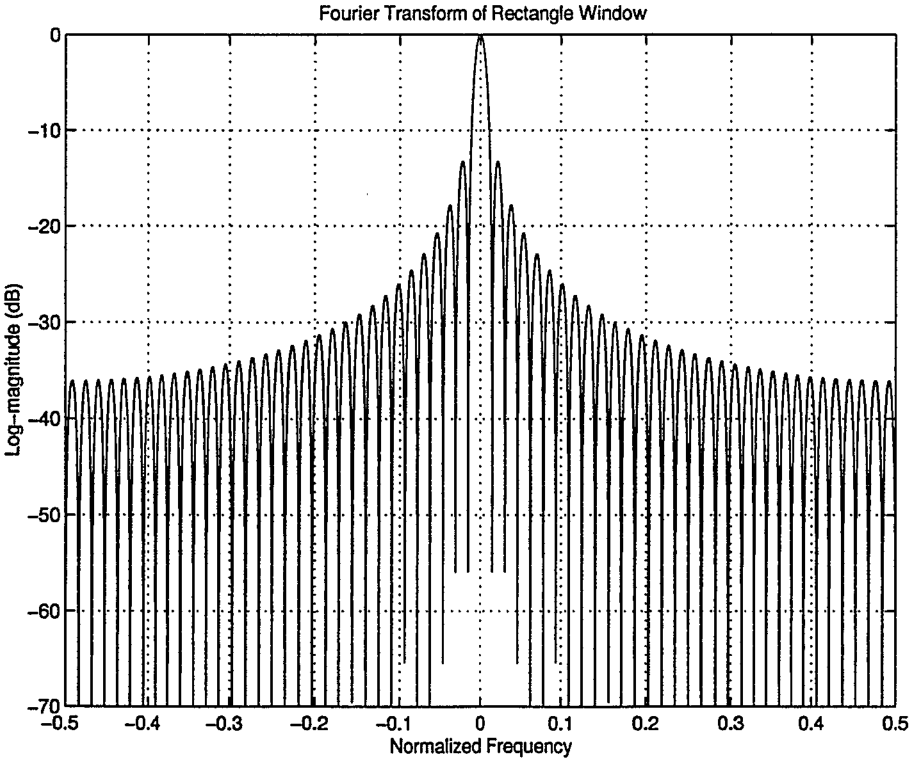

(b) Fourier Transform of the Above Window

Figure 4.1: Averaged Spectra Related to the Use of the Rectangle Window

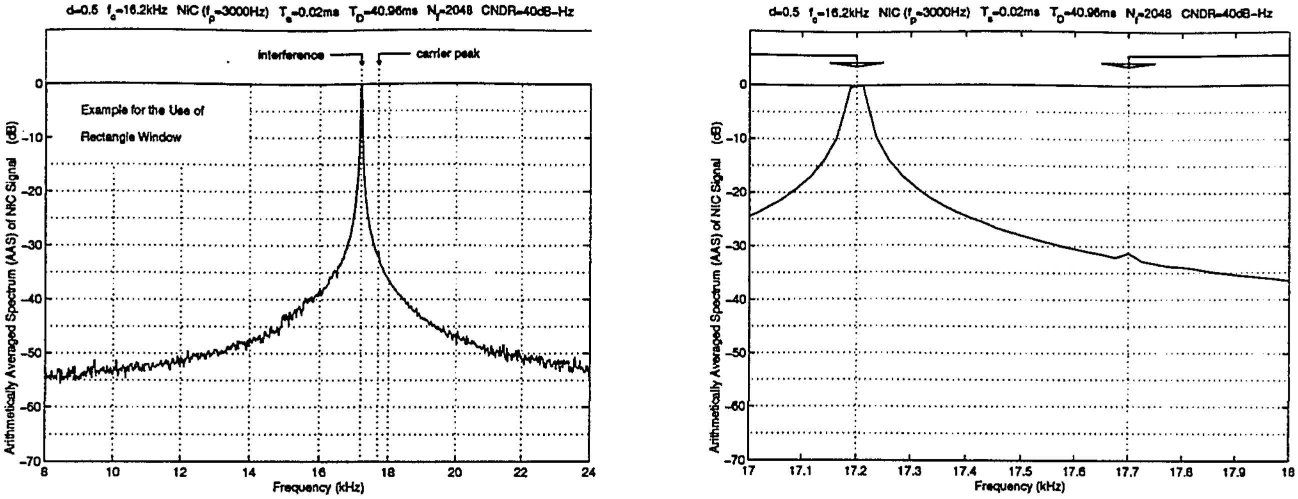

(c) AAS of an ELT with CW Interference

(f) Detailed AAS in (c)

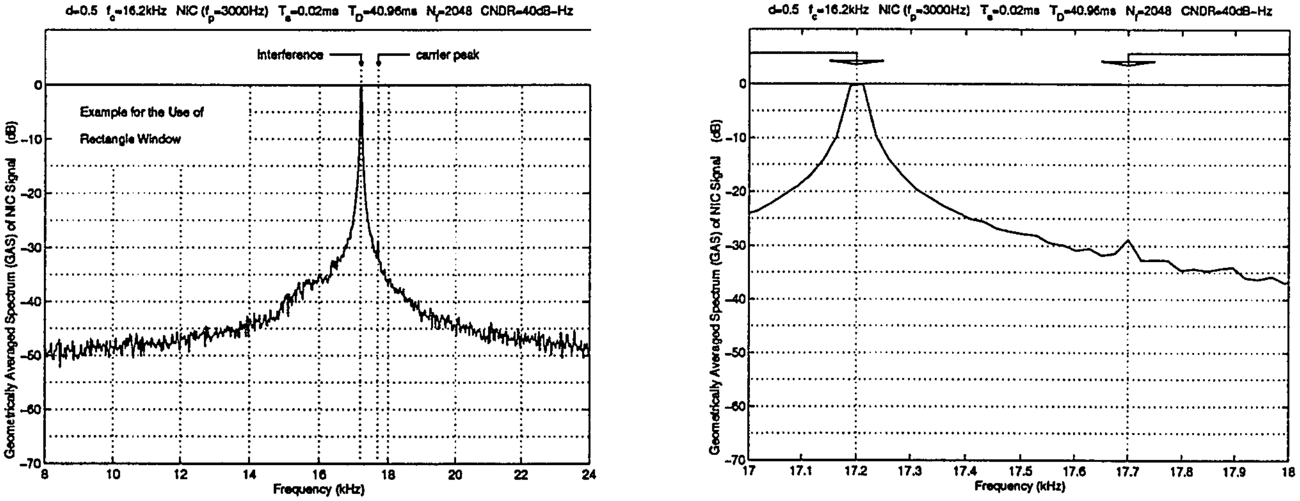

(d) GAS of an ELT with CW Interference

(g) Detailed GAS in (d)

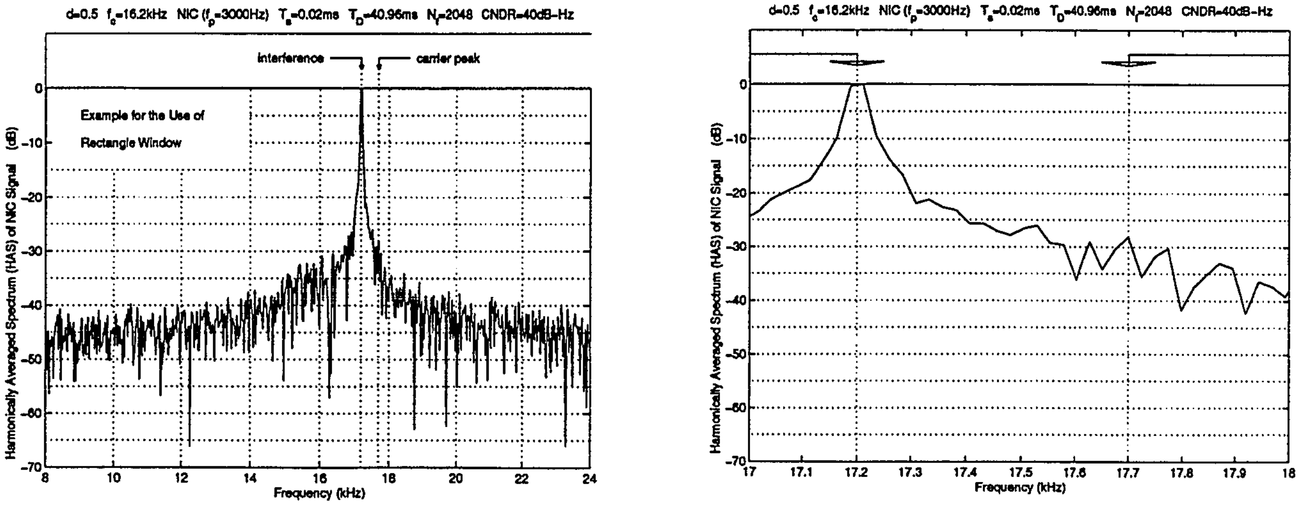

(e) HAS of an ELT with CW Interference

(h) Detailed HAS in (e)

Figure 4.1: Averaged Spectra Related to the Use of the Rectangle Window

sults are presented in Figs. 4.2 through 4.6 for the windows listed in Table 4.1. Specifically, with part (a) in each of Figs. 4.2 through 4.6, a window of 64 time domain samples is presented. With part (b) in each figure, the corresponding Fourier transform is demonstrated. Using 2048 time domain samples for calculating a periodogram, we show in parts (c), (d), and (e) in each figure the AAS, the GAS, and the HAS, respectively, with the details provided in parts (f), (g), and (h) of each figure.

Comparisons can be made between Fig. 4.1, which is the example of not using the windowing technique, and any one of Figs. 4.2 through 4.6 (see Table 4.1). One indicator of window performance is the highest sidelobe level (relative to the mainlobe). Another criterion is the width of the window at the half-power points (the 3-dB bandwidth). It can be seen that the application of a windowing technique to the same set of data enhances the ELT signal and the carrier peak of the ELT signal is now clearly visible. Although the data window has reduced the sidelobe level of the interference, there is an increase in the 3-dB bandwidth of the mainlobe. Thus, a compromise must be reached in window selection.

Generally speaking, it is important to use a window which is not rectangular. A good strategy is to select the minimum in 3-dB mainlobe bandwidth which still provides sufficient sidelobe reduction. This could be done by first scanning the data set with a 1k FFT. For heavy CW interference, the Hanning, Blackman, and Bohman windows are particularly attractive since they provide strong roll-off whereas many other windows (such as Riesz and Hamming) do not.

Shown in	Window Name	Highest Sidelobe Level (dB)	3-dB BW (bins)
Fig. 4.1	Rectangle Window	-13	0.89
Fig. 4.2	Riesz Window	-21	1.16
Fig. 4.3	Hamming Window	-43	1.30
Fig. 4.4	Hanning Window	-32	1.44
Fig. 4.5	Blackman Window	-58	1.68
Fig. 4.6	Bohman Window	-46	1.71

Table 4.1: Windowing Techniques [27]

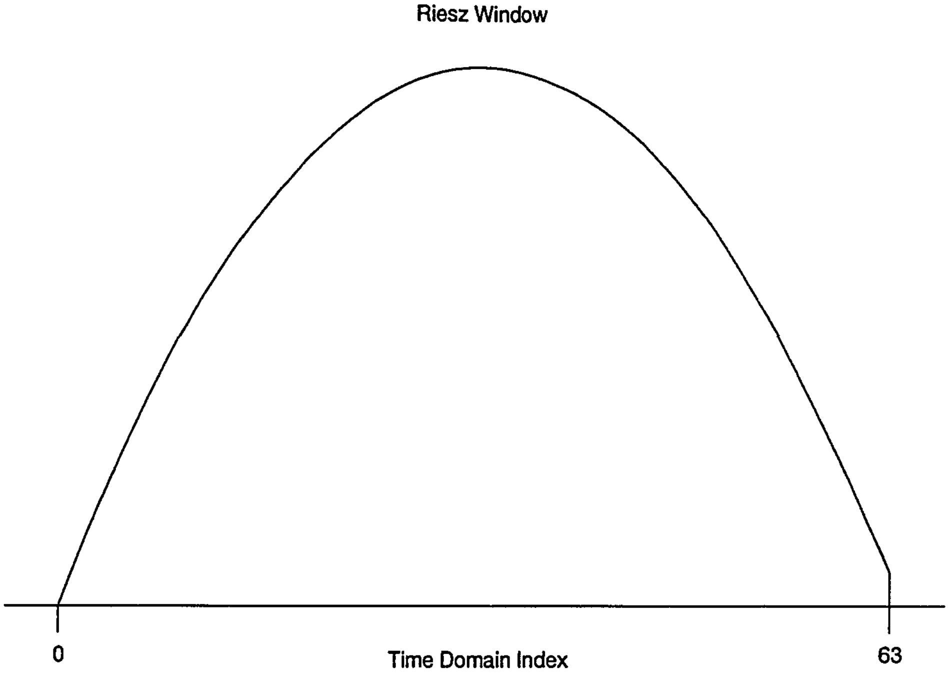

(a) Window of 64 Time Domain Samples

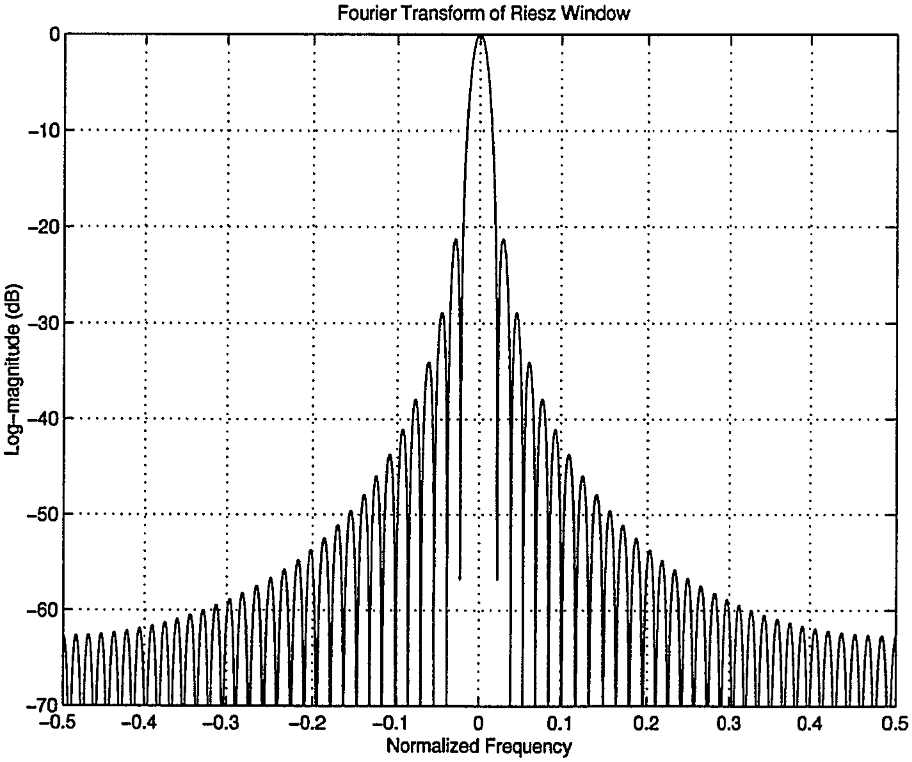

(b) Fourier Transform of the Above Window

Figure 4.2: Averaged Spectra Related to the Use of the Riesz Window

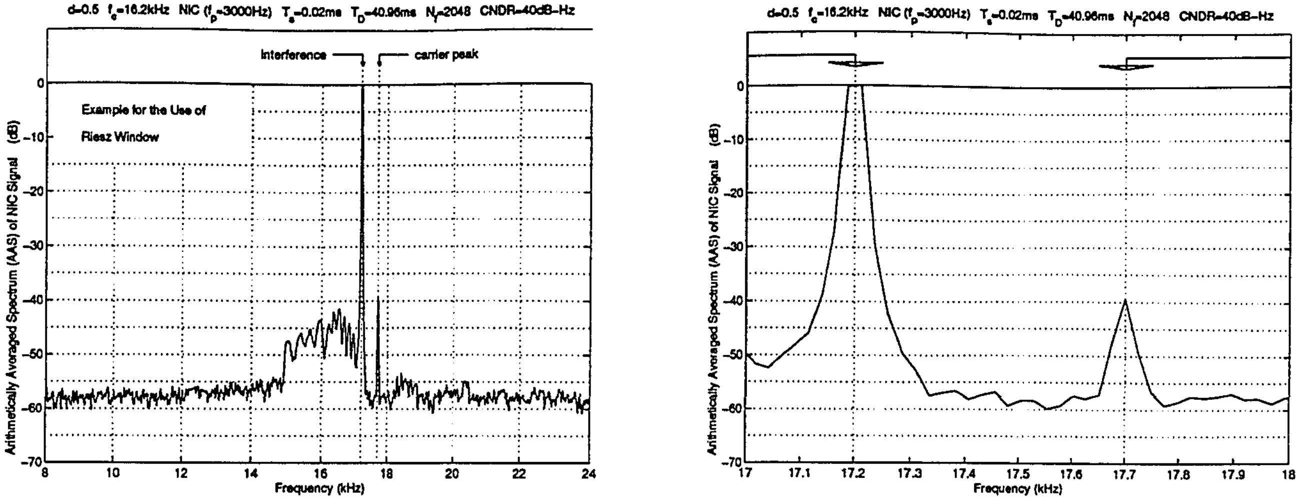

(c) AAS of an ELT with CW Interference

(f) Detailed AAS in (c)

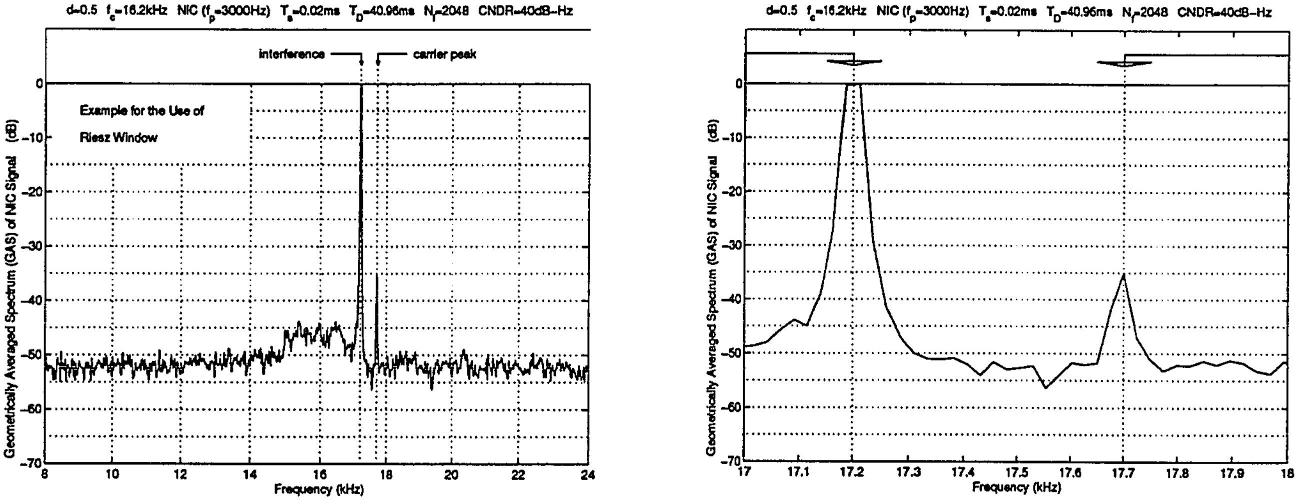

(d) GAS of an ELT with CW Interference

(g) Detailed GAS in (d)

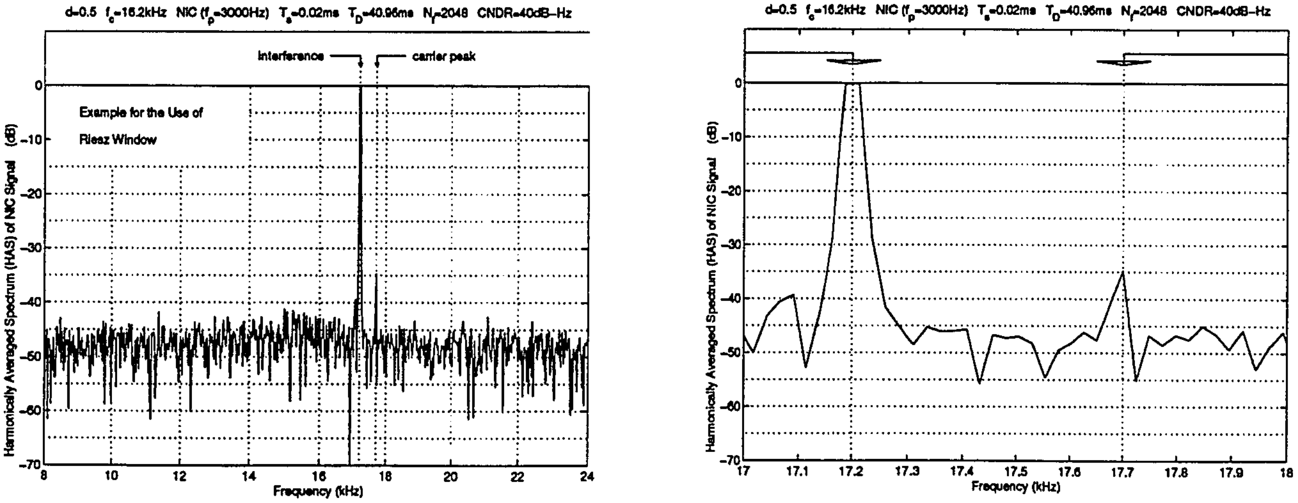

(e) HAS of an ELT with CW Interference

(h) Detailed HAS in (e)

Figure 4.2: Averaged Spectra Related to the Use of the Riesz Window

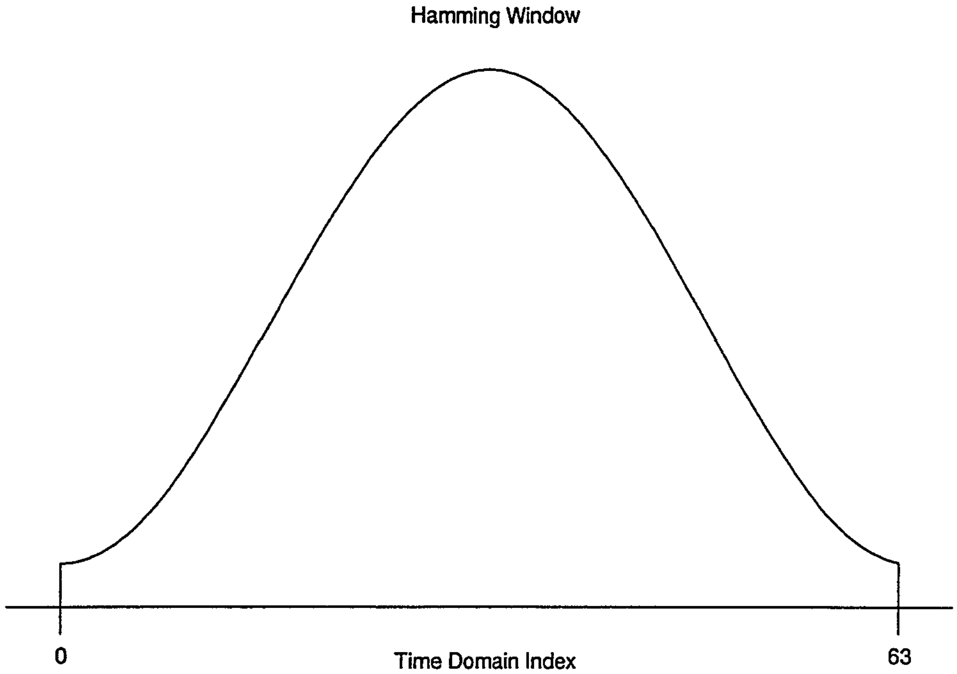

(a) Window of 64 Time Domain Samples

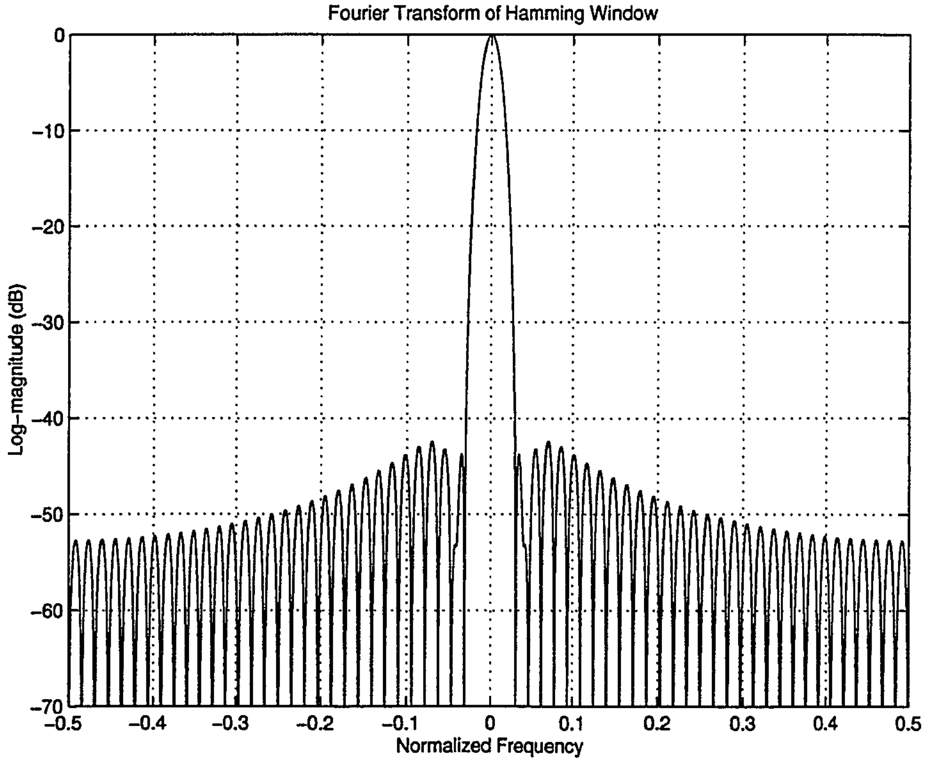

(b) Fourier Transform of the Above Window

Figure 4.3: Averaged Spectra Related to the Use of the Hamming Window

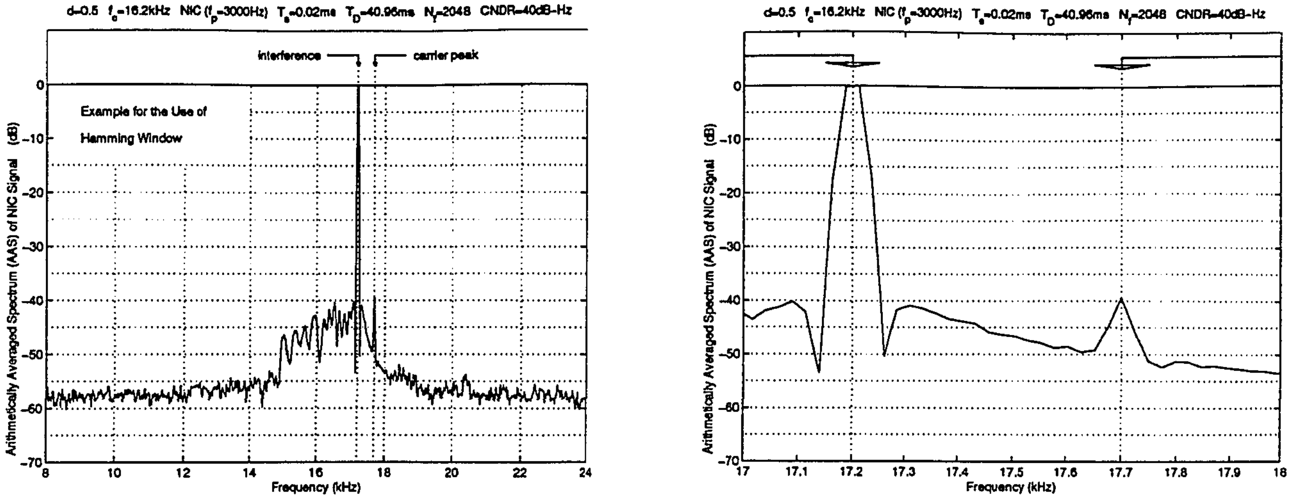

(c) AAS of an ELT with CW Interference

(f) Detailed AAS in (c)

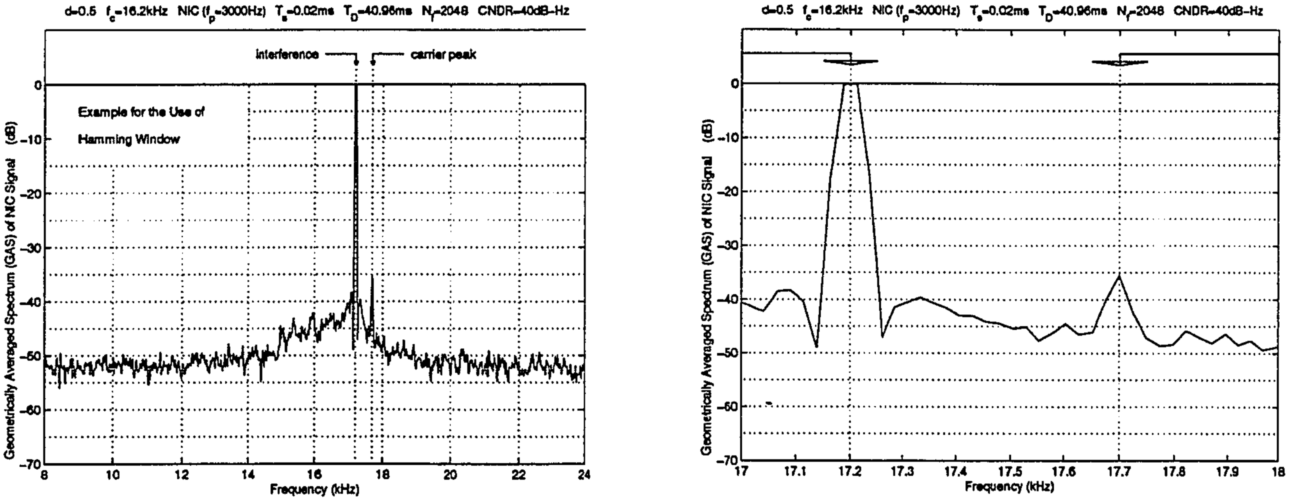

(d) GAS of an ELT with CW Interference

(g) Detailed GAS in (d)

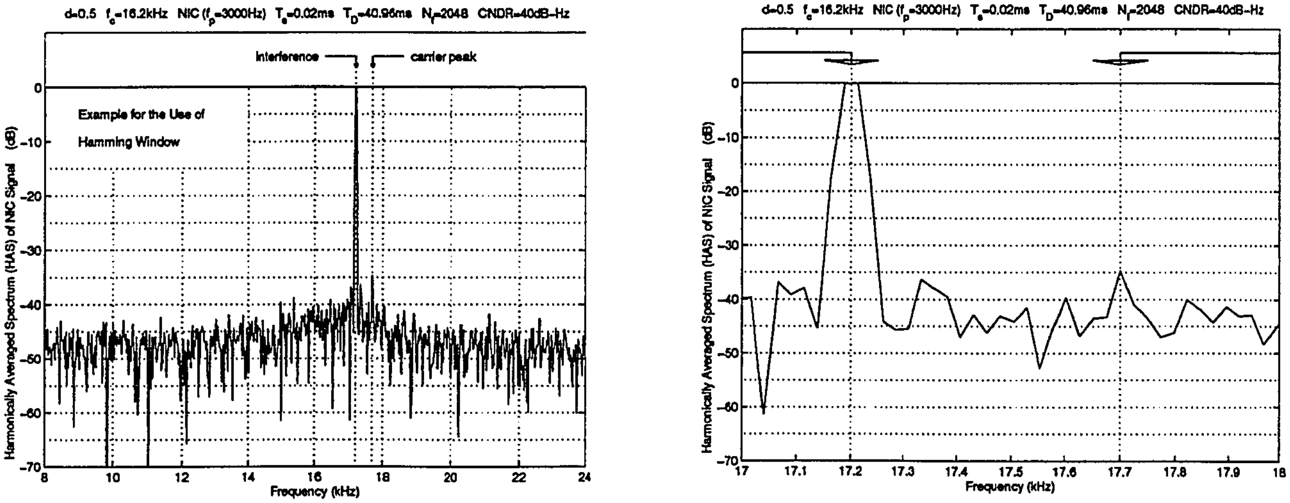

(e) HAS of an ELT with CW Interference

(h) Detailed HAS in (e)

Figure 4.3: Averaged Spectra Related to the Use of the Hamming Window

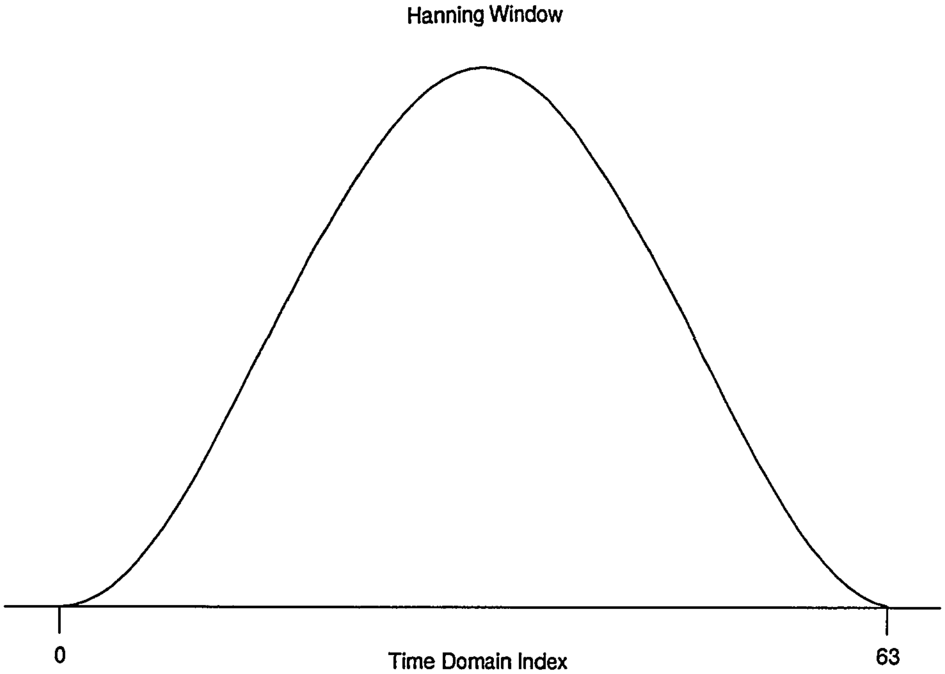

(a) Window of 64 Time Domain Samples

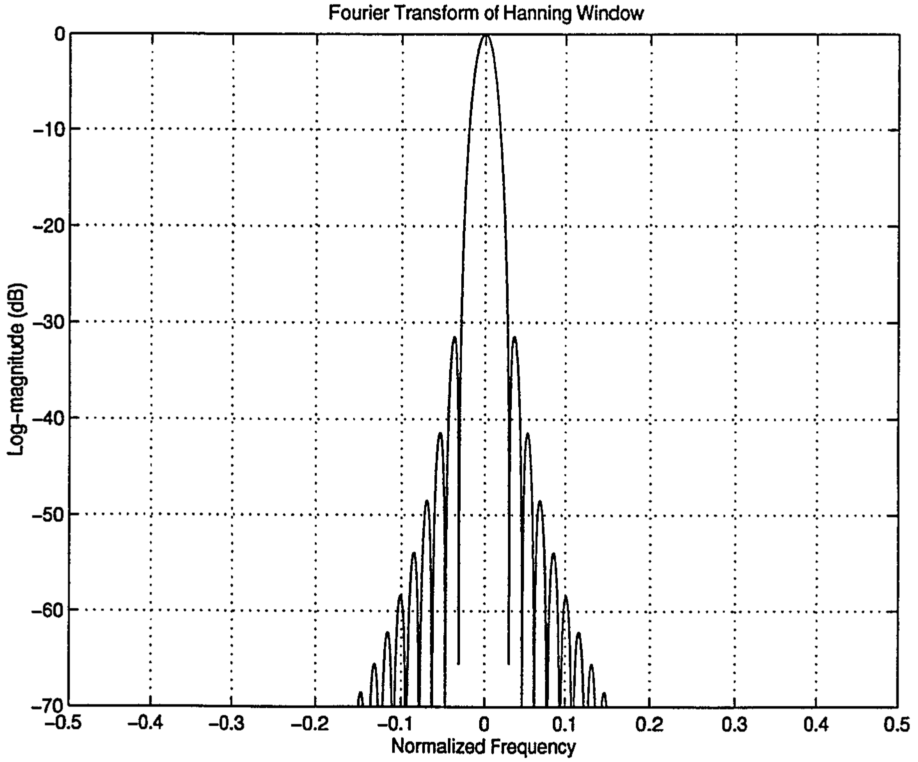

(b) Fourier Transform of the Above Window

Figure 4.4: Averaged Spectra Related to the Use of the Hanning Window

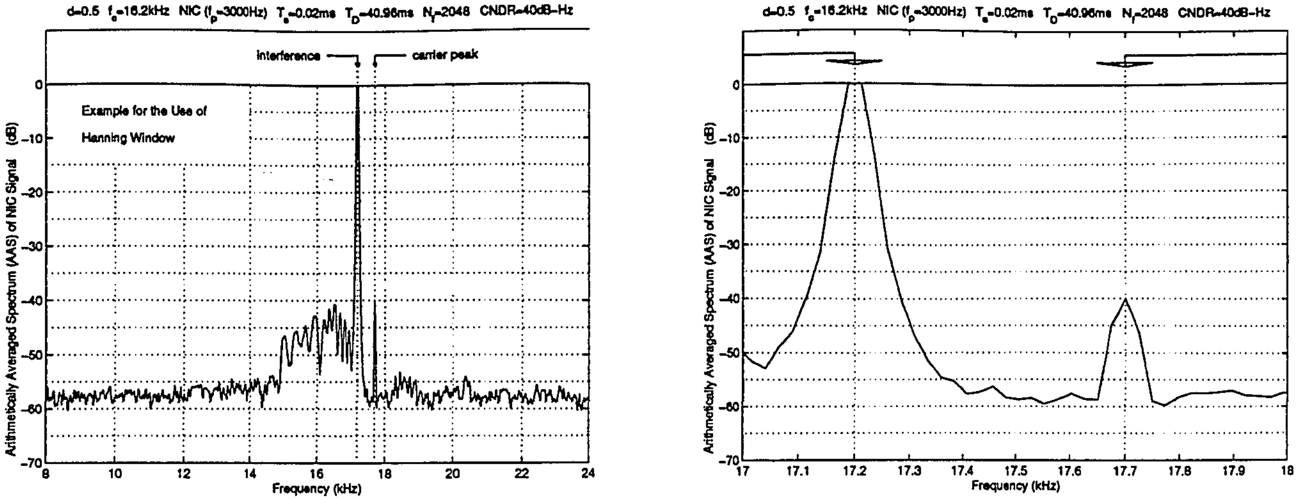

(c) AAS of an ELT with CW Interference

(f) Detailed AAS in (c)

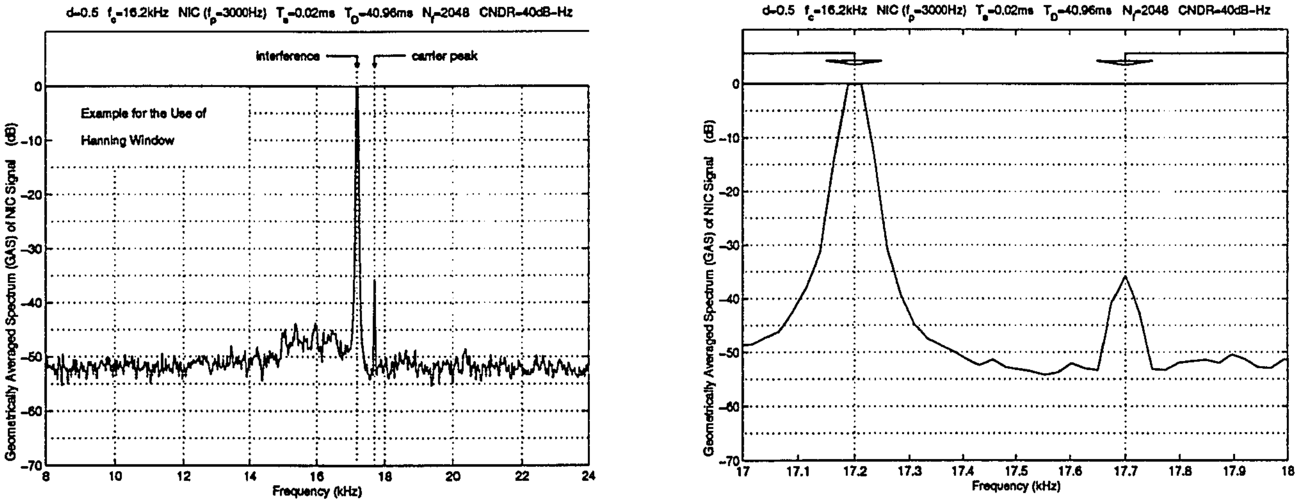

(d) GAS of an ELT with CW Interference

(g) Detailed GAS in (d)

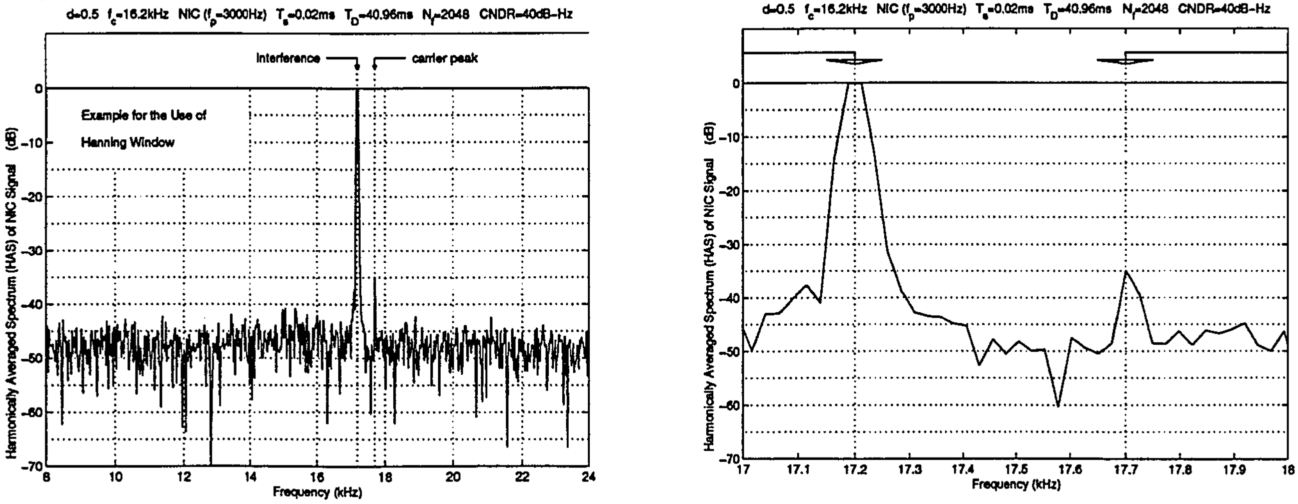

(e) HAS of an ELT with CW Interference

(h) Detailed HAS in (e)

Figure 4.4: Averaged Spectra Related to the Use of the Hanning Window

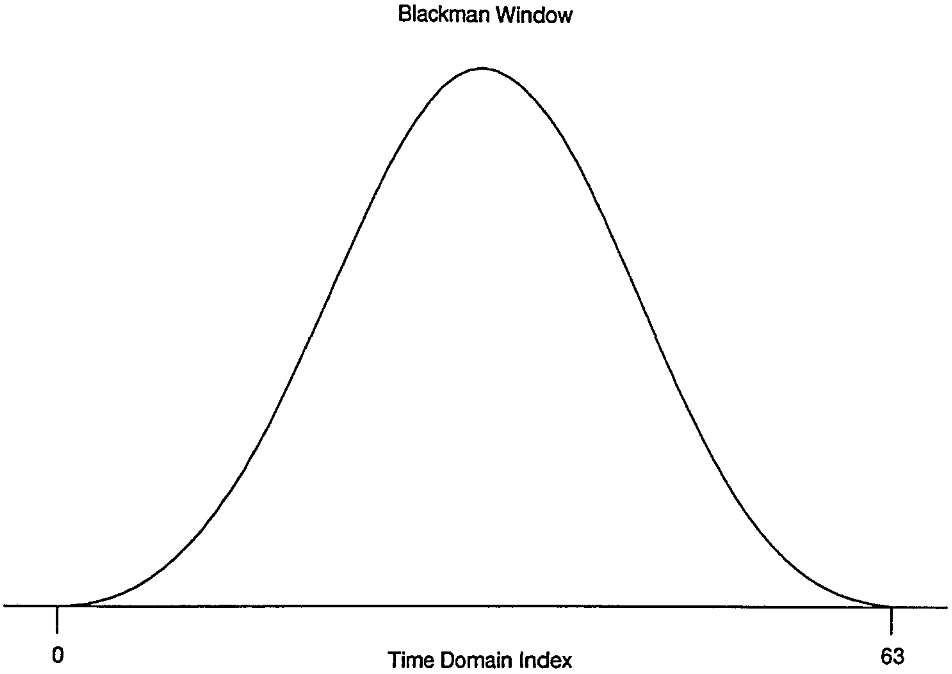

(a) Window of 64 Time Domain Samples

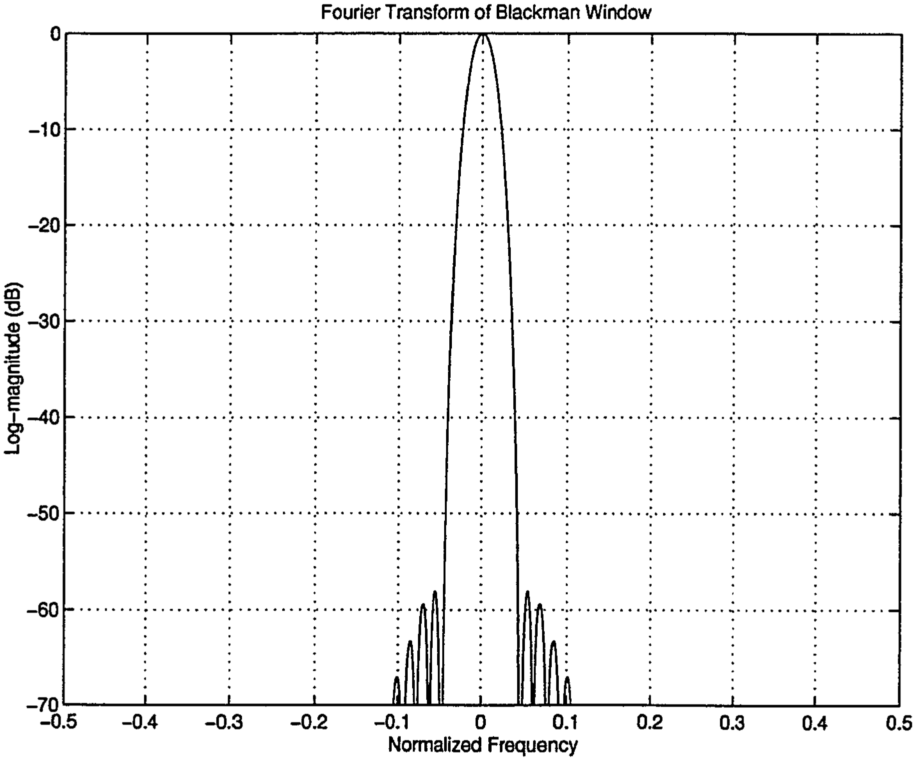

(b) Fourier Transform of the Above Window

Figure 4.5: Averaged Spectra Related to the Use of the Blackman Window

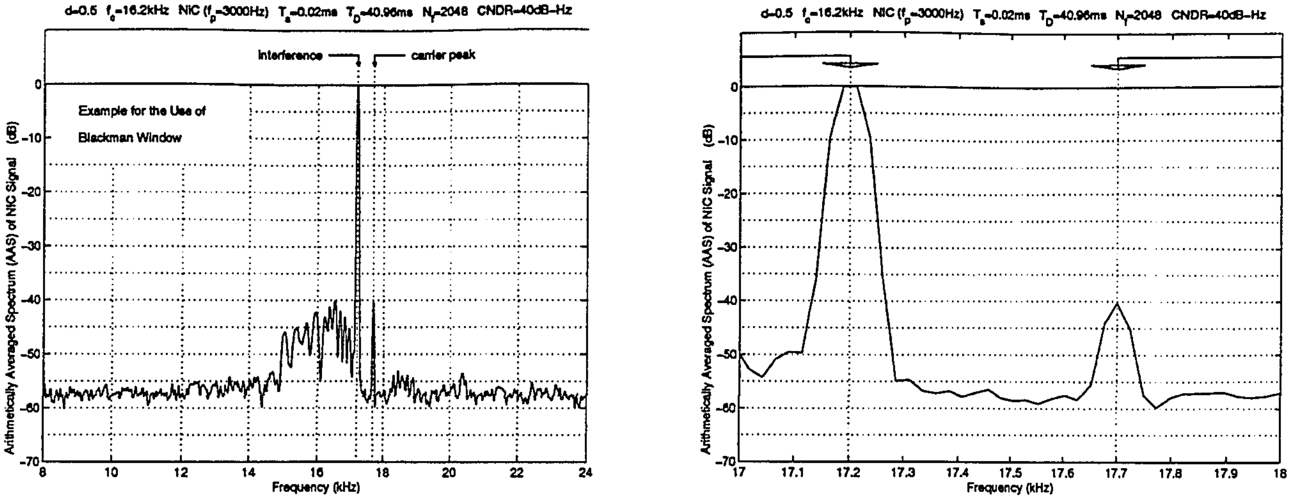

(c) AAS of an ELT with CW Interference

(f) Detailed AAS in (c)

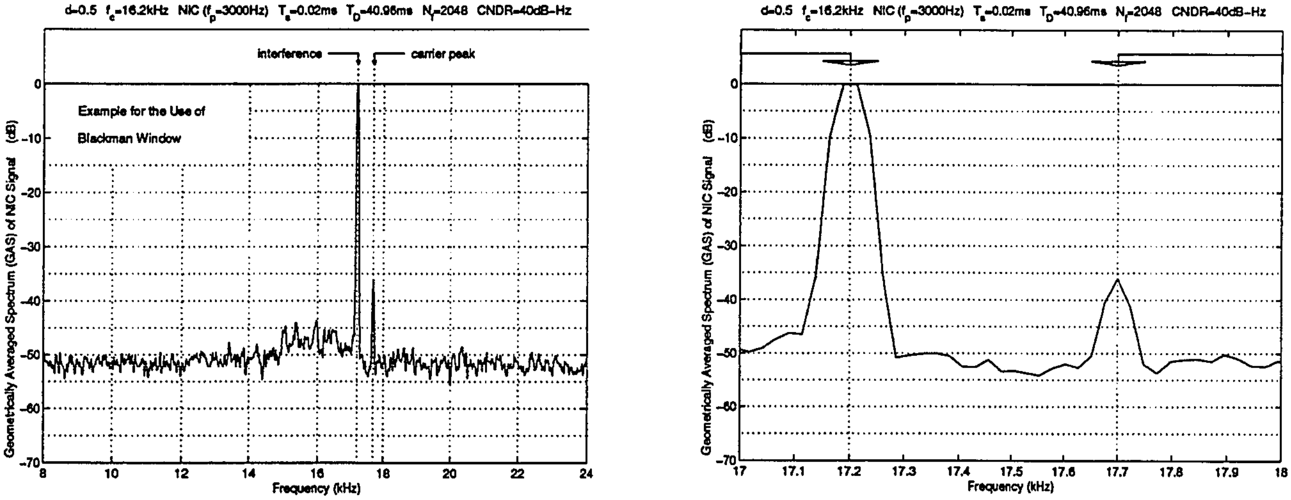

(d) GAS of an ELT with CW Interference

(g) Detailed GAS in (d)

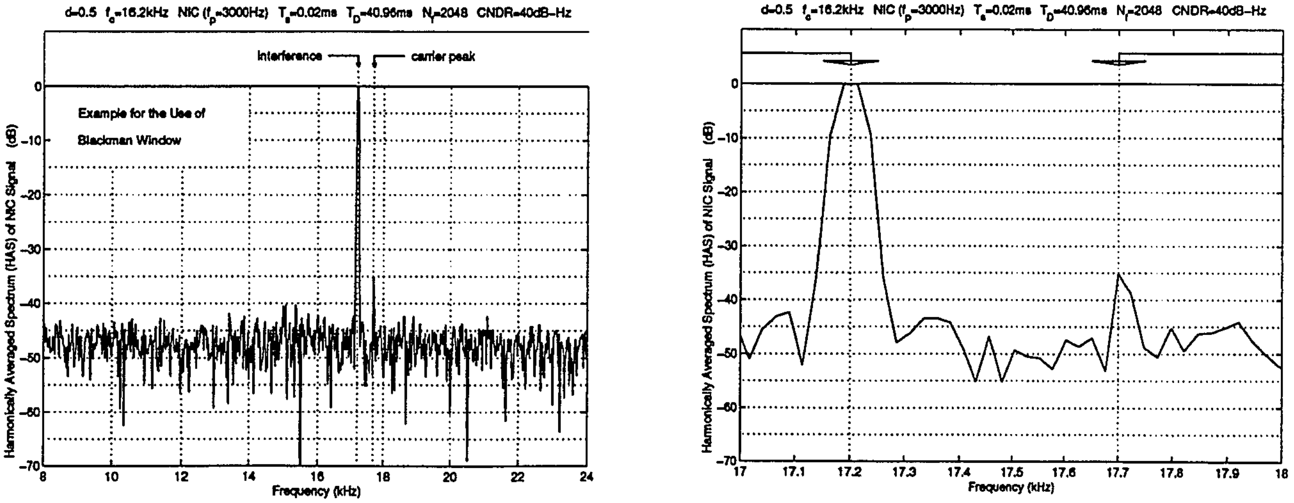

(e) HAS of an ELT with CW Interference

(h) Detailed HAS in (e)

Figure 4.5: Averaged Spectra Related to the Use of the Blackman Window

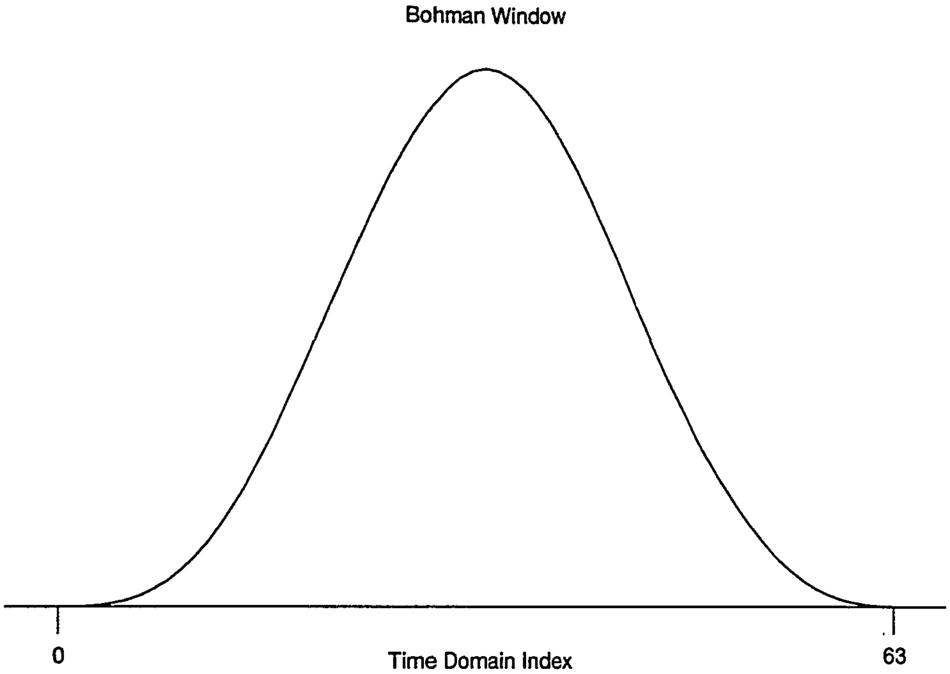

(a) Window of 64 Time Domain Samples

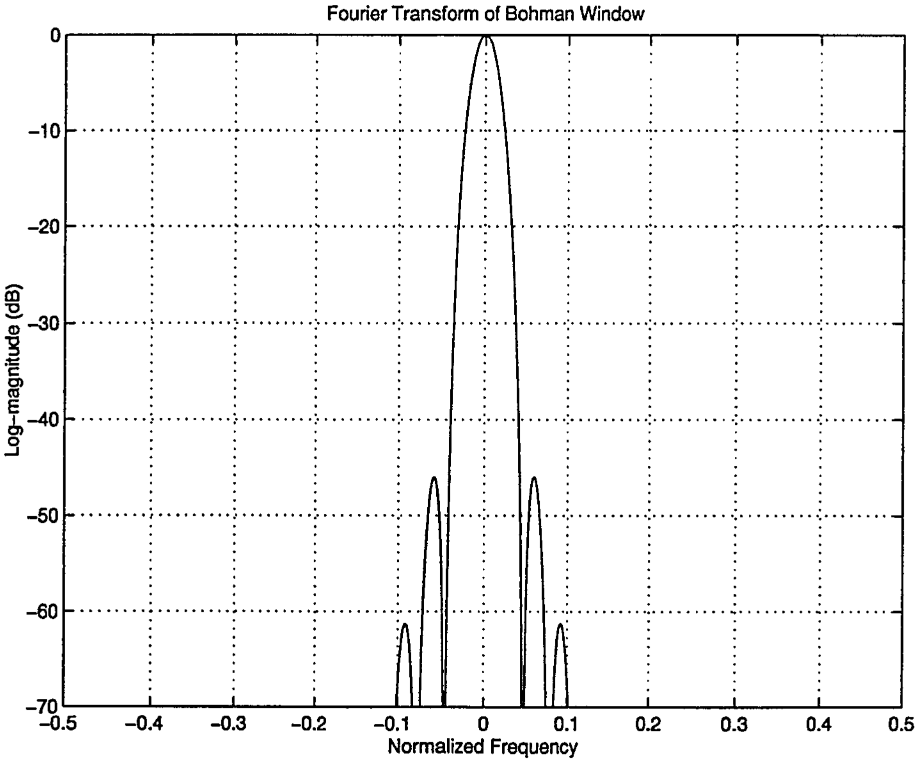

(b) Fourier Transform of the Above Window

Figure 4.6: Averaged Spectra Related to the Use of the Bohman Window

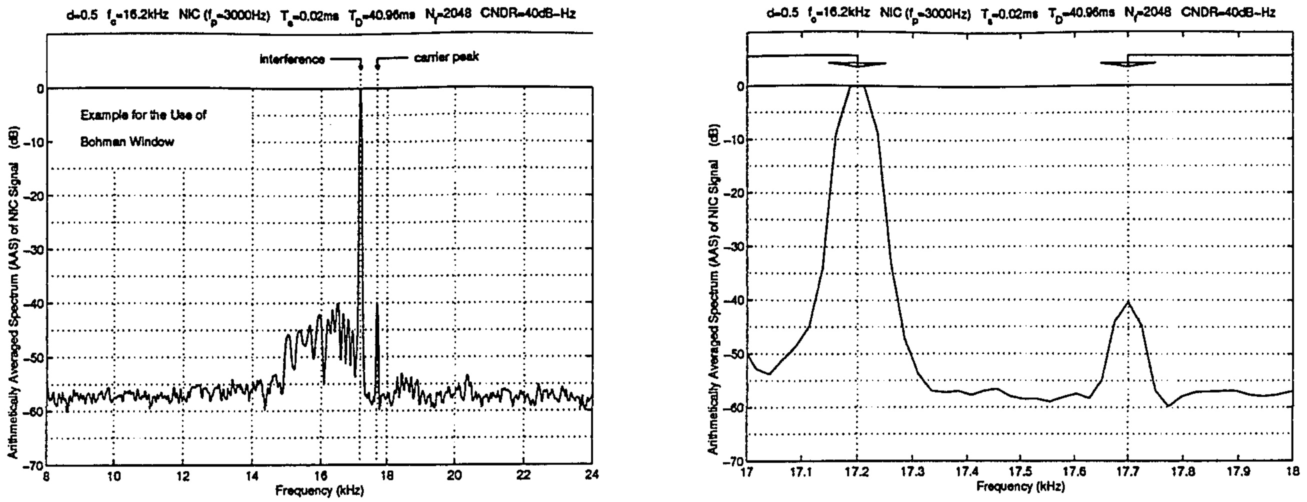

(c) AAS of an ELT with CW Interference

(f) Detailed AAS in (c)

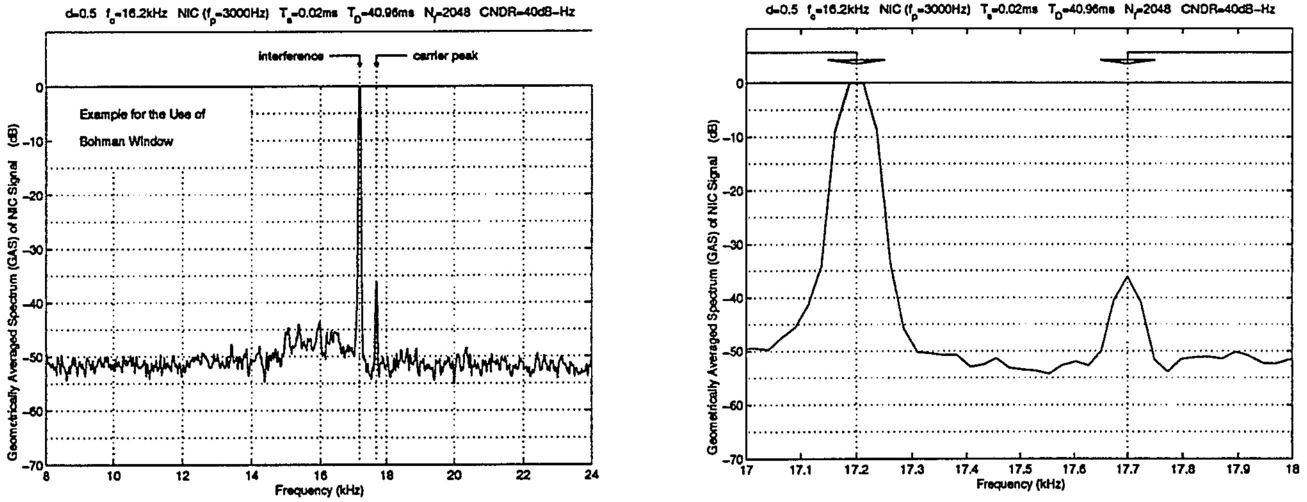

(d) GAS of an ELT with CW Interference

(g) Detailed GAS in (d)

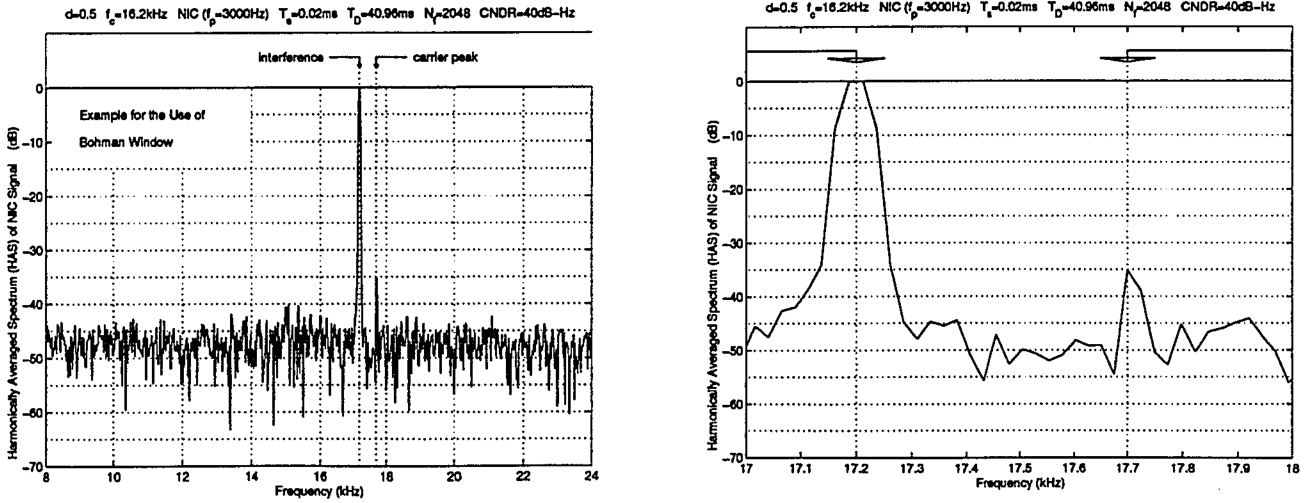

(e) HAS of an ELT with CW Interference

(h) Detailed HAS in (e)

Figure 4.6: Averaged Spectra Related to the Use of the Bohman Window

4.3 AM Carrier Interference Suppression

An amplitude-modulated (AM) interference carrier wave may be described as a function of time t in the form [23]

$$i_{\mathrm{AM}}(t) = A_i[1 + k_a m(t)] \cos(2\pi f_i t) \tag{4.3.1}$$

where A_i is the interference carrier amplitude, f_i is the interference carrier frequency, k_a is a constant called the *amplitude sensitivity* of the modulation, and $m(t)$ is the modulating signal. For convenience, we have assumed that the initial phase of the interference carrier wave is zero.

4.3.1 Single Carrier with Strong AM

If the value of k_a in (4.3.1) is large enough, then we will have a single carrier interference with strong AM. In our computer simulations, we have used a simple modulating signal such that

$$m(t) = \sin(2\pi f_m t) \tag{4.3.2}$$

where f_m has a value of 6 Hz. We have shown an NIC signal with this kind of interference in Fig. 4.7.

Specifically, we show an NIC signal plus noise in Fig. 4.7(a). Note that, the time range in Fig. 4.7(a) is 5 ms. We have also shown a single carrier (whose frequency is 17.1 kHz) with strong AM ($k_a = 0.98$ in this example) in Fig. 4.7(b). Note that, the time range in Fig. 4.7(b) is about 1 s and almost 6 complete cycles in the envelope of the carrier waveform can be recognized.

We add the waveforms of Figs. 4.7(a) and (b) together to form the received time domain signal. Then, we use this combined signal (to which the Blackman windows had been applied) to calculate 24 consecutive periodograms which have been shown in Fig. 4.7(c). Due to the strong AM, not all of the 24 periodograms have the same spectral height at frequency of 17.1 kHz in Fig. 4.7(c). Actually, periodograms 4, 8, 12, 16, 20, and 24 (which correspond to the 6 valley parts in the envelope of the carrier waveform shown in Fig. 4.7(b)) provide a spectral height which is a little lower than the spectral height offered by the other periodograms at a frequency of 17.1 kHz. There is also a variation in the 24 spectral heights located at a frequency of 17.2 kHz which is the position of the carrier peak of the NIC signal used in this example. Since this variation is not large enough, it is hard for us to recognize it in Fig. 4.7(c).

Then, we use the 24 periodograms shown in Fig. 4.7(c) to calculate the AAS in Fig. 4.7(d), the GAS in Fig. 4.7(e), and the HAS in Fig. 4.7(f) respectively. For the AAS of Fig. 4.7(d), the interference peak is 8 dB higher than the NIC ELT signal carrier peak while for the GAS of Fig. 4.7(e), the interference peak is 4 dB higher than the NIC ELT signal carrier peak and for the HAS of Fig. 4.7(f), the interference peak is 3 dB lower than the NIC ELT signal carrier peak. Clearly, GAS and HAS provide some margin of interference suppression in this case.

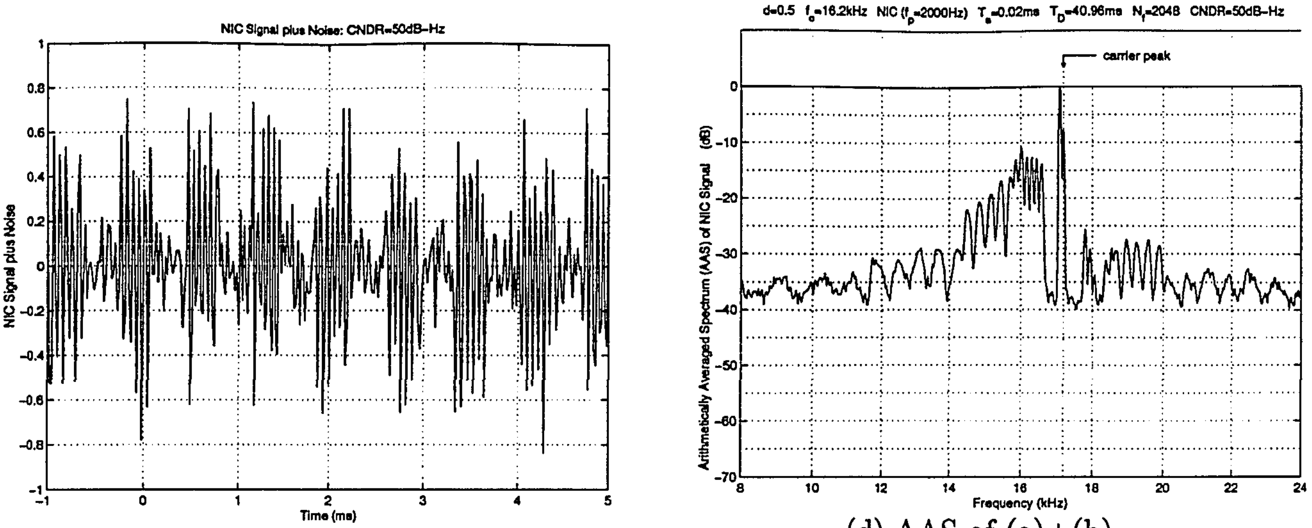

(a) NIC Signal plus Noise (d) AAS of (a)+(b)

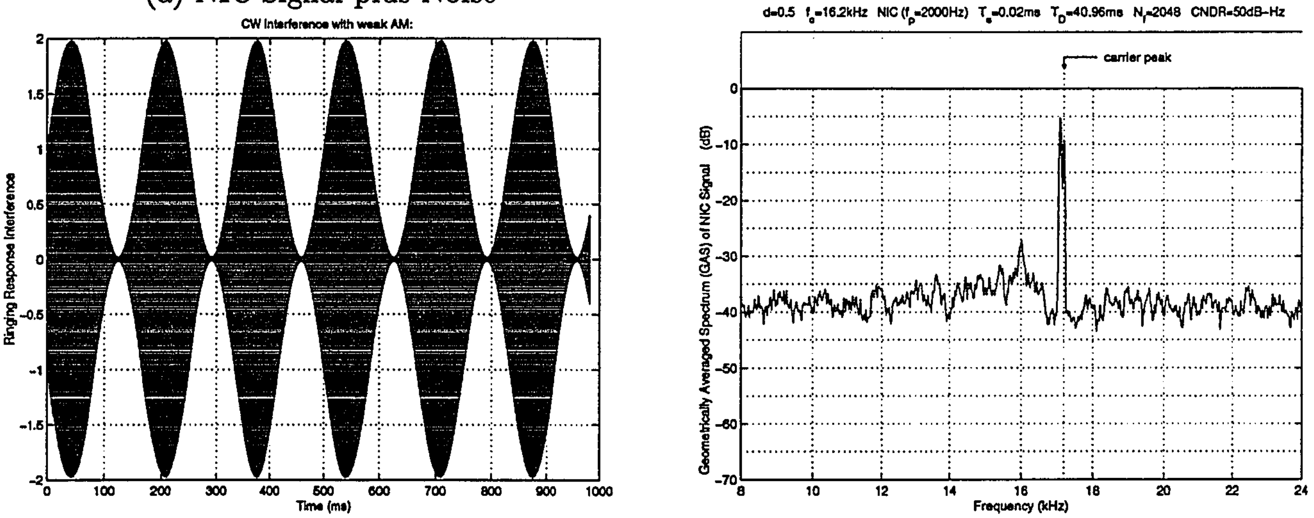

(b) Single Carrier with Strong AM (e) GAS of (a)+(b)

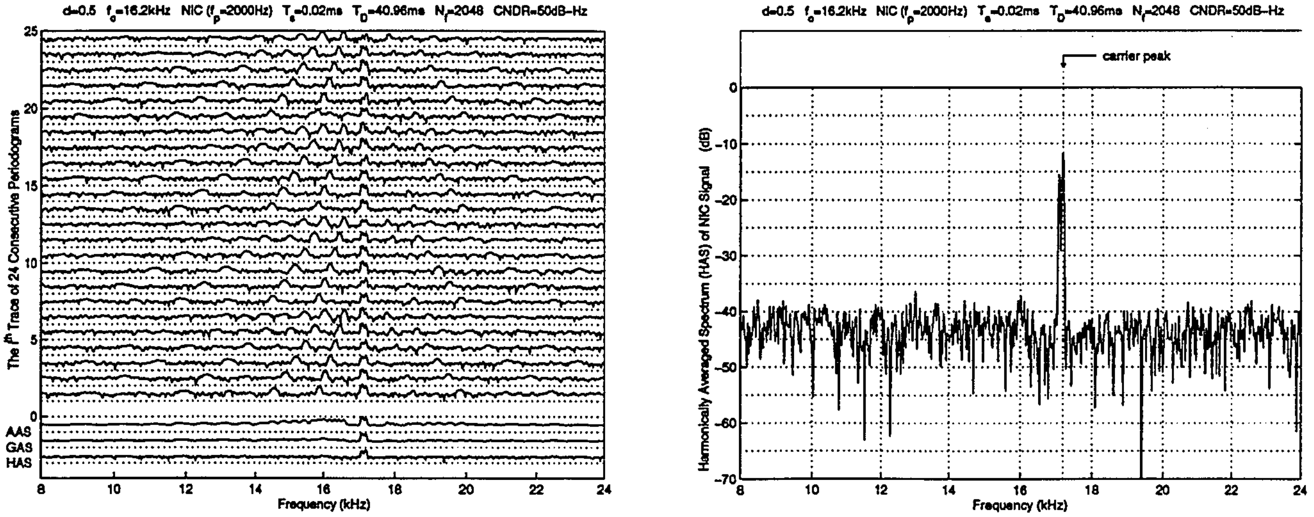

(c) Periodograms of (a)+(b) (f) HAS of (a)+(b)

Figure 4.7: Single Carrier with Strong AM

4.3.2 Single Carrier with Weak AM

If the value of k_a in (4.3.1) is small enough, then we will have a single carrier interference with weak AM. In our computer simulations, we have used a simple modulating signal such that

$$m(t) = \sin(2\pi f_m t) \tag{4.3.3}$$

where f_m has a value of 6 Hz. We have shown an NIC signal with this kind of interference in Fig. 4.8.

Specifically, we show an NIC signal plus noise in Fig. 4.8(a). Note that, the time range in Fig. 4.8(a) is 5 ms. We have also shown a single carrier (whose frequency is 17.1 kHz) with weak AM ($k_a = 0.02$ in this example) in Fig. 4.8(b). Note that, the time range in Fig. 4.8(b) is about 1 s and almost 6 complete cycles in the envelope of the carrier waveform can be recognized.

We add the waveforms of Figs. 4.8(a) and (b) together to form the received time domain signal. Then, we use this combined signal (to which the Blackman windows had been applied) to calculate 24 consecutive periodograms which have been shown in Fig. 4.8(c). Regardless of the weak AM, all of the 24 periodograms have the same spectral height at a frequency of 17.1 kHz in Fig. 4.8(c). Actually, even in periodograms 4, 8, 12, 16, 20, and 24 (which correspond to the 6 valley parts in the envelope of the carrier waveform shown in Fig. 4.8(b)), we have a spectral height which is almost equal to the spectral height offered by the other periodograms at a frequency of 17.1 kHz. There is a variation in the 24 spectral heights located at a frequency of 17.2 kHz which is the position of the carrier peak of the NIC signal used in this example. Since this variation is not large, it is difficult to recognize in Fig.

4.8(c).

With the 24 periodograms shown in Fig. 4.8(c), calculate the AAS in Fig. 4.8(d), the GAS in Fig. 4.8(e), and the HAS in Fig. 4.8(f). For the AAS of Fig. 4.8(d), the interference peak is 8 dB higher than the NIC ELT signal carrier peak while for the GAS of Fig. 4.8(e), the interference peak is 9 dB higher than the NIC ELT signal carrier peak and for the HAS of Fig. 4.8(f), the interference peak is 12 dB higher than the NIC ELT signal carrier peak. Clearly, GAS and HAS lose some margin of interference suppression in this case.

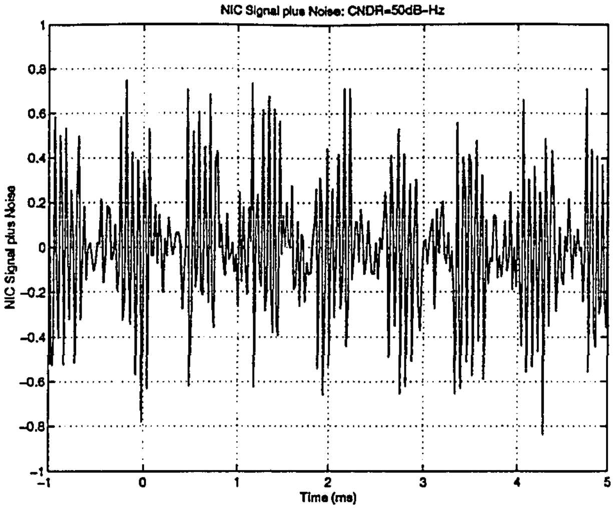

(a) NIC Signal plus Noise

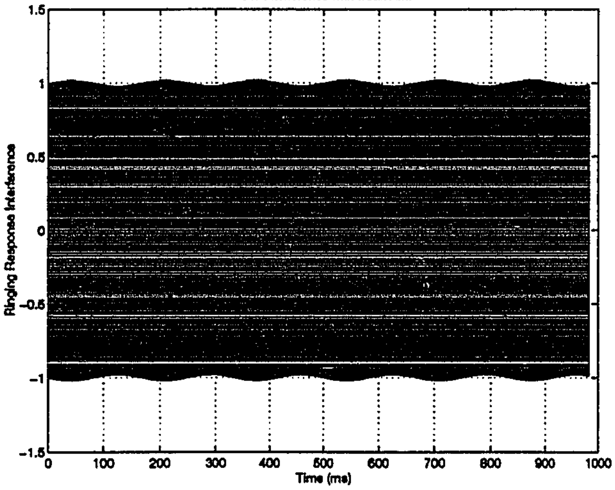

(b) Single Carrier with Weak AM

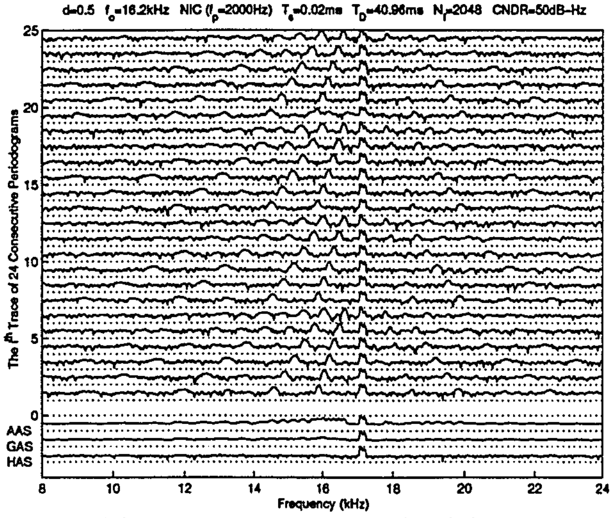

(c) Periodograms of (a)+(b)

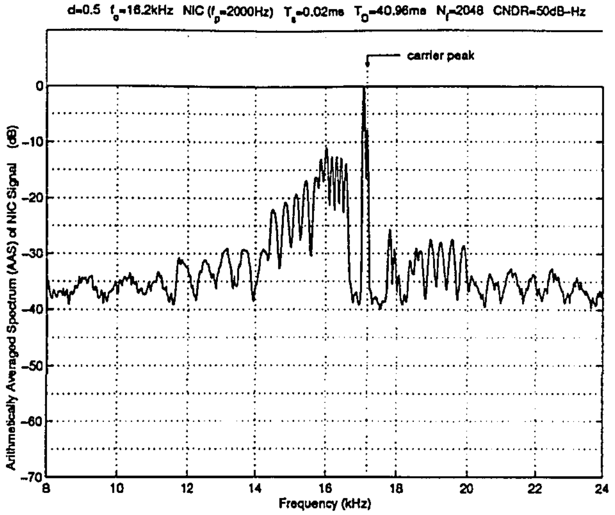

(d) AAS of (a)+(b)

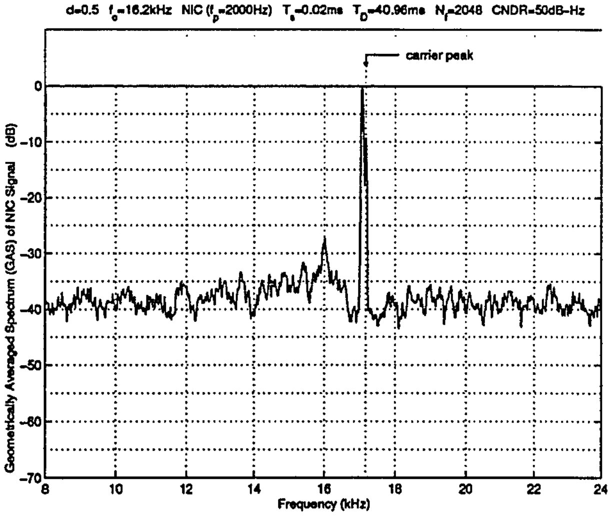

(e) GAS of (a)+(b)

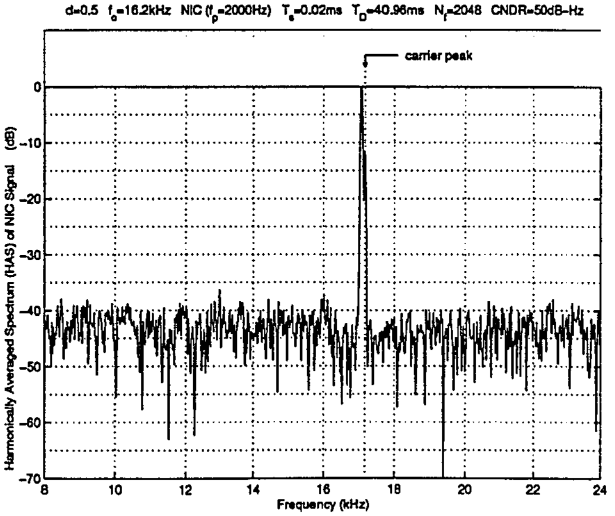

(f) HAS of (a)+(b)

Figure 4.8: Single Carrier with Weak AM

4.4 On-Off Modulation Interference Suppression

On-Off Modulation interference may be described as a carrier which is ON for short durations of less than a few milliseconds. If the carrier is much longer, then it is considered to be CW interference. Mathematically, On-Off Modulation interference can be characterized as a function of time t in the form

$$i_{\text{On-Off}}(t) = A_i \cos(2\pi f_i t) \sum_{n=-\infty}^{\infty} \Theta p(t - nT_p) \tag{4.4.1}$$

where A_i is the interference carrier amplitude, f_i is the interference carrier frequency, Θ is a random variable having only two values, *i.e.*, 1 which corresponds to "On" and 0 which corresponds to "Off", and square wave

$$p(t) = \begin{cases} 1 & 0 \le t < T_p \\ 0 & \text{otherwise} \end{cases} \tag{4.4.2}$$

with T_p being a constant much smaller than $T_D \times K$, where T_D is the length of data used to calculate each periodogram, while K is the number of periodograms used to calculate each averaged spectrum.

A number of computer simulations have been carried out to investigate the abilities of AAS, GAS, and HAS to suppress On-Off Modulation interference. Note that, to increase the difficulty in the suppression of On-Off Modulation interference, assume 0.75 as the probability for each interference being ON. Correspondingly, the probability for each interference being OFF is 0.25. Also note that, all of these On-Off Modulation interference sources have arbitrary amplitudes and phases and are modulated randomly.

In Fig. 4.9(a), we show an ICE signal. In Fig. 4.9(b), it can be seen that a total of

17 On-Off Modulation interferences have been introduced. In Fig. 4.9(c), we show 24 consecutive periodograms of (a) plus (b) multiplied by a scaling parameter which is equal to 2. Note that, the Blackman windows are applied to the time-domain samples before we calculate the periodograms. In Fig. 4.9(d), it can be seen that these 17 interferences are distributed in a fashion of one interference per 1000 Hz within the range from 8 kHz to 24 kHz. In Figs. 4.9(d), (e), and (f), the abilities of AAS, GAS, and HAS to suppress On-Off Modulation Interference is demonstrated.

In Fig. 4.10(a), we show an ICE signal. In Fig. 4.10(b), it can be seen that a total of 81 On-Off Modulation interferences have been introduced. In Fig. 4.10(c), we show 24 consecutive periodograms of (a) plus (b) multiplied by a scaling parameter which is equal to 10. Note that, the Blackman windows are applied to the time-domain samples before we calculate the periodograms. In Fig. 4.10(d), it can be seen that these 81 interferences are distributed in a fashion of one interference per 200 Hz within the range from 8 kHz to 24 kHz. In Figs. 4.10(d), (e), and (f), the abilities of AAS, GAS, and HAS to suppress On-Off Modulation Interference is demonstrated.

With these examples, it is clear that both GAS and HAS completely suppress On-Off Modulation interference while AAS completely fails.

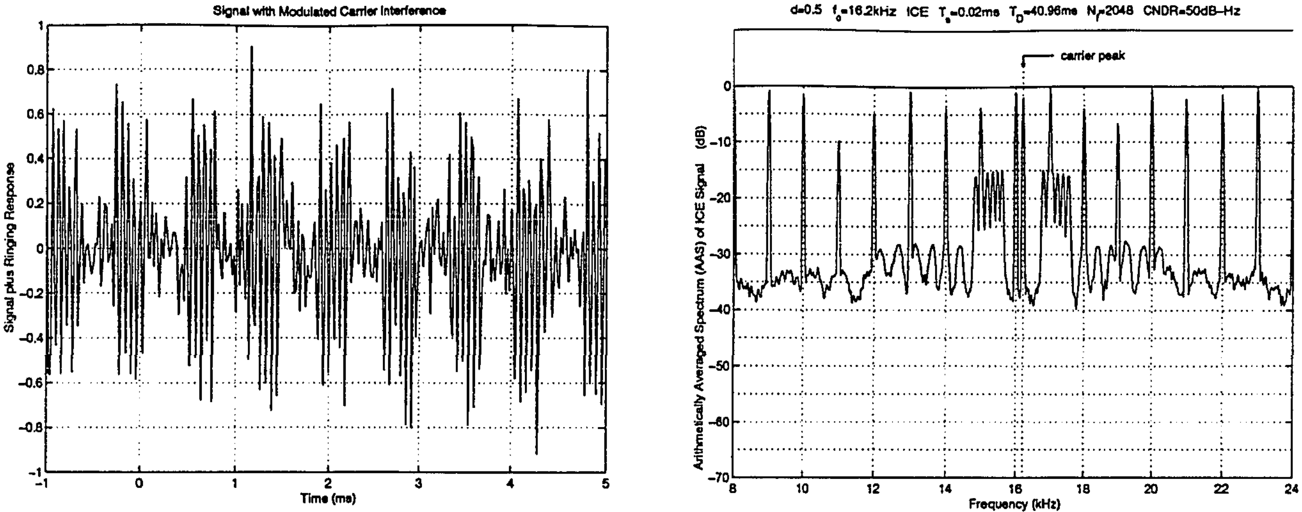

(a) ELT Signal plus Noise

(d) AAS of (a)+(b)×2

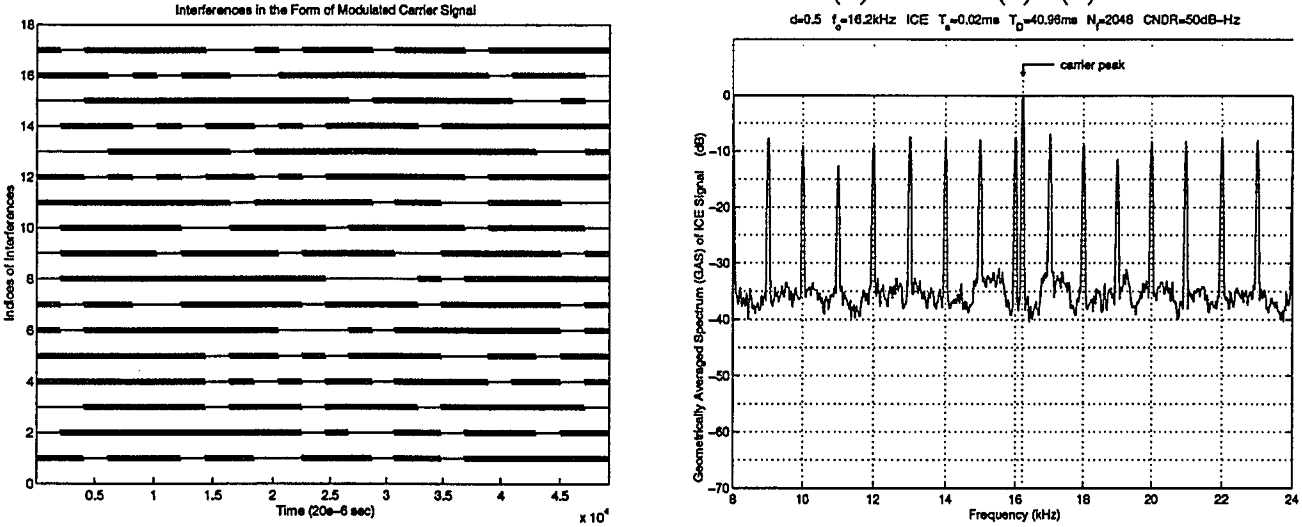

(b) On-Off Modulation Interference

(e) GAS of (a)+(b)×2

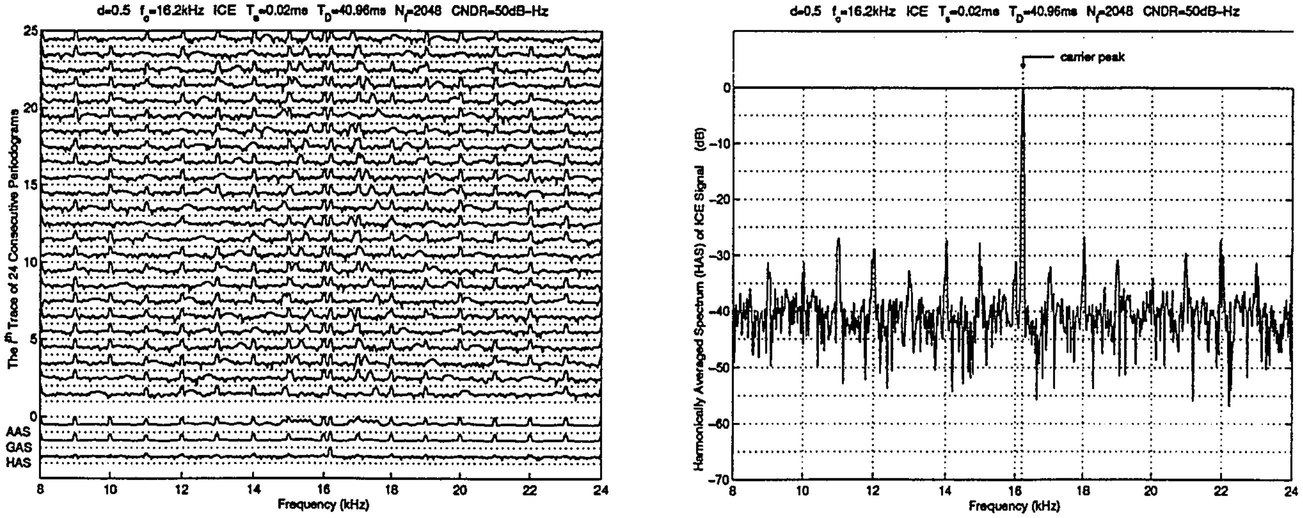

(c) Periodograms of (a)+(b)×2

(f) HAS of (a)+(b)×2

Figure 4.9: On-Off Modulation Interference Suppression: 17 Interference Sources

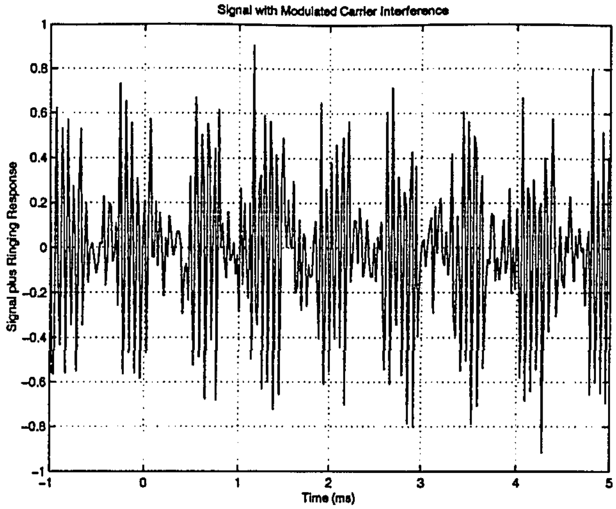

(a) ELT Signal plus Noise

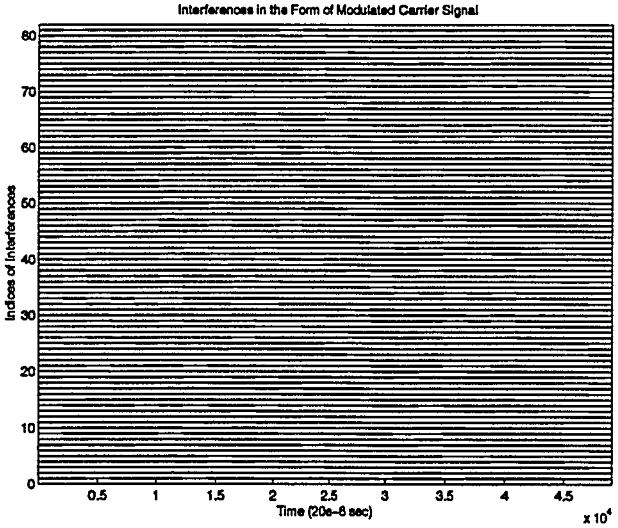

(b) On-Off Modulation Interference

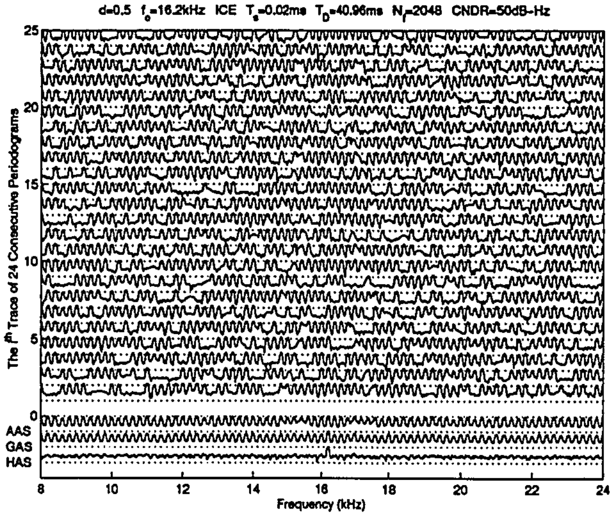

(c) Periodograms of (a)+(b)×10

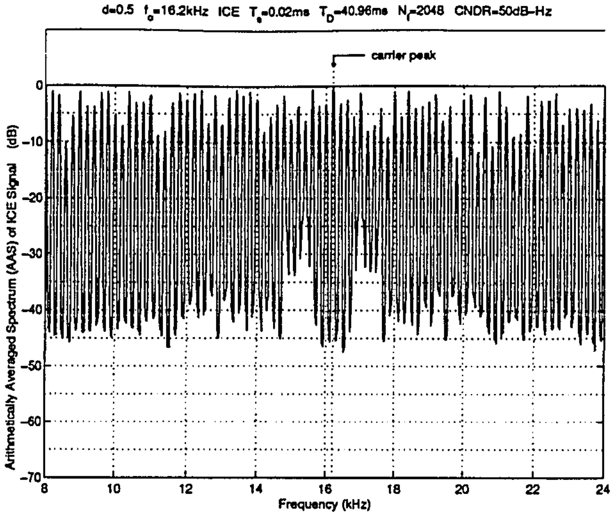

(d) AAS of (a)+(b)×10

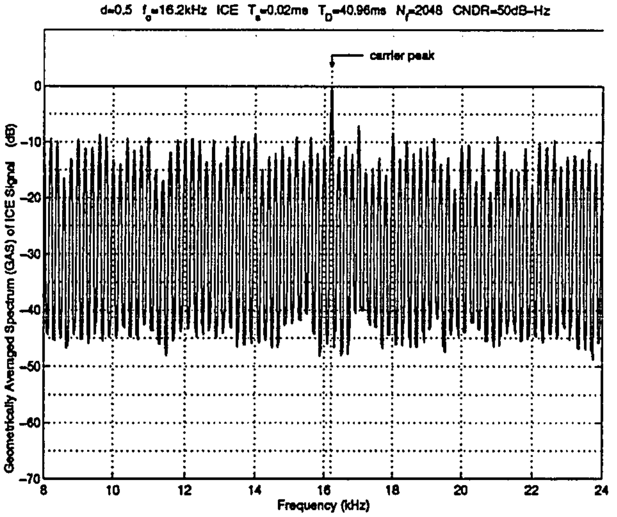

(e) GAS of (a)+(b)×10

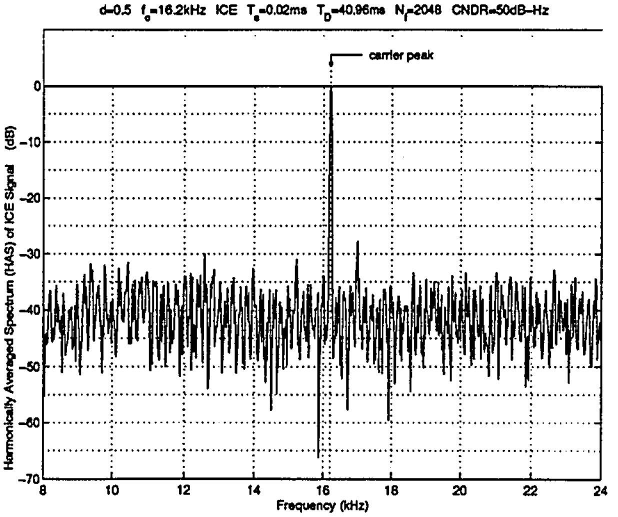

(f) HAS of (a)+(b)×10

Figure 4.10: On-Off Modulation Interference Suppression: 81 Interference Sources

4.5 Swept Carrier Interference Suppression

Swept Carrier interference can be generated by sweeping a carrier from outside the passband of the receiver through the passband and back outside the passband. This type of interference causes two difficulties. First, there is the interference generated while in the passband. Second, there is the interference produced in sweeping from in-band to out-of-band or vice versa. If the sweep rate is sufficiently high, the receiver "ringing response" is excited and the receiver is jammed [14]. If the sweep rate is low, then the interference appears in each window which is the case depicted here.

A Swept Carrier interference may be described as a function of time t in the form

$$i_{SC}(t) = A_i \cos(2\pi f_i(t)t) \tag{4.5.1}$$

where A_i is the interference carrier amplitude, and the interference carrier frequency

$$f_i(t) = f_{\text{low}} + \frac{f_{\text{high}} - f_{\text{low}}}{t_{\text{high}} - t_{\text{low}}} \cdot (t - t_{\text{low}}) \tag{4.5.2}$$

That is, at time t_{low} the interference carrier frequency $f_i(t)$ has a value equal to f_{low} while at time t_{high} the interference carrier frequency $f_i(t)$ has a value equal to f_{high}. For convenience, we have assumed that the phase of the interference carrier wave is zero in (4.5.1).

A number of computer simulations have been carried out to investigate the abilities of AAS, GAS, and HAS to suppress Swept Carrier interference. The five cases shown in Figs. 4.11 to 4.15 are arbitrarily chosen. Note that, the Blackman windows are applied to the time-domain samples before we calculate the periodograms.

In Case 1 shown in Fig. 4.11, we have added one Swept Carrier interference to a desired ICE signal. In this case, the Swept Carrier interference is arranged to sweep the whole frequency range just once from low frequency to high frequency during the data length for 24 consecutive periodograms needed for calculate AAS, GAS, or HAS.

In Case 2 shown in Fig. 4.12, we have added two Swept Carrier interferences to the desired ICE signal. In this case, the Swept Carrier interferences are arranged to sweep the whole frequency range shown. More specifically, one interference is arranged to sweep from low frequency to high frequency while the other from high frequency to low frequency.

In Case 3 shown in Fig. 4.13, we have added one Swept Carrier interference to the desired ICE signal. The Swept Carrier interference is arranged to sweep the whole frequency range shown twice during the data length for 24 consecutive periodograms.

In Case 4 shown in Fig. 4.14, we have added one Swept Carrier interference to a desired ICE signal. The Swept Carrier interference is arranged to sweep the whole frequency range shown four times during the data length for 24 consecutive periodograms.

In Case 5 shown in Fig. 4.15, we have added one Swept Carrier interference to the desired ICE signal. The Swept Carrier interference is arranged to sweep the whole frequency range shown eight times during the data length for 24 consecutive periodograms.

With these cases, it is clear that both GAS and HAS completely suppress Swept Carrier interference while AAS completely fails.

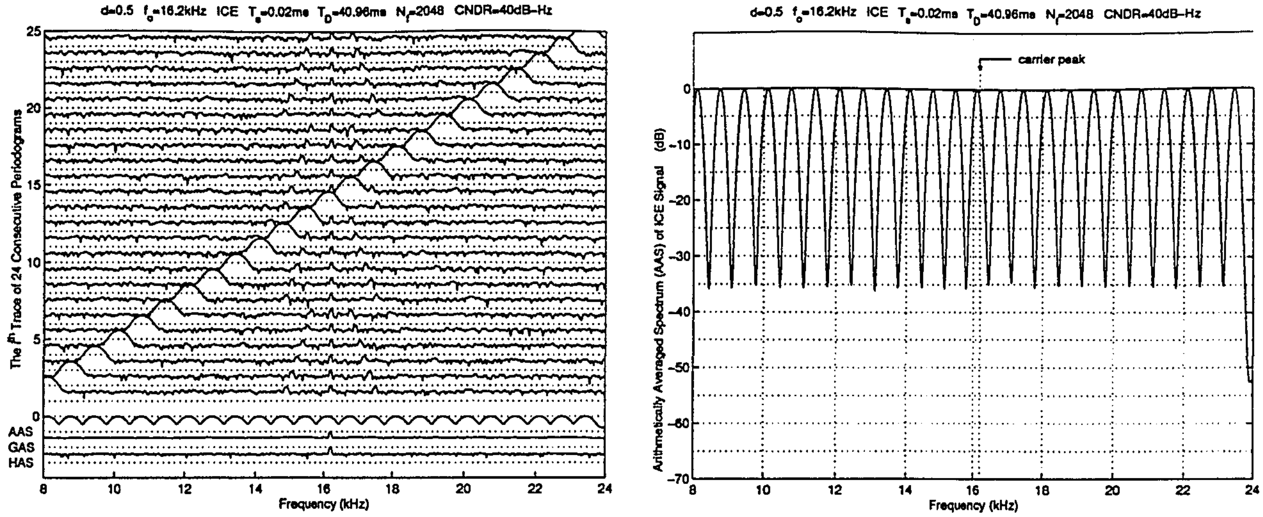

(a) Periodograms

(b) AAS

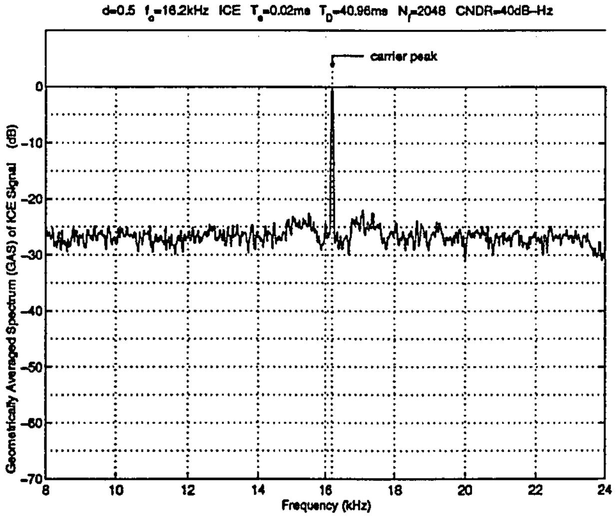

(c) GAS

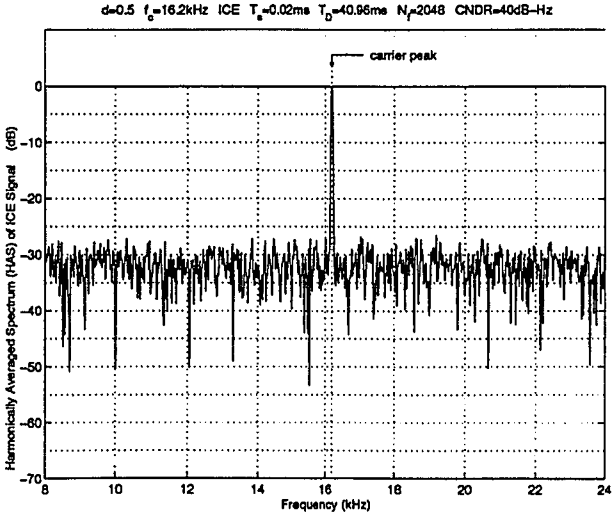

(d) HAS

Figure 4.11: Swept Carrier Interference Suppression — Case 1

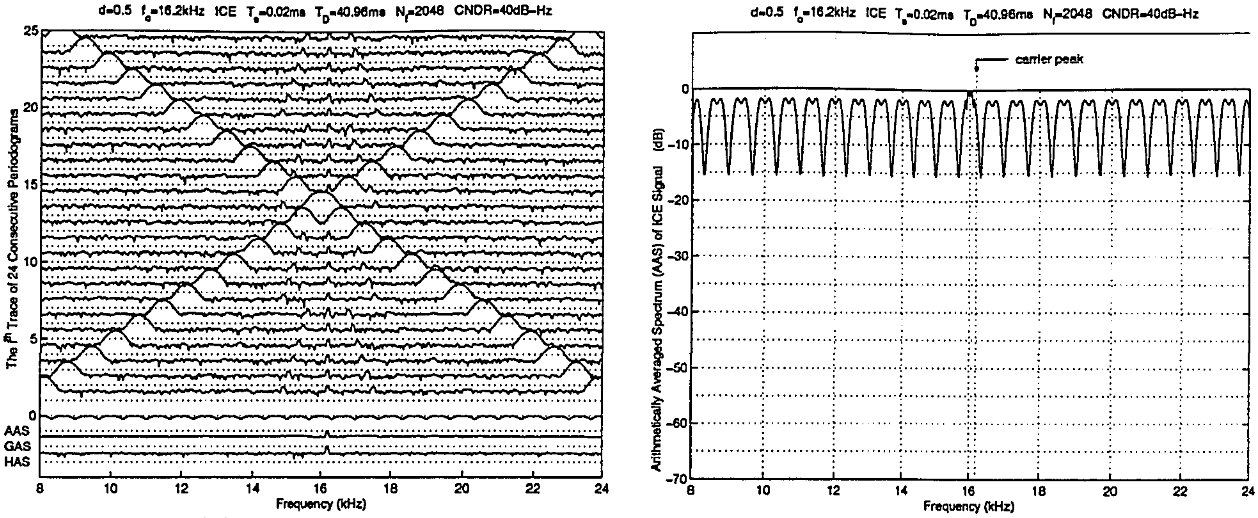

(a) Periodograms

(b) AAS

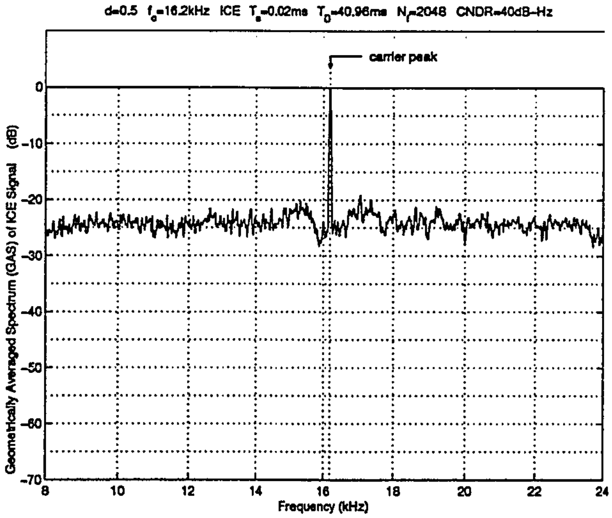

(c) GAS

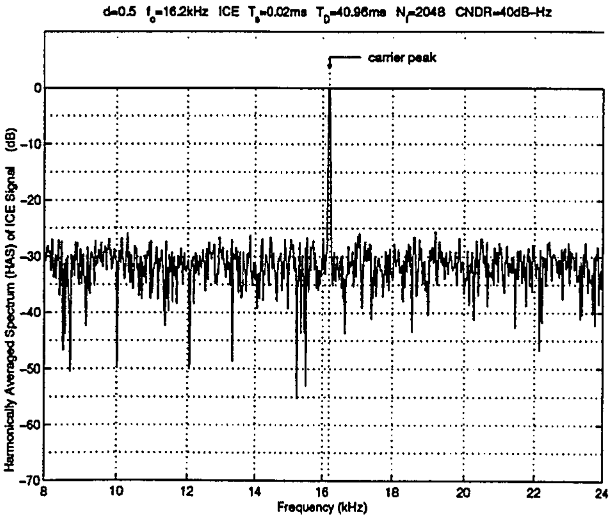

(d) HAS

Figure 4.12: Swept Carrier Interference Suppression — Case 2

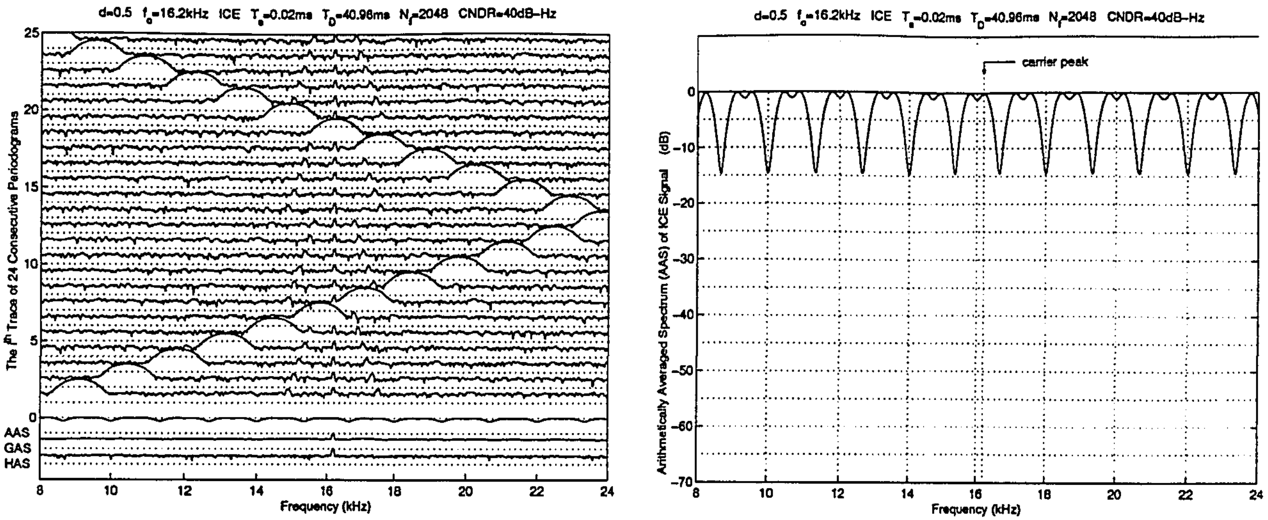

(a) Periodograms

(b) AAS

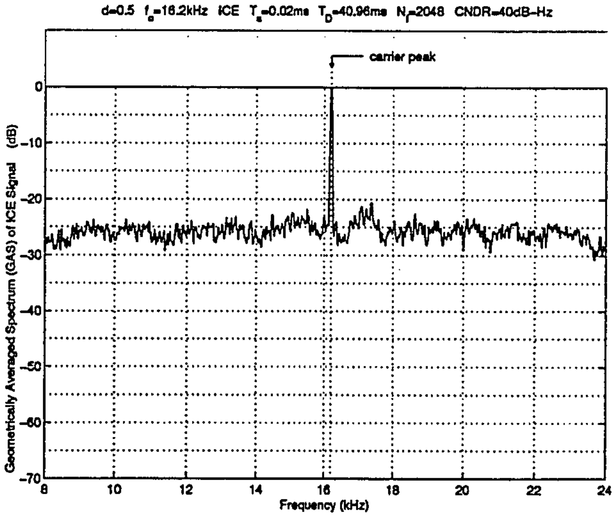

(c) GAS

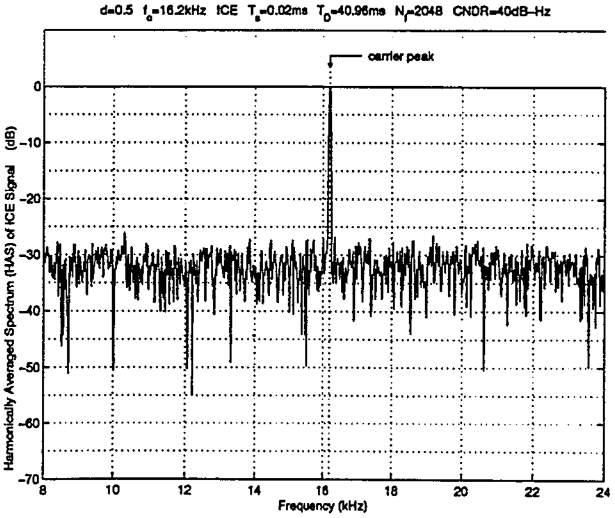

(d) HAS

Figure 4.13: Swept Carrier Interference Suppression — Case 3

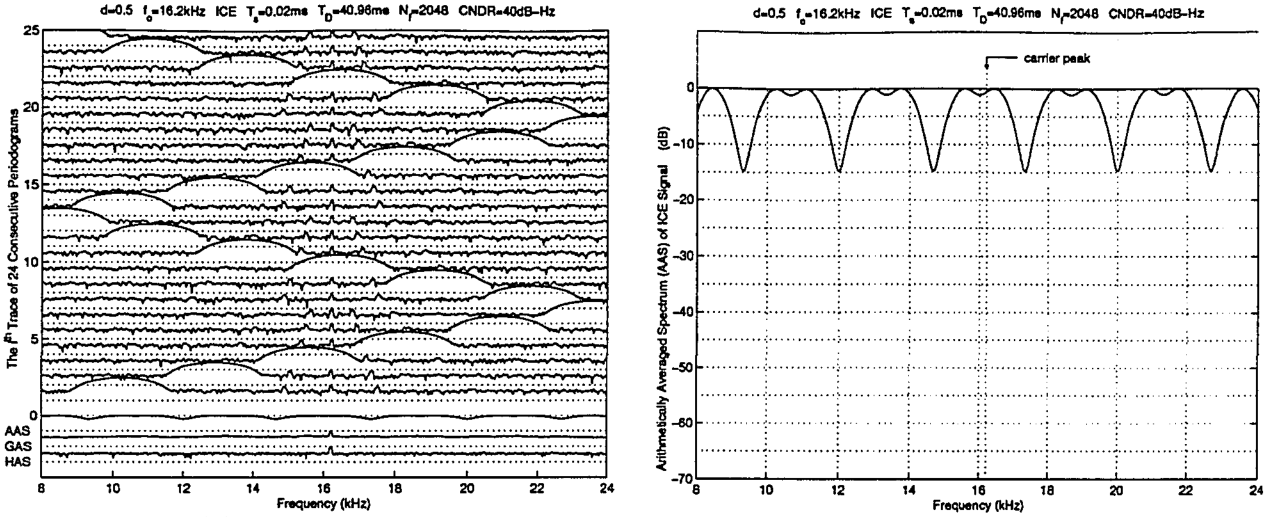

(a) Periodograms (b) AAS

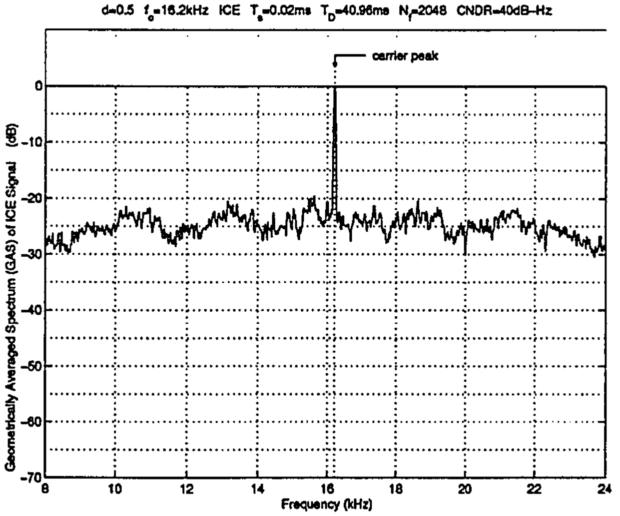

(c) GAS

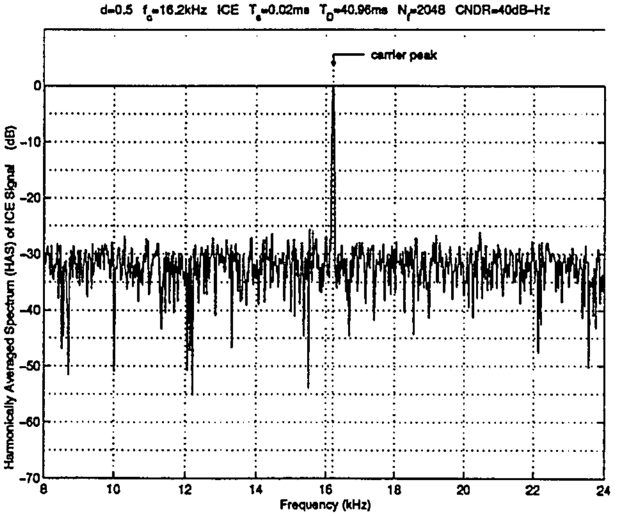

(d) HAS

Figure 4.14: Swept Carrier Interference Suppression — Case 4

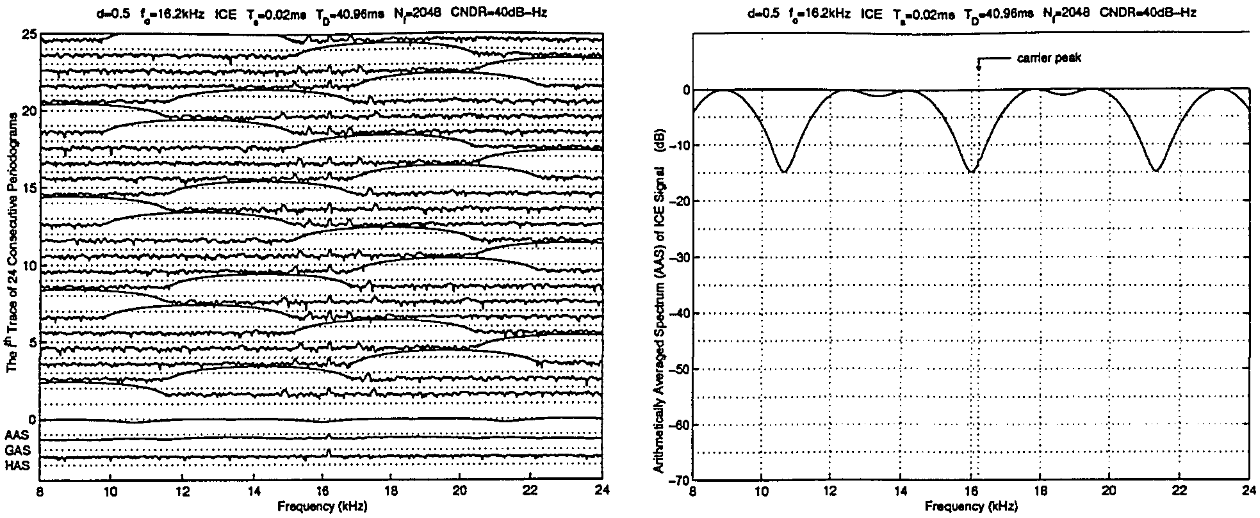

(a) Periodograms (b) AAS

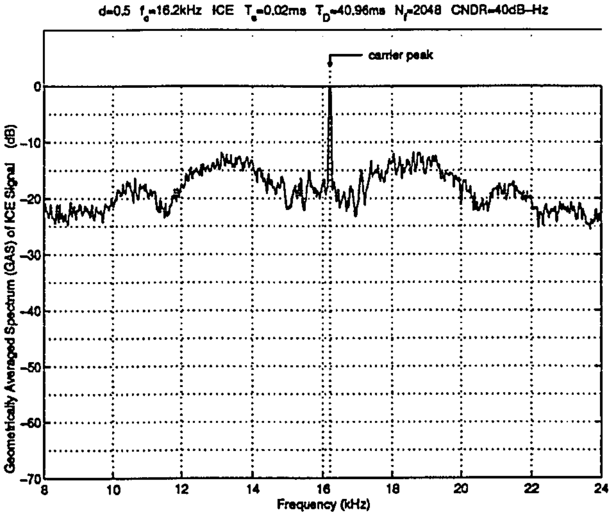

(c) GAS

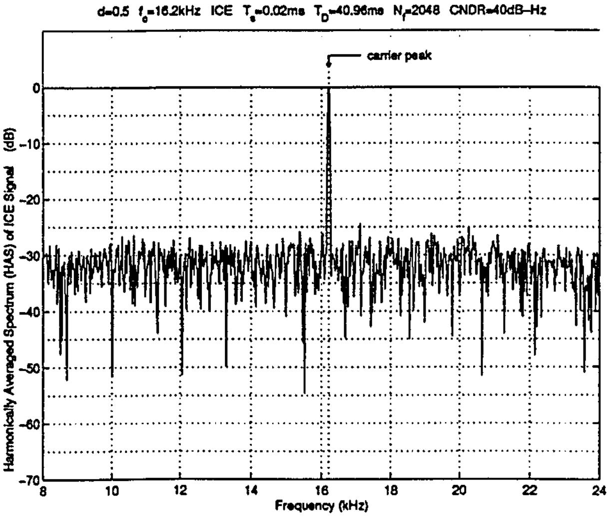

(d) HAS

Figure 4.15: Swept Carrier Interference Suppression — Case 5

4.6 Ringing Response Interference Suppression

This type of interference is due to short duration pulses where the pulse duration is small compared to the reciprocal of the bandwidth of the receiver. In this case, the pulse may be either video or modulated carrier. For modulated carrier pulses, the signal can be simplistically represented by [25]

$$r(t) = A\exp[-at]\sin[2\pi f_R t] \tag{4.6.1}$$

where A is the amplitude, a is the damping constant which is a function of the bandwidth and the phase linearity of the receiver, f_R is the center frequency of the receiver passband (for narrowband system), and t is the time [14].

Normally, this type of interference fills a relatively large part of the bandwidth of the receiver and thus appears to be "wideband interference." Since a usually results from a complicated combination of the overall bandwidth and phase characteristics of the system, its value is seldom known. However, it can be expected to lie in the range

$$B/20 < a < B/5 \tag{4.6.2}$$

where B is the 3 dB bandwidth of the receiver [14]. Note that, in our computer simulations, being curious what will happen if we go further, we have investigated cases of not only $a = B/20$ and $a = B/5$ but also $a = B/1$.

A number of computer simulations have been carried out to investigate the abilities of AAS, GAS, and HAS to suppress Ringing Response interference. In fact, to increase the difficulty in the suppression of this kind of interference, we have used 6 consecutive ringing responses within the whole data record length T_D as Ringing Response interference in our computer simulations. Note that, the Blackman windows are applied to the time-domain samples before we calculate the periodograms.

In Figs. 4.16 to 4.20, we add a Ringing Response interference to an ICE signal where CNDR is equal to 60 dB. In these figures, values of f_R include: 10000 Hz; 16200 Hz; and, 22000 Hz. In Figs. 4.16 to 4.18, the parameter a is equal to $B/20$ while the Ringing Response interference strength in terms of amplitude is 10000 times the ICE signal. In Fig. 4.19, the parameter a is equal to $B/5$ while the Ringing Response interference strength in terms of amplitude is 50000 times the ICE signal. In Fig. 4.20, the parameter a is equal to $B/1$ while the Ringing Response interference strength in terms of amplitude is 4,500,000 times the ICE signal.

In Figs. 4.21 to 4.25, we add Ringing Response interference to an NIC signal where CNDR is equal to 40 dB. In these figures, values of f_R include: 11500 Hz; 17700 Hz; and, 23500 Hz. In Figs. 4.21 to 4.23, the parameter a is equal to $B/20$ while the Ringing Response interference strength in terms of amplitude is 1,000,000 times the NIC signal. In Fig. 4.24, the parameter a is equal to $B/5$ while the Ringing Response interference strength in terms of amplitude is 5,000,000 times the NIC signal. In Fig. 4.25, the parameter a is equal to $B/1$ while the Ringing Response interference strength in terms of amplitude is 50,000,000 times the NIC signal.

What is special in Figs. 4.17, 4.19, 4.20, 4.22, 4.24, and 4.25 is that the frequency of Ringing Response interference is exactly at the carrier peak of the ELT signal. It can be seen that, even in this kind of crucial situation, HAS and GAS perform successfully while AAS completely fails.

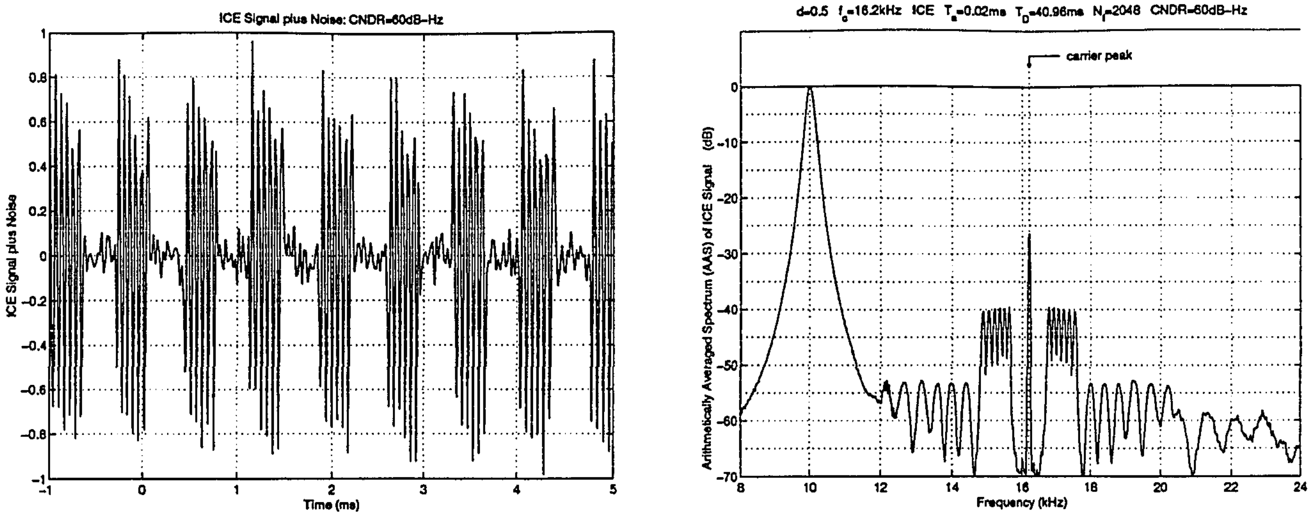

(a) ICE Signal plus Noise

(d) AAS of (a)+(b)×10000

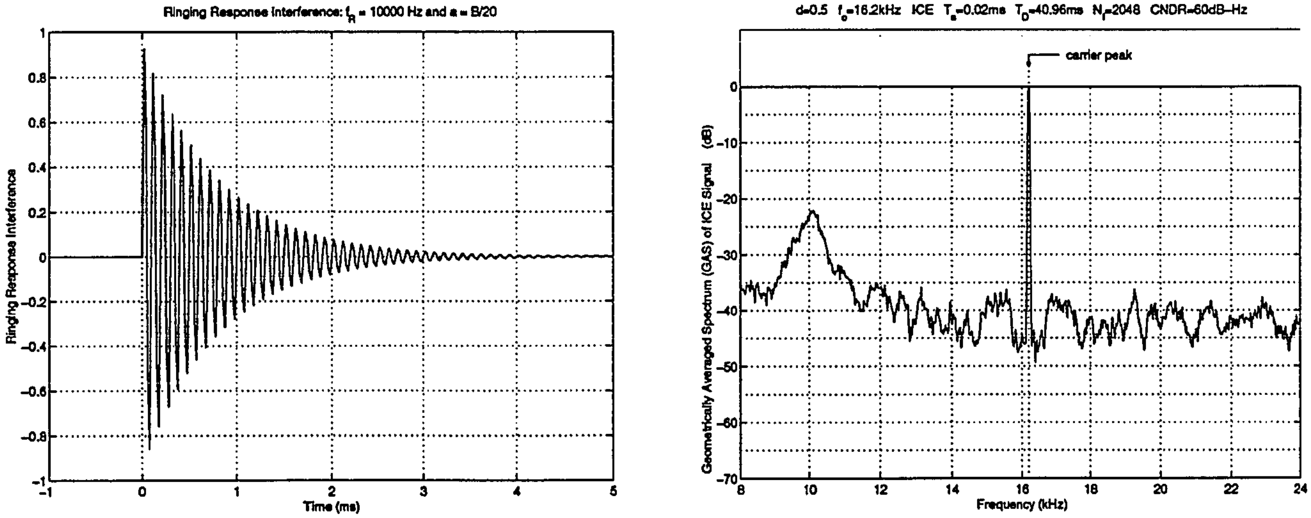

(b) Ringing Response Interference

(e) GAS of (a)+(b)×10000

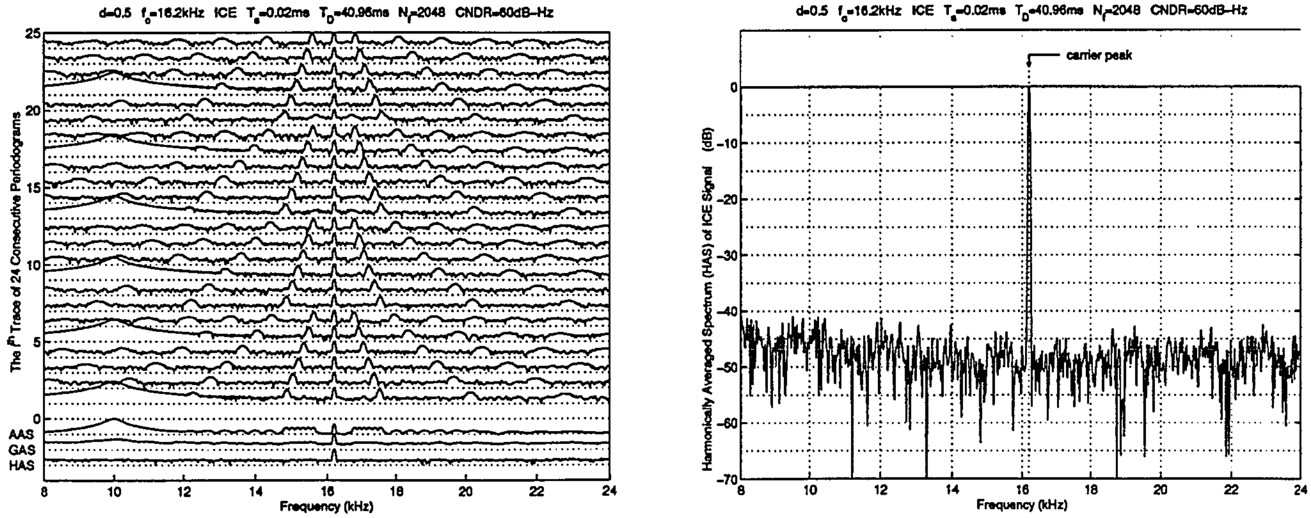

(c) Periodograms of (a)+(b)×10000

(f) HAS of (a)+(b)×10000

Figure 4.16: Ringing Response Interference: $f_R = 10000$ Hz, $a = B/20$

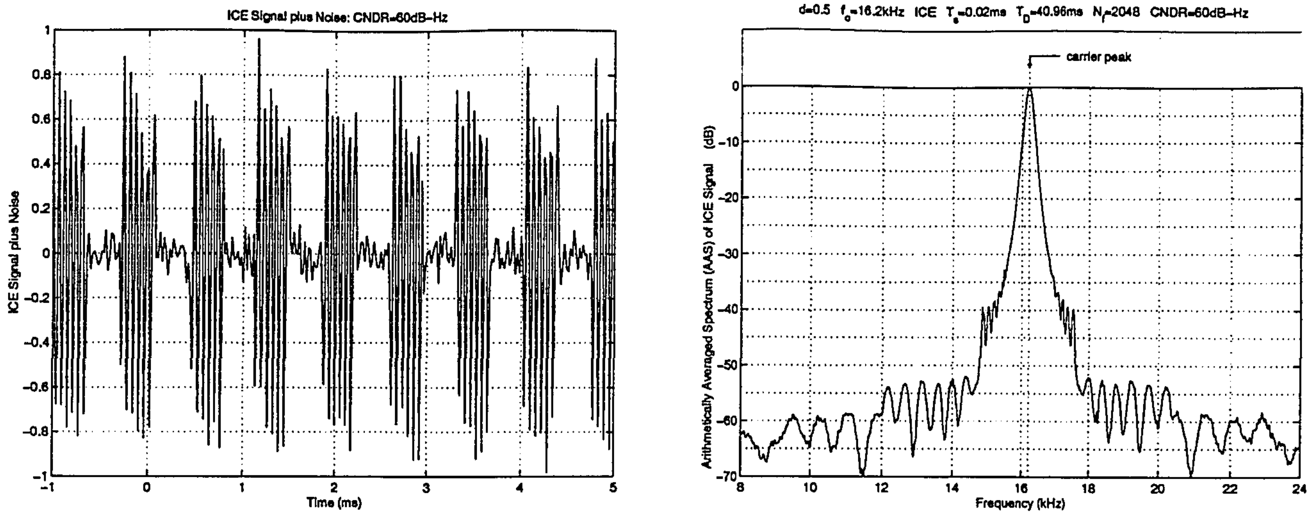

(a) ICE Signal plus Noise

(d) AAS of (a)+(b)×10000

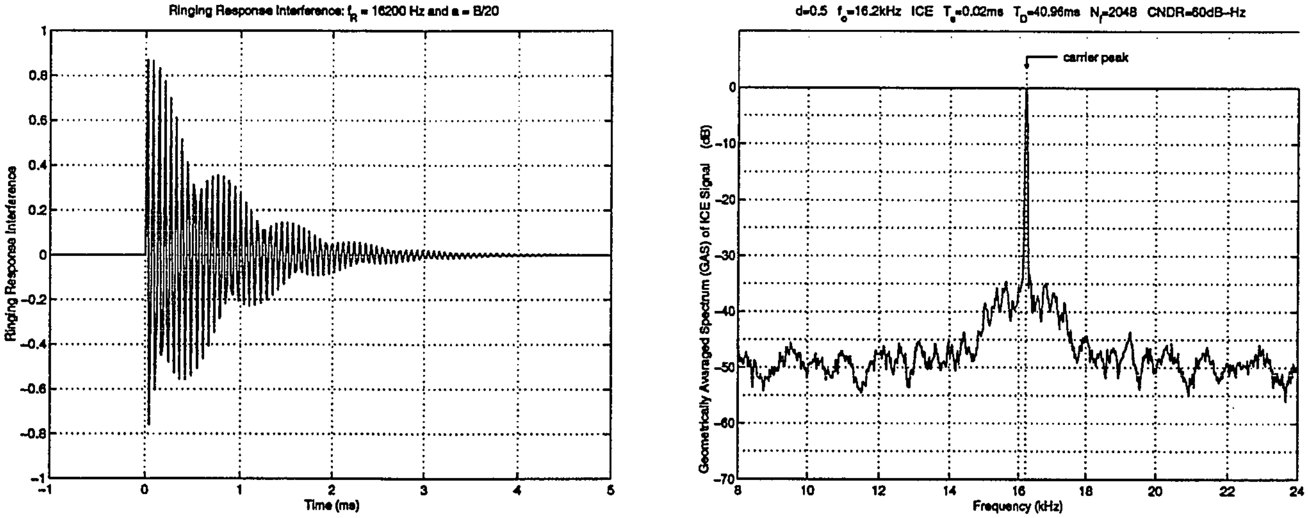

(b) Ringing Response Interference

(e) GAS of (a)+(b)×10000

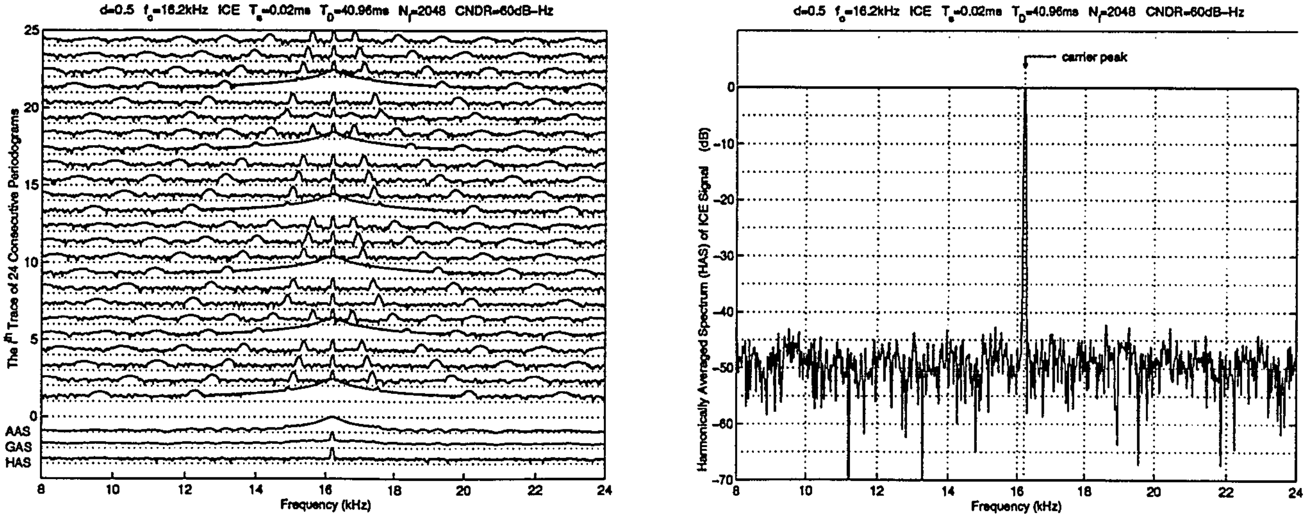

(c) Periodograms of (a)+(b)×10000

(f) HAS of (a)+(b)×10000

Figure 4.17: Ringing Response Interference: $f_R = 16200$ Hz, $a = B/20$

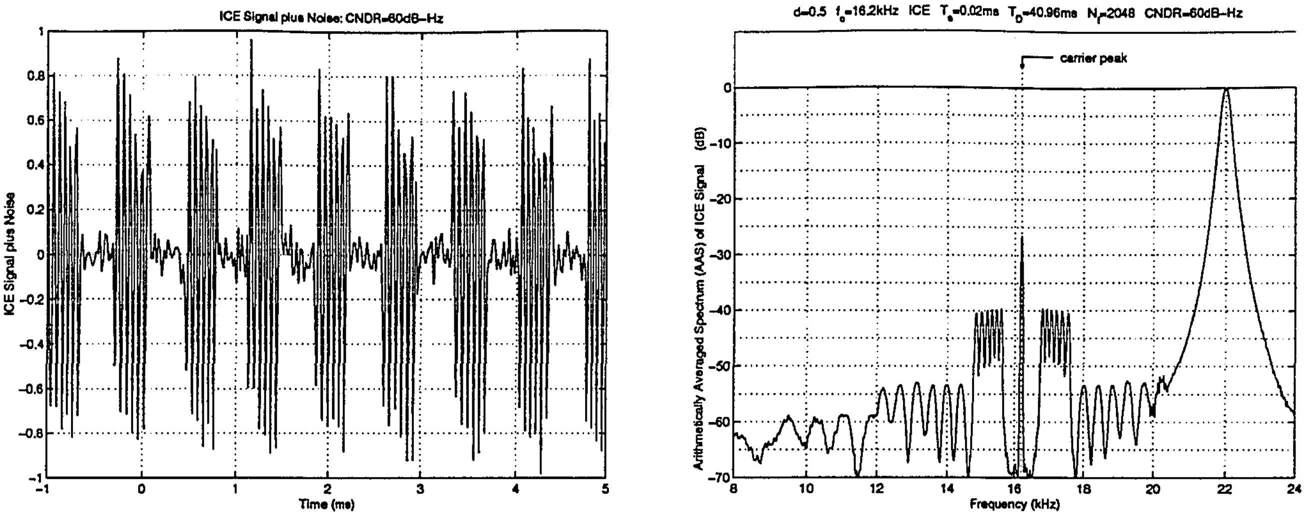

(a) ICE Signal plus Noise (d) AAS of (a)+(b)×10000

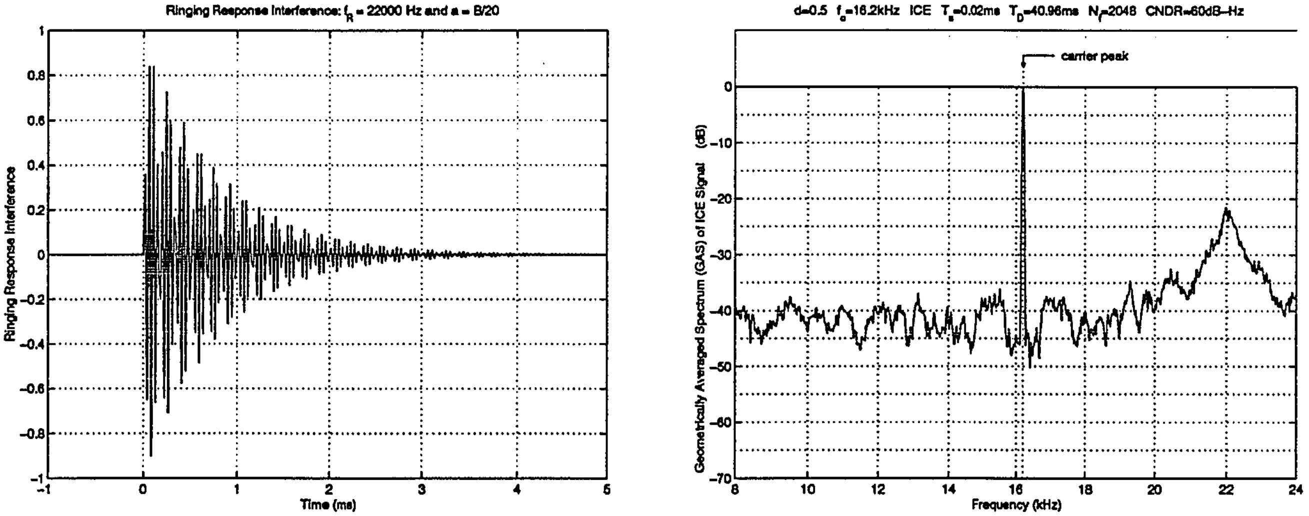

(b) Ringing Response Interference (e) GAS of (a)+(b)×10000

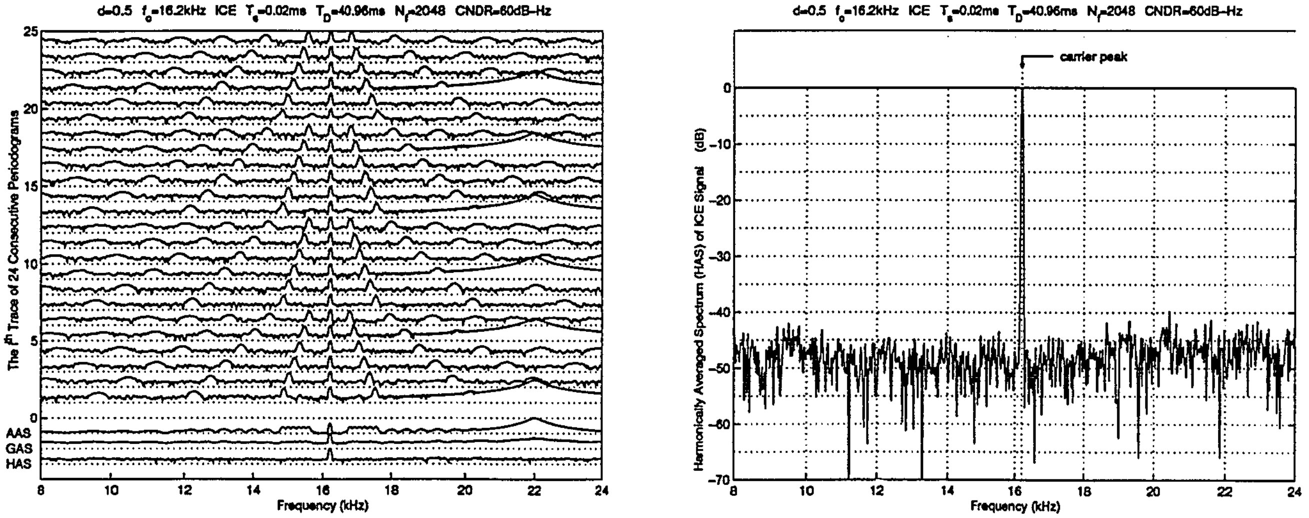

(c) Periodograms of (a)+(b)×10000 (f) HAS of (a)+(b)×10000

Figure 4.18: Ringing Response Interference: $f_R = 22000$ Hz, $a = B/20$

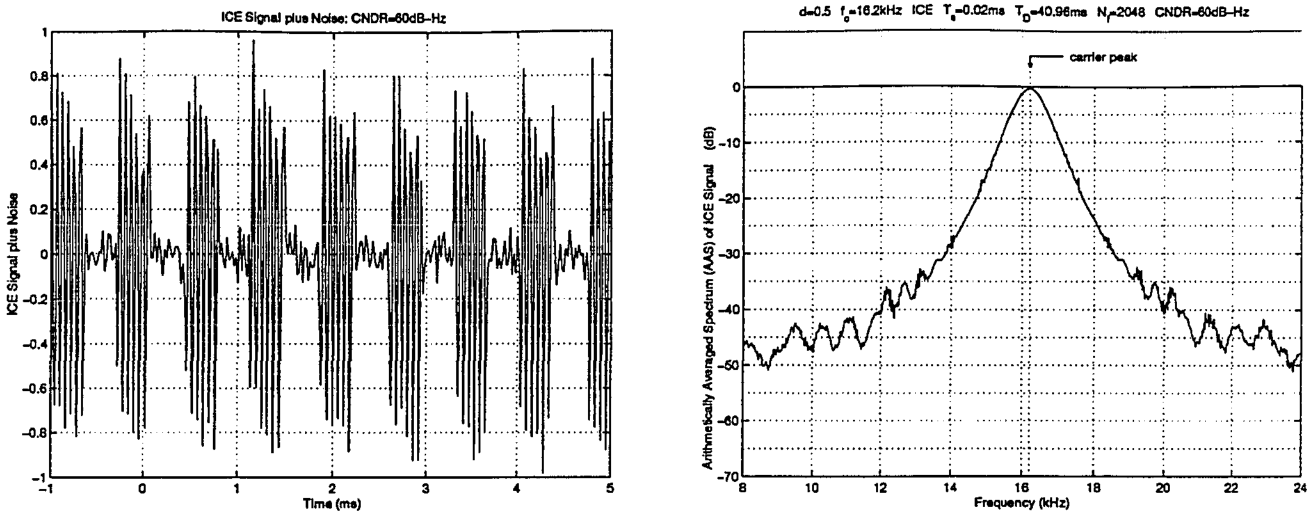

(a) ICE Signal plus Noise

(d) AAS of (a)+(b)×50000

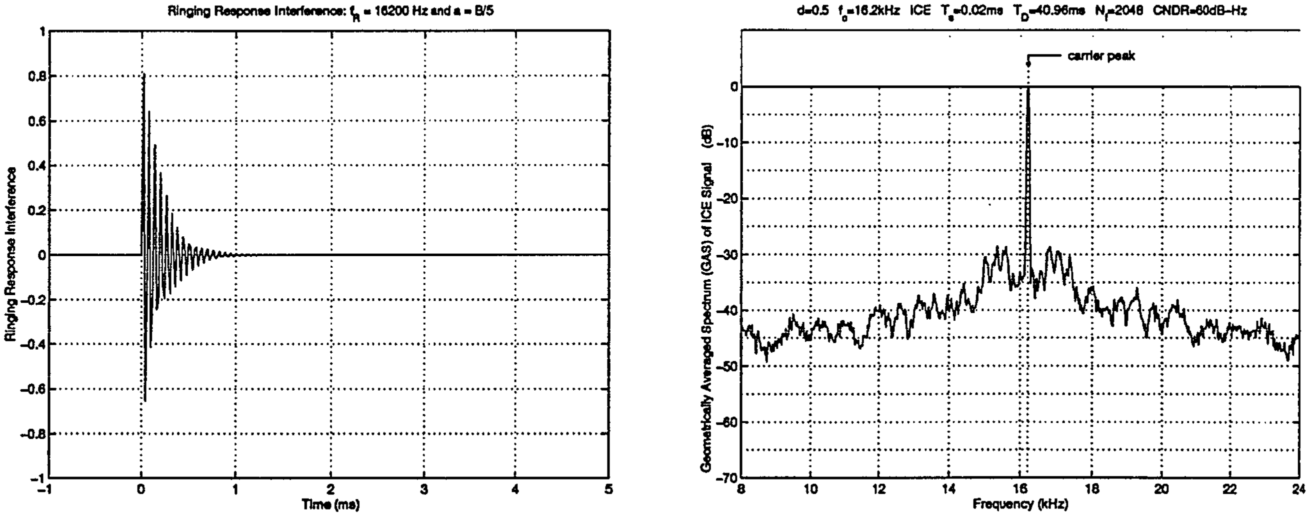

(b) Ringing Response Interference

(e) GAS of (a)+(b)×50000

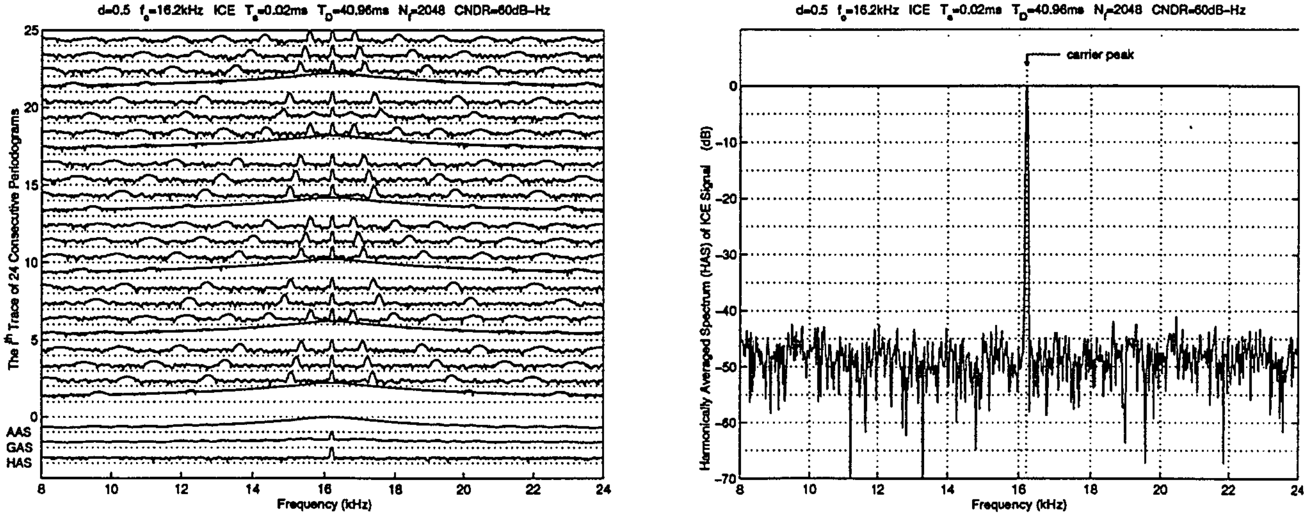

(c) Periodograms of (a)+(b)×50000

(f) HAS of (a)+(b)×50000

Figure 4.19: Ringing Response Interference: $f_R = 16200$ Hz, $a = B/5$

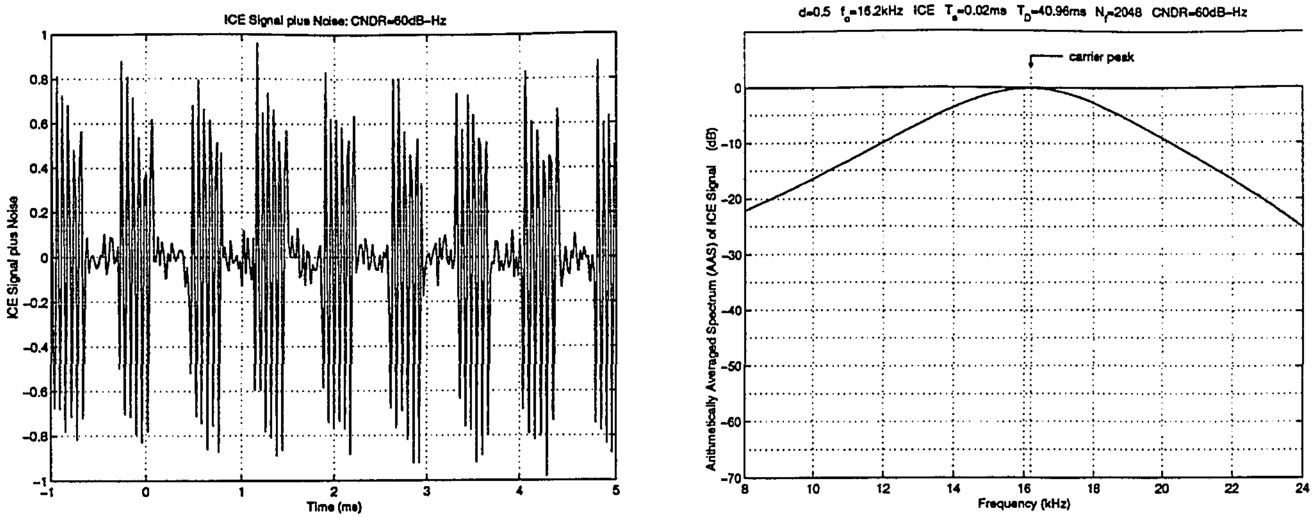

(a) ICE Signal plus Noise

(d) AAS of (a)+(b)×4500000

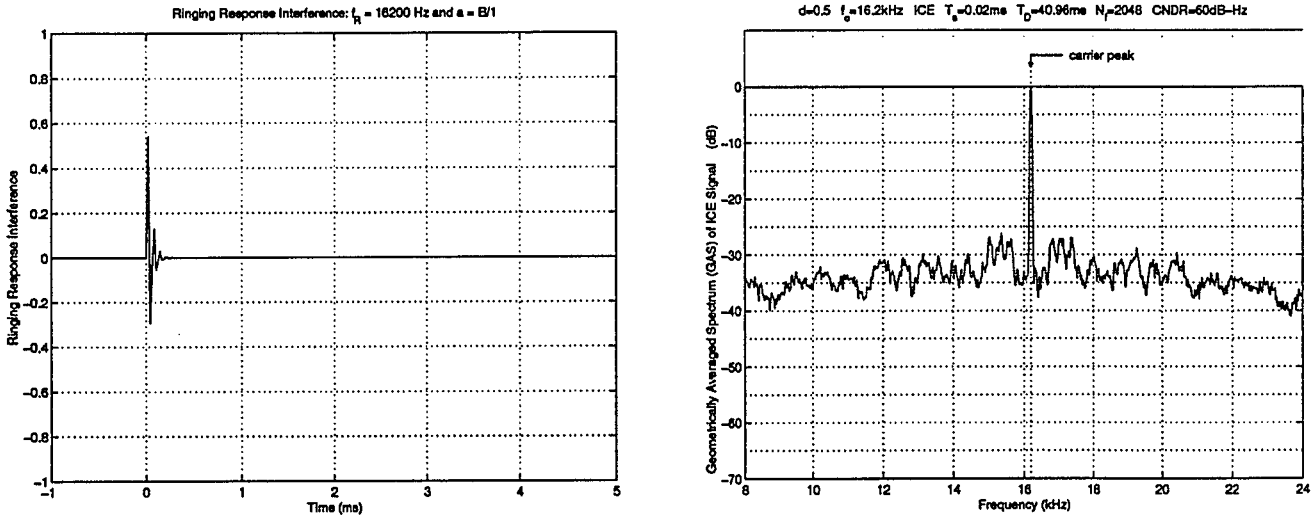

(b) Ringing Response Interference

(e) GAS of (a)+(b)×4500000

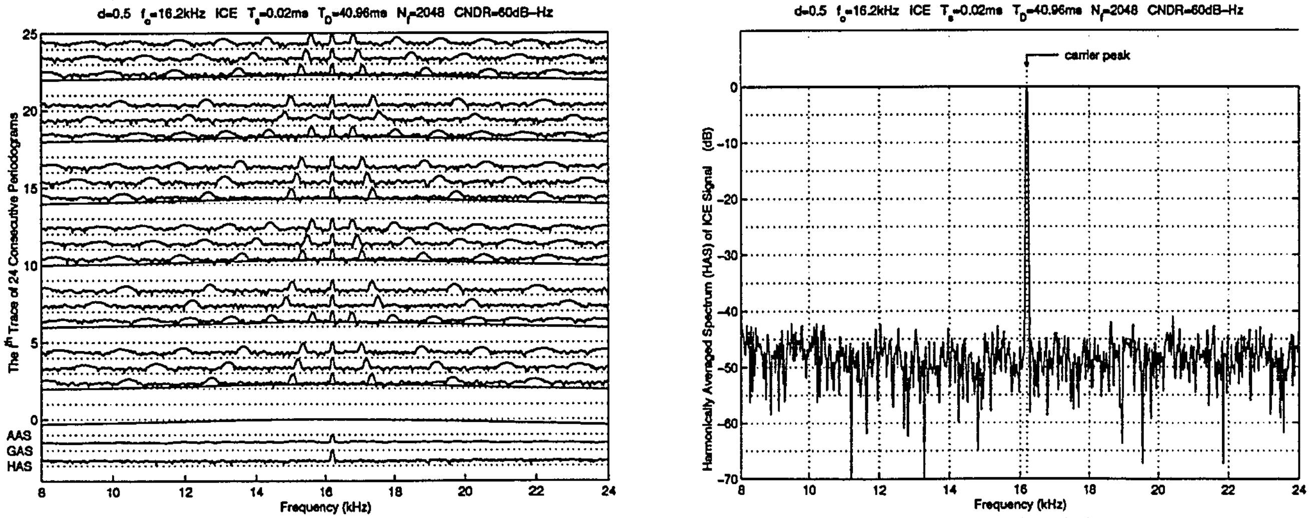

(c) Periodograms of (a)+(b)×4500000

(f) HAS of (a)+(b)×4500000

Figure 4.20: Ringing Response Interference: $f_R = 16200$ Hz, $a = B/1$

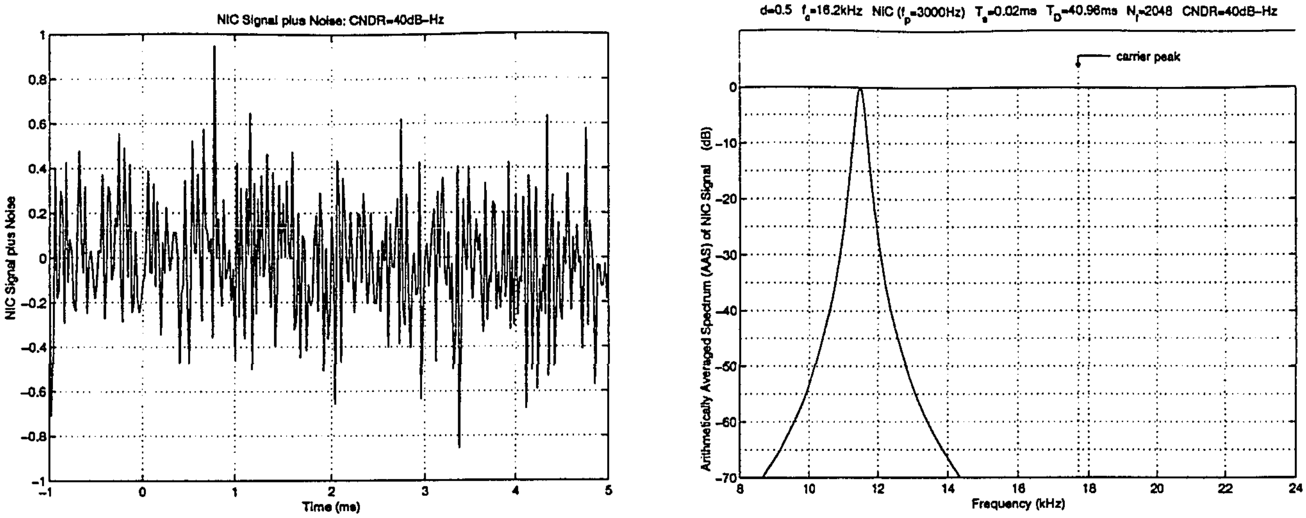

(a) NIC Signal plus Noise

(d) AAS of (a)+(b)×1000000

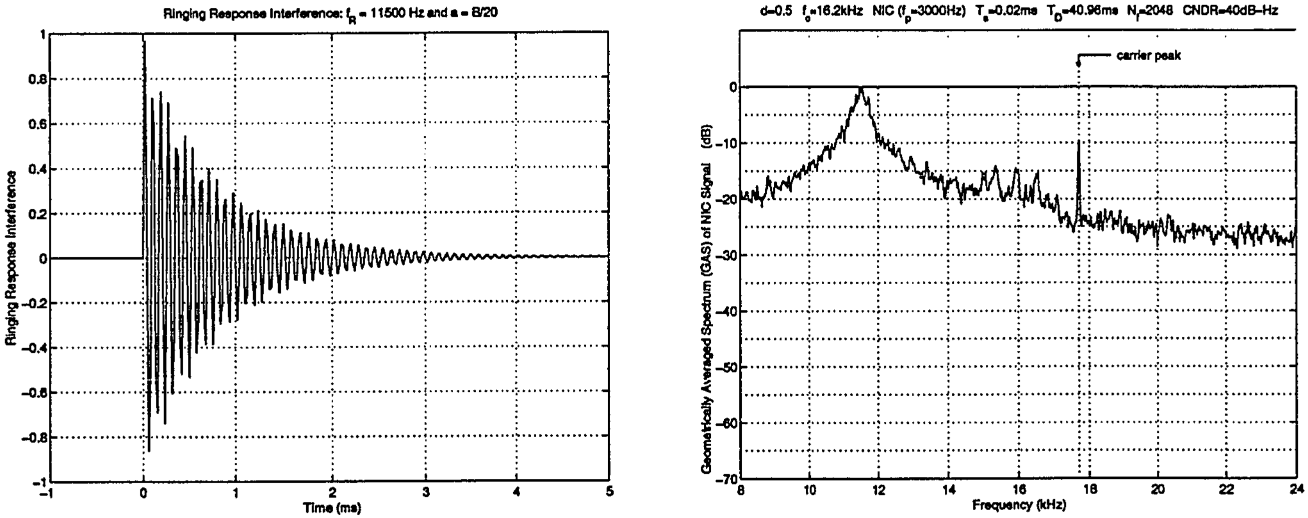

(b) Ringing Response Interference

(e) GAS of (a)+(b)×1000000

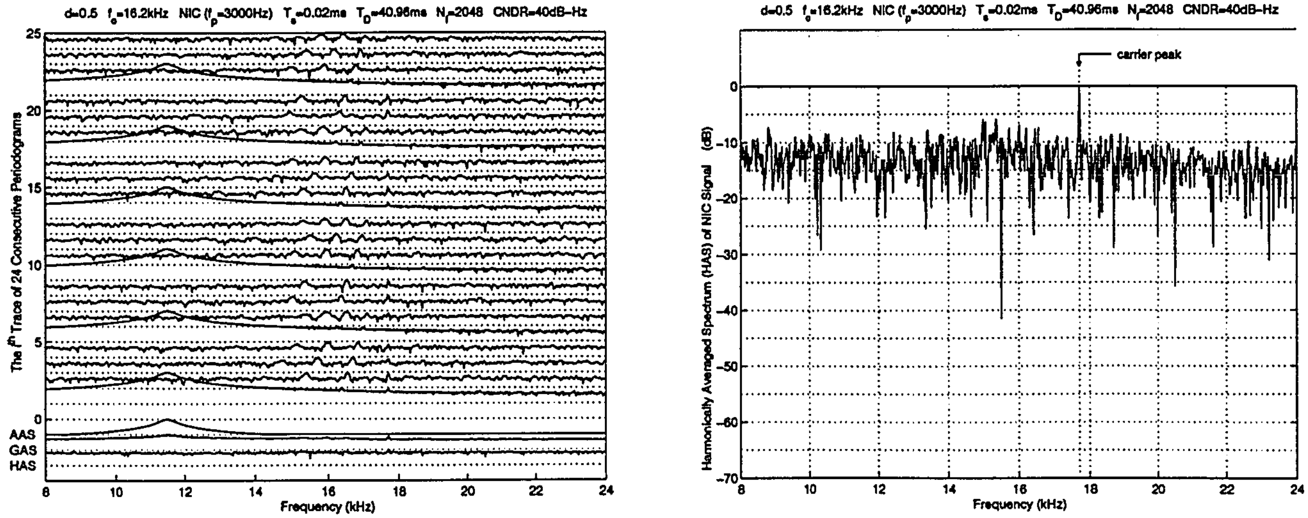

(c) Periodograms of (a)+(b)×1000000

(f) HAS of (a)+(b)×1000000

Figure 4.21: Ringing Response Interference: $f_R = 10000$ Hz, $a = B/20$

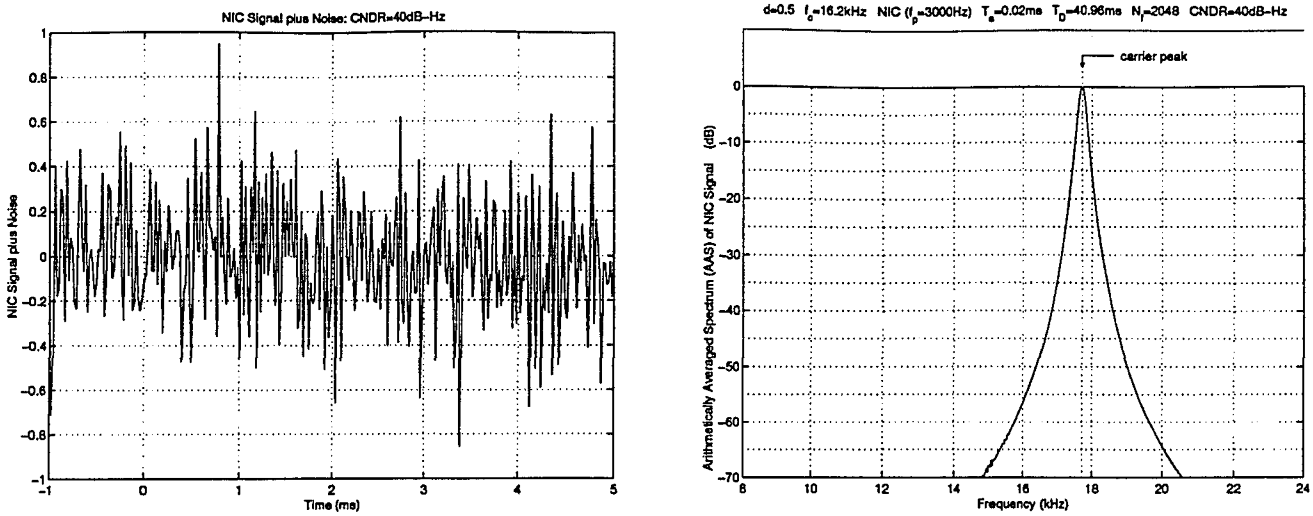

(a) NIC Signal plus Noise

(d) AAS of (a)+(b)×1000000

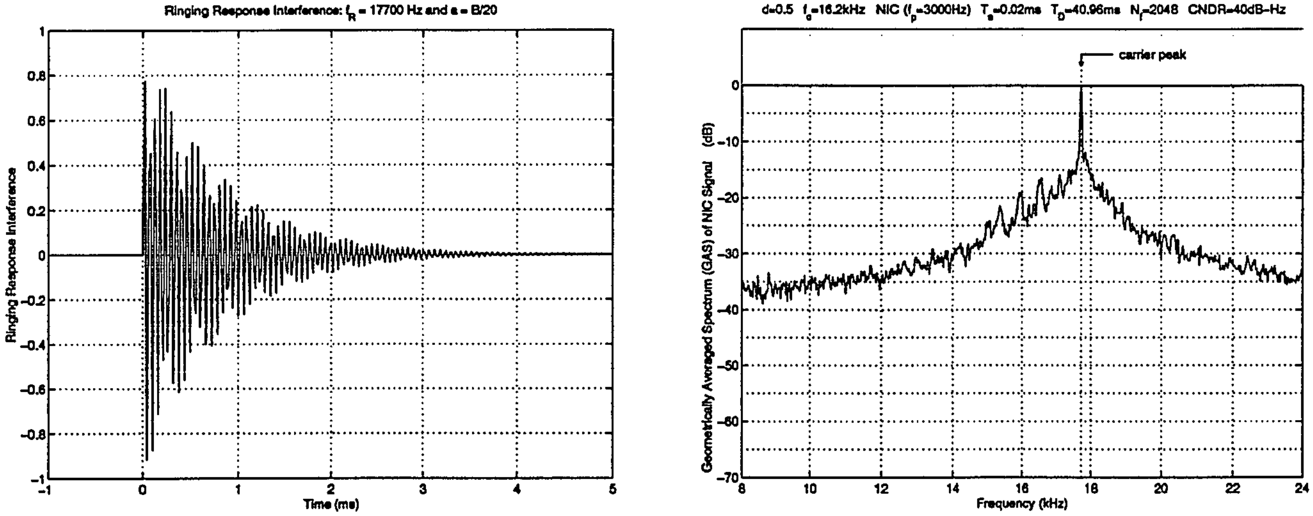

(b) Ringing Response Interference

(e) GAS of (a)+(b)×1000000

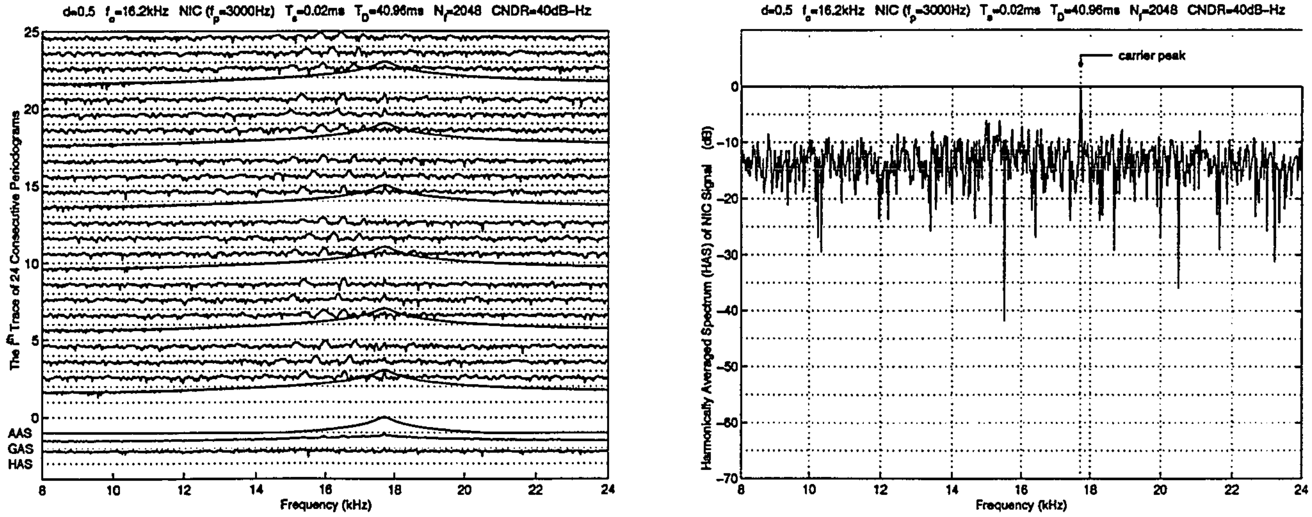

(c) Periodograms of (a)+(b)×1000000

(f) HAS of (a)+(b)×1000000

Figure 4.22: Ringing Response Interference: $f_R = 16200$ Hz, $a = B/20$

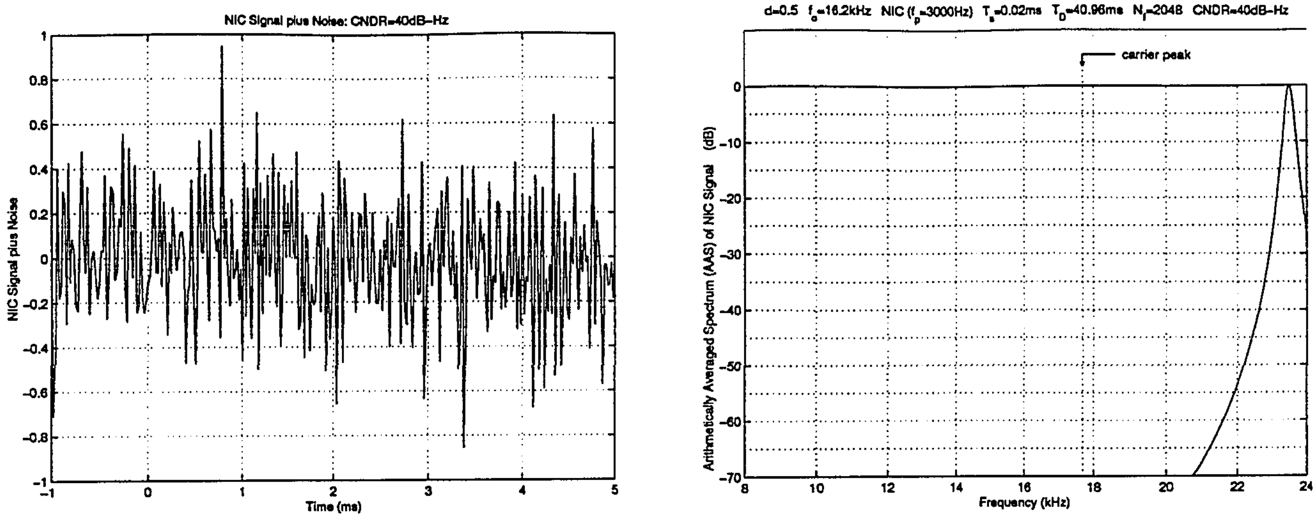

(a) NIC Signal plus Noise

(d) AAS of (a)+(b)×1000000

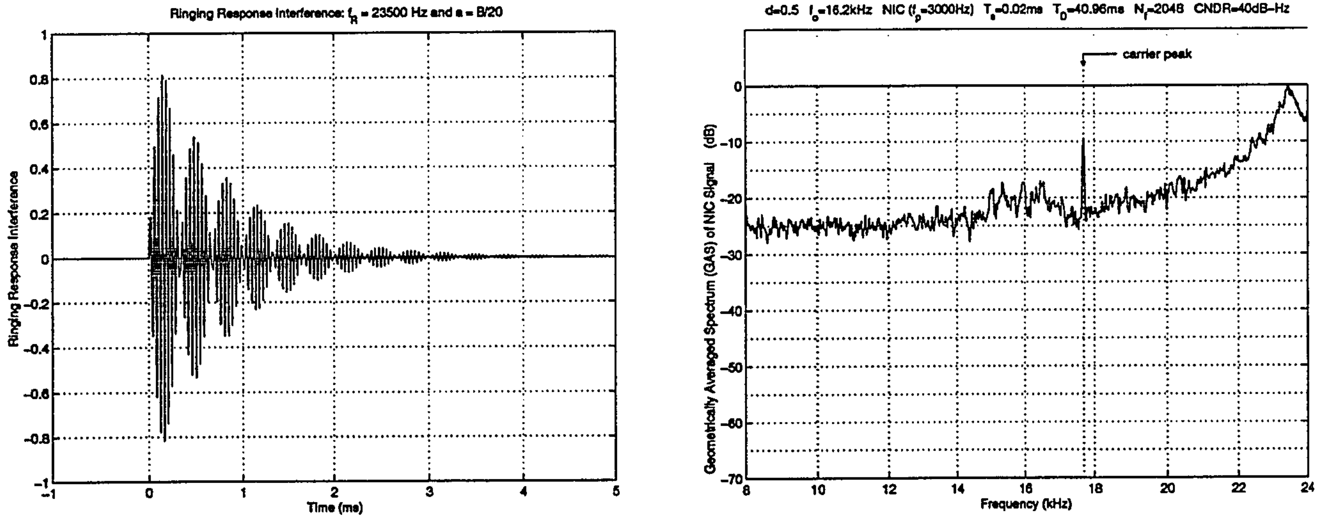

(b) Ringing Response Interference

(e) GAS of (a)+(b)×1000000

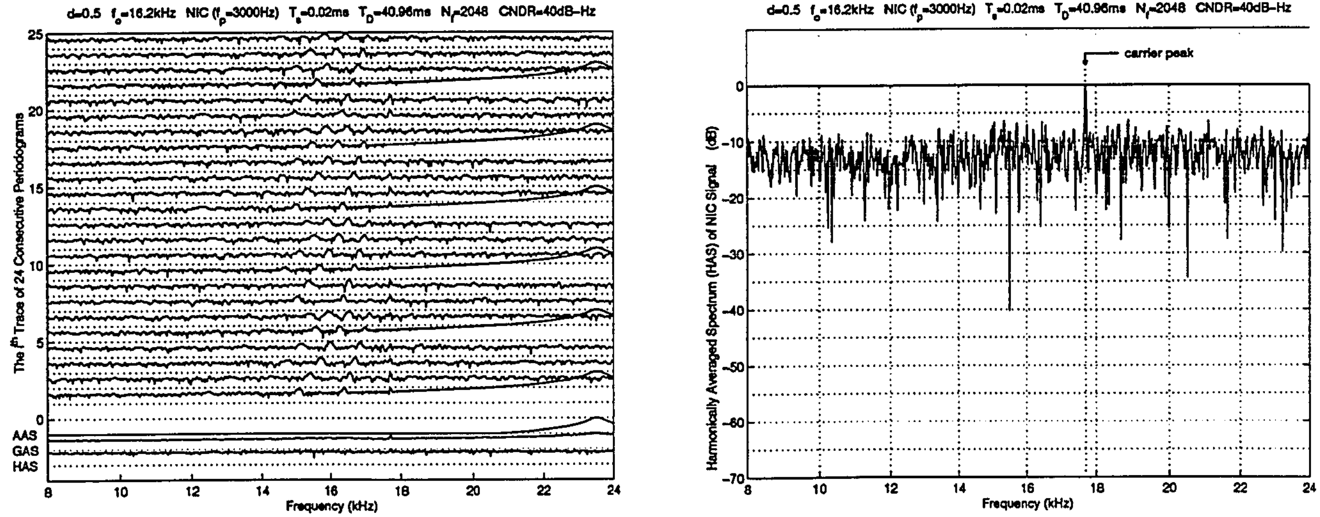

(c) Periodograms of (a)+(b)×1000000

(f) HAS of (a)+(b)×1000000

Figure 4.23: Ringing Response Interference: $f_R = 22000$ Hz, $a = B/20$

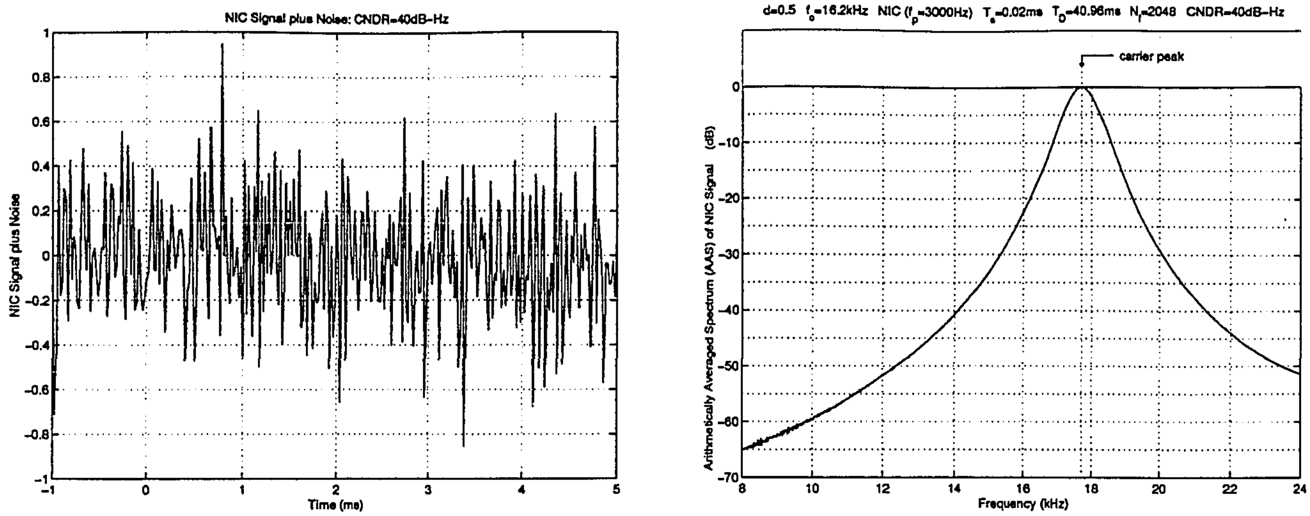

(a) NIC Signal plus Noise (d) AAS of (a)+(b)×5000000

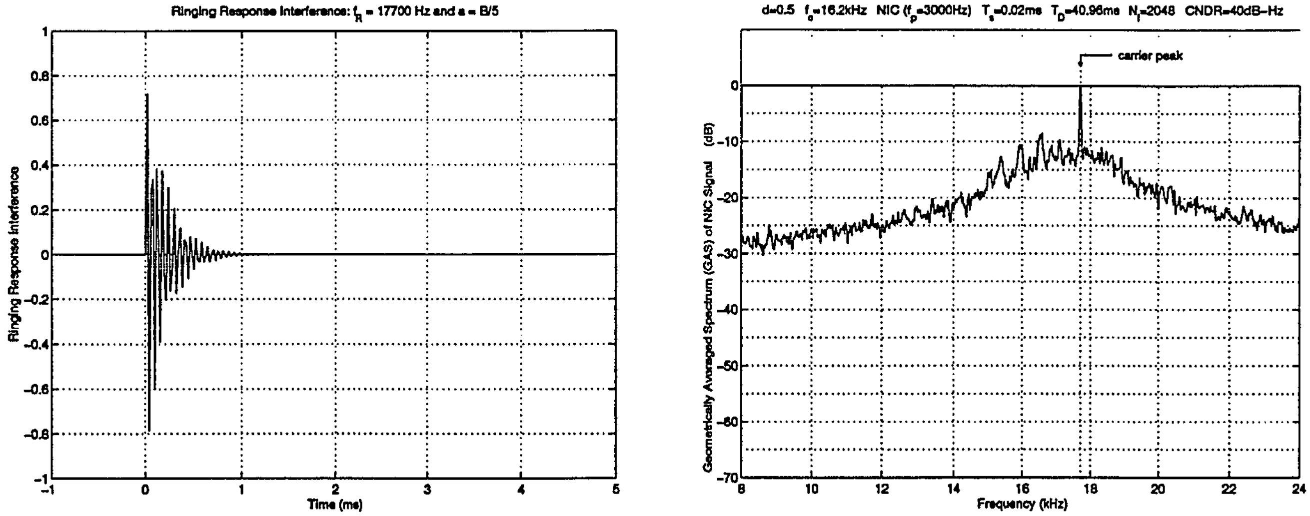

(b) Ringing Response Interference (e) GAS of (a)+(b)×5000000

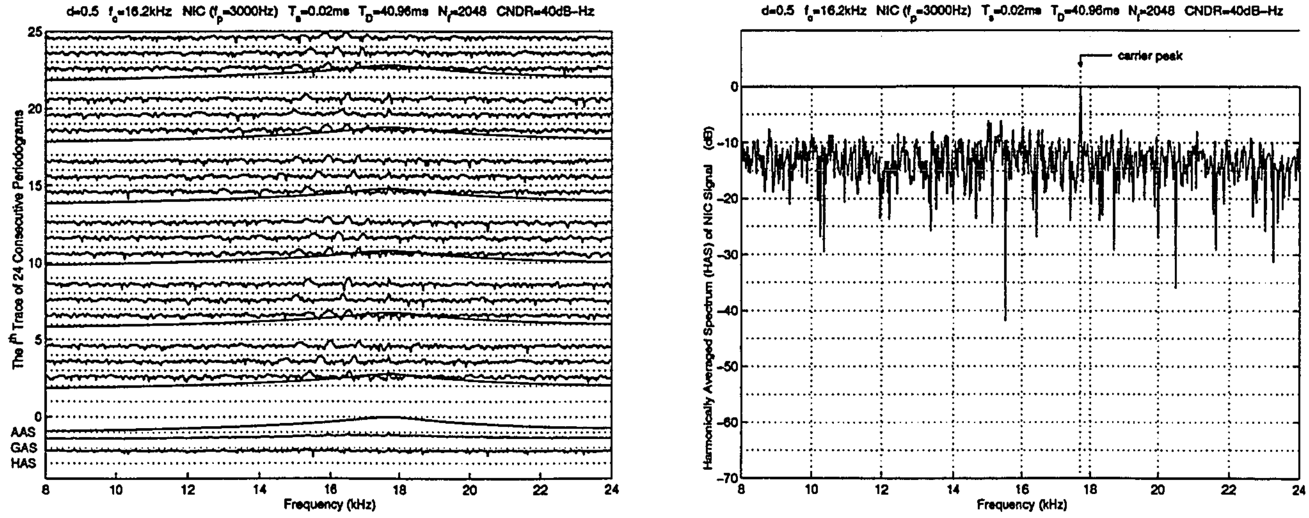

(c) Periodograms of (a)+(b)×5000000 (f) HAS of (a)+(b)×5000000

Figure 4.24: Ringing Response Interference: $f_R = 16200$ Hz, $a = B/5$

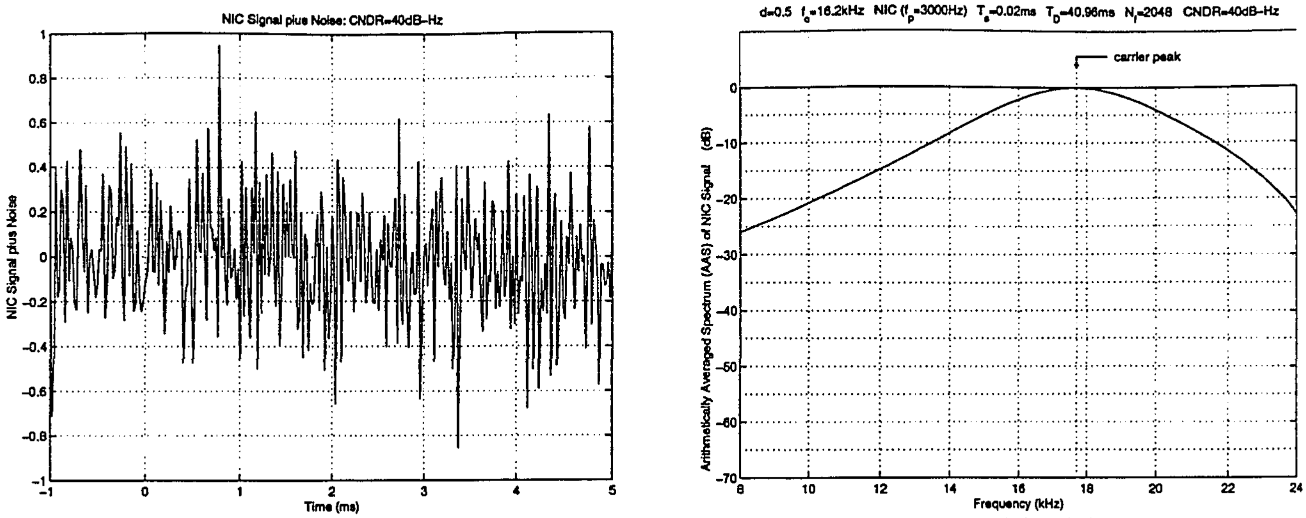

(a) NIC Signal plus Noise

(d) AAS of (a)+(b)×50000000

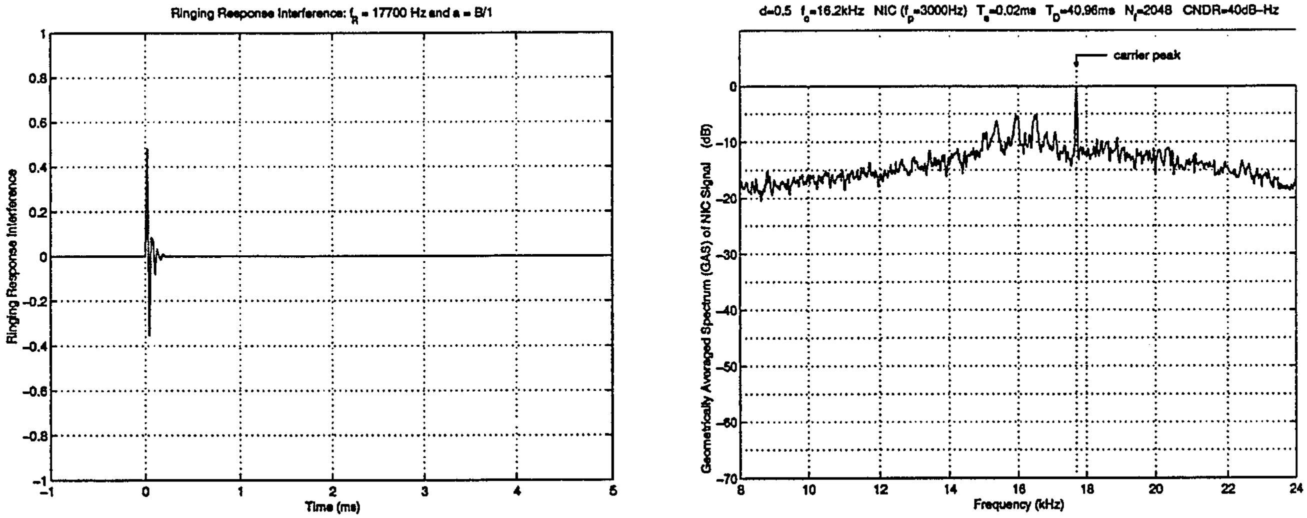

(b) Ringing Response Interference

(e) GAS of (a)+(b)×50000000

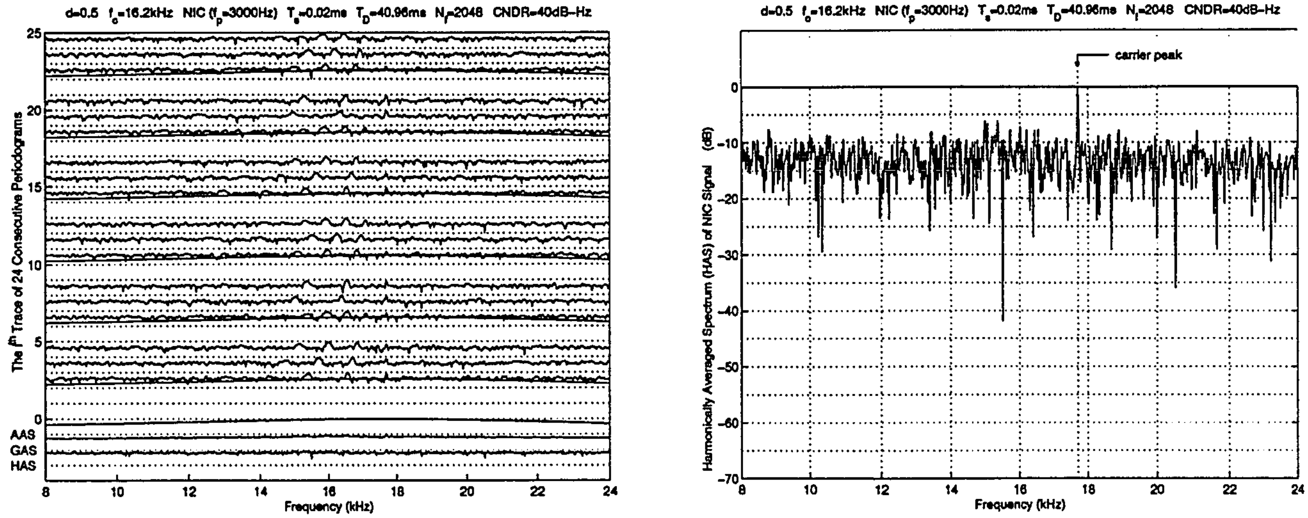

(c) Periodograms of (a)+(b)×50000000

(f) HAS of (a)+(b)×50000000

Figure 4.25: Ringing Response Interference: $f_R = 16200$ Hz, $a = B/1$

4.7 Summary

All sources in the COSPAS-SARSAT system are classed as narrowband since the system bandwidth is very small compared to the carrier frequency, i.e., $B \ll f_R$ [14]. However within the band we may denote different bandwidths of interference. For instance, an unmodulated carrier produces near line spectrum interference. Other sources essentially fill a part of or the entire 25 kHz bandwidth. Thus in the literature people have used these classifications: CW is interference produced by an unmodulated carrier, NB is narrowband interference such as that produced by voice (5 to 10 kHz), and WB is wideband interference which fills most of the 25 kHz bandwidth [14].

In summary, we give a comparison among AAS, GAS, and HAS in Table 4.2.

Type of Interference	AAS	GAS	HAS	Note
Single Carrier with Strong AM	worst	middle	best	Fig. 4.7
Single Carrier with Weak AM	best	middle	worst	Fig. 4.8
On-Off Modulation	fail	good	very good	Figs. 4.9 to 4.10
Swept Carrier	fail	very good	very good	Figs. 4.11 to 4.15
Ringing Response	fail	good	very good	Figs. 4.16 to 4.25

TABLE 4.2: Performance of Interference Suppression by AAS, GAS, and HAS

Chapter 5

Satellite Pass Data

5.1 Introduction

This chapter examines real satellite pass data. First, the method of data collection and reformatting into a rate of 50,000 samples per second is discussed. Then, a Quiet Satellite Pass Data is analyzed and compared to AWGN. The similarity between the approximation for the probability density function of AWGN and the approximation for the probability density function of quiet satellite pass data is demonstrated. AM Carrier interference, including Single Carrier interference with strong AM and Single Carrier interference with weak AM, are found to exist in practice. Using the result offered by AAS as the benchmark, it is shown that the performances of GAS and HAS are quite different when the AM is strong or weak. On-Off Modulation interference is identified and processed. Some cases of Swept Carrier interference are seen to exist. Random interference is investigated. It is shown that both GAS and HAS completely suppress these 3 kinds of interference, while AAS does not. In Section 5.7, ICE and

NIC Model SARSAT Data are presented. In Section 5.8, it is shown that the FME model can represent ELT signals existing in reality. We also discuss briefly in Section 5.9 a possible ELT signal for which a model cannot presently be envisaged. Note that, the Blackman window is employed in the experimental processing described in this chapter.

5.1.1 Signal Processing Methodology

Our discussion centers on the use of the 121.5 MHz carrier, although the results also apply to the 243 MHz signal [21]. The distress signal received at the earth station is converted to a frequency band between 0 and 25kHz. The nominal value of any ELT signal is 121.5 MHz and this is mixed to the bandcenter frequency of 12.5 kHz. Due to satellite motion, there is a Doppler frequency shift in the signal of up to about ±3 kHz for the ELT signals and a further ±3 kHz spread due to differences in crystal operation between ELT units. Thus, the 25 kHz signal bandwidth appears to be adequate although some signals may fall outside this range. Since the tape recorder is used at this point, the tape recorded data are therefore related to a frequency band between 0 and 25 kHz. The processing strategies employed here are AAS, GAS, and HAS. These averaged spectra are obtained by averaging consecutive periodograms in different ways. We apply Blackman windows to the consecutive sampled data blocks in the time domain before we calculate these consecutive periodograms.

Note that, the existing system divides the recorded data into blocks in a fashion that there is 50% overlap between any two consecutive blocks. Then, the periodograms of the blocks are averaged. This is equivalent to the arithmetically averaged value of two non-overlapped AAS estimates (which are calculated by arithmetically averaging non-overlapped blocks having odd sequence numbers and even sequence numbers, respectively, as discussed in this thesis) and is referred to here as overlapped AAS. That is, the overlapped AAS is defined by

$$\begin{aligned}
&\mathrm{AAS}_{\mathrm{over}} \\
&= \frac{1}{2K}\sum_{k=1}^{2K} S_k(f) \\
&= \frac{1}{2}\left[\frac{1}{K}\sum_{k=\text{odd numbers}} S_k(f) + \frac{1}{K}\sum_{k=\text{even numbers}} S_k(f)\right] \\
&= \frac{1}{2}\left[\text{non-overlapped AAS of odd blocks} + \text{non-overlapped AAS of even blocks}\right]
\end{aligned} \tag{5.1.1}$$

If K is large enough, then there is no significant difference between the non-overlapped AAS of blocks having odd sequence numbers and the non-overlapped AAS of blocks having even sequence numbers. Combining the estimates decreases the variance of the spectral estimate with a concomitant increase in interference. Thus, the existing strategy and the AAS process are essentially the same.

5.1.2 Data Collection

In this chapter, we use satellite pass data collected by the Department of National Defense (DND) through the Honeywell Model 101 Portable Magnetic Tape Recorder / Reproducer [28]. With this device (see Fig. 5.1), the signal is recorded at a speed of 15 inches per second and reproduced at a speed of 7.5 inches per second. In this way, the recorded bandwidth of 25 kHz is reduced to 12.5 kHz allowing the data to be

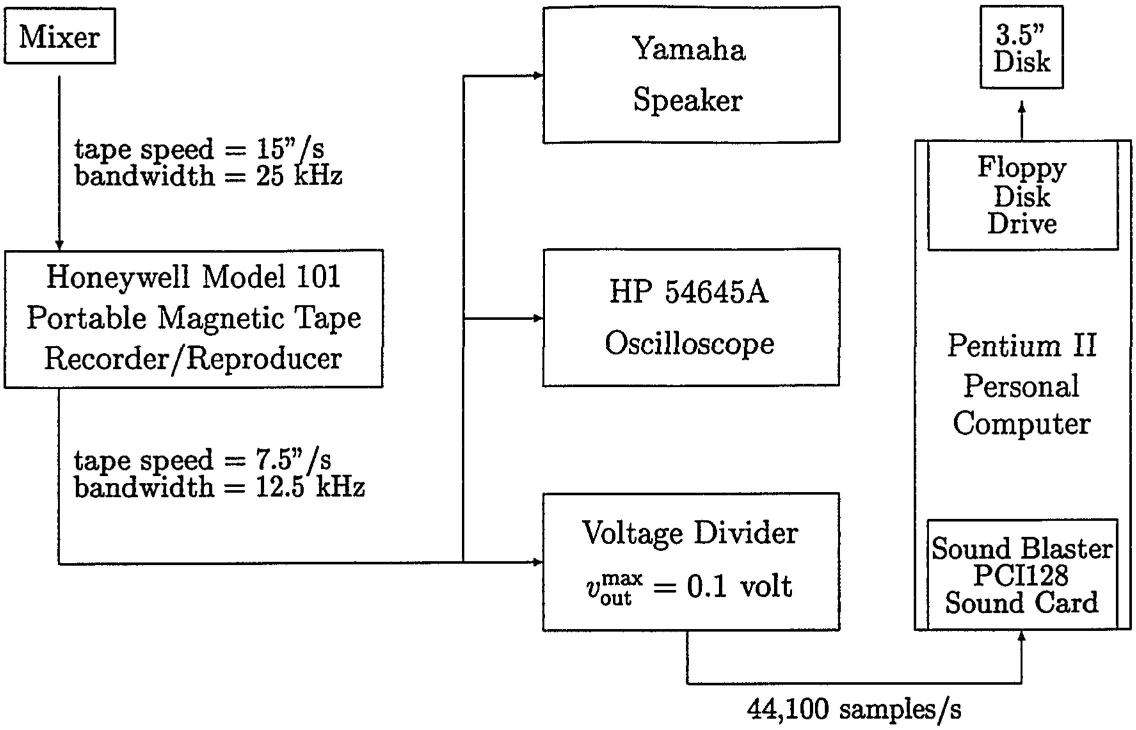

Figure 5.1: Arrangement for Digital Data Preparation

sampled at 44,100 samples per second, which is the maximum sampling rate offered by the sampler.

The Sound Blaster PCI128 sound card and the associated Creative Audio Software [29] were installed in a Pentium II personal computer. Since this sampler can only accommodate a voltage signal with a maximum amplitude of less than 0.1 volt, a voltage divider is inserted between the Honeywell Model 101 Portable Magnetic Tape Recorder/Reproducer and the Sound Blaster PCI128 sound card. The output signal coming from the Honeywell Model 101 Portable Magnetic Tape Recorder/Reproducer can be monitored by not only a Yamaha Speaker but also an HP 54645A Oscilloscope. Finally, the digital data are recorded on a 3.5" disk and every 88,200 data samples on this disk represent a time interval of 1 s.

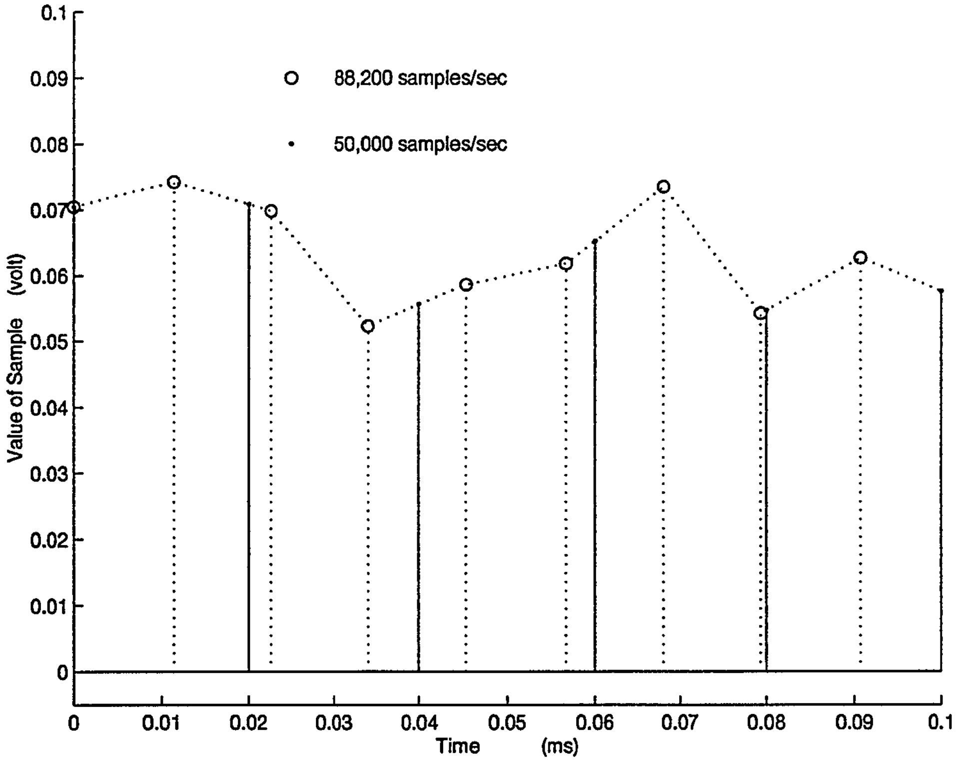

Figure 5.2: Conversion from 88,200 samples/s to 50,000 samples/s

We converted the data rate of 88,200 samples per second to the data rate of 50,000 samples per second by interpolation (see Fig. 5.2) before performing any further operations on the sampled data. The choice of the sampling rate of 50,000 samples per second in our ELT signal processing is the lowest sampling rate (*i.e.*, the *Nyquist rate* [23]) when the signal bandwidth is 25 kHz.

5.2 Quiet Satellite Pass

For simplicity, the signals are assumed to be perturbed by an *additive, zero-mean, stationary, white, Gaussian noise* [23]. We refer to such a noise as an *additive white Gaussian noise* (AWGN).

5.2.1 Time Waveforms

We show the time waveform of the first trace of an AWGN created by computer simulation in Fig. 5.3(a). We have also shown the time waveform of the first trace of a quiet satellite pass in Fig. 5.4(a). The first eighth of Figs. 5.3(a) and 5.4(a) can be found in Figs. 5.3(b) and 5.4(b), respectively. The approximation for the probability density function of the data contained by K traces of AWGN created by computer simulation is shown in Fig. 5.5 while the approximation for the probability density function of the data contained by K traces of a quiet satellite pass is shown in Fig. 5.6. By comparison, the similarity between Fig. 5.3 and Fig. 5.4, and Fig. 5.5 and Fig. 5.6 indicates that quiet satellite pass data are very close to AWGN. For example, both of the two PDFs shown in Figs. 5.5 and 5.6 have zero mean. Also the two curves shown in Figs. 5.5 and 5.6 almost coincide, and their PDFs have almost equal variance.

5.2.2 Frequency Plots

We have shown the periodograms and the averaged spectra AAS, GAS, and HAS of an AWGN created by computer simulation in Fig. 5.7. We have also shown the periodograms, AAS, GAS, and HAS of a quiet satellite pass in Fig. 5.8. By comparison, the similarity between Fig. 5.7 and Fig. 5.8 can be appreciated. For example, in both of Figs. 5.7 and 5.8, the averaged spectra are almost flat. Also, the differences between AAS and GAS in both of Figs. 5.7 and 5.8 are about 10 dB while the differences between AAS and HAS in both of Figs. 5.7 and 5.8 are approximately 12 dB.

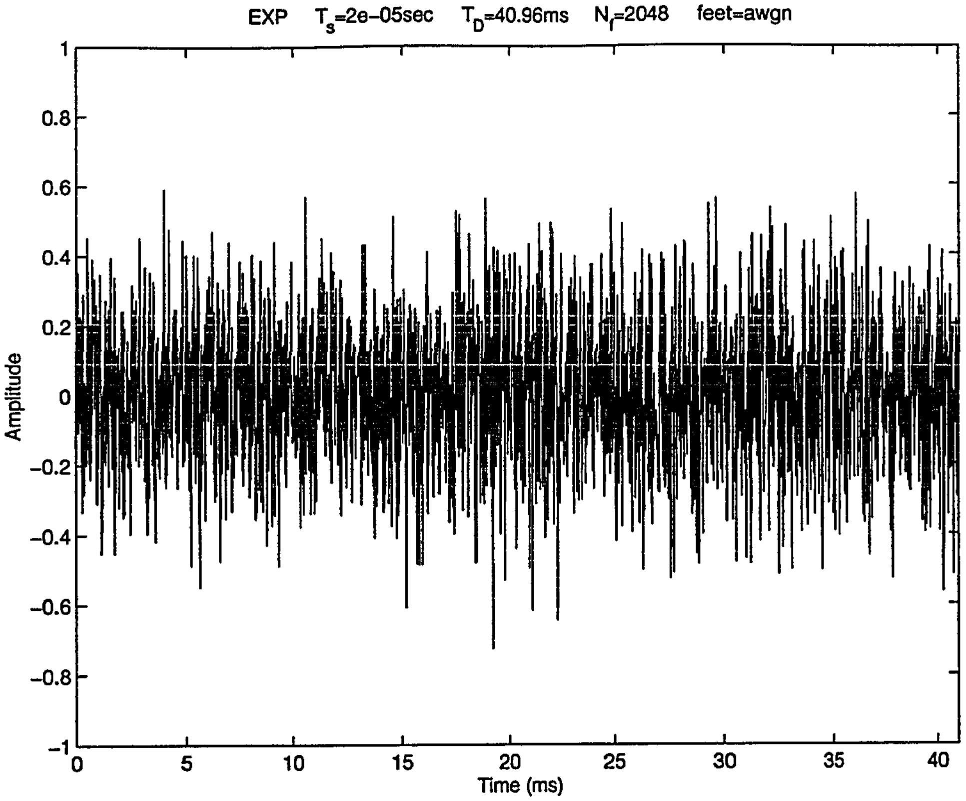

(a) the whole length

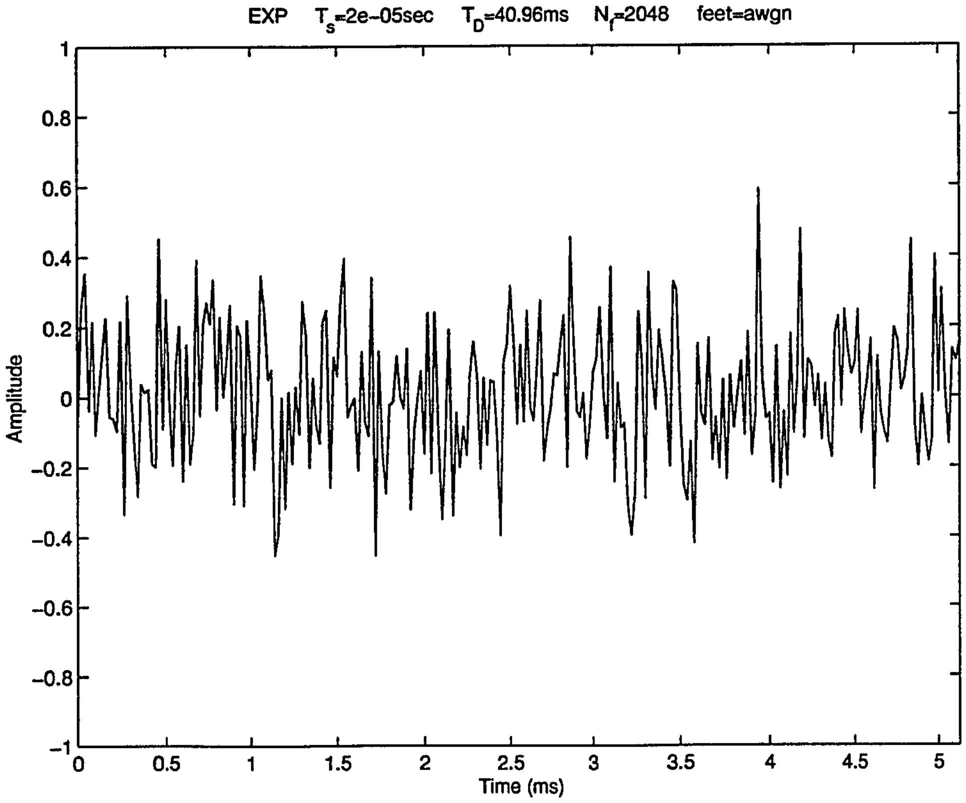

(b) the first eighth

Figure 5.3: Time Waveform of the 1st Trace of an AWGN Created by Computer

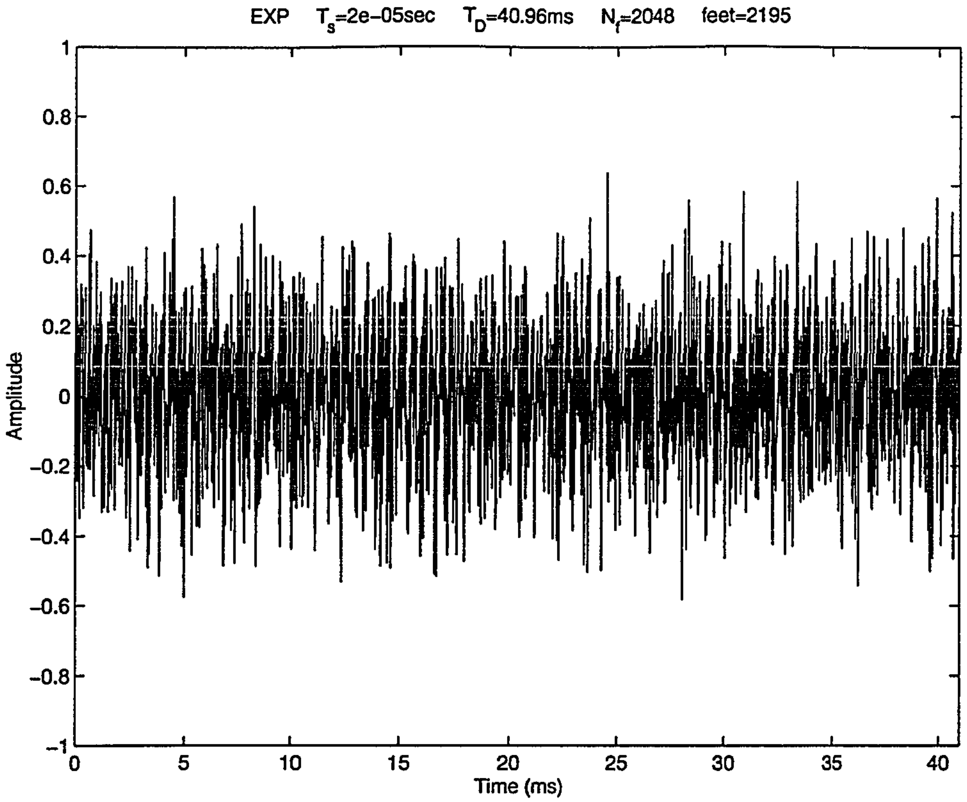

(a) the whole length

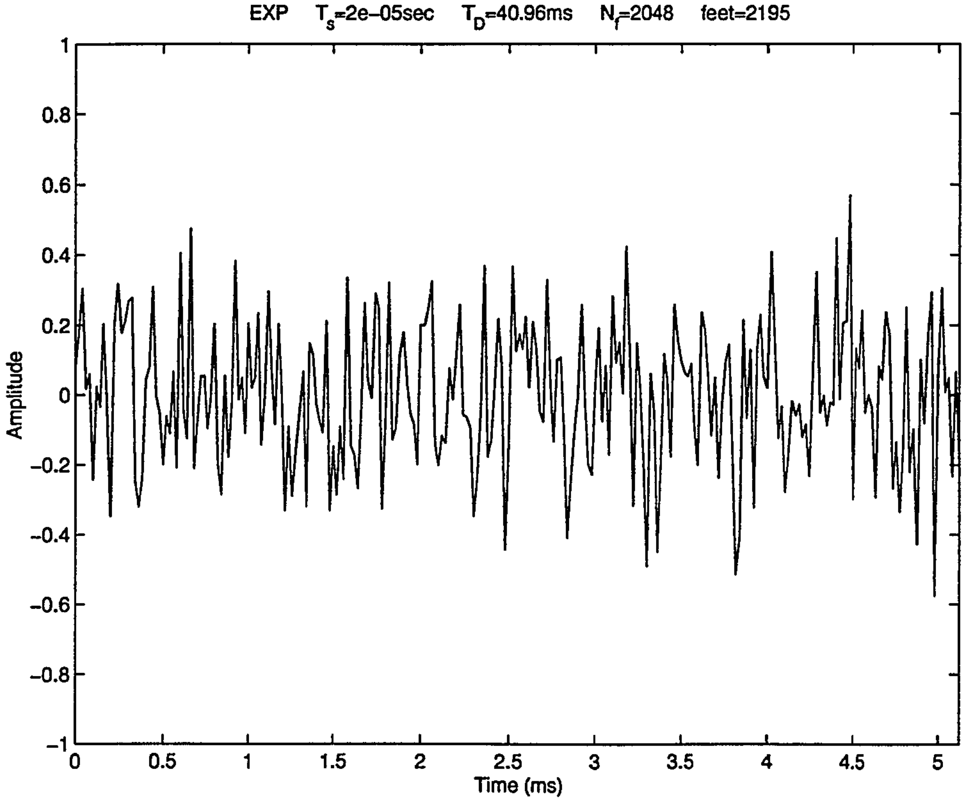

(b) the first eighth

Figure 5.4: Time Waveform of the 1st Trace of a Quiet Satellite Pass

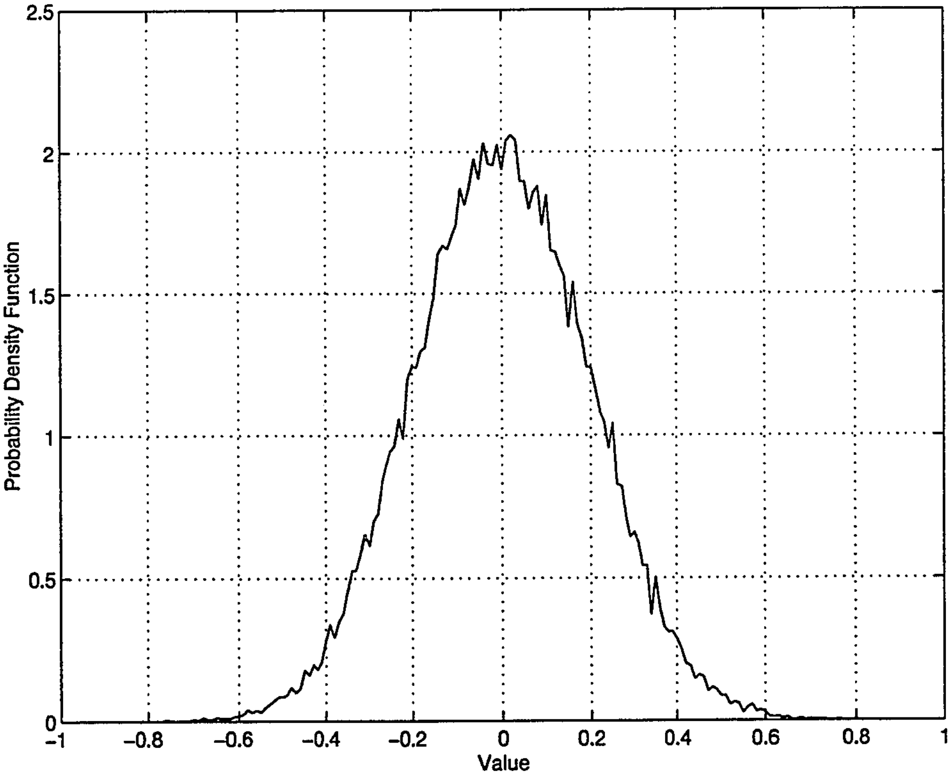

Figure 5.5: The Approximation for the PDF of AWGN Created by Computer

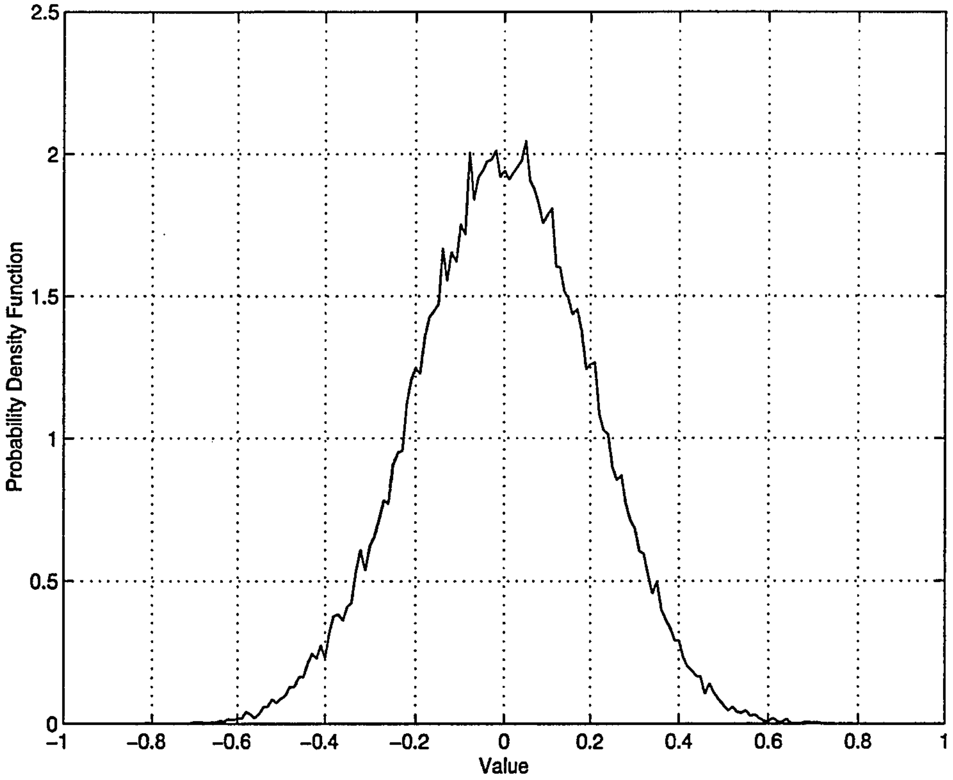

Figure 5.6: The Approximation for the PDF of a Quiet Satellite Pass

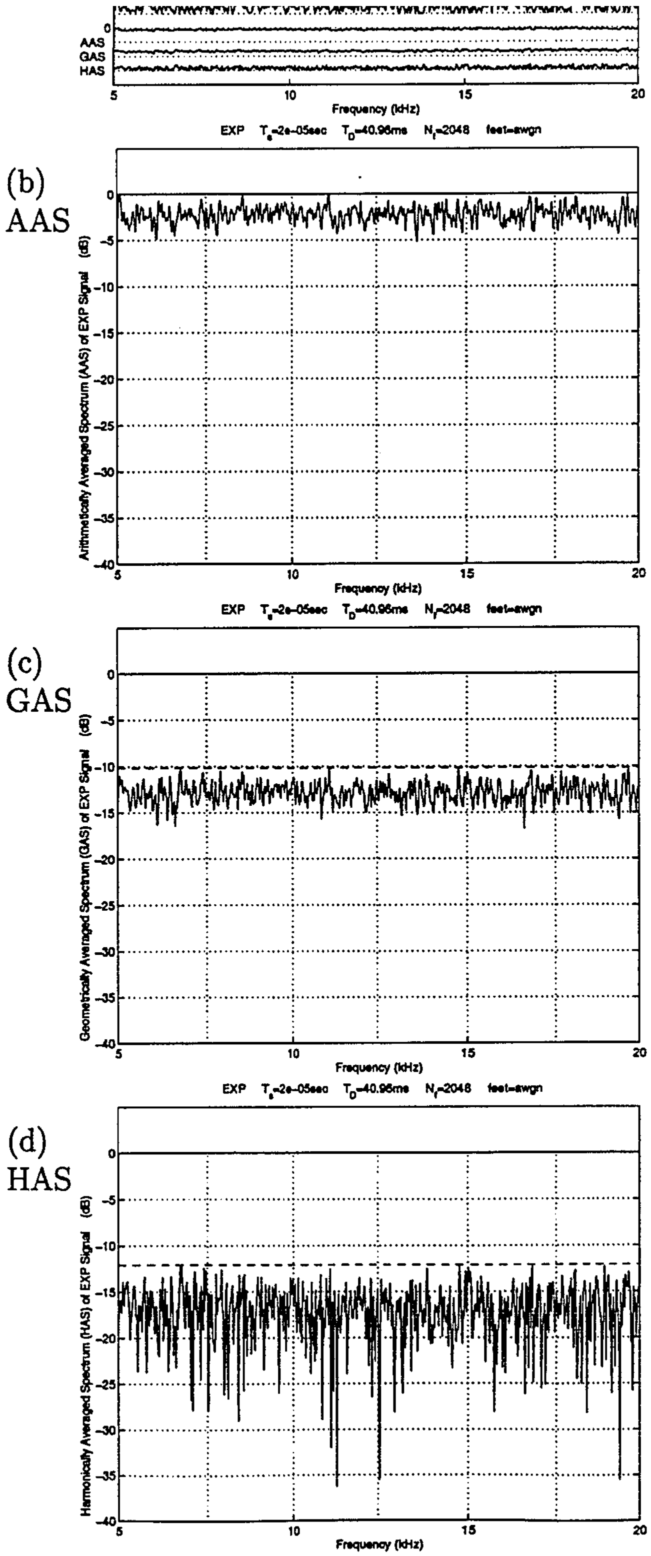

Figure 5.7: AWGN Created by Computer

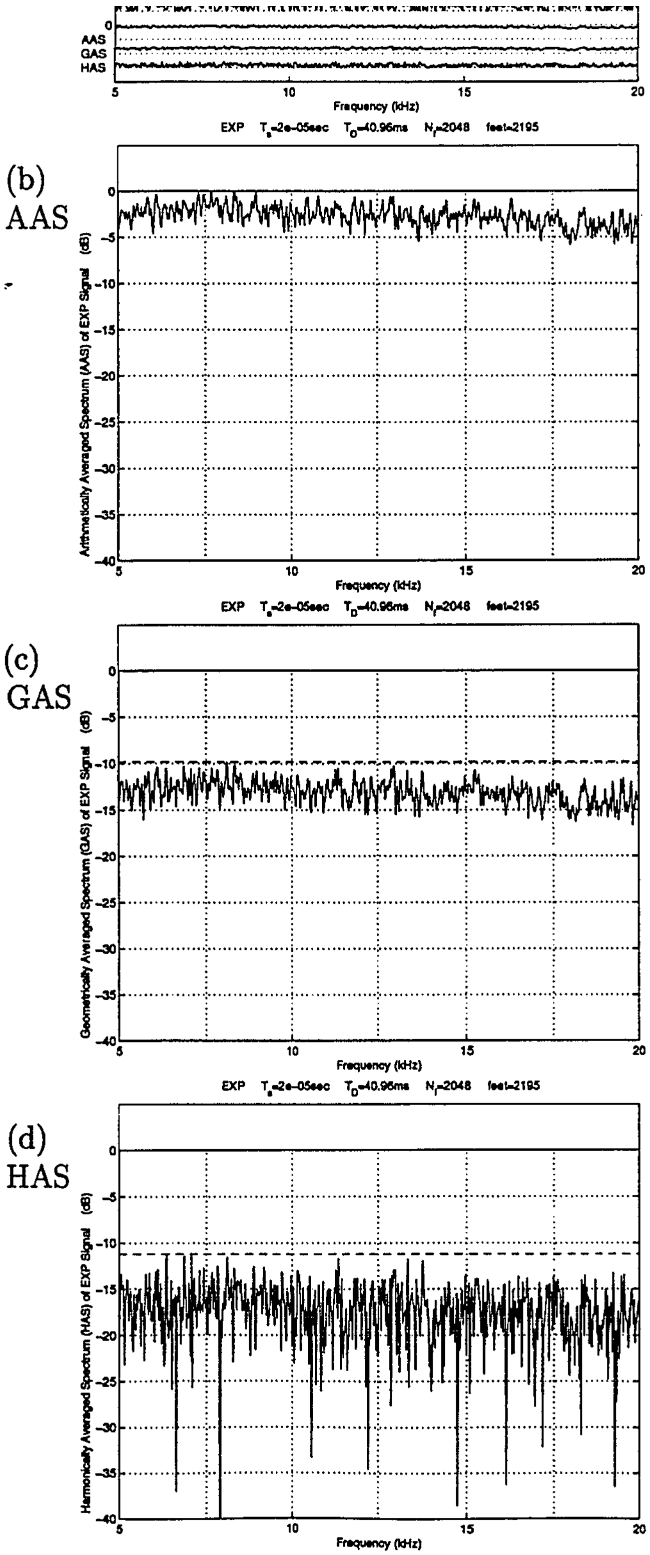

Figure 5.8: Quiet Satellite Pass

5.3 AM Carrier Interference

5.3.1 Single Carrier with Strong AM Interference

In Subsection 4.3.1, we discussed the computer simulation of a single carrier interference with strong AM (see Fig. 4.7). The following presentation serves as experimental support.

Frequency Plots

We have shown the periodograms and the spectral averages AAS, GAS, and HAS of a single carrier with strong AM interference at a frequency of 10.9 kHz in Fig. 5.9. Fig. 5.10 shows detailed plots of Fig. 5.9. Due to the strong AM, not all of the 24 periodograms in Fig. 5.9(a) have the same spectral height. Actually, periodograms 9, 12, 17, 19, 21, and 24 provide a spectral height which is much lower than the spectral height offered by the other periodograms. Note that, since the difference between the spectral height of the interference and the background-level is more than 20 dB, which is the dynamic range used to show each of the 24 periodograms, only a few small ripples can be seen at some frequencies apart from the frequency of 10.9 kHz.

We then use the 24 periodograms to calculate the AAS in Fig. 5.9(b), the GAS in Fig. 5.9(c), and the HAS in Fig. 5.9(d), respectively. Note that, in these figures, we have used a dynamic range of 40 dB.

In the order of Figs. 5.9(b), (c), and (d) and due to (2.2.31), we have 0 dB, -6 dB, and -9 dB at the frequency of 10.9 kHz which is the position of the interference. That is, the interference has an AAS peak which is 6 dB higher than its GAS peak and 9 dB higher than its HAS peak. Therefore, we may be able to deduce that this is a carrier with strong AM interference.

Time Waveforms

Time waveforms of the 16th and 17th traces of the carrier with strong AM interference at 10.9 kHz are illustrated in Figs. 5.11(a) and 5.12(a), respectively. Both cover a time interval of 40.96 ms which is the value of T_D in this example where T_D is the length of data record used to calculate a periodogram. The first eighth of Figs. 5.11(a) and 5.12(a) can be found in Figs. 5.11(b) and 5.12(b), respectively. Both cover a time interval of 40.96/8 ms. Note that, to create Figs. 5.11 and 5.12, we have used a filter (having a passband from 10.5 kHz to 11.3 kHz) in frequency domain in a line-off manner. The passband of this filter can be seen in Figs. 5.10(b), (c), or (d). More specifically, after we had obtained Fig. 5.9(a), for each of the 24 periodograms, we keep the frequency domain samples within the passband of the filter and replace the remaining points with zeros. Then, we apply an inverse FFT on the filtered data obtaining Figs. 5.11 and 5.12, demonstrating that we do have carrier with strong AM interference in this example.

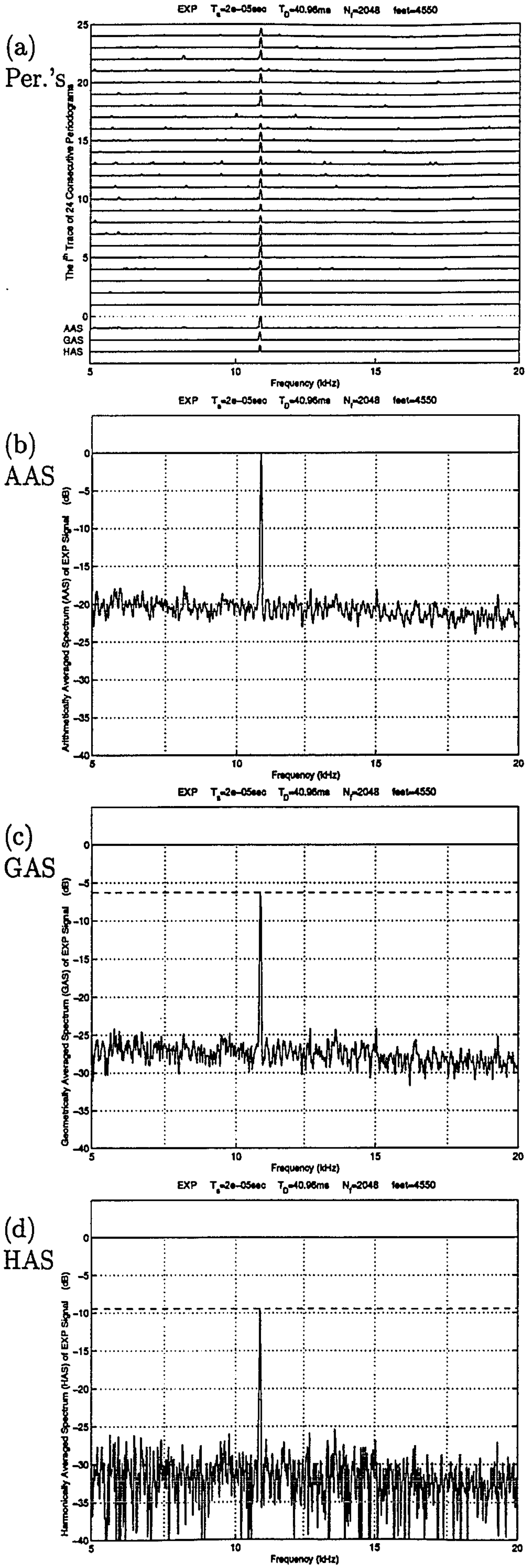

Figure 5.9: Single Carrier with Strong AM

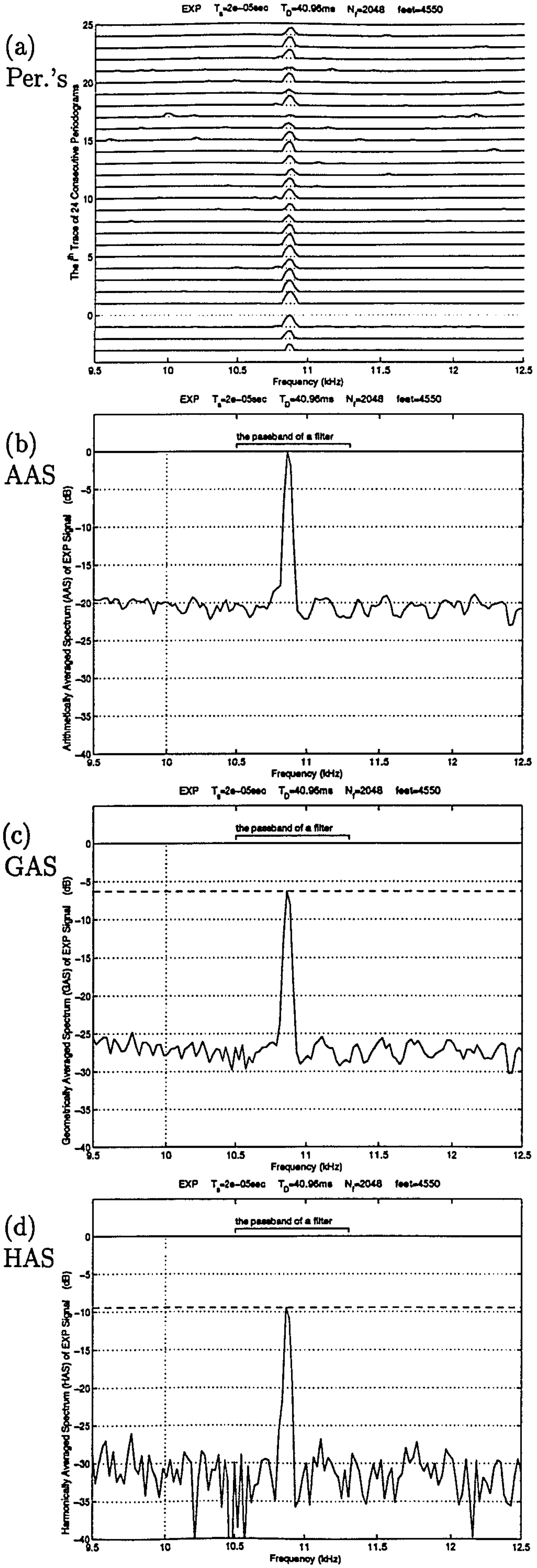

Figure 5.10: Details of the LHS Figure

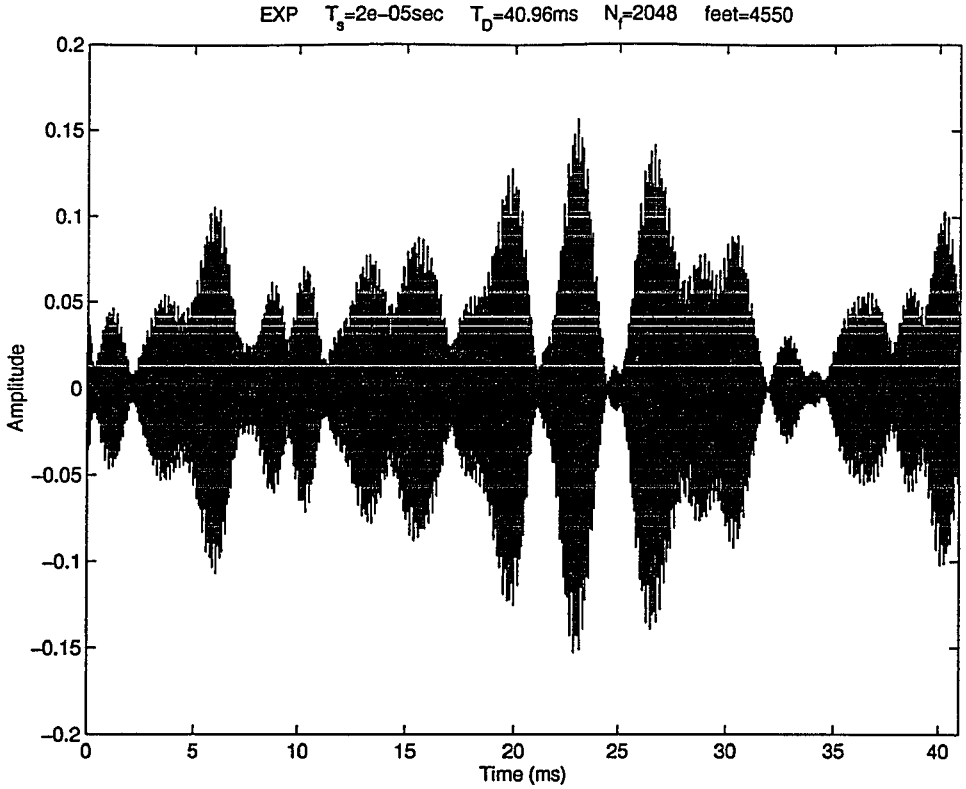

(a) the whole length

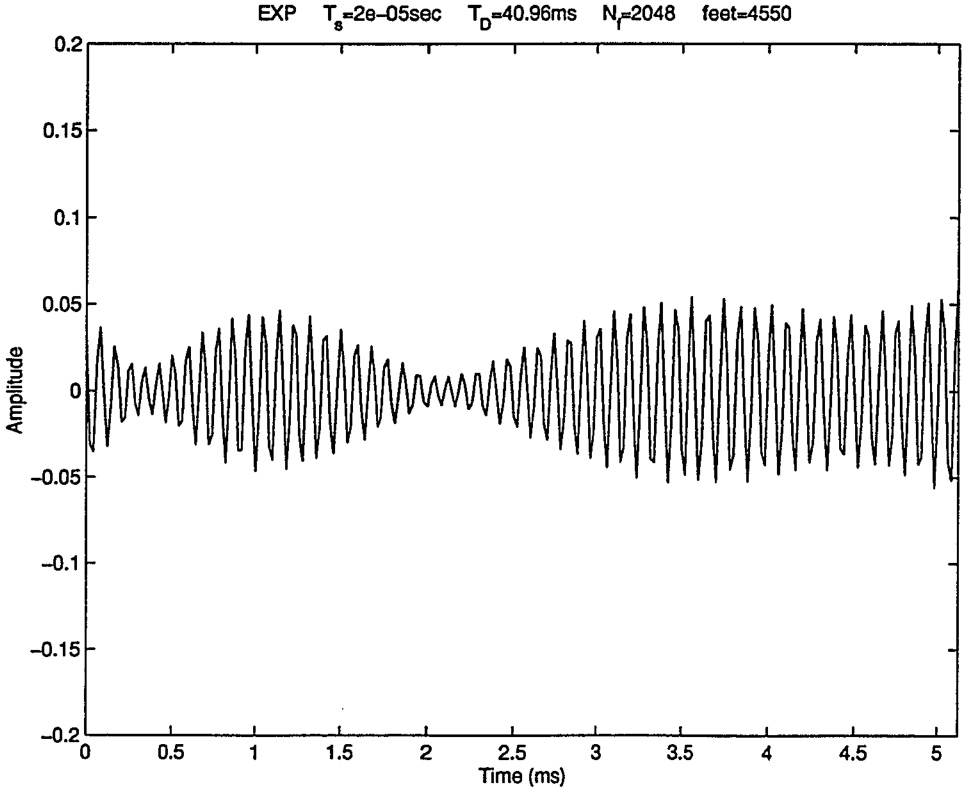

(b) the first eighth

Figure 5.11: Time Waveform of the 16th Trace of a Single Carrier with Strong AM

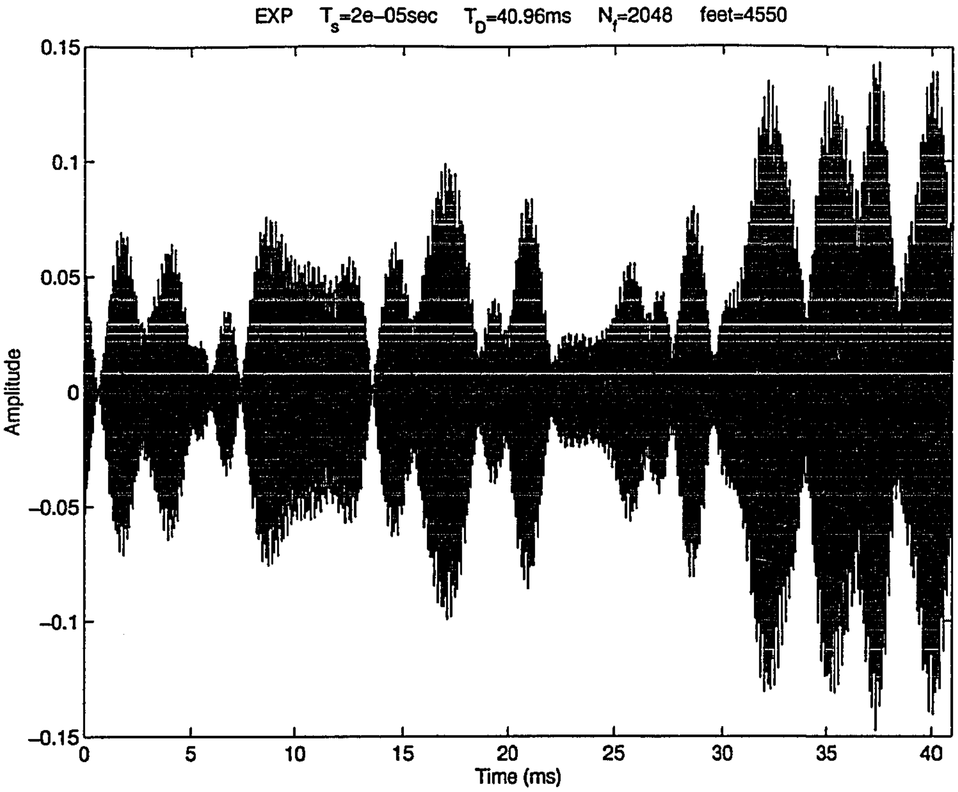

(a) the whole length

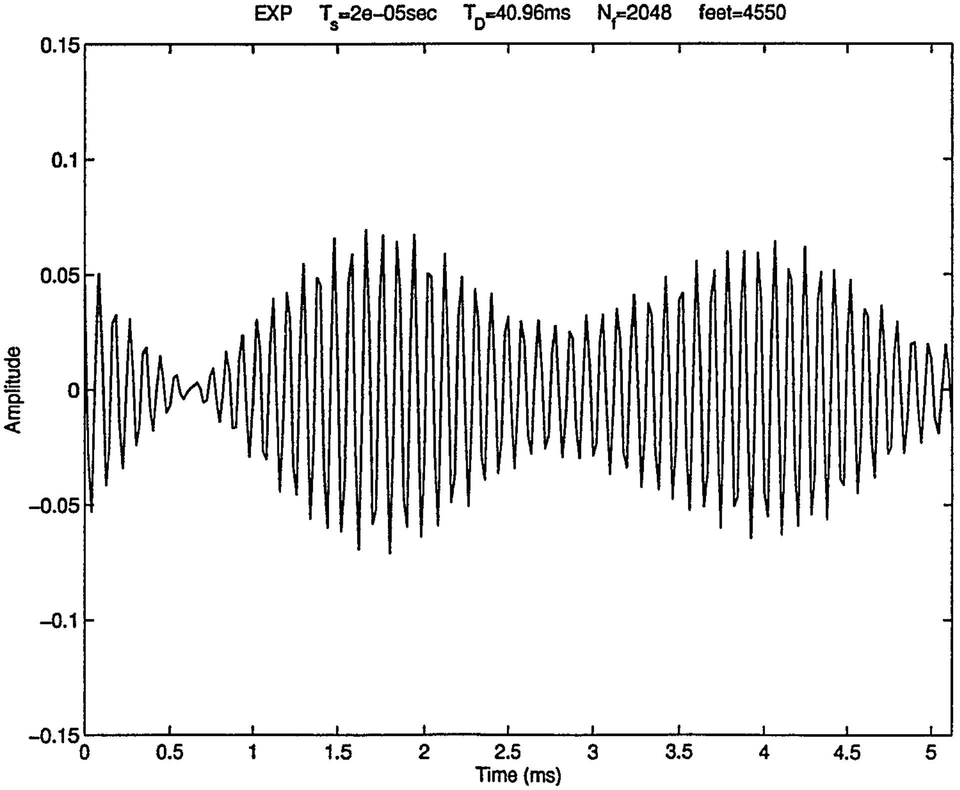

(b) the first eighth

Figure 5.12: Time Waveform of the 17th Trace of a Single Carrier with Strong AM

5.3.2 Single Carrier with Weak AM Interference

In Subsection 4.3.2, we discussed the computer simulation of a single carrier interference with weak AM (see Fig. 4.8). The following presentation serves as experimental support to the discussion associated with the computer simulation shown in Fig. 4.8.

Frequency Plots

We have shown the periodograms and the spectral averages AAS, GAS, and HAS of a single carrier with weak AM interference at a frequency of 12.4 kHz in Fig. 5.13. This kind of interference is close to pure CW interference. Fig. 5.14 provides detailed plots of Fig. 5.13. Due to the weak AM, all of the 24 periodograms in Fig. 5.13(a) have almost the same spectral height. Note that, since the difference between the spectral height of the interference at the frequency of 12.4 kHz and the background-level is more than 20 dB which is the dynamic range used to show each of the 24 periodograms, nothing much can be seen at any frequency apart from the frequency of 12.4 kHz.

We then use the 24 periodograms to calculate the AAS in Fig. 5.13(b), the GAS in Fig. 5.13(c), and the HAS in Fig. 5.13(d), respectively. Note that, in these figures, we use a dynamic range of 40 dB. The carrier peaks for the interference are almost the same which demonstrates that AAS, GAS and HAS working together have the ability to identify the characteristic of the interference, *i.e.*, strong carrier with weak AM modulation.

Time Waveforms

Time waveforms of the 16th and 17th traces of the carrier with weak AM interference at 12.4 kHz are illustrated in Figs. 5.15(a) and 5.16(a), respectively. Both cover a time interval of 40.96 ms which is the value of T_D in this example where T_D is the length of data record used to calculate a periodogram. The first eighth of Figs. 5.15(a) and 5.16(a) can be found in Figs. 5.15(b) and 5.16(b), respectively. Both cover a time interval of 40.96/8 ms. Note that, to create Figs. 5.15 and 5.16, we have used a filter (having a passband from 12.2 kHz to 12.6 kHz) in frequency domain in a line-off manner. The passband of this filter can be seen in Figs. 5.14(b), (c), or (d). More specifically, after we had obtained Fig. 5.13(a), for each of the 24 periodograms, we keep the frequency domain samples within the passband of the filter and replace the remaining points with zeros. Then, we take an inverse FFT on the filtered data obtaining Figs. 5.15 and 5.16, demonstrating that we do have carrier with weak AM interference in this example.

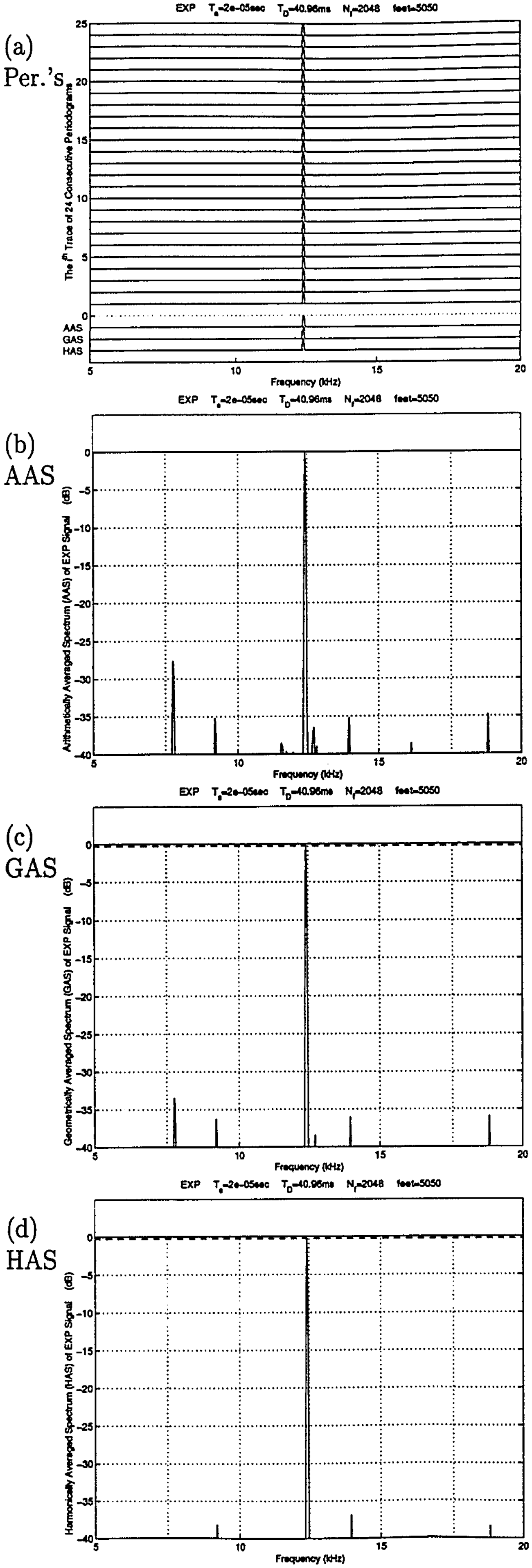

Figure 5.13: Single Carrier with Weak AM

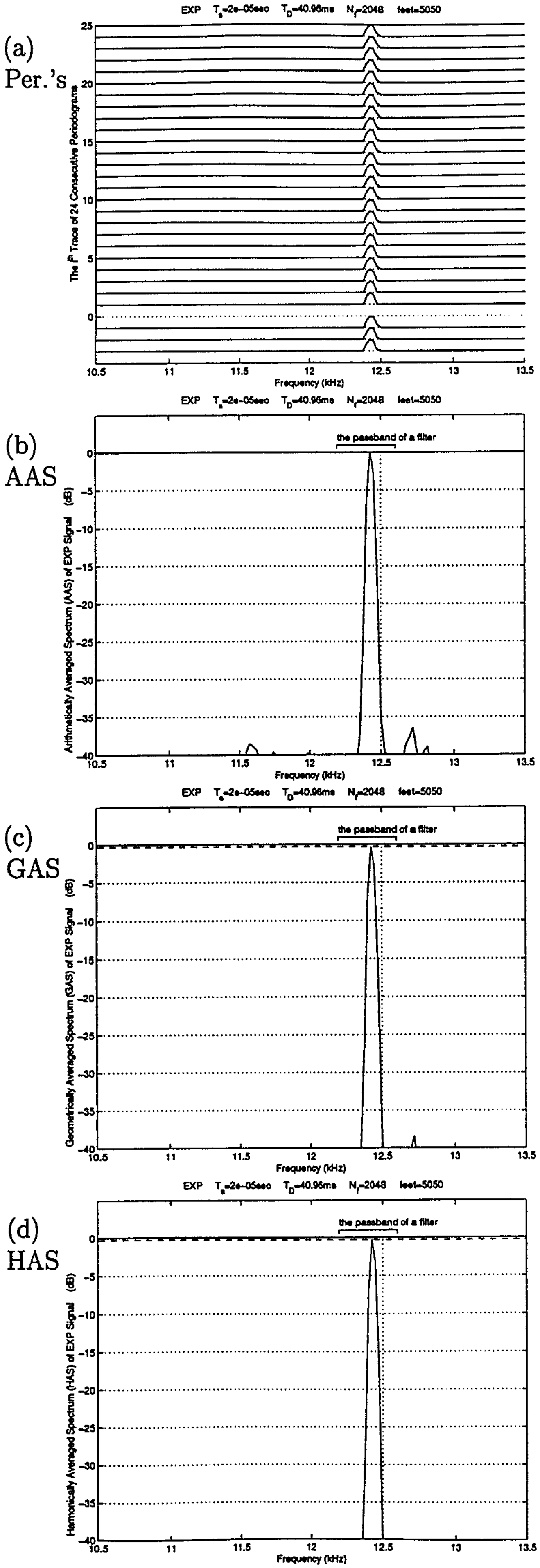

Figure 5.14: Details of the LHS Figure

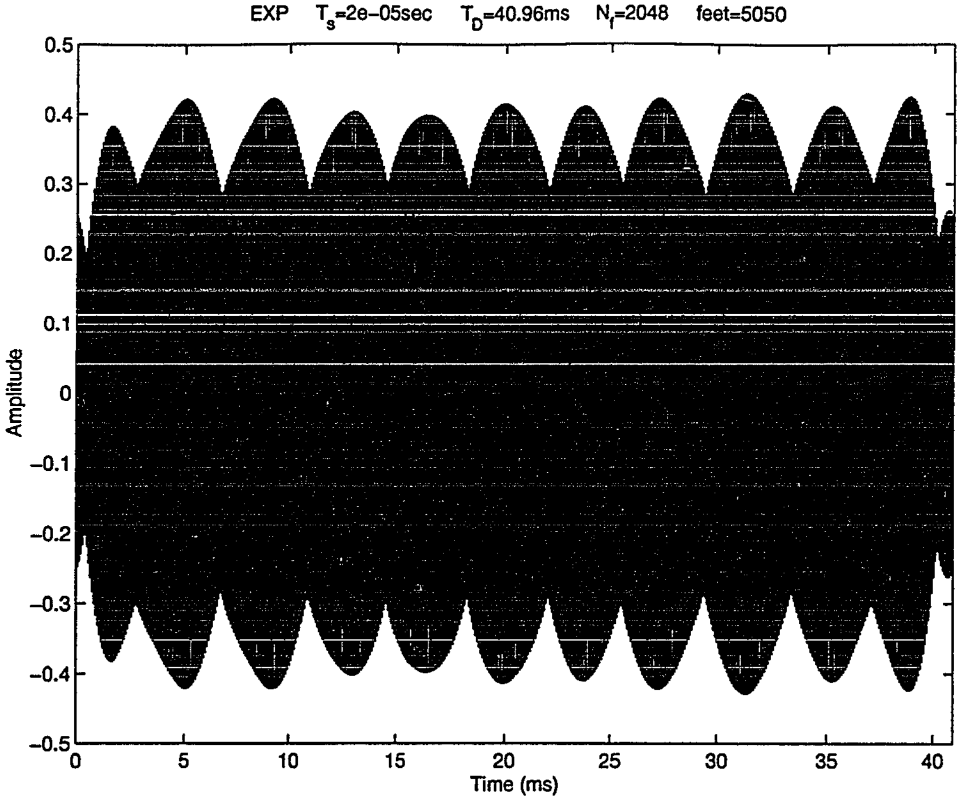

(a) the whole length

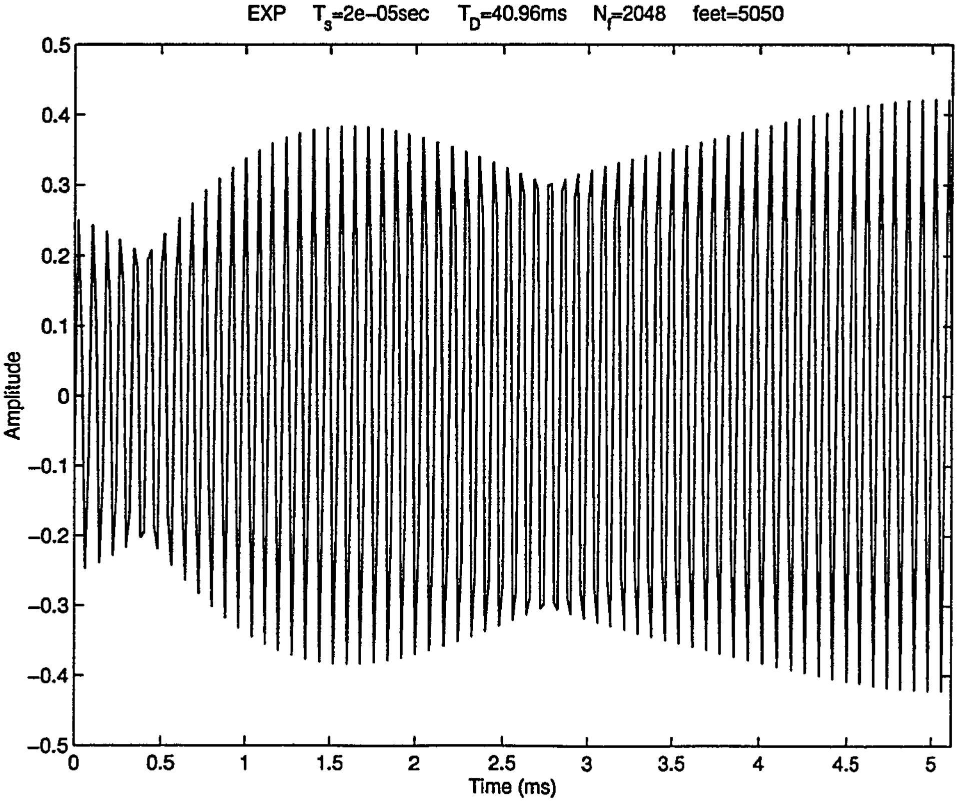

(b) the first eighth

Figure 5.15: Time Waveform of the 16th Trace of a Single Carrier with Weak AM

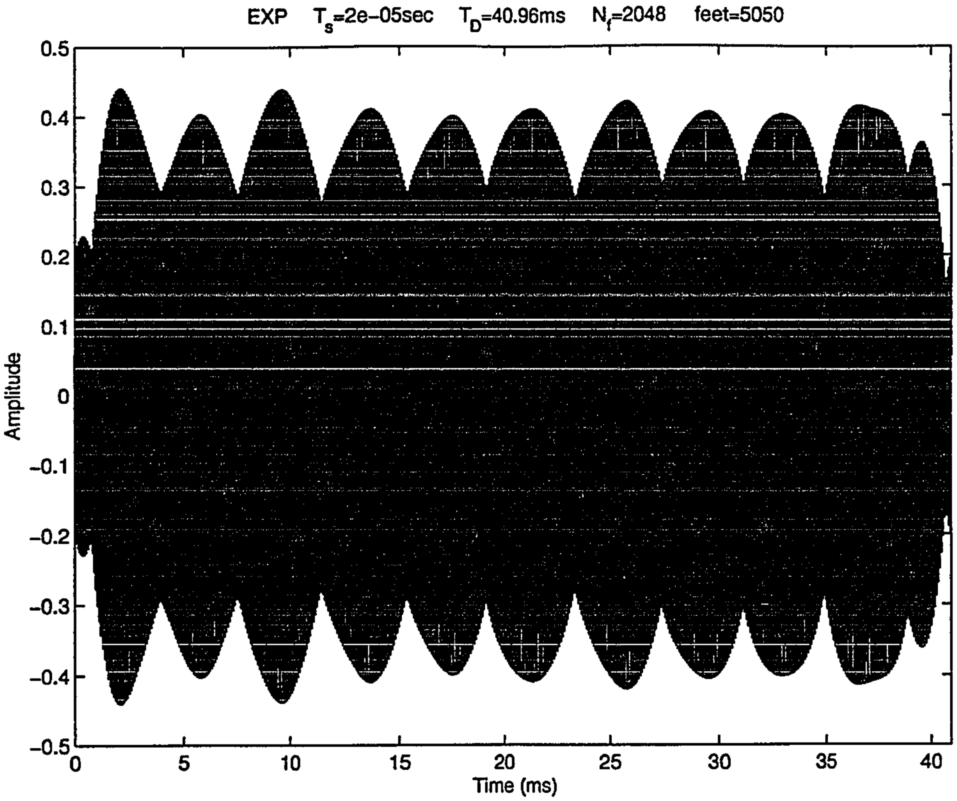

(a) the whole length

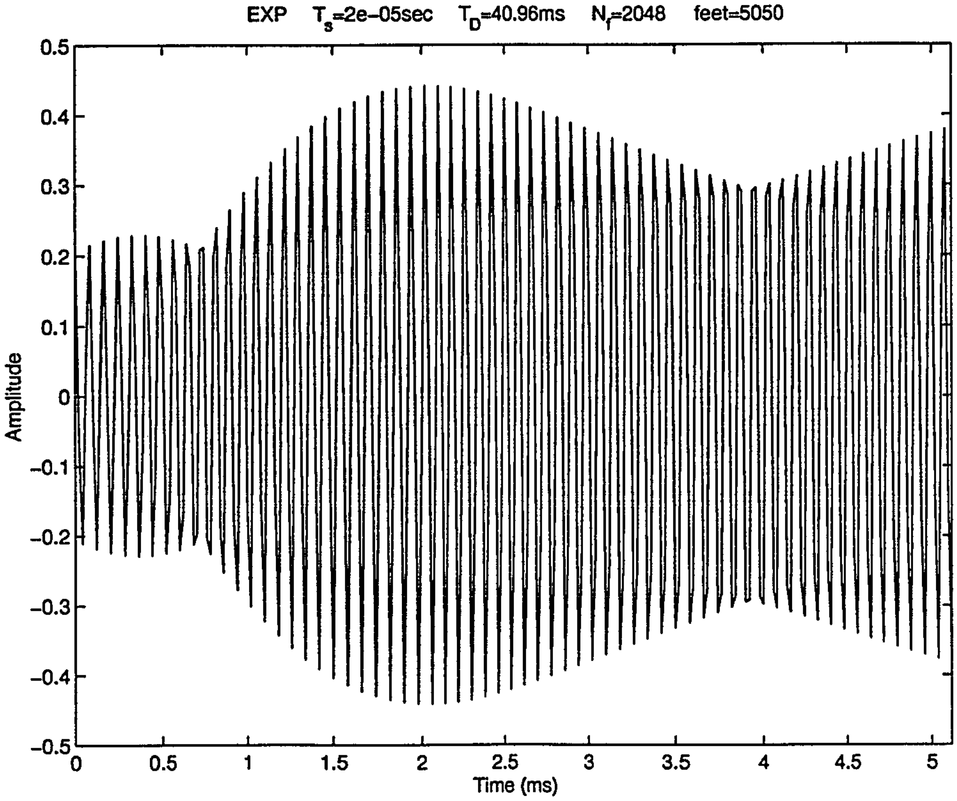

(b) the first eighth

Figure 5.16: Time Waveform of the 17th Trace of a Single Carrier with Weak AM

5.4 On-Off Modulation Interference

In Section 4.4, we discussed the computer simulation of On-Off modulation interference suppression (see Figs. 4.9 and 4.10). The following presentation serves as experimental support to the discussion associated with the computer simulation shown in Figs. 4.9 and 4.10.

The periodograms and spectral averages AAS, GAS, and HAS of an On-Off modulation interference having a carrier frequency of 7.9 kHz is illustrated in Fig. 5.17, respectively. Fig. 5.18 provides detailed plots of Fig. 5.17.

We observe in Fig. 5.17(a) that due to the On-Off modulation, not all of the 24 periodograms have the same spectral height at the frequency of 7.9 kHz. Note that, the interference is "On" from periodogram 1 to periodogram 8 and "Off" from periodogram 9 to periodogram 24, so the name On-Off modulation interference. We have used 20 dB as the dynamic range to show each of the 24 periodograms in Fig. 5.17(a).

Then we employ these 24 periodograms to calculate the AAS in Fig. 5.17(b), the GAS in Fig. 5.17(c), and the HAS in Fig. 5.17(d), respectively, using a dynamic range of 40 dB.

The interference spectral peak at 7.9 kHz in Fig. 5.17(b) is about 10 dB higher than the surrounding background while the ELT signal peak at about 11 kHz is 4 dB higher than the surrounding background. In Fig. 5.17(c), the interference spectral peak is only 5 dB higher than the surrounding background while the ELT signal peak is 3 dB higher than the surrounding background. Thus, the GAS has reduced the On-Off Modulation interference by 4 dB relative to the ELT signal.

The interference spectral peak at 7.9 kHz in Fig. 5.17(b) is about 10 dB higher than the surrounding background while the ELT signal peak at about 18 kHz is 5 dB higher than the surrounding background. In Fig. 5.17(c), the interference spectral peak is only 5 dB higher than the surrounding background while the ELT signal peak is 3 dB higher than the surrounding background. Thus, the GAS has reduced the On-Off Modulation interference by 3 dB relative to the ELT signal.

The interference spectral peak at 7.9 kHz in Fig. 5.17(b) is about 10 dB higher than the surrounding background while the almost CW carrier peak at 19.4 kHz is 17 dB higher than the surrounding background. In Fig. 5.17(c), the interference spectral peak is only 5 dB higher than the surrounding background while the almost CW carrier peak is 20 dB higher than the surrounding background. Thus, the GAS has reduced the On-Off Modulation interference by 8 dB relative to the almost CW carrier.

In Fig. 5.17(d) for HAS, it can be seen that the On-Off Modulation interference spectral peak at 7.9 kHz and the ELT signal peak at about 11 kHz essentially vanish while the CW carrier peak at 19.4 kHz is 23 dB higher than the surrounding background.

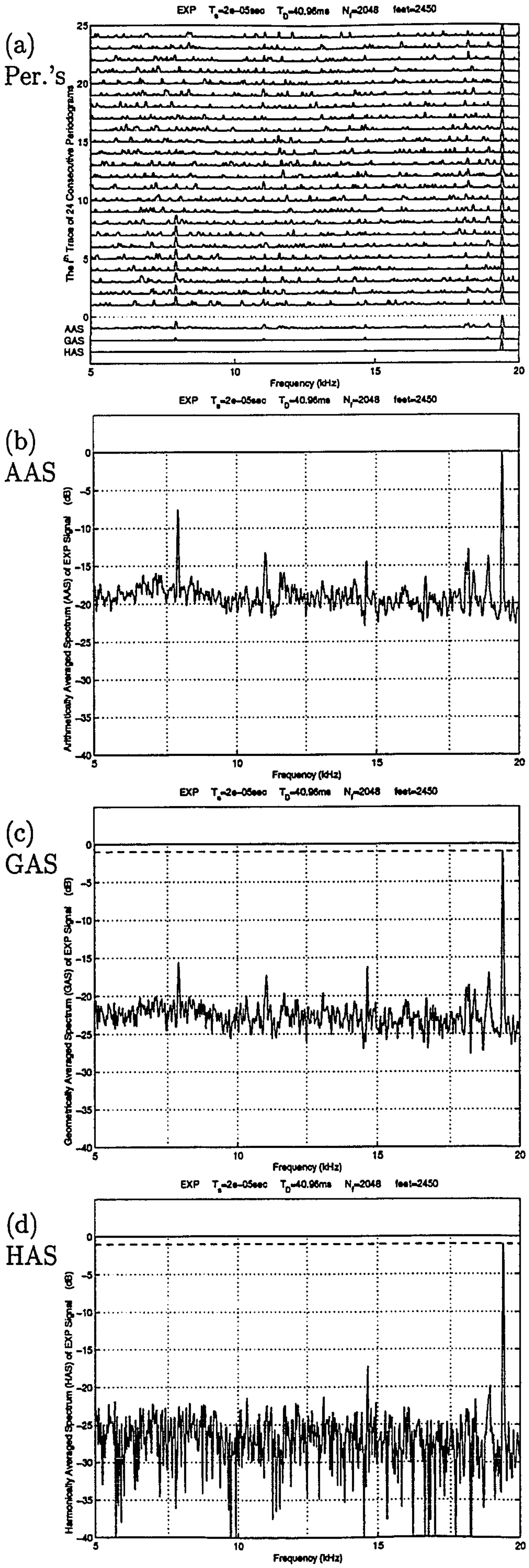

Figure 5.17: On-Off Modulation

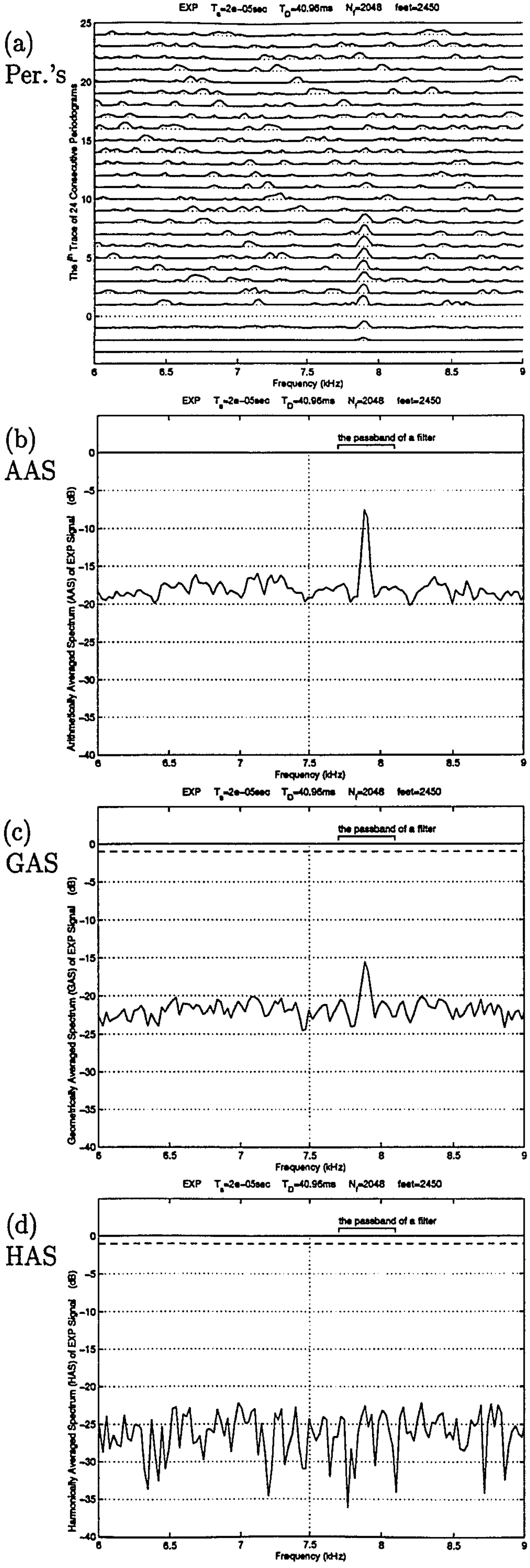

Figure 5.18: Details of the LHS Figure

5.5 Swept Carrier Interference

In Section 4.5, we discussed the computer simulation of swept carrier interference suppression (see Figs. 4.11 through 4.15). The following presentation serves as experimental support.

5.5.1 Frequency Plots

The periodograms and spectral averages AAS, GAS, and HAS of two swept carrier interferences (whose carrier frequencies sweep from 15.1 kHz to 14.5 kHz in Fig. 5.19 and from 14.1 kHz to 13.7 kHz in Fig. 5.21, respectively) represent the 1st and 2nd examples, respectively. Fig. 5.20 and Fig. 5.22 provide the detailed plots of Fig. 5.19 and Fig. 5.21, respectively.

Firstly, we observe Fig. 5.19(a) where the interference sweeps from its original position at the frequency of 15.1 kHz on periodogram 20 to its final position at the frequency of 14.5 kHz on periodogram 24. Note that, since the difference between the spectral height of the interference within the frequency interval from 14.5 kHz to 15.1 kHz and the background-level is more than 20 dB which is the dynamic range used to show each of the 24 periodograms, only a few small ripples can be seen on the other periodograms apart from periodograms 20 through 24 and at some frequencies apart from the frequency interval from 14.5 kHz to 15.1 kHz on periodograms 20 through 24 in Fig. 5.19(a).

Employing these 24 periodograms, calculate the AAS in Fig. 5.19(b), the GAS in Fig. 5.19(c), and the HAS in Fig. 5.19(d), respectively, using a dynamic range of

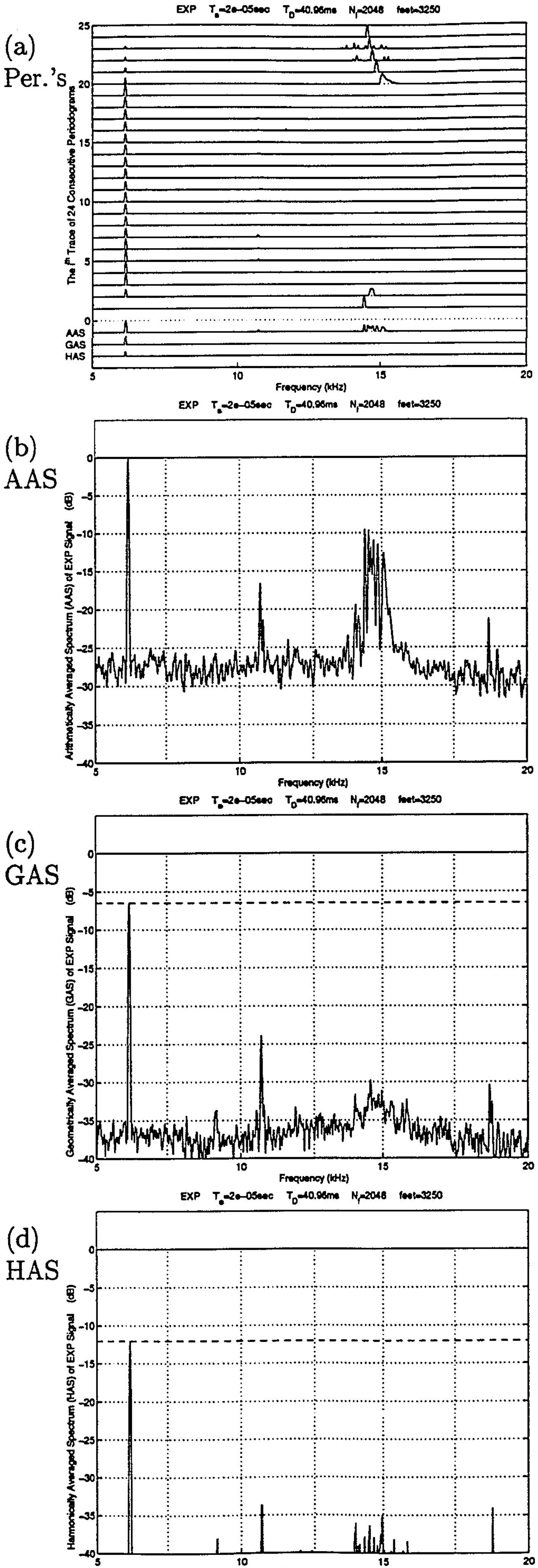

Figure 5.19: Swept Carrier Interference (1)

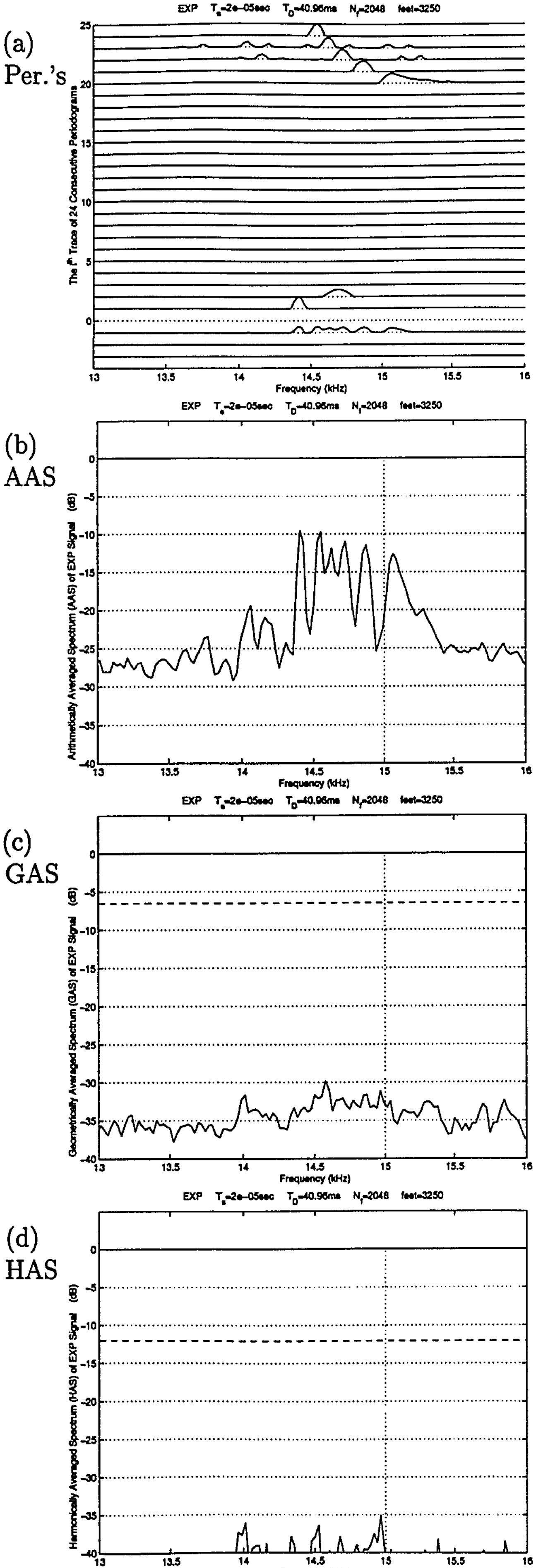

Figure 5.20: Details of the LHS Figure

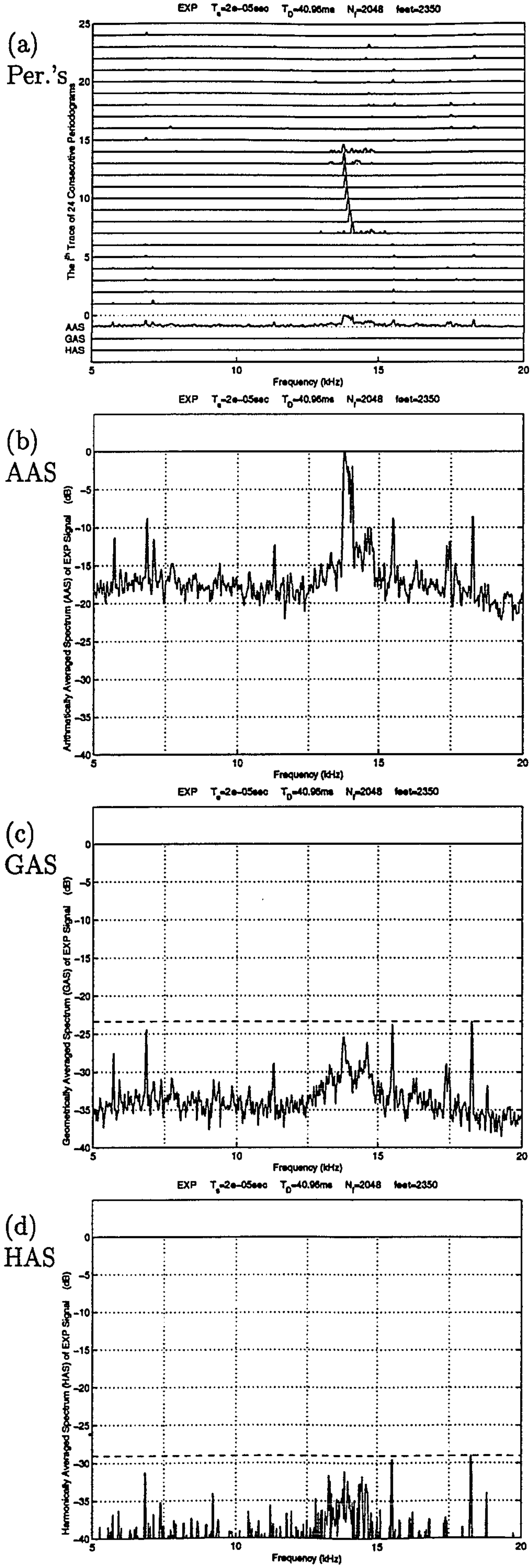

Figure 5.21: Swept Carrier Interference (2)

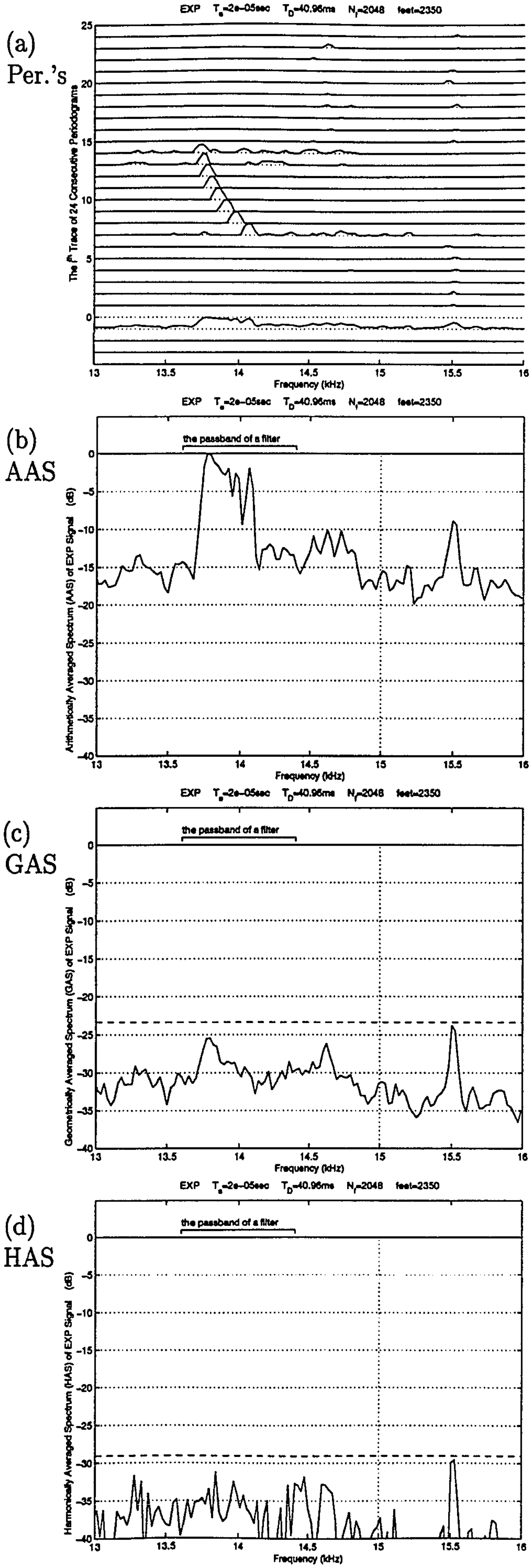

Figure 5.22: Details of the LHS Figure

40 dB. The AAS plot shows the Swept Carrier interference to be 15 to 17 dB above the background. Contrast this with the GAS plot and the HAS plot where the Swept Carrier interference has been almost eliminated entirely.

Secondly, we observe Fig. 5.21(a) where the interference sweeps from its original position at the frequency of 14.1 kHz on periodogram 7 to its final position at the frequency of 13.7 kHz on periodogram 14. Note that, since the difference between the spectral height of the interference within the frequency interval from 13.7 kHz to 14.1 kHz and the background-level is more than 20 dB which is the dynamic range used to show each of the 24 periodograms, only a few small ripples can be seen on the other periodograms apart from periodograms 7 through 14 and at some frequencies apart from the frequency interval from 13.7 kHz to 14.1 kHz on periodograms 7 through 14 in Fig. 5.21(a).

Employing these 24 periodograms, calculate the AAS in Fig. 5.21(b), the GAS in Fig. 5.21(c), and the HAS in Fig. 5.21(d), respectively, using a dynamic range of 40 dB. The AAS plot shows the Swept Carrier interference to be 15 to 17 dB above the background. Contrast this with the GAS plot and the HAS plot where the Swept Carrier interference has been almost eliminated entirely.

5.5.2 ICE Signal Detection in Swept Carrier Interference

We have shown the periodograms and spectral averages AAS, GAS, and HAS of an ICE signal having a carrier peak at 14.015 kHz in Fig. 5.23 while Fig. 5.24 provides detailed plots of Fig. 5.23. It can be seen in Fig. 5.23(a) that from the first periodogram to the last periodogram the carrier peak keeps the same height.

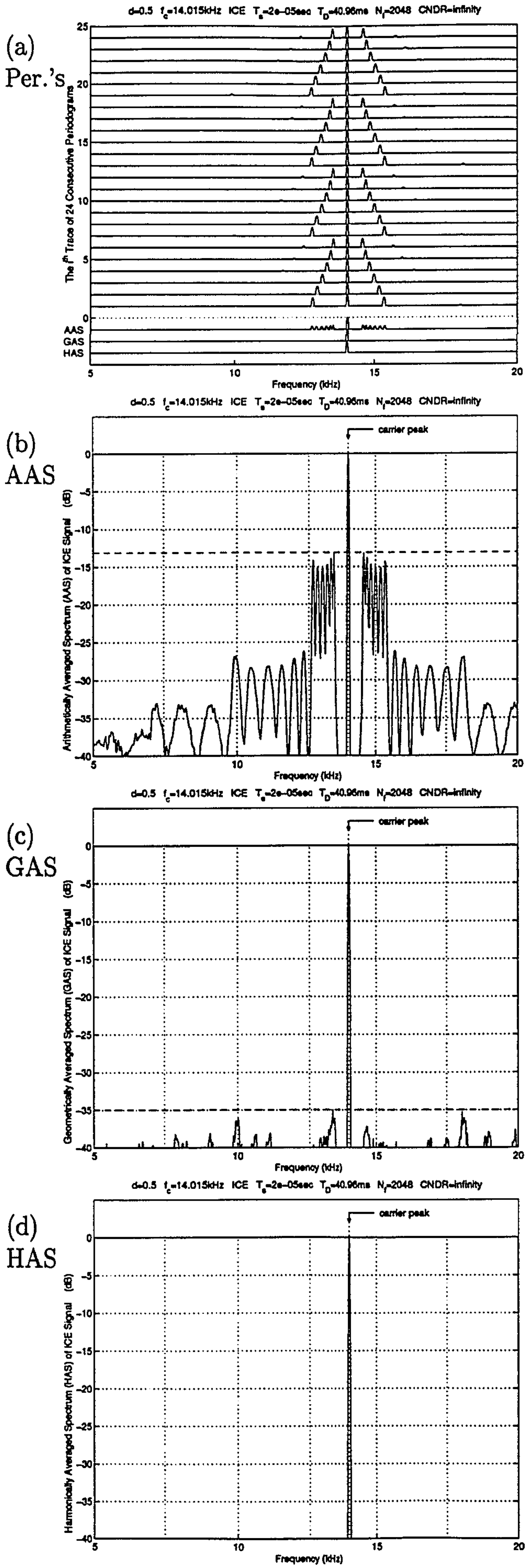

Figure 5.23: An ICE Signal at 14.015 kHz

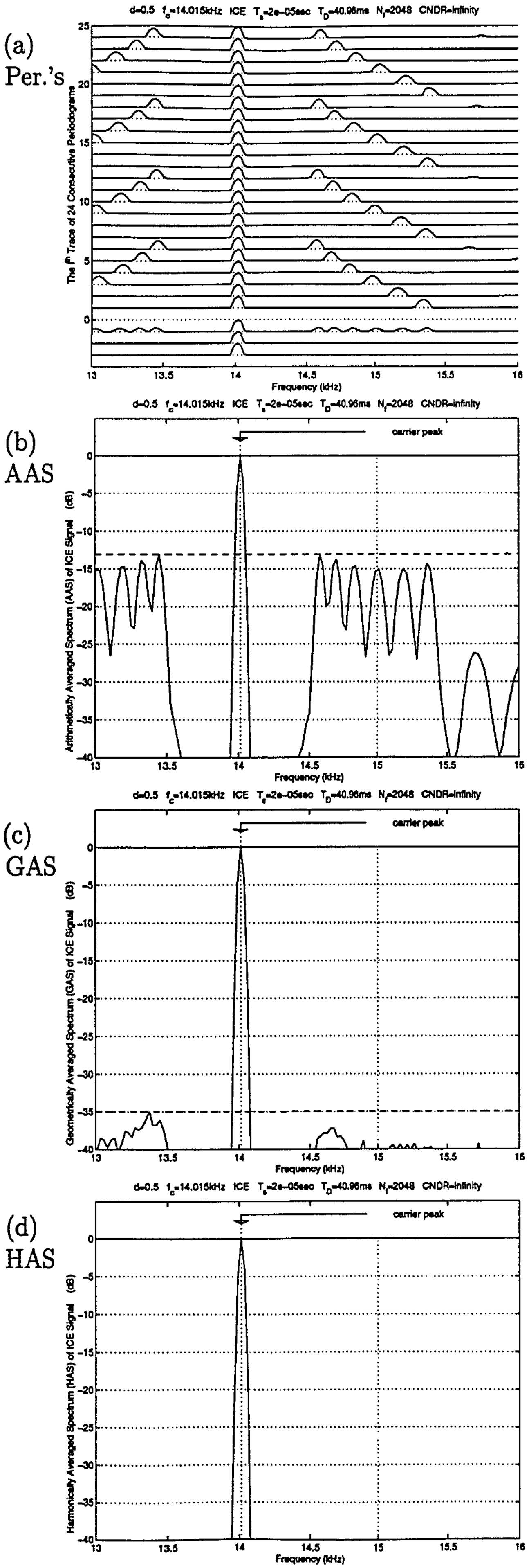

Figure 5.24: Details of the LHS Figure

Due to this fact and (2.2.30), for the AAS in Fig. 5.23(b), the GAS in Fig. 5.23(c), and the HAS in Fig. 5.23(d), the carrier peaks have the same height which has been normalized to 0 dB. Also, it can be seen in Fig. 5.23(a) that from the first periodogram to the last periodogram, the lower sideband peak and the upper sideband peak move in a symmetric way. Due to this fact and (2.2.31), the lower frequency sideband and the upper frequency sideband presented by the AAS in Fig. 5.23(b) disappear almost completely from the GAS in Fig. 5.23(c) and disappear completely from the HAS in Fig. 5.23(d).

If we add this ICE signal to the background shown in Fig. 5.21 whose detailed plots are provided in Fig. 5.22, then the periodograms and spectral averages AAS, GAS, and HAS of this ICE signal plus a swept carrier interference are what are shown in Fig. 5.25 while Fig. 5.26 provides detailed plots of Fig. 5.25. One cannot find any difference between Fig. 5.21(a) which is due to real Swept Carrier interference from 13.7 kHz to 14.1 kHz only and Fig. 5.25(a) which is due to an ICE signal (having carrier frequency of 14.015 kHz) immersed in real Swept Carrier interference from 13.7 kHz to 14.1 kHz. This observation applies to the comparison between Fig. 5.21(b) and Fig. 5.25(b) in a similar way. That is, the AAS completely fails in detecting the ICE signal immersed in real Swept Carrier interference in this example. However, things change in the GAS shown in Fig. 5.25(c) where we have an ICE carrier peak which is 16 dB above the background noise level and in the HAS shown in Fig. 5.25(d) where we have an ICE carrier peak which is 20 dB above the background noise level. It is obvious that both GAS and HAS offer a performance which is much better than what can be provided by AAS in this example.

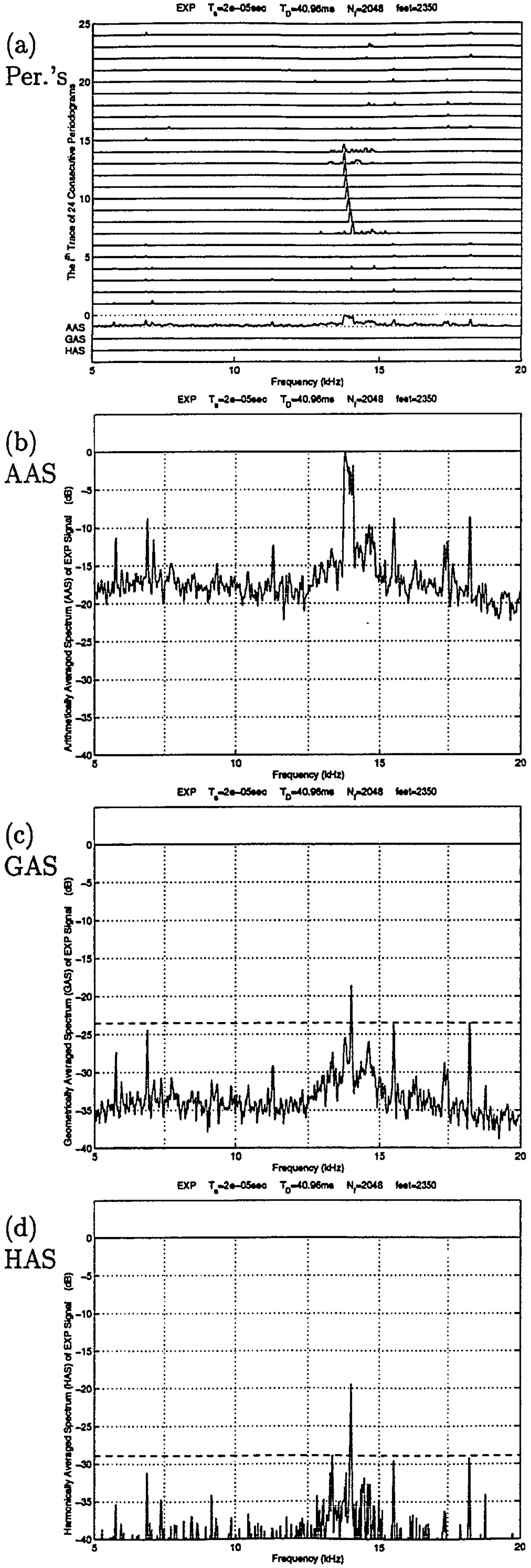

Figure 5.25: ICE Signal plus Swept Carrier

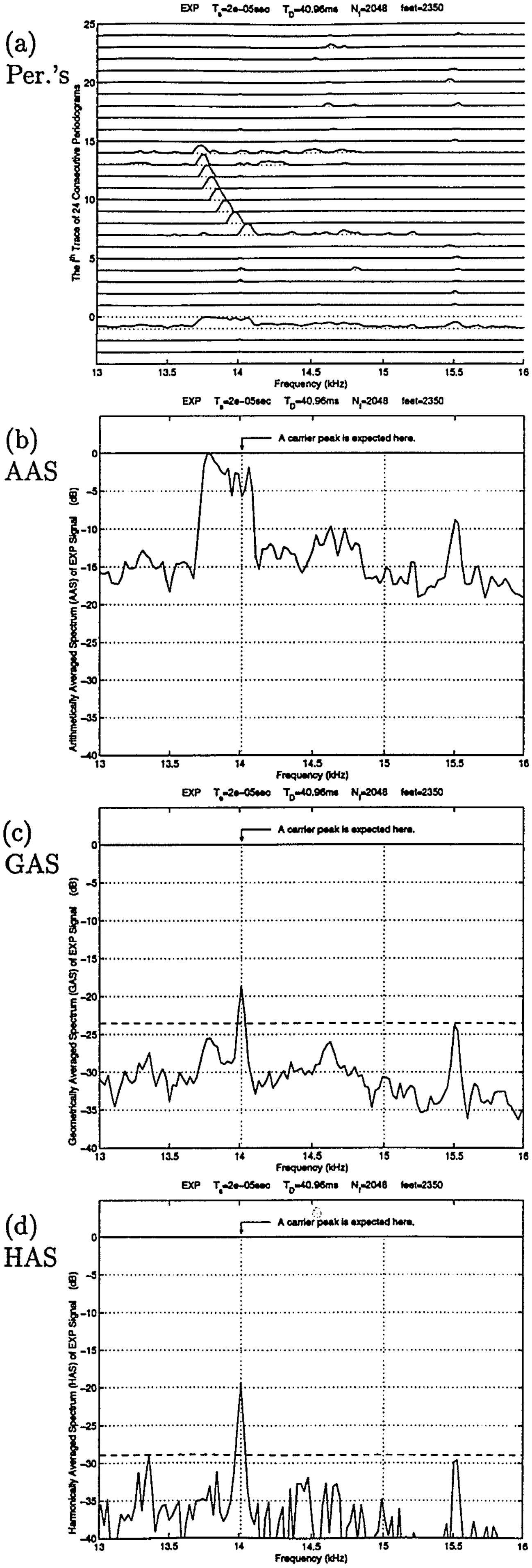

Figure 5.26: Details of the LHS Figure

5.6 Random Interference

An example of Random interference obtained from real satellite pass data is presented in Fig. 5.27. Detailed plots are provided in Fig. 5.28.

In Fig. 5.27(a), which covers the frequency range from 5 kHz to 20 kHz, there are many ubiquitous frequency buds between 7 kHz and 10 kHz and carrier peaks at 5.5 kHz and 8.2 kHz. Comparing Figs. 5.27(b), 5.27(c) and 5.27(d) which display the AAS, GAS and HAS plots, it is clear that the Random interference is reduced by the two latter averaging techniques. Had the carrier peak at 8.2 kHz been due to an ELT signal, then its presence would have been enhanced.

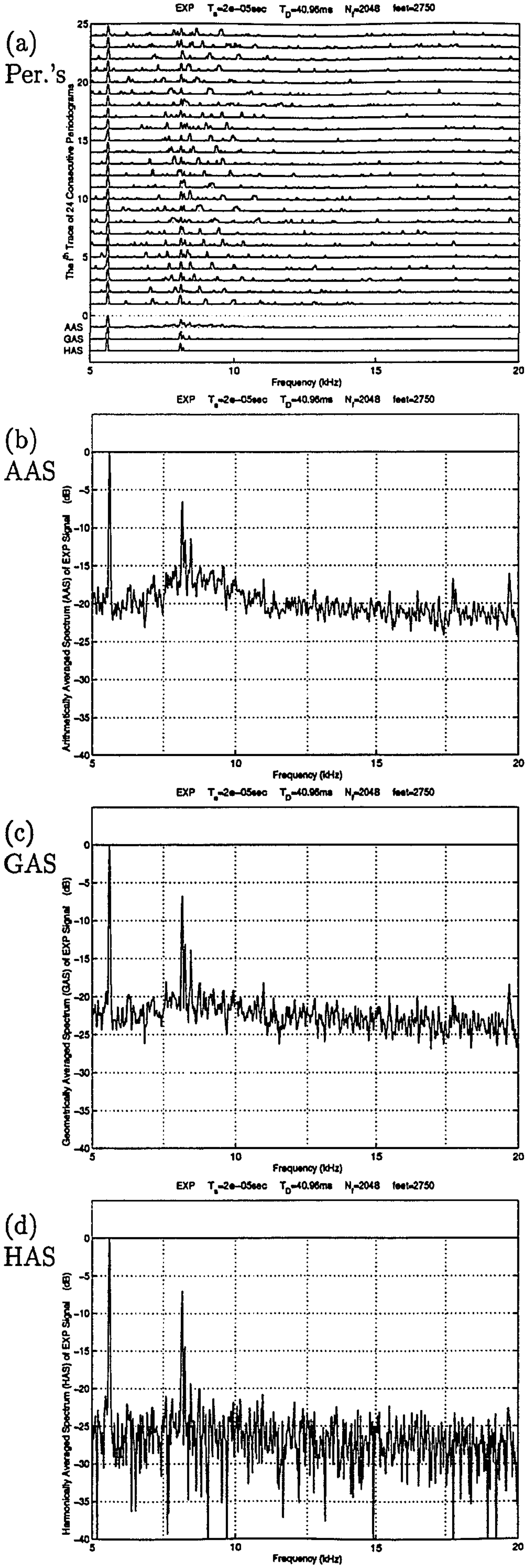

Figure 5.27: Random Interference

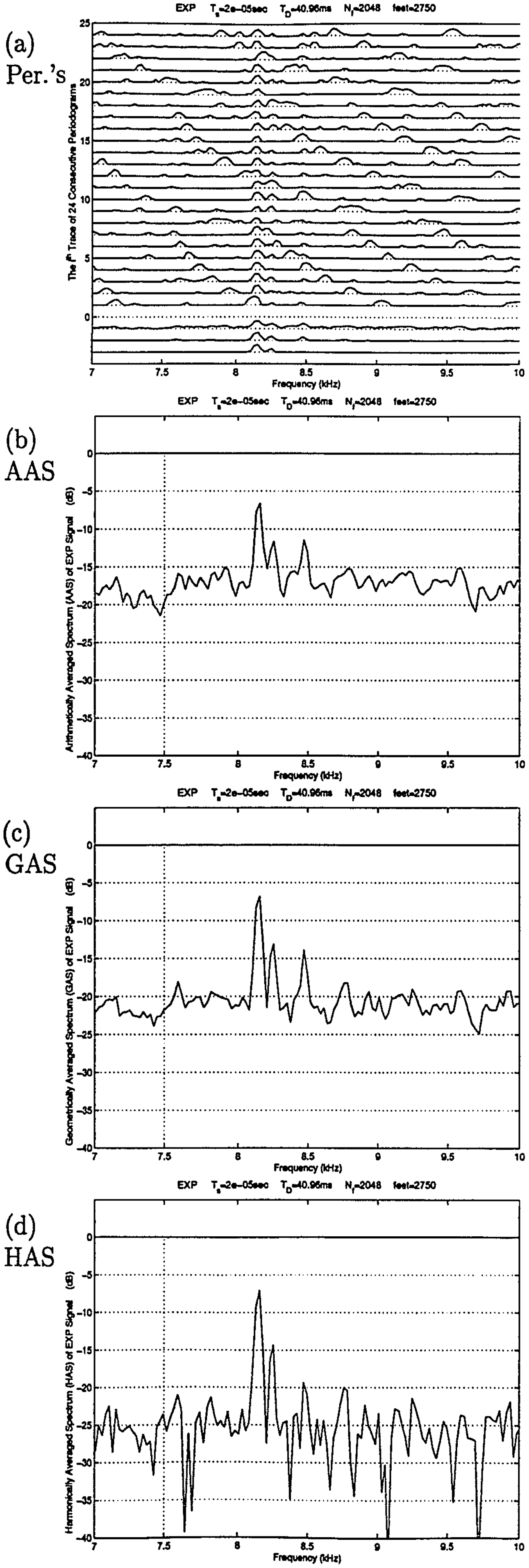

Figure 5.28: Details of the LHS Figure

5.7 ICE and NIC Model SARSAT Data

5.7.1 Real ICE Signal

In Subsection 2.3.1, we discussed the ICE signal model. The following presentation serves as experimental support for the discussion associated with the ICE signal model. We have shown the periodograms and spectral averages AAS, GAS, and HAS of an ELT signal (whose carrier frequency is about 14.2 kHz) in Fig. 5.29. This ELT signal is recognized as a "good" ELT signal. The most convincing characteristics can be seen in 5.29(a) where we use 20 dB as the dynamic range. At every one of these 24 consecutive periodograms, the carrier peak is stable at about 14.2 kHz. In addition, from the 1st periodogram to the 24th periodogram, a lower sideband peak moves from 12.6 kHz to 14.2 kHz while an upper sideband peak moves from 15.8 kHz to 14.2 kHz. Since the lower frequency sideband and the upper frequency sideband are symmetric around the carrier frequency peak at 14.2 kHz, this ELT signal is a real ICE signal.

Note that, all of the 24 periodograms have almost the same spectral height at the frequency of 14.2 kHz.

Plots of the AAS, GAS and HAS are provided in Figs. 5.29(b), 5.29(c) and 5.29(d), respectively, where we have used a dynamic range of 40 dB. The ELT carrier peak of the AAS plot is about 10 dB higher than the background. For the GAS and HAS plots, these values are 12 dB and 13 dB, respectively. Fig. 5.30 provides the detailed plots of Fig. 5.29.

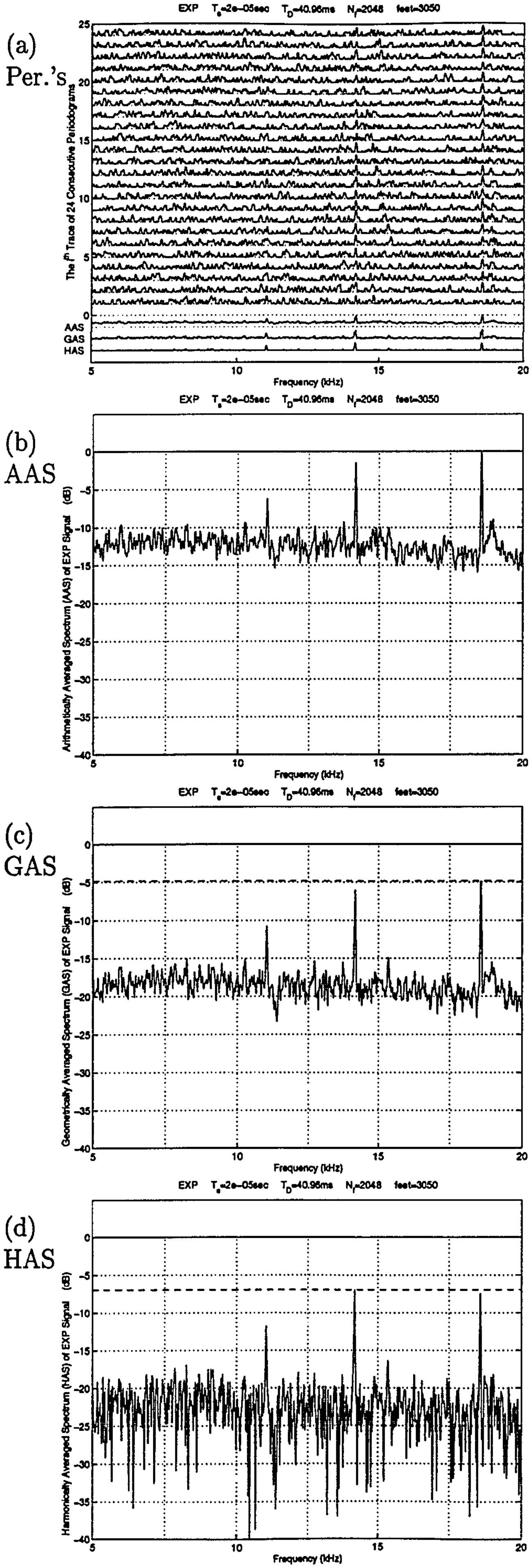

Figure 5.29: Real ICE Signal

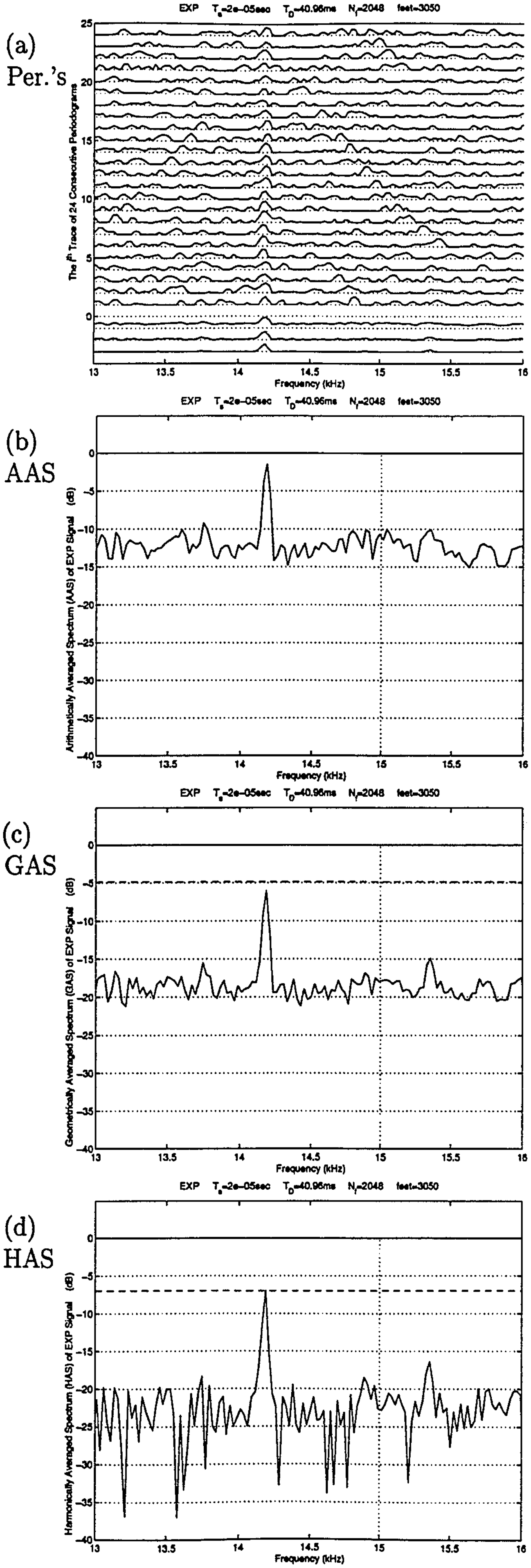

Figure 5.30: Details of the LHS Figure

5.7.2 Real NIC Signal

In Subsection 2.3.2, we discussed the NIC signal model. The following presentation serves as experimental evidence. During our investigation of the tape recorded data, a NIC similar to a NARCO signal [12] having a carrier peak at about 17 kHz was recognized along with several CW interfering sources and an FME signal at 19 kHz. The periodograms and spectral averages AAS, GAS, and HAS are shown in Fig. 5.31. The characteristics can be seen in 5.31(a). For most of these 24 consecutive periodograms, the carrier peak is stable at the position of about 17 kHz although for some periodograms the carrier peak cannot be seen due to the 20 dB dynamic range. The lower frequency sideband moves from 15.5 kHz to 16.5 kHz while the upper frequency sideband cannot be seen due to the 20 dB dynamic range. Since the lower frequency sideband and the upper frequency sideband are not symmetric, with respect to the carrier frequency at 17 kHz, this ELT signal is an NIC signal.

Then we use the 24 periodograms shown in Fig. 5.31(a) to calculate the AAS in Fig. 5.31(b), the GAS in Fig. 5.31(c), and the HAS in Fig. 5.31(d), respectively, using a dynamic range of 40 dB. Fig. 5.32 provides detailed plots. The carrier peak for the NIC signal is about 8 dB higher than the background for both AAS and GAS averaging. However, for HAS averaging, the spectral peak is almost eliminated since there is too much variation in this peak for HAS to be of value.

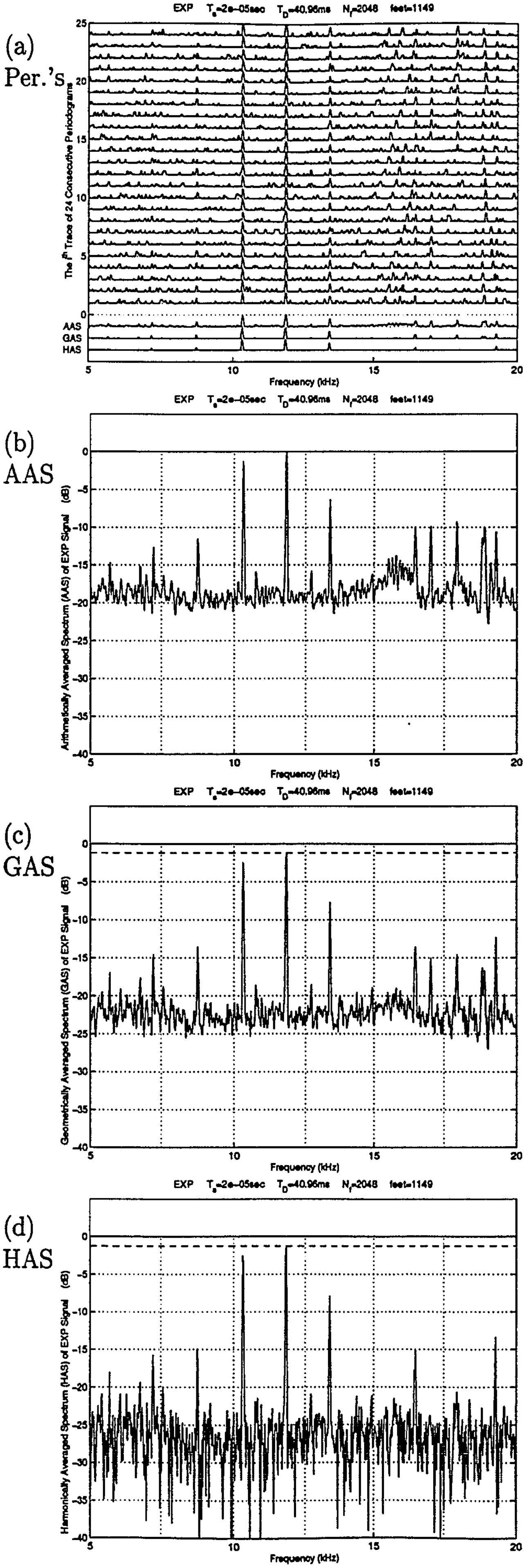

Figure 5.31: Real NIC Signal

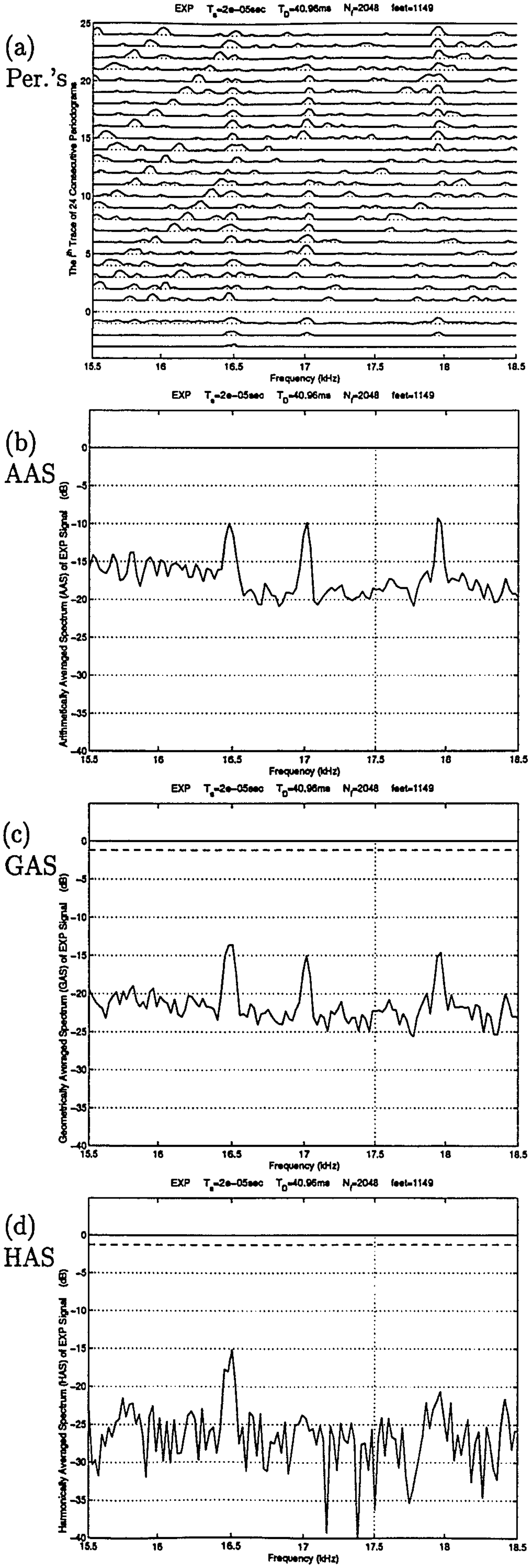

Figure 5.32: Details of the LHS Figure

5.8 FME Model SARSAT Data

5.8.1 Signal Identification

In Subsection 2.3.4, we discussed the FME signal model. The following presentation serves as experimental support to the discussion associated with the FME signal model. By investigating the tape recorded data, we found an ELT signal which can be represented by the FME model. The periodograms and spectral averages AAS, GAS, and HAS show an FME signal in the neighborhood of 18.5 kHz in Fig. 5.33 (details in Fig. 5.34). We observe in Fig. 5.33(a) that the ELT signal at the frequency of 18.5 kHz is a possible FME signal. Note the dynamic range is 20 dB. The most convincing characteristics can be presented as follows. The carrier peak is not stable over the 24 consecutive periodograms. Rather, from periodogram 1 to periodogram 6, from periodogram 7 to periodogram 17, and from periodogram 18 to periodogram 24, the carrier peak moves gradually to the left. Moreover, from the 6th periodogram to the 16th periodogram, for example, the lower frequency sideband moves from 17.0 kHz to 18.0 kHz while the upper frequency sideband moves from 20.0 kHz to 19.0 kHz. That is, the lower frequency sideband and the upper frequency sideband are nearly symmetric with respect to the carrier frequency. Thus, it appears that this ELT signal is an FME signal.

For this FME signal, all of the carrier peaks of the 24 periodograms have almost the same spectral height in the neighborhood of 18.5 kHz.

Then, we use the 24 periodograms shown in Fig. 5.33(a) to calculate the AAS in Fig. 5.33(b), the GAS in Fig. 5.33(c), and the HAS in Fig. 5.33(d), respectively. Note

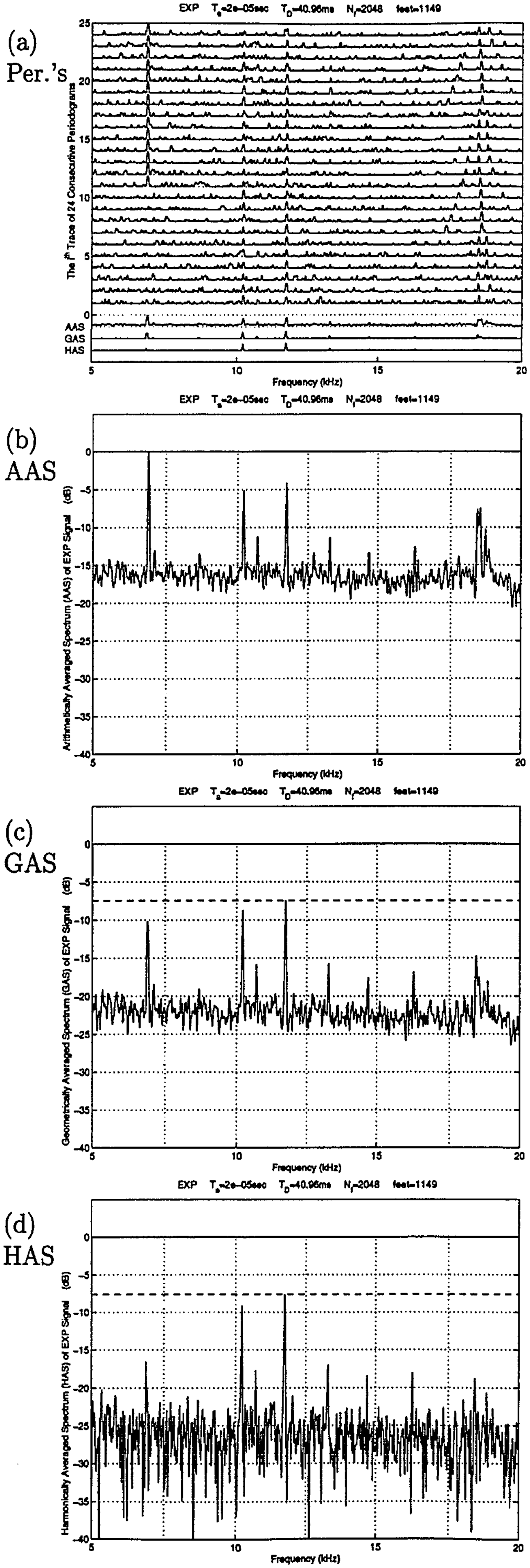

Figure 5.33: Carrier Instability of Signal

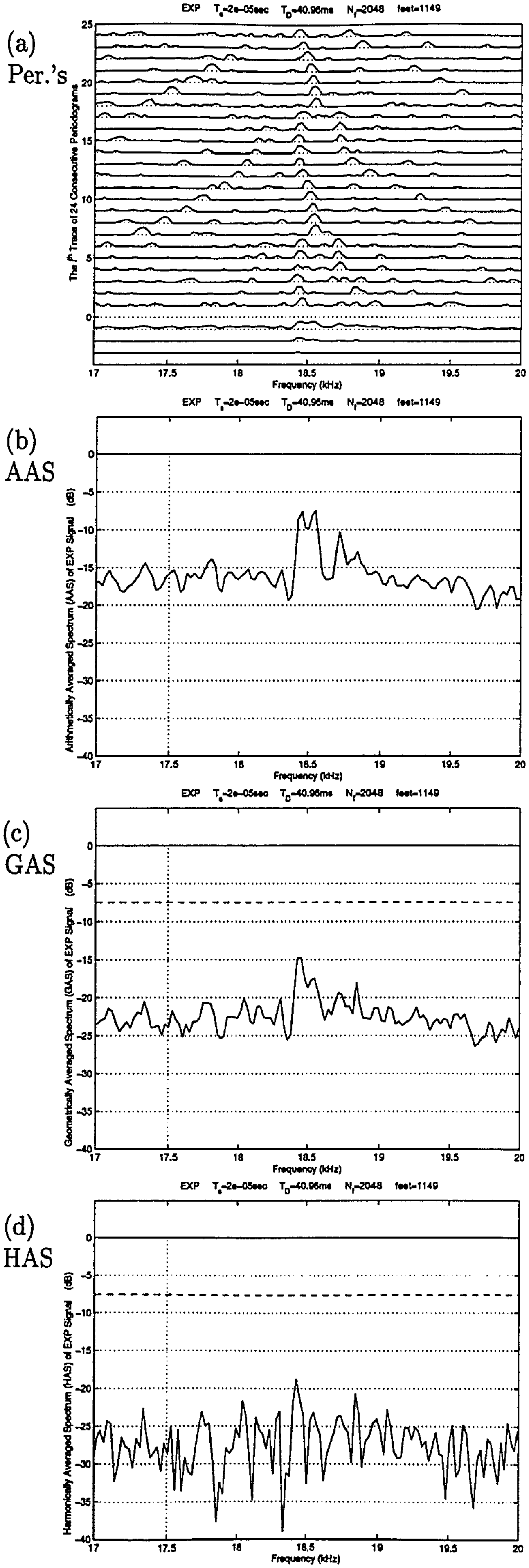

Figure 5.34: Details of the LHS Figure

that, these carrier peaks have become so wide that it is hard to call them the carrier peaks. The detailed AAS spectrum, shown in Fig. 5.34(b) exhibits the expected FM shape described in Fig. 2.24 while the GAS and HAS spectral averages tend to create a single peak. Obviously, a combination of all three averages could be of benefit in identifying the FME signal and measuring the carrier peak.

5.8.2 Signal Analysis

We have re-produced Fig. 5.33(a) in the expanded plot of Fig. 5.35. By checking the frequency range from 18.359 kHz to 18.652 kHz, which has been shown in Fig. 5.35, it can be seen that the carrier peaks of this FME signal move right to left from a center frequency of 18.506 kHz. Note that, our FFT frequency bin width is equal to

$$W_{\text{bin}} = \frac{50000}{2048} \approx 24.41 \text{ Hz} \tag{5.8.2}$$

where 50000 samples per second is the sampling rate and 2048 is the number of samples used in an FFT in this example. Therefore, 18.359 kHz, 18.506 kHz, and 18.652 kHz are actually the 752nd, 758th, and 764th bin frequencies, respectively.

Based on this observation, we find that a small adjustment in the frequency domain can be done in this kind of situation. Specifically, we line up the maximum value points within the frequency range from 18.359 kHz to 18.652 kHz onto the center frequency 18.506 kHz. After this adjustment, the new periodograms and the AAS, GAS, and HAS of this FME signal are shown in Fig. 5.36 with details in Fig. 5.37. By comparing Figs. 5.33 and 5.34 with Figs. 5.36 and 5.37, the improvement can be easily appreciated.

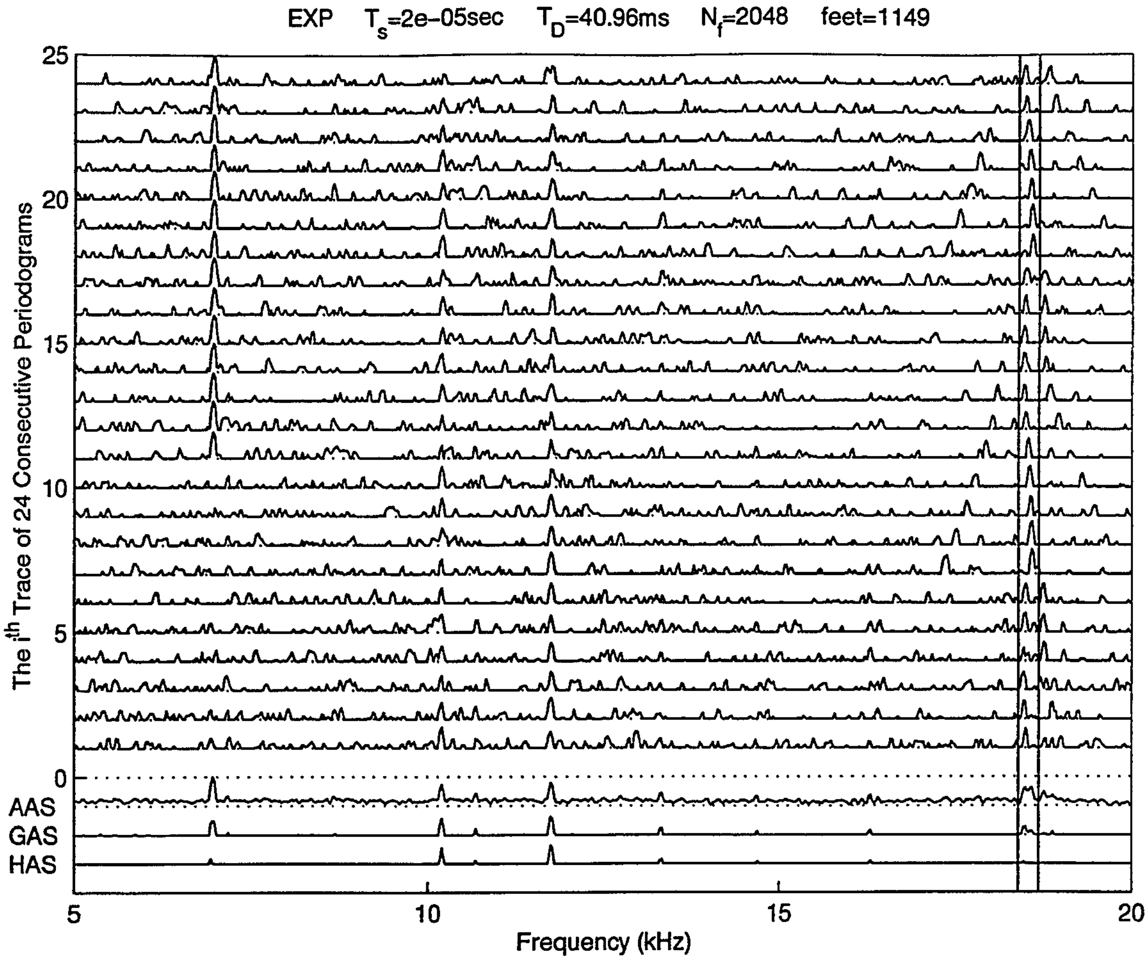

Figure 5.35: Rulers on Periodograms of a Strong Signal with Carrier Instability Before Adjustment

Finally, note the reduction in On-Off Modulation interference at 7 kHz by employing GAS and HAS rather than AAS.

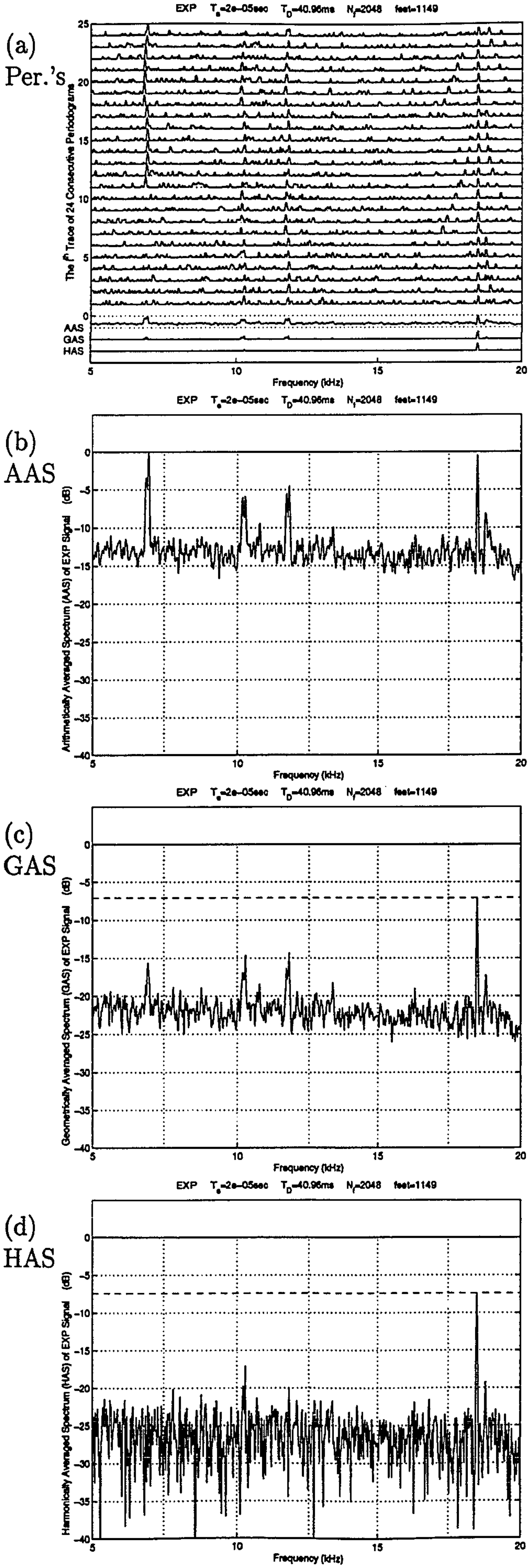

Figure 5.36: Adjustment for FME Signal

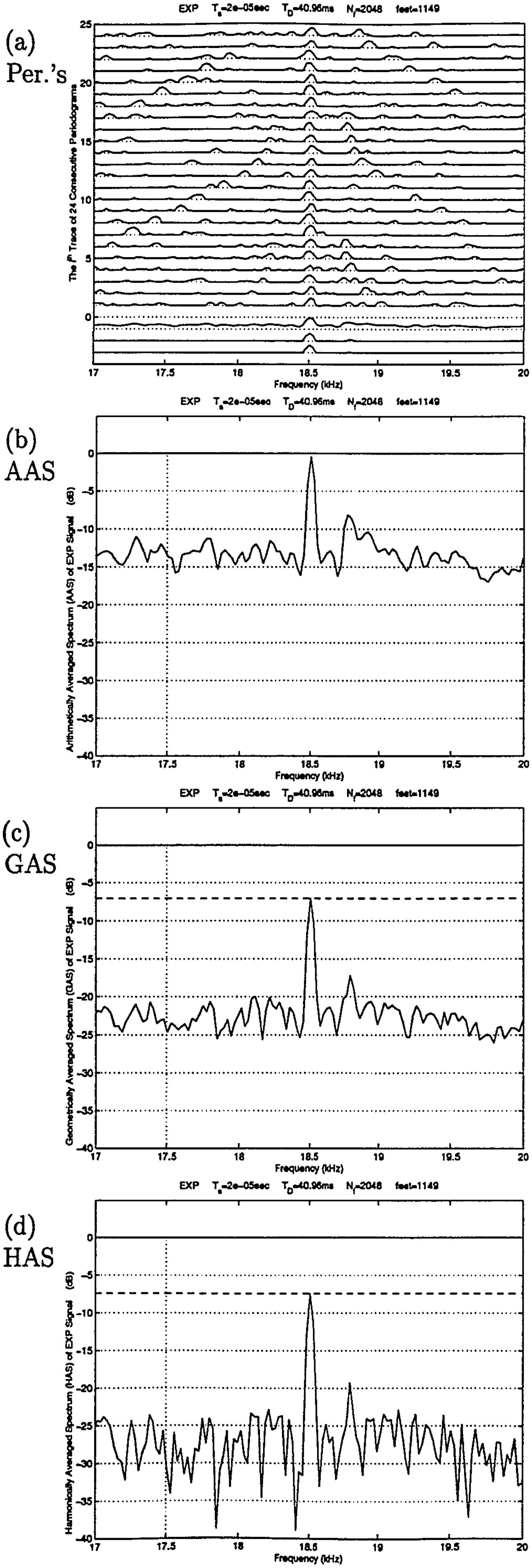

Figure 5.37: Details of the LHS Figure

5.9 Another Possible ELT Signal

In Fig. 5.38 (with details in Fig. 5.39), there is a possible example of an ELT signal obtained from real satellite pass data for which a model cannot presently be envisaged. The signal has two carrier peaks at about 14 kHz in each periodogram of Fig. 5.38(a) and both lower and upper sidebands which slide in towards the carrier peaks. Unfortunately, the CNDR is too low to make further identification easily possible.

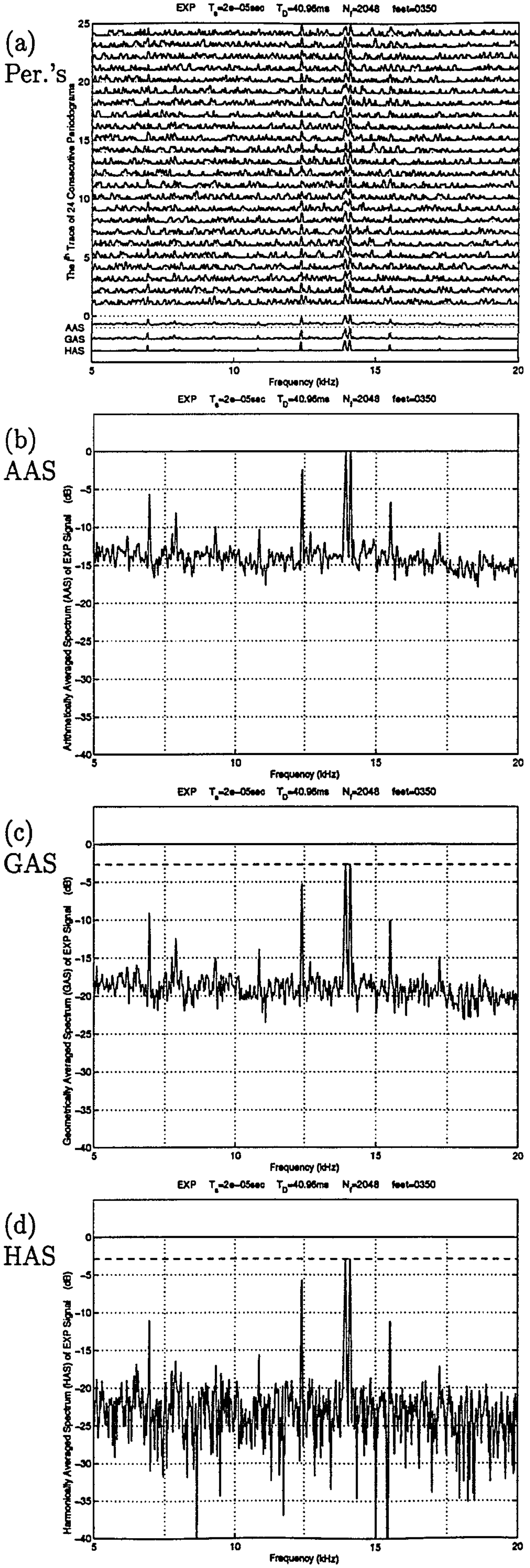

Figure 5.38: Possible ELT Signal

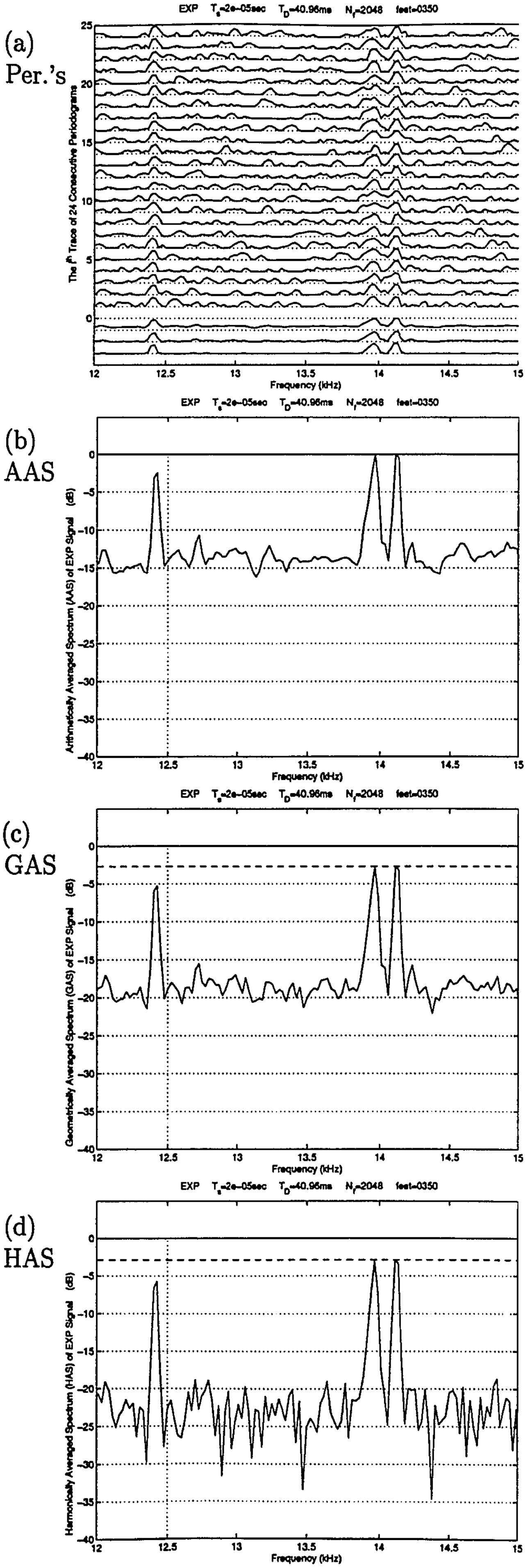

Figure 5.39: Details of the LHS Figure

5.10 Summary

This chapter examines real satellite pass data. The method of data collection and reformatting was described. Then, we demonstrated that Quiet Satellite Pass Data behaves much like an AWGN.

Next, we found that the investigation for AM Carrier interference including Single Carrier interference with strong AM and Single Carrier interference with weak AM, On-Off Modulation interference, and Swept Carrier interference closely match the corresponding predictions offered in Chapter 4. Regarding these 3 kinds of interference, the results provided in this chapter can be listed as follows: (1) Carrier interference with strong AM can be detected since at the carrier frequency of the interference, AAS is substantially larger than GAS which is larger than HAS as predicted theoretically and verified by computer simulation. (2) Carrier interference with weak AM can be detected since at the carrier frequency of the interference, AAS, GAS and HAS are almost equal as predicted theoretically and verified by computer simulation. (3) The performance of GAS or HAS is superior to that of AAS in terms of On-Off interference suppression. (4) GAS and HAS detect the carrier peak of ELT signals while AAS fails for Swept Carrier interference as predicted theoretically and verified by computer simulation.

We also studied Random interference in this chapter. The conclusion here is that GAS and HAS enhance carrier peaks in Random interference.

For real ICE signal data, the heights of the carrier peaks calculated by AAS, GAS, and HAS are almost equal while by using GAS and HAS, the sideband levels are decreased from the sideband level in AAS, resulting in improved detection of carrier peaks. For real NIC signal data, GAS and HAS may eliminate the carrier peak if the carrier peak varies strongly in magnitude. For FME which is a new ELT model, the AAS exhibits the expected FM shape while the GAS and HAS spectral averages tend to create a single peak. Obviously, a combination of all three averages could be of benefit to the identification of all ELT signals and the measurement of their carrier peaks.

Chapter 6

Conclusions

In this thesis, new processing techniques for detecting ELT signals in an interfering background are investigated, based on not only theoretical analyses but also computer simulations and experimental processing. The new methods involve the use of the Geometrically Averaged Spectrum (GAS) and the Harmonically Averaged Spectrum (HAS) in addition to the Arithmetically Averaged Spectrum (AAS).

6.1 From Theoretical Analyses

From theoretical analyses, it is concluded that:

1) Many problems plague the COSPAS/SARSAT system. Not the least of these is interference emanating from myriad sources on earth which adds to the uplinked ELT signals.

2) AAS, GAS, and HAS, which are three different methods of averaging consecutive periodograms, can provide different spectral estimates for ELT signals.

3) For the Ideal Coherent ELT (ICE) signals, the height of the carrier peak is maintained for all three methods while by using GAS and HAS, the sideband levels are decreased from the sideband level in AAS, resulting in improved detection in carrier peaks.

4) For the Non-Ideal Coherent (NIC) ELT signals, GAS and HAS produce a reduction in the height of the carrier peak relative to the height of the carrier peak in AAS as well as a reduction in sideband levels. However for certain cases, the reduction in sideband levels is larger than the reduction in carrier peak, resulting in enhanced detection in carrier peaks.

5) No spectral averaging method is able to detect carrier peaks for the Non-Coherent ELT (NCE) signals.

6) In addition to existing models for ELT signals, it is possible to suggest a new model in which the carrier frequency of the ELT signal changes during the sweep period. This new model is called the Frequency Modulated ELT (FME) signal and is found to exist in real SARSAT data.

7) Mathematical analyses, based on a set of spectral values at a certain frequency, shows why AAS, GAS, and HAS provide different estimates. The AAS estimate, which gives the arithmetically averaged value of the set of spectral values, is naturally used as the benchmark when we compare AAS, GAS, and HAS estimates. The values given by both the GAS and HAS estimates are less than that given by the AAS estimate, if the spectral values are different which is the usual case.

8) Stepsize and middlevalue are 2 new variables which affect the values of AAS, GAS, and HAS. Although the value of AAS depends on the middlevalue only, the

values of GAS and HAS depend on both of these 2 newly recognized variables rather than the stepsize or the middlevalue alone.

9) The value of AAS is independent of the value of the ratio of the stepsize divided by the middlevalue while the values of GAS and HAS are monotonically decreasing functions of the value of this ratio.

10) The amount of the reduction from AAS to GAS or the amount of the reduction from AAS to HAS are monotonically increasing functions of the value of the ratio of the stepsize divided by the middlevalue. From frequency to frequency, these reductions can be very significantly different from each other, since the values of this ratio can be very significantly different from each other.

11) One will benefit by using GAS or HAS rather than AAS whenever the amount of the reduction from AAS to GAS or HAS of the desired signal is less than the amount of the reduction from AAS to GAS or HAS of the undesired signal.

6.2 From Computer Simulations

From computer simulations, it is concluded that:

1) With a background of AWGN and for ICE and NIC signals, the GAS and HAS provide an improvement over the AAS in detecting the carrier peak of an ELT signal if the CNDR is large; *i.e.*, 18 to 25 dB-Hz. For low values of CNDR, say 15 dB-Hz, the performance of the AAS is better than either GAS or HAS.

2) In order to combat the sidelobe problem produced by CW interference, it is important to use a window which is not rectangular. A good strategy is to select

the minimum in 3-dB mainlobe bandwidth which still provides sufficient sidelobe reduction.

3) For heavy CW interference, the Hanning, Blackman, and Bohman windows are particularly attractive since they provide strong roll-off whereas many other windows (such as Riesz and Hamming) do not. The Blackman window used in the computer simulation and experimental processing is particularly attractive since it broadens the mainlobe thus reducing the effects of ELT carrier instability while providing strong rolloff of the sidelobes.

4) Background interference can be suppressed. In particular: For AM Carrier interference, GAS and HAS provide some margin of interference suppression for a single carrier interference with strong AM while GAS and HAS lose some margin of interference suppression for a single carrier interference with weak AM. Both GAS and HAS completely suppress On-Off Modulation interference, Swept Carrier interference, and Ringing Response interference, while AAS does not.

6.3 From Experimental Processings

From experimental processings, it is concluded that:

1) AWGN and quiet satellite pass data are spectrally similar.

2) Carrier interference with strong AM can be detected since at the carrier frequency of the interference, AAS is greatly larger than GAS which is greatly larger than HAS as predicted theoretically and verified by computer simulation.

3) Carrier interference with weak AM can be detected since at the carrier frequency

of the interference, AAS is almost equal to GAS which is almost equal to HAS as predicted theoretically and verified by computer simulation.

4) The performance of GAS or HAS is superior to that of AAS in terms of On-Off interference suppression.

5) GAS and HAS detect the carrier peak of ELT signals while AAS fails for Swept Carrier interference as predicted theoretically and verified by computer simulation.

6) GAS and HAS enhance carrier peaks in Random interference.

7) For real ICE signals, the heights of the carrier peaks offered by AAS, GAS, and HAS are almost equal to each other while by using GAS and HAS, the sideband levels are decreased from the sideband level in AAS, resulting in improved detection in carrier peaks.

8) For real NIC signals, GAS and HAS may eliminate ELT carrier peaks if the carrier peak varies strongly in magnitude. That is, sometimes AAS is better than GAS and HAS.

9) For FME, which is a new ELT model, the AAS exhibits the expected FM shape while the GAS and HAS spectral averages tend to create a single peak.

6.4 Final Conclusion

The results of letting AAS, GAS, and HAS work together are compared to that of using only AAS in this thesis and reviewed from 3 aspects in this chapter. It is seen that the new strategy shows superior performance over the original method in a congested signal environment even though interference power exceeds ELT signal power.

Bibliography

[1] Werstiuk, H.:COSPAS-SARSAT: A System Overview, In Proc. Int. Electrical and Electronics Conf., Toronto, ON, Sept. 1983, 169-171.

[2] Werstiuk, H., and Winter, A. E.: The Search and Rescue Satellite (SARSAT) System Project, Presented at AGARD Symp. on Operational Modelling of the Aerospace Environment, Ottawa, ON, April, 1978.

[3] Bibby, R. J. and Kozminchuk, B. W.: The location accuracy performance of the Canadian 121.5 MHz COSPAS-SARSAT signal processor, In International Electrical, Electronics Conference Proceedings, Sept. 26-28, 1983, 176-179.

[4] Gallagher, B.: COSPAS-SARSAT: A beacon for those in distress, Journal of the British Interplanetary Society, v. 42, n. 6, June 1989, 291-296.

[5] Aksnes, K., Anderson, P. H., and Haugen, E.: A precise multipass method for satellite Doppler positioning, Celestial Mechanics, v. 44, n. 4, 1988/89, 317-338.

[6] B.L. Gambhir, R.G. Wallace, D.W. Affens, and J.F. Bellantoni, "Improved COSPAS/SARSAT Locating with Geostationary Satellite Data," *IEEE Trans-*

actions on Aerospace and Electronic Systems, Vol. AES-32, No. 4, (Oct. 1996), pp. 1405-1411

[7] http://psbsgi1.nesdis.noaa.gov:8080/SARSAT/dict.html

[8] http://psbsgi1.nesdis.noaa.gov:8080/SARSAT/sats.html

[9] http://psbsgi1.nesdis.noaa.gov:8080/SARSAT/history.html

[10] http://psbsgi1.nesdis.noaa.gov:8080/SARSAT/luts.html

[11] http://www.sarsat.noaa.gov/

[12] C.R. Carter, E. Casas and T. Chung, "Emergency Locator Transmitter (ELT) Signal Models for SARSAT," *Can. Elec. Eng. J.*, Vol. 11, No. 2, 1986, pp. 43-49. 1985.

[13] http://psbsgi1.nesdis.noaa.gov:8080/SARSAT/false.html

[14] C.R. Carter and T. Chung, "Interference in the 121.5/243 MHz SARSAT Frequency Bands," *IEEE Transactions on Aerospace and Electronic Systems,* Vol. AES-21, No. 6, (Nov. 1985), pp. 804-817

[15] P. Small, Mississauga firm mum as 3 rd plane in 2 years disappears, The Toronto Star, p. A3, October 20, 1996.

[16] Staff: Plane search ends. The Hamilton Spectator, (Thursday, Sept. 20, 1990), A4.

[17] Canadian Press : Signals snarl search for downed jet, The Hamilton Spectator, (Wednesday, Sept. 12, 1990), A1 and A4.

[18] Canadian Press: Pilot error blamed in ditching of plane. The Hamilton Spectator, (Friday, Nov. 2, 1990), D15.

[19] D. Roddy, *Satellite Communications*, Prentice Hall, 1989

[20] W.L. Pritchard and J.A. Sciulli, *Satellite Communication Systems Engineering*, Prentice-Hall, Inc., 1986

[21] T. Chung and C.R. Carter, "Basic Concepts in the Processing of SARSAT Signals," *IEEE Transactions on Aerospace and Electronic Systems,* Vol. AES-23, No. 2, (Mar. 1987), pp. 175-198

[22] K. Tomiyasu, "Tutorial Review of Synthetic-Aperture Radar (SAR) with Applications to Imaging of Ocean Surface," *Proceedings of the IEEE, 66* (May 1978), pp. 563-583.

[23] S. Haykin, *Communication Systems*, Second Edition, John Wiley & Sons, 1983

[24] E. Casas and C.R. Carter, "Emergency Locator Transmitter (ELT) Signal Models and Frequency Estimation for the Search and Rescue Satellite (SARSAT)," *Communications Research Laboratory,* No. CRL-118, August 1983.

[25] H. Martin, "A Generalized Model of Man Made Electrical Noise," *Proceedings of IEEE Symposium on Electromagnetic Compatibility,* Atlanta, GA, (June 20-22, 1978), pp.347-357

[26] Steven M. Kay, *Modern Spectral Estimation: Theory And Application*, Prentice-Hall, 1988.

[27] F.J. Harris, "On the Use of Windows for Harmonic Analysis with the Discrete Fourier Transform," *Proc. IEEE,* Vol. 66, pp. 51-83, Jan. 1978.

[28] *Honeywell Operator's Manual — Model 101 Tape Recorder/Reproducer*, Honeywell Test Instruments Division, Denver, Colorado, August, 1982.

[29] *Getting Started — Sound Blaster PCI128 and Creative Audio Software*, Creative Labs Inc. and Ensoniq Corp., Milpitas, CA., June, 1998.

[30] E. Beckenbach and R. Bellman, *An Introduction to Inequalities*, Random House, 1961.

[31] E.F. Beckenbach and R. Bellman, *Inequalities*, Second Revised Printing, Springer-Verlag, Berlin · Heidelberg · New York, 1965.

[32] D.S. Mitrinović in cooperation with P.M. Vasić, *Analytic Inequalities*, Springer-Verlag New York · Heidelberg · Berlin, 1970.

[33] P.S. Bullen, D.S. Mitrinović, and P.M. Vasić (Eds.), *Means and Their Inequalities*, D. Reidel Publishing Company, 1988.

[34] D.S. Mitrinović, J.E. Pečarić, and V. Volenec, *Recent Advances in Geometric Inequalities*, Kluwer Academic Publishers, 1989.

[35] G. Hardy, J.E. Littlewood, and G. Pólya, *Inequalities*, Second Edition, Cambridge Mathematical Library, Cambridge University Press, 1988.